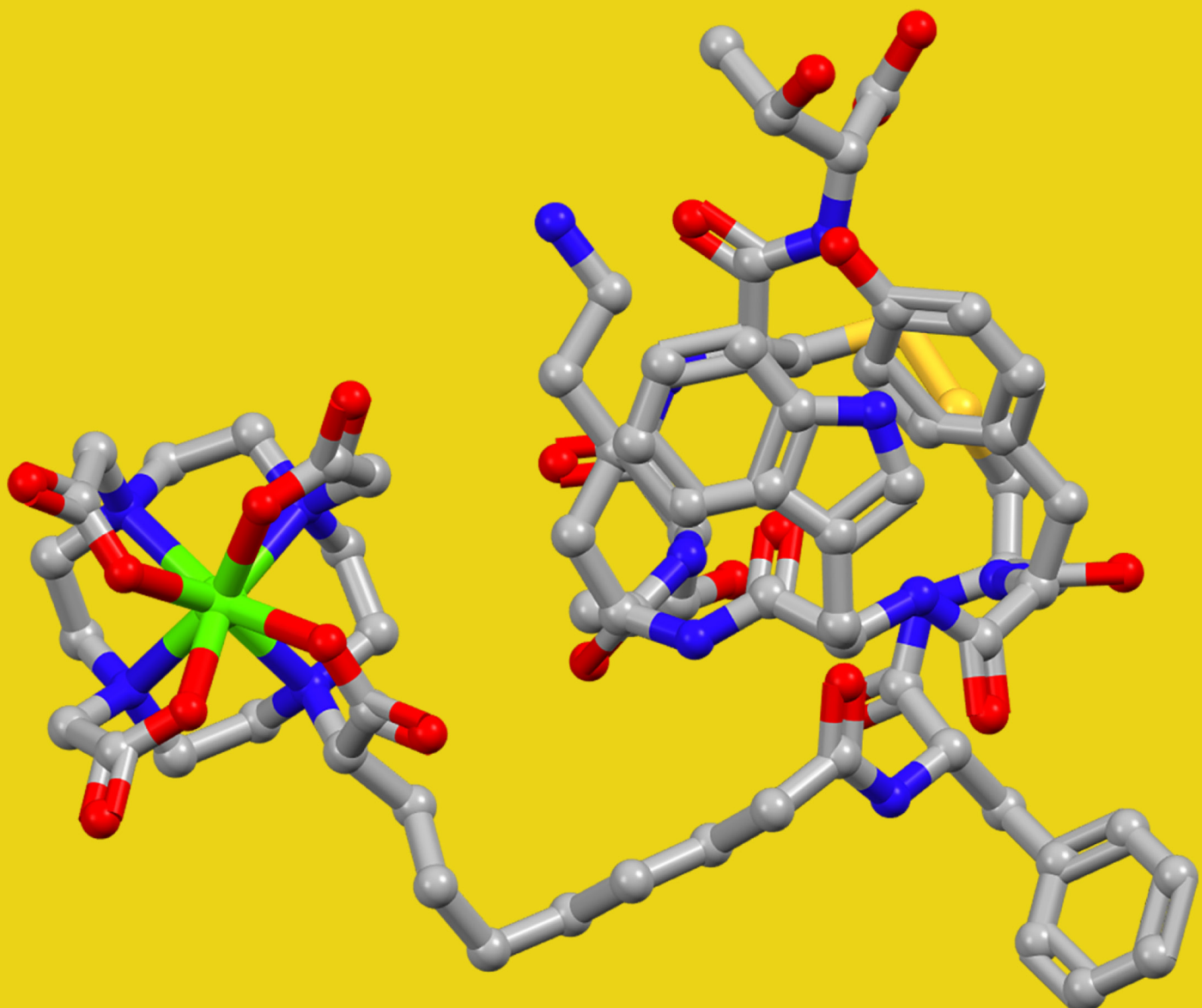


THE CHEMISTRY OF IMAGING PROBES

EDITED BY: Lorenzo Tei and Zsolt Baranyai

PUBLISHED IN: Frontiers in Chemistry





Frontiers Copyright Statement

© Copyright 2007-2018 Frontiers Media SA. All rights reserved.

All content included on this site, such as text, graphics, logos, button icons, images, video/audio clips, downloads, data compilations and software, is the property of or is licensed to Frontiers Media SA ("Frontiers") or its licensees and/or subcontractors. The copyright in the text of individual articles is the property of their respective authors, subject to a license granted to Frontiers.

The compilation of articles constituting this e-book, wherever published, as well as the compilation of all other content on this site, is the exclusive property of Frontiers. For the conditions for downloading and copying of e-books from Frontiers' website, please see the Terms for Website Use. If purchasing Frontiers e-books from other websites or sources, the conditions of the website concerned apply.

Images and graphics not forming part of user-contributed materials may not be downloaded or copied without permission.

Individual articles may be downloaded and reproduced in accordance with the principles of the CC-BY licence subject to any copyright or other notices. They may not be re-sold as an e-book.

As author or other contributor you grant a CC-BY licence to others to reproduce your articles, including any graphics and third-party materials supplied by you, in accordance with the Conditions for Website Use and subject to any copyright notices which you include in connection with your articles and materials.

All copyright, and all rights therein, are protected by national and international copyright laws.

The above represents a summary only. For the full conditions see the Conditions for Authors and the Conditions for Website Use.

ISSN 1664-8714
ISBN 978-2-88945-598-0
DOI 10.3389/978-2-88945-598-0

About Frontiers

Frontiers is more than just an open-access publisher of scholarly articles: it is a pioneering approach to the world of academia, radically improving the way scholarly research is managed. The grand vision of Frontiers is a world where all people have an equal opportunity to seek, share and generate knowledge. Frontiers provides immediate and permanent online open access to all its publications, but this alone is not enough to realize our grand goals.

Frontiers Journal Series

The Frontiers Journal Series is a multi-tier and interdisciplinary set of open-access, online journals, promising a paradigm shift from the current review, selection and dissemination processes in academic publishing. All Frontiers journals are driven by researchers for researchers; therefore, they constitute a service to the scholarly community. At the same time, the Frontiers Journal Series operates on a revolutionary invention, the tiered publishing system, initially addressing specific communities of scholars, and gradually climbing up to broader public understanding, thus serving the interests of the lay society, too.

Dedication to Quality

Each Frontiers article is a landmark of the highest quality, thanks to genuinely collaborative interactions between authors and review editors, who include some of the world's best academicians. Research must be certified by peers before entering a stream of knowledge that may eventually reach the public - and shape society; therefore, Frontiers only applies the most rigorous and unbiased reviews.

Frontiers revolutionizes research publishing by freely delivering the most outstanding research, evaluated with no bias from both the academic and social point of view. By applying the most advanced information technologies, Frontiers is catapulting scholarly publishing into a new generation.

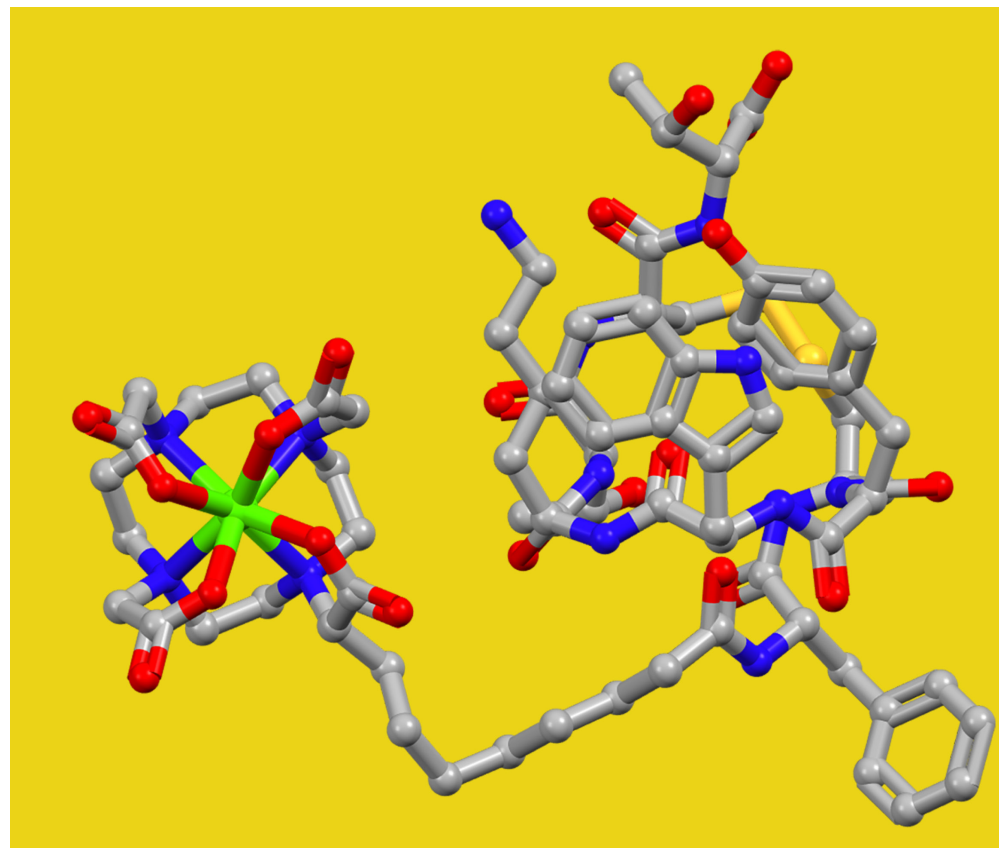
What are Frontiers Research Topics?

Frontiers Research Topics are very popular trademarks of the Frontiers Journals Series: they are collections of at least ten articles, all centered on a particular subject. With their unique mix of varied contributions from Original Research to Review Articles, Frontiers Research Topics unify the most influential researchers, the latest key findings and historical advances in a hot research area! Find out more on how to host your own Frontiers Research Topic or contribute to one as an author by contacting the Frontiers Editorial Office: researchtopics@frontiersin.org

THE CHEMISTRY OF IMAGING PROBES

Topic Editors:

Lorenzo Tei, Università degli Studi del Piemonte Orientale "Amedeo Avogadro", Italy
Zsolt Baranyai, Bracco Imaging, Italy



Targeted metal-based imaging probe.

Image: Lorenzo Tei and Zsolt Baranyai.

Over the past decades, the field of molecular imaging has been rapidly growing involving multiple disciplines such as medicine, biology, chemistry, pharmacology and biomedical engineering. Any molecular imaging procedure requires an imaging probe that is an agent used to visualize, characterize and quantify biological processes in living systems. Such a probe typically consists of an agent that usually produces signal for imaging purpose, a targeting moiety, and a linker connecting the targeting moiety and the signaling agent.

Many challenging problems of molecular imaging can be addressed by exploiting the great possibilities offered by modern synthetic organic and coordination chemistry and the powerful procedures provided by conjugation chemistry. Thus, chemistry plays a decisive role in the development of this cutting-edge methodology.

Currently, the diagnostic imaging modalities include Magnetic Resonance Imaging (MRI), Computed Tomography (CT), Ultrasound (US), Nuclear Imaging (PET, SPECT), Optical Imaging (OI) and Photoacoustic Imaging (PAI). Each of these imaging modalities has its own advantages and disadvantages, and therefore, a multimodal approach combining two techniques is often adopted to generate complementary anatomical and functional information of the disease. The basis for designing imaging probes for a given application is dictated by the chosen imaging modality, which in turn is dependent upon the concentration and localization profile (vascular, extracellular matrix, cell membrane, intracellular, near or at the cell nucleus) of the target molecule. The development of high-affinity ligands and their conjugation to the targeting vector is also one of the key steps for pursuing efficient molecular imaging probes.

Other excellent reviews, text and monographs describe the principles of biomedical imaging, focusing on molecular biology or on the physics behind the techniques. This Research Topic aims to show how chemistry can offer molecular imaging the opportunity to express all its potential.

Citation: Tei, L., Baranyai, Z., eds. (2018). *The Chemistry of Imaging Probes*. Lausanne: Frontiers Media. doi: 10.3389/978-2-88945-598-0

Table of Contents

06 Editorial: The Chemistry of Imaging Probes

Lorenzo Tei and Zsolt Baranyai

1. MAGNETIC RESONANCE IMAGING (MRI) AGENTS

Gd^{III}-BASED AGENTS

08 Optimizing the Relaxivity of MRI Probes at High Magnetic Field Strengths With Binuclear Gd^{III} Complexes

Loredana Leone, Giuseppe Ferrauto, Maurizio Cossi, Mauro Botta and Lorenzo Tei

Mn^{II}-BASED AGENTS

20 Effect of the Nature of Donor Atoms on the Thermodynamic, Kinetic and Relaxation Properties of Mn(II) Complexes Formed With Some Trisubstituted 12-Membered Macrocyclic Ligands

Zoltán Garda, Enikő Molnár, Ferenc K. Kálmán, Richárd Botár, Viktória Nagy, Zsolt Baranyai, Ernő Brücher, Zoltán Kovács, Imre Tóth and Gyula Tircsó

Eu^{II} AGENTS

34 Synthesis, Characterization, and Handling of Eu^{II}-Containing Complexes for Molecular Imaging Applications

Lina A. Basal and Matthew J. Allen

CHEMICAL EXCHANGE SATURATION TRANSFER AGENTS

46 ParaCEST Agents Encapsulated in Reverse Nano-Assembled Capsules (RACs): How Slow Molecular Tumbling Can Quench CEST Contrast

Annah Farashishiko, Jacqueline R. Slack, Mauro Botta and Mark Woods

FLUORINE-BASED AGENTS

53 Fluorinated Paramagnetic Complexes: Sensitive and Responsive Probes for Magnetic Resonance Spectroscopy and Imaging

Katie L. Peterson, Kriti Srivastava and Valérie C. Pierre

ULTRASOUND TRIGGERED THERANOSTIC AGENTS

74 Sonosensitive MRI Nanosystems as Cancer Theranostics: A Recent Update

Francesca Garello and Enzo Terreno

2. LANTHANIDE LUMINESCENT PROBES

81 Luminescence Properties of Self-Aggregating Tb^{III}-DOTA-Functionalized Calix[4]arenes

Florian Mayer, Sriram Tiruvadi Krishnan, Daniel T. Schühle, Svetlana V. Eliseeva, Stéphane Petoud, Éva Tóth and Kristina Djanashvili

3. DUAL MRI-SINGLE PHOTON EMISSION COMPUTED TOMOGRAPHY PROBES

- 90 A Novel Metal-Based Imaging Probe for Targeted Dual-Modality SPECT/MR Imaging of Angiogenesis**

Charalampos Tsoukalas, Dimitrios Psimadas, George A. Kastis, Vassilis Koutoulidis, Adrian L. Harris, Maria Paravatou-Petsotas, Maria Karageorgou, Lars R. Furenlid, Lia A. Moulopoulos, Dimosthenis Stamopoulos and Penelope Bouziotis

4. POSITRON EMISSION TOMOGRAPHY PROBES

- 105 Synthesis of Symmetrical Tetrameric Conjugates of the Radiolanthanide Chelator DOTPI for Application in Endoradiotherapy by Means of Click Chemistry**

Alexander Wurzer, Adrienn Vágner, Dávid Horváth, Flóra Fellegi, Hans-Jürgen Wester, Ferenc K. Kálmán and Johannes Notni

- 116 Equilibrium Thermodynamics, Formation, and Dissociation Kinetics of Trivalent Iron and Gallium Complexes of Triazacyclononane-Triphosphinate (TRAP) Chelators: Unraveling the Foundations of Highly Selective Ga-68 Labeling**

Adrienn Vágner, Attila Forgács, Ernő Brücher, Imre Tóth, Alessandro Maiocchi, Alexander Wurzer, Hans-Jürgen Wester, Johannes Notni and Zsolt Baranyai



Editorial: The Chemistry of Imaging Probes

Lorenzo Tei^{1*} and Zsolt Baranyai²

¹ Dipartimento di Scienze e Innovazione Tecnologica, Università del Piemonte Orientale "Amedeo Avogadro", Alessandria, Italy, ² Bracco Imaging (Italy), Colleretto Giacosa, Italy

Keywords: molecular imaging probes, chelating ligands, contrast agents, coordination chemistry, thermodynamic and kinetic stability

Editorial on the Research Topic

The Chemistry of Imaging Probes

Over the past decades, the field of molecular imaging (MI) has been rapidly growing involving multiple disciplines such as medicine, biology, chemistry, pharmacology and biomedical engineering. An *in vivo* MI protocol non-invasively provides visual and quantitative information on normal or pathological processes at the cellular or sub-cellular level. Currently, molecular imaging can be performed in the clinical environment via Magnetic Resonance Imaging (MRI), Optical Imaging (OI), Positron Emission Tomography (PET), Single-Photon Emission Computed Tomography (SPECT), Computed Tomography (CT) and Ultrasound (US). Each of these imaging modalities has its own advantages and disadvantages, and therefore, a multimodal approach combining two techniques is often adopted to generate complementary anatomical and functional information of the disease (Anderson and Lewis, 2017).

The key requirement for any molecular imaging procedure is a chemical agent, called the imaging probe. This probe typically consists of two chemical entities: one that produces a signal for imaging and another, a targeting vector, which enables the probe to specifically visualize, characterize and quantify biological processes in living systems. The optimization of the probes involves several different aspects ranging from the design of imaging units that exhibit enhanced sensitivity and lower toxicity, to the control of the structural and electronic features of the targeting moiety responsible for the molecular recognition (Long and Wong, 2015). In this research topic we present a series of original research and review articles that summarize the chemistry of molecular imaging, both in terms of optimization of the MI probe and in terms of application of different imaging techniques such as MRI, PET/SPECT, OI, and US.

The optimization of MRI contrast agents (CAs) is pursued to obtain more stable, safer and more efficient probes for potential application in molecular imaging. In particular, two dinuclear Gd(III) complexes and their relaxometric characterization have been reported by Leone et al. demonstrating that a significant contribution of second sphere water molecules is responsible for the strong relaxivity enhancement observed over a large range of magnetic field strengths. Regarding Mn(II) complexes of 12-membered macrocyclic ligands as a promising alternative to Gd-based CAs, Tircsó et al. have reviewed the relationship between ligand structure and physicochemical properties of the complexes. The rigidity of the macrocycle and proper selection of the donor atoms in the sidearm are the key structural features that control the thermodynamic and the dissociation kinetic properties of these macrocyclic Mn(II) complexes.

The synthesis, characterization and handling of Eu(II)-containing complexes have been reviewed by Basal and Allen showing how these air-sensitive probes can provide an intriguing and promising approach to new MRI molecular imaging procedures. The review especially focuses on the reduction of Eu(III) to produce Eu(II)-containing complexes and

OPEN ACCESS

Edited and reviewed by:

Luis António Dias Carlos,
University of Aveiro, Portugal

*Correspondence:

Lorenzo Tei
lorenzo.tei@uniupo.it

Specialty section:

This article was submitted to
Inorganic Chemistry,
a section of the journal
Frontiers in Chemistry

Received: 05 June 2018

Accepted: 08 June 2018

Published: 26 June 2018

Citation:

Tei L and Baranyai Z (2018) Editorial:
The Chemistry of Imaging Probes.
Front. Chem. 6:253.
doi: 10.3389/fchem.2018.00253

on the handling of Eu(II)-containing samples to prevent oxidation and obtain accurate data.

Chemical Exchange Saturation Transfer (CEST) continues to attract increasing attention as an alternative MR imaging modality to T_1 shortening agents. A contribution from Farashishiko et al. reports on an attempt to improve the sensitivity of these agents by incorporating a large payload of paraCEST agents into a reverse-assembled nanocapsule. Unfortunately, the result was not an amplification of the CEST effect, but quenching of the signal, attributed to an increase of the transverse relaxation rate of chelate protons caused by slow molecular tumbling of the complex in the nanosized system.

^{19}F -containing imaging probes can be advantageously employed in MRI and Magnetic Resonance Spectroscopy (MRS) because virtually there is no background ^{19}F MR signal *in vivo*. In the present topic, theories and strategies of improving the sensitivity of ^{19}F probes with paramagnetic metal ions have been reviewed by Peterson et al. In particular, the paper focuses on a theory that predicts the impact of certain molecular parameters on the sensitivity of fluorine-based probes.

The *in vivo* application of MRI—theranostic probes whose activation is induced by ultrasound, thermal or mechanical effects (sonosensitive probes) has been reviewed by Garello and Terreno. This work shows how these probes can be used for real-time monitoring of triggered drug release. These liposome based nano/microvesicles are composed of a biocompatible membrane responsive to US and an aqueous core loaded with a MRI probe and a therapeutic agent. A significantly better therapeutic effect was observed using US triggered drug release in comparison to traditional therapies.

The investigation of the luminescence properties of a Tb(III)-DOTA-calix[4]arene derivative was carried out by Mayer et al. with the aim to design dual MR/optical imaging probes. The paper shows how the calix[4]arene core with its four aromatic rings acts as an effective sensitizer of Tb-centred luminescence

but different substituents on the lower rim can cause micellar aggregation leading to a significant decrease in the intensity of Tb(III) luminescence.

A dual-modality iron oxide nanoplatform for *in vivo* targeted SPECT and MRI investigation of tumor vascularization has been developed by Tsoukalas et al. The NPs were coated with $^{99\text{m}}\text{Tc}$ radiolabeled Bevacizumab (BCZM) monoclonal antibodies (specific affinity to vascular endothelial growth factor—VEGF-A—receptor). Initial *in vivo* SPECT and MRI studies revealed the suitability of Fe_3O_4 -DMSA-SMCC-BCZM for targeted dual-modality imaging.

The use of conjugates comprised of more than one targeting biomolecule (multimers) is a well-established and straightforward way to enhance the target affinity and uptake of radiotherapeutics. For this purpose, Wurzer et al. designed a DOTA-tetraphosphinate chelator (DOTPI) possessing four terminal carboxylic acid moieties to obtain tetrameric bioconjugates. The favorable properties of the ^{177}Lu labeled tetrameric DOTPI(PSMA)₄ conjugates for targeted radionuclide therapy have been demonstrated in *in vitro* and *in vivo* studies.

In order to rationalize the influence of metal ion contamination [e.g., Ti(IV), Fe(III), Cu(II), Zn(II) or Al(III)] on ^{68}Ga labeling, the physicochemical properties of Ga(TRAP) and Fe(TRAP) (TRAP = triazacyclonane phosphinic acid) were investigated in detail by Vágner et al. Equilibrium and kinetic data showed that the stability constants and the dissociation rates of Ga(III)- and Fe(III)-complexes are very similar. However, the slower formation of Fe(TRAP) allows selective labeling of TRAP with ^{68}Ga (III) even in presence of Fe(III) contamination in the eluate.

AUTHOR CONTRIBUTIONS

The authors have made a substantial, direct, and intellectual contribution to the work, and approved it for publication.

REFERENCES

- Anderson, C. J., and Lewis, J. S. (2017). Current status and future challenges for molecular imaging. *Phil. Trans. R. Soc. A* 375:20170023. doi: 10.1098/rsta.2017.0023
- Long, N., and Wong, W.-T. (2015). *The Chemistry of Molecular Imaging*. New York, NY: John Wiley & Sons.

Conflict of Interest Statement: The authors declare that the research was conducted in the absence of any commercial or financial relationships that could be construed as a potential conflict of interest.

Copyright © 2018 Tei and Baranyai. This is an open-access article distributed under the terms of the Creative Commons Attribution License (CC BY). The use, distribution or reproduction in other forums is permitted, provided the original author(s) and the copyright owner are credited and that the original publication in this journal is cited, in accordance with accepted academic practice. No use, distribution or reproduction is permitted which does not comply with these terms.



Optimizing the Relaxivity of MRI Probes at High Magnetic Field Strengths With Binuclear Gd^{III} Complexes

Loredana Leone¹, Giuseppe Ferrauto², Maurizio Cossi¹, Mauro Botta¹ and Lorenzo Tei^{1*}

¹ Dipartimento di Scienze e Innovazione Tecnologica, Università degli Studi del Piemonte Orientale “Amedeo Avogadro,” Alessandria, Italy, ² Department of Molecular Biotechnology and Health Sciences, Molecular Imaging Centre, University of Torino, Torino, Italy

OPEN ACCESS

Edited by:

Carlos Lodeiro,
Faculdade de Ciências e Tecnologia
da Universidade Nova de Lisboa,
Portugal

Reviewed by:

Eurico J. Cabrita,
Faculdade de Ciências e Tecnologia
da Universidade Nova de Lisboa,
Portugal
Guo-Hong Tao,
Sichuan University, China

*Correspondence:

Lorenzo Tei
lorenzo.tei@uniupo.it

Specialty section:

This article was submitted to
Inorganic Chemistry,
a section of the journal
Frontiers in Chemistry

Received: 25 January 2018

Accepted: 19 April 2018

Published: 15 May 2018

Citation:

Leone L, Ferrauto G, Cossi M,
Botta M and Tei L (2018) Optimizing the Relaxivity of MRI Probes at High Magnetic Field Strengths With Binuclear Gd^{III} Complexes.
Front. Chem. 6:158.
doi: 10.3389/fchem.2018.00158

The key criteria to optimize the relaxivity of a Gd(III) contrast agent at high fields (defined as the region ≥ 1.5 T) can be summarized as follows: (i) the occurrence of a rotational correlation time τ_R in the range of ca. 0.2–0.5 ns; (ii) the rate of water exchange is not critical, but a $\tau_M < 100$ ns is preferred; (iii) a relevant contribution from water molecules in the second sphere of hydration. In addition, the use of macrocycle-based systems ensures the formation of thermodynamically and kinetically stable Gd(III) complexes. Binuclear Gd(III) complexes could potentially meet these requirements. Their efficiency depends primarily on the degree of flexibility of the linker connecting the two monomeric units, the absence of local motions and the presence of contribution from the second sphere water molecules. With the aim to maximize relaxivity (per Gd) over a wide range of magnetic field strengths, two binuclear Gd(III) chelates derived from the well-known macrocyclic systems DOTA-monopropionamide and HPDO3A (Gd₂**L1** and Gd₂**L2**, respectively) were synthesized through a multistep synthesis. Chemical Exchange Saturation Transfer (CEST) experiments carried out on Eu₂**L2** at different pH showed the occurrence of a CEST effect at acidic pH that disappears at neutral pH, associated with the deprotonation of the hydroxyl groups. Then, a complete ¹H and ¹⁷O NMR relaxometric study was carried out in order to evaluate the parameters that govern the relaxivity associated with these complexes. The relaxivities of Gd₂**L1** and Gd₂**L2** (20 MHz, 298 K) are 8.7 and 9.5 mM⁻¹ s⁻¹, respectively, +77% and +106% higher than the relaxivity values of the corresponding mononuclear GdDOTAMAP-En and GdHPDO3A complexes. A significant contribution of second sphere water molecules was accounted for the strong relaxivity enhancement of Gd₂**L2**. MR phantom images of the dinuclear complexes compared to GdHPDO3A, recorded at 7 T, confirmed the superiority of Gd₂**L2**. Finally, ab initio (DFT) calculations were performed to obtain information about the solution structure of the dinuclear complexes.

Keywords: gadolinium, macrocyclic ligands, multimeric contrast agents, magnetic resonance imaging-high field, chemical exchange saturation transfer, relaxometry, DFT

INTRODUCTION

The success of Magnetic Resonance Imaging (MRI) as a clinical diagnostic technique is mainly related to its superb temporal and spatial resolution that allow the clear delineation and differentiation of soft tissues and to its low invasiveness that leads to high patient acceptability. MRI contrast agents (CAs) are used for a large fraction of clinical scans (40–50%) to increase tissue contrast on relaxation weighted images by shortening the relaxation times of the water molecules in their proximity. Some 400 million doses of gadolinium have been administered for MRI scans since 1988. Currently, clinically employed CAs are low molecular weight, nonspecific Gd^{III} complexes with polyaminocarboxylate ligands that are capable to enhance the longitudinal relaxation rate ($R_1 = 1/T_1$) of water protons in the extracellular space. The increase in R_1 induced by one millimolar concentration of the paramagnetic ion is called relaxivity (r_1), a key parameter that depends on several structural and dynamic features of the Gd^{III} complex. Among the most important are the molecular rotation (τ_R), the electronic relaxation times ($T_{1,2e}$) and the residence lifetime of the coordinated water molecule(s) (τ_M) (Caravan et al., 1999; Botta and Tei, 2012; Merbach et al., 2013).

Typically, the commercially available Gd-based CAs have limited contrast enhancement capability (r_1 about 3–4 mM⁻¹s⁻¹ at 0.47 T and 37°C), much lower than that theoretically attainable (Geraldes and Laurent, 2009). Furthermore, their relaxivity values steadily decrease with increasing the magnetic field strength, e.g., r_1 of GdHPDO3A at 11.7 T and 37°C is 2.9 mM⁻¹s⁻¹ (Delli Castelli et al., 2013). Therefore, over the years, great research efforts have been made to optimize the structural and dynamic properties of the Gd^{III} complexes in order to achieve higher relaxivities, in particular in the high fields range. However, the interplay of the different contributions often resulted in non-optimized systems or probes that afford remarkable results only for a specific application. For example, blood pool contrast agents, such as MS-325, were designed to exploit their strong binding to slow tumbling molecules (i.e., Human Serum Albumin) for MR angiographic applications (Caravan et al., 2002), but this strategy gives high longitudinal relaxivity between 0.5 and 1.0 T and then sharply drops with increasing field thus, at fields > 1.5 T, macromolecular agents are hardly superior to small molecular weight chelates.

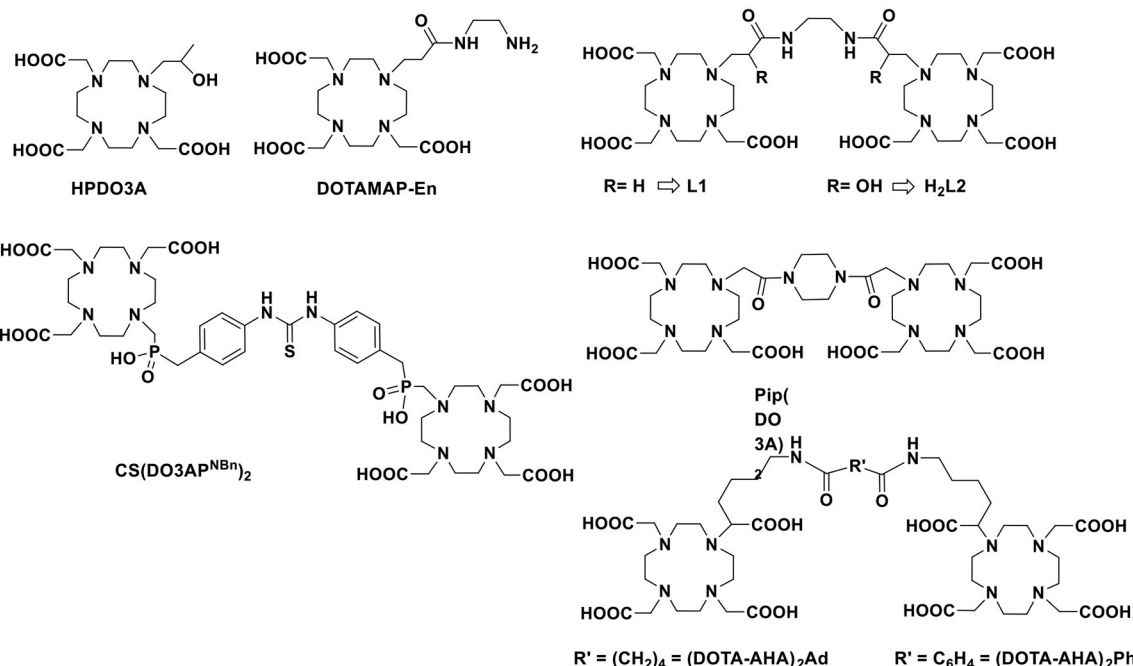
Nonetheless, although nowadays the majority of MRI scanners used in clinics operates at 1.5 T, more than one-quarter are 3 T machines and 7 T whole body human scanners are also available on the market. Therefore, a specific strategy for r_1 enhancement of metal-based probes at high field, i.e., a Gd-complex that will maintain its r_1 constant at least in the 1.5–3.0 T range, is extremely necessary to obtain a better contrast enhancement with lower amounts of CAs administered.

In recent reviews, it has been nicely shown that the use of systems with rotational correlation times in the range of ~0.5–2.0 ns and coordinated water molecule(s) in a relatively fast exchange rate ($\tau_M \sim 10$ –100 ns) would allow the increase of r_1 at magnetic field strengths > 1.5 T (Caravan et al., 2009; Helm, 2010). However, in accordance with recent investigations, we

surmised that ditopic Gd^{III} chelates with a molecular rotational correlation time (τ_R) in the range 0.2–0.5 ns (i.e., Gd-complexes with molecular mass in the range of ca. 1–3 kDa) and a short, rigid and hydrophilic linker between the two chelating units could represent an optimal solution. In fact, in such systems the rigidity of the spacer should reduce the local mobility of the monomeric Gd-units and enable a better correlation between global and local motions. Moreover, a hydrophilic spacer might favor the presence of a network of hydrogen bonded water molecules that can contribute greatly to the relaxivity through the second sphere contribution (Botta, 2000). A residence lifetime of the inner sphere water molecule (τ_M) preferably below 100 ns would complete the characteristics of these ditopic Gd^{III} chelates.

There are several approaches to design ditopic Gd-complexes as clearly delineated by Caravan and co-workers (Boros et al., 2012), being the one with an organic scaffold at the barycentre the most used strategy. In their example, they used an amino acid-like, fast exchanging Gd-complex (DOTAla) suitable for solid phase peptide synthesis and integration into hydrophilic polypeptide structures. They also investigated the possibility to rigidify the multimeric structure by forming disulphide bridges between cysteine moieties. Other examples of ditopic systems were reported by using GdDOTA-monoamide (Powell et al., 1996; Tei et al., 2009b), GdHPDO3A (Ranganathan et al., 1998), GdDOTA (Fontes et al., 2015) or GdDOTA-monophosphinate (Rudovsky et al., 2006) derivatives linked by aliphatic or heterocyclic groups (Scheme 1). The relaxivity enhancement of these systems as compared to monomeric Gd-complexes was often very much dependent on the water exchange rate or on the rigidity of the linker. We were also inspired by the recently reported self-assembling of two oppositely charged macrocyclic Gd-chelates that resulted in a small-sized dimeric system with high relaxivity at high frequencies thanks to improved inner- and second-sphere relaxivity contributions (Lawson et al., 2015). Remarkably, the additional contribution of about 30–40% from water molecules in the second coordination sphere was considered responsible of the increased performance of the ditopic probe.

Finally, we must consider that the kinetic inertness toward dissociation/transmetallation reactions is a fundamental parameter to consider in the design of novel MRI probe to aim for *in vivo* applications. Therefore, although a couple of examples of kinetically inert $q = 2$ Gd-complexes have been reported (Tircsó et al., 2006; Vagner et al., 2016), we will concentrate on two well-established $q = 1$ systems based on the macrocyclic systems HPDO3A (10-(2-hydroxypropyl)-1,4,7-tetraazacyclododecane-1,4,7-triacetic acid) and DOTAMAP (1,4,7,10-tetraazacyclododecane-1-propionamido-4,7,10-triacetic acid). These two chelates have been chosen because GdHPDO3A is the well-established, clinically approved MRI agent ProHance commercialized by Bracco (Delli Castelli et al., 2013) and GdDOTAMAP has been reported as a kinetically inert and fast exchanging Gd-complex (Tei et al., 2009a, 2015) that has also been recently exploited for the synthesis of high relaxivity multimeric systems (Boros et al., 2012). Thus, we present here the synthesis of two new ditopic chelators **L1** (DOTAMAP)₂ and **H₂L2** (HPA-DO3A)₂ (Scheme 1) and a complete ¹H and ¹⁷O NMR relaxometric study on the Gd^{III} complexes and a



SCHEME 1 | Chemical structure of chelating ligands discussed in this work.

CEST characterization on Eu₂L2. Furthermore, ab initio DFT calculations were used to obtain information on the structure of Gd₂L2 in solution, on the possible presence of second hydration sphere water molecules and on the internal mobility of the chelates about the linker.

MATERIALS AND METHODS

All chemicals were purchased from Sigma-Aldrich or Alfa Aesar unless otherwise stated and were used without further purification. The ¹H and ¹³C NMR spectra were recorded using a Bruker Advance III 500 MHz (11.4 T) spectrometer equipped with 5 mm PABBO probes and BVT-3000 temperature control unit. Chemical shifts are reported relative to TMS and were referenced using the residual proton solvent resonances. HPLC analyses and mass spectra were performed on a Waters HPLC-MS system equipped with a Waters 1525 binary pumps. Analytical measurements were carried out on a Waters Atlantis RPC18 column (5 μm 4.6 \times 100 mm) and on a Waters Atlantis prep T3 OBD (5 μm 19 \times 100 mm) for preparative purposes. Electrospray ionization mass spectra (ESI MS) were recorded using a SQD 3100 Mass Detector (Waters), operating in positive or negative ion mode, with 1% v/v formic acid in methanol as the carrier solvent.

1,2-Diacrylamidoethane

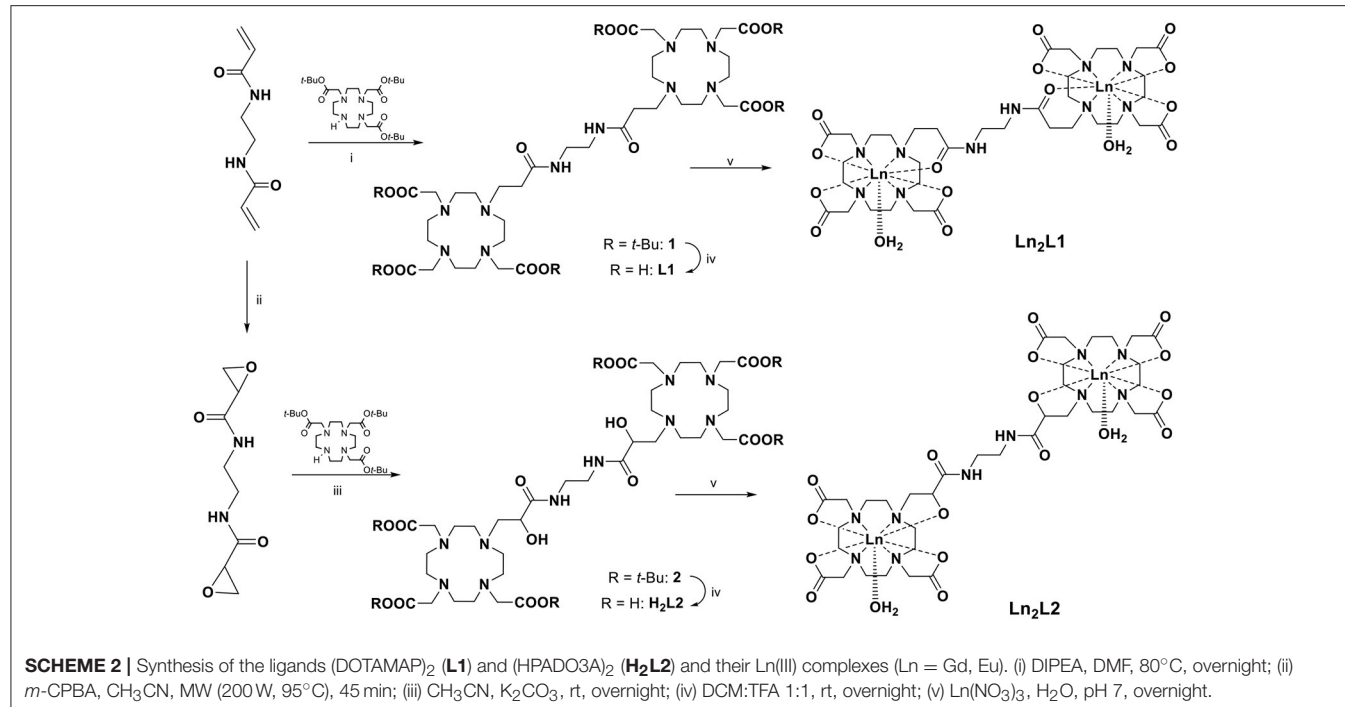
To a stirred solution of ethylenediamine (0.110 mL, 100 mg, 1.66 mmol) and K₂CO₃ (0.7 g, 5 mmol) in dry CH₃CN (2 mL), acryloyl chloride (0.3 mL, 0.33 g, 3.65 mmol) was added dropwise at 0°C and left stirring at r.t overnight, then filtered and

evaporated in vacuo to obtain the pure product. Analytical HPLC: Pump A: NH₄OAc (7 mM, pH 5.5); Pump B = ACN; flow = 1 mL/min; 0–10 min = 100% A; 10–15 min = 100% B; 15–24 min = 100% B; 24–25 min = 100% A; t_r = 17.18 min.

Yield 250 mg (90%); MS (ESI⁺): m/z: 169.17 [M+H]⁺ ¹H NMR (500MHz, CD₃CN, 25°C): δ = 6.85 (brs, 1H; NH-), 6.14 (m, ²J (H,H) = 2.5 Hz, ³J (H,H) = 4.8 Hz, 2H; CH₂ = CH), 5.59 (dd, ²J (H,H) = 2.5 Hz, ³J (H,H) = 4.8 Hz, 1H; CH₂ = CH-), 3.33 (d, ³J (H,H) = 2.8 Hz; 2H, CO-NH-CH₂) ppm. ¹³C{¹H}NMR (125MHz, CD₃CN, 25°C): δ = 166.6 (CO-NH-CH₂), 132.4 (CH₂ = CH), 125.9 (CH₂ = CH), 39.9 (-CO-NH-CH₂-) ppm.

Gd₂(DOTAMAP)₂ (Gd₂L1)

A solution of DO3A(t-Bu)₃ (50 mg, 0.097 mmol) and DIPEA (30 μL , 0.17 mmol) in DMF (2.5 mL) was added dropwise to 1,2-diacrylamidoethane (7 mg, 0.044 mmol) in DMF (1 mL) under N₂. The reaction was allowed to stir at 80°C overnight. Then, the crude mixture was evaporated in vacuo and the resulting oil was dissolved in a solution 1:1 of DCM: TFA and stirred at room temperature overnight. Then, the solvent mixture was evaporated under reduced pressure to obtain a yellow oil that was dissolved in H₂O. Complexation was performed directly on the unpurified sample: Ln(NO₃)₃ (Ln = Gd and Eu; 0.5 M aqueous solutions) was added to a solution of the ligand in water (2 mL). The pH was gradually adjusted to 7 and the solution stirred at room temperature overnight. The pH was then increased to 10 to precipitate excess Ln^{III} as hydroxide. The solution was centrifuged (4,000 rpm, 3 min, r.t.) and the supernatant filtered through a 0.2 μm filter. The pH was re-adjusted to 7 and the solvent removed in vacuo. The Ln^{III}-complexes were purified on



preparative HPLC with the following method: Pump A: NH₄OAc (7 mM, pH 5.5); Pump B = ACN; flow = 20 mL/min; 0–4 min = 100% A; 4–14 min = 100% B; 14–15 min = 100% B; 15–16 min = 100% A. Gd₂L1: t_r = 6.69 min; Yield: 30% (16 mg, 0.014 mmol). MS (ESI⁺): *m/z*: 585.2 [(M+2H)/2]⁺. Eu₂L1: t_r = 7.01 min Yield: 25% (12 mg, 0.010 mmol). MS (ESI⁺): *m/z*: 580.1 [(M+2H)/2]⁺.

N,N'-(ethane-1,2-diyl)bis(oxirane-2-carboxamide)

1,2-diacrylamidoethane (100 mg, 0.6 mmol) and *m*-chloroperbenzoic acid (1 g, 4.76 mmol) were dissolved in CH₃CN (3 mL) and reacted in a MW (CEM, DISCOVER SP) reactor (45 min, 95°C, 200 W). The solution was then evaporated in vacuo, dissolved in 1 mL H₂O:ACN (1:1) and purified in preparative HPLC with the following method: Pump A: NH₄OAc (7 mM, pH 5.5); Pump B = ACN; flow = 20 mL/min; 0–10 min = 100% A; 10–15 min = 100% B; 15–24 min = 100% B; 24–25 min = 100% A; t_r = 13.06 min. Forty-eight milligram (0.24 mmol, 40% yield) of a white powder were obtained. MS (ESI⁺): *m/z*: 201.25 [M+H]⁺; ¹H NMR (500 MHz, CD₃CN, 25°C): δ = 3.27 (m, 2H; CO-NH-CH₂), 3.20 (m, 1H; CO-CH-CH₂), 2.89, 2.73 (m,m, 2H; CO-CH-CH₂) ppm. ¹³C{¹H}NMR (125 MHz, CD₃CN, 25°C): δ = 170.6 (CO-NH-CH₂), 49.9 (CO-CH-CH₂) 47.6 (CO-CH-CH₂), 39.6 (CO-NH-CH₂) ppm.

(HPA-DO3A)₂(tBu)₆

N,N'-(ethane-1,2-diyl)bis(oxirane-2-carboxamide) (18 mg, 0.09 mmol) was dissolved in dry CH₃CN (5 mL) and K₂CO₃ (50 mg, 0.36 mmol) and DO3A(*t*-Bu)₃ (92 mg, 0.18 mmol) were added to the solution and stirred overnight at room temperature. After

filtration and evaporation under reduced pressure, the mixture was purified on silica (CH₃CN: NH₃ (10%)) to give the product 2. Analytical HPLC: Pump A: H₂O (0.1% TFA); Pump B = MeOH; flow = 1 mL/min; 0–3 min = 70% A; 3–18 min = 100% B; 18–24 min = 100% B; 24–25 min = 70% A; t_r = 14.58 min. 28 mg (0.023 mmol, 25% yield) of a pale yellow oil were obtained. MS (ESI⁺): *m/z*: 615.8 [(M+2H)/2]⁺. ¹H NMR (500 MHz, CD₃CN, 25°C): δ = 3.89 (dd, 2H; N-CH₂-CH-CO-), 3.29 (m, 4H; N-CH₂-CH-CO), 3.20 (m, 12H; N-CH₂-CO-OC(CH₃)₃), 2.68–2.84 (m, 32H; cyclen), 1.44 (s, 54 H; N-CH₂-CO-OC(CH₃)₃) ppm. ¹³C{¹H}NMR (125 MHz, CD₃CN, 25°C): δ = 174.8 (N-CH₂-CO-OC(CH₃)₃), 172.0 (N-CH₂-CH-CO); 81.1 (N-CH₂-CO-OC(CH₃)₃), 71.0 (-N-CH₂-CH-CO), 58.7 (N-CH₂-CH-CO), 58.1 (N-CH₂-CO-OC(CH₃)₃), 53.8, 52.9, 52.8.

(HPA-DO3A)₂ (**H₂L2**)

Compound 2 (28 mg, 0.023 mmol) was dissolved in a 1:1 solution of DCM:TFA and stirred overnight at room temperature. After evaporation under reduced pressure, ligand **H₂L2** was obtained in 95% yield (18 mg, 0.021 mmol). MS (ESI⁺): *m/z*: 447.8 [(M+2H)/2]⁺. ¹H NMR (500 MHz, CD₃CN, 25°C): δ = 4.62 (dd, 2H; N-CH₂-CH-CO), 4.12 (m, 4H; N-CH₂-CH-CO), 3.61 (m, 12H; N-CH₂-COOH, 12H), 3.15–3.50 (m, 32H; cyclen,) ppm. ¹³C{¹H}NMR (125 MHz, CD₃CN, 25°C): δ = 173.2 (N-CH₂-CH-CO), 173.2 (N-CH₂-CO-OH), 66.4 (N-CH₂-CH-CO), 55.4 (N-CH₂-CH-CO-), 54.4 (N-CH₂-COOH), 53.2, 51.0, 50.3, 48.7, (cyclen), 38.6 (CO-NH-CH₂) ppm.

Ln(III) Complexes

Ln(NO₃)₃ (Ln = Gd and Eu; 0.5 M aqueous solutions) was added to a solution of the ligand in water (2 mL). The pH was gradually adjusted to 7 and the solution stirred at room temperature

overnight. The pH was then increased to 10 to precipitate excess Ln^{III} as hydroxide. The solution was centrifuged (4,000 rpm, 3 min, r.t.) and the supernatant filtered through a $0.2\ \mu\text{m}$ filter. The pH was re-adjusted to 7 and the solvent removed in vacuo. Analytical HPLC: Pump A: H_2O ; Pump B = MeOH; flow = 1 mL/min; 0–3 min = 100% A; 3–18 min = 100% B. $\text{Gd}_2\text{L2}$: $t_r = 9.35$ min. MS (ESI $^+$): m/z : 600.98 [(M+2H)/2] $^+$; $\text{Eu}_2\text{L2}$: $t_r = 9.01$ min. MS (ESI $^+$): m/z : 596.68 [(M+2H)/2] $^+$. The concentration of Ln-complexes was assessed by using the Evan's method.

Chemical Exchange Saturation Transfer (CEST) Experiment

Z-spectra of $\text{Eu}_2\text{L2}$ water solutions at different pH in a range between 4.0 and 9.1 were acquired at 21°C , 7T on a Bruker Avance 300 spectrometer equipped with a microimaging probe. A frequency offset range of ± 100 ppm was investigated. A typical RARE (Rapid Acquisition with Refocused Echoes) spin-echo sequence with TE 3 ms, TR 5 s and RARE factor 16 was used. An isotropic 64×64 acquisition matrix with a FOV of 12 mm and a slice thickness of 1 mm was used. The whole sequence was preceded by a saturation scheme consisting of a continuous rectangular wave pulse 2 s long with a radiofrequency B_1 field of $12\ \mu\text{T}$. The Z-spectra were interpolated by smoothing splines to identify the zero-offset on a pixel-by-pixel basis of the bulk water and, then, to assess the correct ST% value over the entire range of frequency offsets investigated. Custom-made software, compiled in the Matlab platform (Mathworks Inc., Natick, MA), was used (Stancanello et al., 2008; Terreno et al., 2009). The extent of CEST effect was calculated as follows:

$$\text{ST\%} = \left(1 - \frac{M_s}{M_0} \right) \times 100 \quad (1)$$

where M_s is the intensity of the bulk water NMR signal after the irradiation on resonance ($\Delta\omega$) of the mobile proton pool and M_0 is the intensity of the bulk water NMR signal after the irradiation at the opposite frequency ($-\Delta\omega$).

Relaxometric Measurements

The water proton longitudinal relaxation rates as a function of the magnetic field strength were measured in non-deuterated aqueous solutions on a Fast Field-Cycling Stelar SmarTracer relaxometer (Stelar s.r.l., Mede (PV), Italy) over a continuum of magnetic field strengths from 0.00024 to 0.25 T (corresponding to 0.01–10 MHz proton Larmor frequencies). The relaxometer operates under computer control with an absolute uncertainty in $1/T_1$ of $\pm 1\%$. Additional longitudinal relaxation data in the range 20–70 MHz were obtained on a Stelar Relaxometer connected to a Bruker WP80 NMR electromagnet adapted to variable-field measurements. The exact concentration of Gd(III) was determined by measurement of bulk magnetic susceptibility shifts of a $t\text{BuOH}$ signal or by inductively coupled plasma mass spectrometry (ICP-MS, Element-2, Thermo-Finnigan, Rodano (MI), Italy). Sample digestion was performed with concentrated HNO_3 (70%, 2 mL) under microwave heating at 160°C for 20 min (Milestone MicroSYNTH Microwave lab station equipped with

an optical fiber temperature control and HPR-1000/6 M six position high pressure reactor, Bergamo, Italy). The ${}^1\text{H}$ T_1 relaxation times were acquired by the standard inversion recovery method with typical 90° pulse width of 3.5 μs , 16 experiments of 4 scans. The temperature was controlled with a Stelar VTC-91 airflow heater equipped with a calibrated copper-constantan thermocouple (uncertainty of $\pm 0.1^\circ\text{C}$).

Variable-temperature ${}^{17}\text{O}$ NMR measurements were recorded on a Bruker Avance III spectrometer (11.7 T) equipped with a 5 mm probe and standard temperature control unit. Aqueous solutions of the complexes containing 2.0% of the ${}^{17}\text{O}$ isotope (Cambridge Isotope) were used. The observed transverse relaxation rates were calculated from the signal width at half-height.

MR-Phantom Imaging

MR images of capillaries filled with 1.5 mM water solutions of $\text{Gd}_2\text{L1}$, $\text{Gd}_2\text{L2}$, or ProHance were acquired at 21°C , 7 T on a Bruker Avance 300 spectrometer equipped with a microimaging probe. $T_{2\text{W}}$ images were acquired by using a standard RARE (Rapid Acquisition with Refocused Echoes) sequence with the following parameters: TR = 5,000 ms, TE = 5.5 ms, FOV = 1×1 cm, slice thickness = 1 mm, RARE factor = 32, matrix size 128×128 . $T_{1\text{W}}$ images were acquired by using a standard MSME (multi-slice multi-echo) sequence with the following parameters: TR = 50 ms, TE = 3.3 ms, FOV = 1×1 cm, slice thickness = 1 mm, matrix size 128×128 . T_1 values were measured by using a Saturation Recovery Spin Echo sequence with the following parameters: TE = 3.8 ms, 16 variable TR ranging from 50 to 5,000 ms, FOV = 1×1 cm, slice thickness = 1 mm).

Theoretical Modeling

Theoretical calculations were performed with Gaussian16 program (Frisch et al., 2016) at the density functional theory (DFT) level with the hybrid functional B3LYP (Becke, 1993), comprising a part of the exact exchange along with Becke's exchange and Lee-Yang-Parr correlation functionals. To limit the computational burden, the following effective core potentials were used for all the heavy atoms, along with the corresponding valence basis sets: LANL2DZ (Hay and Wadt, 1985a,b; Wadt and Hay, 1985) for C, N, O and MWB53 (Dolg et al., 1989) for Gd; long range solvent effects were computed for some systems through the polarizable continuum model (PCM) (Cossi et al., 2003); dispersion energies were included in all the calculations with the atom-atom semiempirical method and parameters proposed by Grimme (Grimme et al., 2010). When computing the complexation energies, Boys' counterpoise correction was applied to compensate the basis set superposition error (BSSE).

RESULTS AND DISCUSSION

Ligand Design and Synthesis

The ligand L1 simply consists of two DOTA-monopropionamide units linked by an ethylene chain, therefore we expect that the relaxometric properties of the Gd complex would be consistent with a system with doubled molecular weight and similar

electronic and water exchange parameters with respect to the monomeric GdDOTAMAP complex (Tei et al., 2009a). On the other hand, in case of the ligand **H₂L2**, there is a substantial change with respect to HPDO3A: a hydroxypropylamide group replaced the hydroxypropyl group in order to generate electron withdrawing effect on the coordinated hydroxyl group and therefore stronger coordinating ability. Moreover, the hydrophilic nature of the amide group is expected to contribute to the overall relaxivity of the system through formation of hydrogen bonds to second sphere water molecules. The two monomeric hydroxypropylamideDO3A chelators were linked again by a short ethylene moiety.

Both chelates were obtained from a bis-acrylamide, ethylene-bis-acrylamide, through a multistep synthesis (**Scheme 2**). The synthesis of (DOTAMAP)₂ (**L1**) started from the Michael addition of the bis-acrylamide to two equivalents of DO3A(*t*Bu)₃ in dimethylformamide (DMF) in the presence of diisopropylethylamine (DIPEA) to give the protected ditopic ligand (**1**), which was immediately subjected to deprotection by reaction with a 1:1 mixture of trifluoroacetic acid (TFA) and dichloromethane (DCM). Then, complexation with Gd(NO₃)₃ was carried out in water at pH 7 and at room temperature. The purification by semi-preparative HPLC-MS was carried out on the final complex to obtain Gd₂**L1** in 22% overall yield. The protected and deprotected ditopic intermediates were not isolated due to the tendency to elimination of the pendant arm to form again the acrylamide. This tendency is highly reduced in the presence of the Gd-complex, although solutions of Gd₂**L1** left in water at pH 7 for more than one month revealed the presence of a small amount of elimination products. A similar approach was followed by Meade and co-workers (Rotz et al., 2015) for the synthesis of a *N*-propargylpropionamide derivative used for the preparation of Gd-labeled gold nanoparticles.

On the other hand, to obtain (HPA-DO3A)₂ (**H₂L2**), the bis-acrylamide was subjected to bis-epoxidation with meta-chloroperbenzoic acid (*m*-CPBA) in acetonitrile (ACN), using microwave heating (70 W, 90°C). After HPLC-MS purification the bis-epoxide was reacted with DO3A(*t*Bu)₃ in ACN in the presence of K₂CO₃ to give the protected HPA-DO3A dimer (**2**) which was purified by column chromatography and finally deprotected with a 1:1 mixture of TFA and DCM. Intermediates and final ligand were characterized by ESI mass spectrometry and ¹H and ¹³C NMR spectroscopy (Figures S7–S14). The Gd^{III} complex Gd₂**L2** was prepared at room temperature by adding Gd(NO₃)₃ to a solution of **H₂L2** while maintaining the pH at 6.5 with diluted NaOH. The excess of free metal ions in the solution was precipitated by the addition of NaOH up to pH 9 and the Gd-complex was isolated through a successive centrifugation, filtration, and lyophilization.

Chemical Exchange Saturation Transfer (CEST) Measurements on Eu₂**L2**

Lanthanide complexes of HPDO3A have been largely used as ParaCEST agents for cell labeling or extracellular/extravascular pH assessment in tumor models because the hydroxyl proton are close enough to the paramagnetic center to be able to generate CEST contrast (Nicholls et al., 2015; Pumphrey et al., 2016; Ferrauto et al., 2017). Moreover, as the exchange rate of the OH

proton is pH dependent, these chelates have been exploited as pH sensitive ParaCEST agents (Delli Castelli et al., 2014). Since the pK_a of these hydroxyl protons can be modulated by inserting electron withdrawing or donating groups in close proximity, the CEST contrast may be used to determine the deprotonation of the hydroxyl group. In the binuclear Ln₂**L2** complexes, the presence of an electron withdrawing amide group close to the hydroxyl group makes the OH proton very acid. Hence, it is reasonable to argue that this group is deprotonated at physiological pH values.

In order to obtain indirect insights into the exchangeable protons of the hydroxyl moieties, Z-and ST-spectra of Eu₂**L2** water solutions at different pH in a range between 4.0 and 9.1 were acquired. In CEST experiment, the resonance of exchangeable protons can be specifically saturated by a proper *rf* pulse. Saturated spins are transferred to bulk water through chemical exchange. In such a way, an indirect saturation of bulk water signal occurs, that can be observed in a ¹H-MR image. Z-spectra reports about bulk water signal as a function of the *rf* offset (Supplementary information, Figure S1). From Z-spectra, the symmetrical analysis allows obtaining ST-spectra, in which saturation transfer is plotted against the *rf* offset. Representative ST-spectra of Eu₂**L2** water solution at pH 4.0, 6.5 and 7.7 are reported in **Figure 1A**. The CEST effect is clearly visible at acid pH, barely visible at pH = 6.5 and completely absent at pH > 7.5. The ST% effect vs. pH is reported in **Figure 1B** showing the disappearance of CEST effect at neutral pH. Thus, this result is in line with the hypothesis of hydroxyl deprotonation at these pH values.

Relaxometric Measurements

The published value of *r*₁ for GdDOTAMAP-En (Tei et al., 2009a) and GdHPDO3A (Delli Castelli et al., 2013), at 0.47 T and 298 K, are 4.9 and 4.6 mM⁻¹ s⁻¹, respectively. These are typical values of the clinical MRI contrast agents, i.e., monohydrated low-molecular weight Gd^{III} chelates that tumble rapidly in solution and whose effectiveness as relaxation agents at high fields (≥ 0.47 T) is defined primarily by their rotational dynamics and thus by their molecular mass. In fact, the different *r*₁ values are associated with different values of τ_R , namely 79 and 65 ps for GdDOTAMAP-En and GdHPDO3A, respectively. The ionic (per Gd) *r*₁ values for the corresponding dimeric complexes, measured under identical experimental conditions, are 8.7 and 9.5 mM⁻¹ s⁻¹ for Gd₂**L1** and Gd₂**L2**, respectively. These values remain almost constant in the pH range 2–10 (Figure S2). These values correspond to relaxivity increases of + 77% and + 106% relative to the *r*₁ values of the corresponding mononuclear GdDOTAMAP-En and GdHPDO3A complexes. The relaxivity gain can be easily attributed to a longer value of the rotational correlation time associated with the increased molecular size, combined with the preservation of the same hydration state (*q* = 1) for each metal ion (Aime et al., 1992). From this information, we deduce that the binuclear complexes are remarkably rigid and compact, with a low degree of rotational flexibility about the linker. However, considering that only the inner-sphere contribution to relaxivity depends on τ_R , while the outer-sphere contribution remains almost unchanged, the

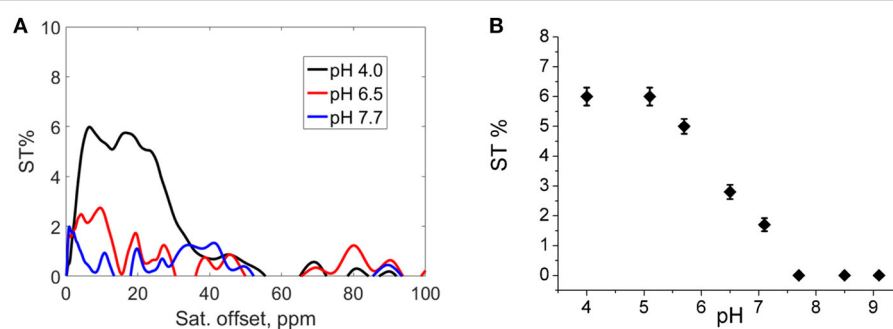


FIGURE 1 | (A) ST-spectra of Eu₂L2 water solution at pH = 4.0 (black line), pH = 6.5 (red line) and pH = 7.7 (blue line); **(B)** ST% vs. pH. (Experimental set-up: B₁ = 12 μT, [Eu₂L2] = 5 mM, T = 21°C).

particularly strong r_1 enhancement measured for Gd₂L2 might suggest the presence of an additional contribution.

To get more insight into the physico-chemical characteristics of these novel ditopic complexes, a detailed ¹H and ¹⁷O NMR relaxometric study was carried out. The magnetic field dependence of r_1 , the so-called nuclear magnetic relaxation dispersion (NMRD) profiles, were measured at 25 and 37°C in the proton Larmor frequency range 0.01–500 MHz, corresponding to magnetic field strengths varying between 2.34×10^{-4} T and 11.7 T (Figure 2). The shape of the NMRD profiles and their temperature dependence (r_1 decreases with increasing temperature, Figures S3, S4) reproduce the general behavior of small Gd^{III} complexes, characterized a plateau at low fields, a dispersion around 4–6 MHz and another region at high fields (> 20 MHz) where r_1 is almost constant or changes very little. The lower values of the relaxivity at 37°C, over the entire range of proton Larmor frequencies investigated, indicate that r_1 is not limited by the water exchange rate (*fast exchange regime*) but rather by the rotational motion, as for the related monomeric complexes. A least-square fit of the profiles was carried out in terms of the established theory of paramagnetic relaxation expressed by the Solomon-Bloembergen-Morgan (Bloembergen and Morgan, 1961) and Freed's (Freed, 1978) equations for the *inner-* (IS) and *outer sphere* (OS) proton relaxation mechanisms, respectively. Because of the large number of parameters involved in the fitting procedure, some of them are usually fixed to known or reasonable values. The hydration number q was fixed to 1; the distance between Gd³⁺ and the protons of the bound water molecule, r , was fixed to 3.0 Å; the distance of closest approach, a , of the *outer sphere* water molecules to Gd³⁺ was set to 4.0 Å and for the relative diffusion coefficient D standard values of 2.24 and 3.1×10^{-5} cm² s⁻¹ (298 and 310 K) were used. The fit was performed using as adjustable parameters τ_R and the electronic relaxation parameters Δ^2 (trace of the squared zero-field splitting, ZFS, tensor) and τ_V (correlation time for the modulation of the transient ZFS).

The residence lifetime of coordinated water, τ_M , does not affect the relaxivity of the systems under the regime of fast exchange. However, the accurate value of this parameter can

be obtained through the measurement of the temperature dependence of the ¹⁷O NMR transverse relaxation rate, R_2 , and paramagnetic shift, $\Delta\omega$, of the solvent water. The data were measured at 11.7 T on 20 and 16 mM solutions of Gd₂L1 and Gd₂L2, respectively, at neutral pH. The experimental data are often reported as reduced transverse relaxation rates, R_{2r} , defined as $1/T_{2r} = R_{2r} = R_{2p}/p_M$, where p_M is the molar fraction of inner-sphere water molecules. The reduced transverse ¹⁷O-relaxation rates and chemical shifts ($\Delta\omega_r$) measured for GdL1 and GdL2 are reported in Figures 3, 4. In both cases $1/T_{2r}$ increases with decreasing temperature over the temperature range studied (275–352 K), indicating high rate of exchange for the bound water molecule. The data were analyzed in terms of the Swift-Connick theory for ¹⁷O relaxation (Swift and Connick, 1962) using as fitting parameters Δ^2 , τ_V , the τ_M value at 298 K, its enthalpy of activation ΔH_M , the scalar Gd-¹⁷O_w coupling constant A/h . Moreover, the temperature dependence of τ_V and τ_R has been considered through their activation energies E_V , set to 1.0 kJ mol⁻¹, and E_R , fixed to 18.0 kJ mol⁻¹. The best-fit parameters are listed in Table 1 and compared with those previously reported for the related mononuclear complexes.

The k_{ex} value obtained for Gd₂L1 (1.0×10^8 s⁻¹; Table 1) is quite similar to that of the parent GdDOTAMAP-En complex, indicating that the formation of the ditopic complex did not significantly alter the coordination geometry around the metal ion. In the case of Gd₂L2, the residence lifetime of the bound water molecule is quite short (5.0 ns) thus suggesting that, unlike the case of the monomeric GdHPDO3A complex, the formation of the dimer involves the occurrence of a predominant population of fast-exchanging TSAP isomer.

The experimental NMRD curves were first analyzed with a model (Model 1) that takes into account the presence of only IS and OS contributions to relaxivity. The profiles are rather well reproduced with the set of parameters listed in Table 1, which clearly show that the r_1 values of the dimeric complexes and their frequency dependence may be attributed predominantly to the slowdown of the rotational motion and then to the longer τ_R values. For Gd₂L1 the increase in the τ_R value with respect to the value reported for GdDOTAMAP-En is 114%. Therefore, the binuclear complex presents a remarkable stereochemical rigidity

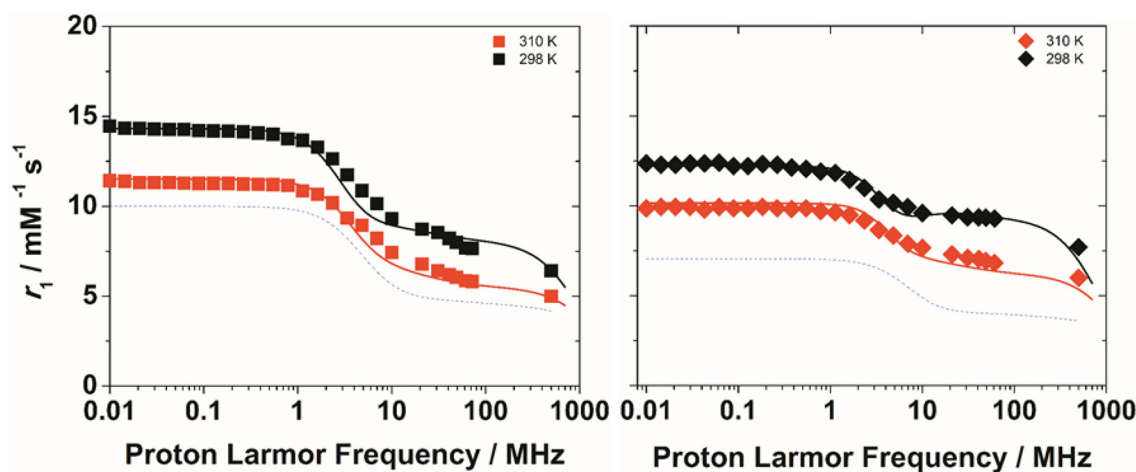


FIGURE 2 | ^1H NMRD profiles of $\text{Gd}_2\text{L1}$ (left) and $\text{Gd}_2\text{L2}$ (right) recorded at 298 K (black symbols) and 310 K (red symbols) and pH 7. The solid lines represent the best fitting results of the experimental data points with the parameters in **Table 1**, Model 1. The dotted lines correspond to the NMRD profile at 298 K of GdDOTAMAP-En (left) and GdHPDO3A (right).

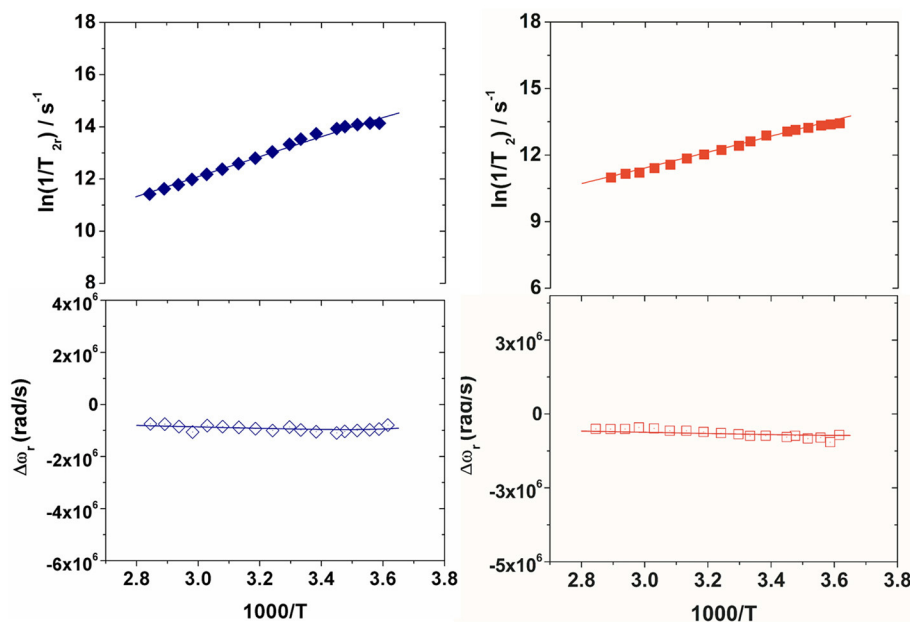


FIGURE 3 | Reduced transverse ^{17}O relaxation rates (top) and chemical shifts (bottom) measured at 11.74 T (pH 7) for $\text{Gd}_2\text{L1}$ (left) and $\text{Gd}_2\text{L2}$ (right). The solid lines correspond to the fits of the data as described in the text.

and the greater molecular mass, compared to the monomer, is entirely translated into a corresponding lengthening of τ_R . In the case of $\text{Gd}_2\text{L2}$ the value of τ_R is 215% longer than the value found for GdHPDO3A. Since the increase in the molecular mass is only of 114% is clear that the r_1 enhancement must be favored by an additional contribution. This might be identified in a sizeable second-sphere (SS) contribution, which corresponds to the presence of water molecules hydrating the complex at a distance from Gd^{3+} sufficiently short (ca. < 4 Å) and with a

residence time sufficiently long to be affected by the rotation (Botta, 2000). We analyzed the NMRD profiles considering also this possible contribution, expressed in terms of two additional parameters: the number q_{SS} of second sphere water molecules and their rotational correlation time, $\tau_{R(\text{SS})}$ (Model 2 in **Table 1**). The average distance from the paramagnetic center has been arbitrarily fixed at 3.5 Å, an intermediate value between those of water molecules in the inner (3.0 Å) and outer (4.0 Å) solvation shell (**Figure 4**). In the case of $\text{Gd}_2\text{L1}$ the best results are obtained

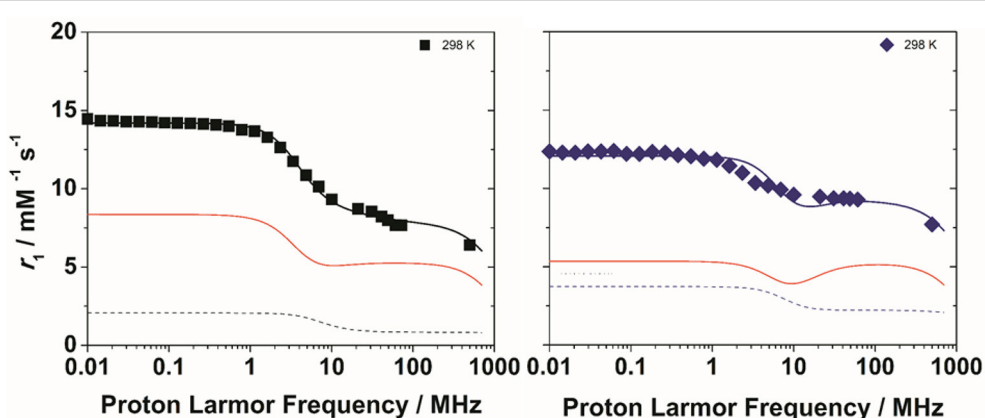


FIGURE 4 | ^1H NMRD profiles of $\text{Gd}_2\text{L1}$ (left) and $\text{Gd}_2\text{L2}$ (right) recorded at 298 K and pH 7. The solid lines represent the best fitting results of the experimental data points with the parameters in **Table 1**, Model 2. The red and dotted lines correspond to the inner and second sphere contributions to the relaxivity, respectively.

TABLE 1 | Best-fit parameters obtained from the analysis of the $1/T_1$ ^1H NMRD profiles (298 and 310 K) and ^{17}O NMR data for GdHPDO3A,^a GdDOTAMAP-En,^b Gd₂L1 and Gd₂L2^c.

Parameter	GdHPDO3A		GdDOTAMAP-En		$\text{Gd}_2\text{L1}$		$\text{Gd}_2\text{L2}$	
	SAP	TSAP			Model 1 (IS+OS)	Model 2 (IS+OS+SS)	Model 1 (IS+OS)	Model 2 (IS+OS+SS)
$298r_1$ ($\text{mM}^{-1} \text{s}^{-1}$)	4.6		4.9		8.7		9.5	
20 MHz								
$310r_1$ ($\text{mM}^{-1} \text{s}^{-1}$)	3.6		3.9		6.8		7.3	
20 MHz								
$298\tau_M$ (ns)	640	8.9	12		10.0 ± 1.2		5.0 ± 0.4	
$298\tau_R$ (ps)	65		79		169 ± 4	140 ± 2	205 ± 3	140^c
Δ^2 (10^{19}s^{-2})	9.9	1.5	3.9		1.3 ± 0.1	1.8 ± 0.1	2.0 ± 0.1	6.2 ± 0.3
$298\tau_V$ (ps)	8	30	15		40 ± 2	36 ± 2	40 ± 2	22 ± 1
ΔH_M (kJ mol $^{-1}$)	53 ^d	15 ^d	29.7		30.6 ± 1.1		29.5 ± 1.1	
A/h (10^6 rad s^{-1})	-3.5		-3.2		-3.5 ± 0.1		-3.4 ± 0.1	
q_{SS}	-		-		-	2	-	4
$298\tau_{R(SS)}$ (ps)	-		-		-	45 ± 2	-	60 ± 4

^a From Delli Castelli et al. (2013); ^b from Tei et al. (2009a); ^c The parameters fixed in the fitting procedure are: $q = 1$, $r_{\text{GdO}} = 2.5 \text{ \AA}$, $r_{\text{GdH}} = 3.0 \text{ \AA}$, $a_{\text{GdH}} = 4.0 \text{ \AA}$, $^{298}D_{\text{GdH}} = 2.24 \times 10^{-5} \text{ cm}^2 \text{ s}^{-1}$, $E_R = 18 \text{ kJ mol}^{-1}$, $E_V = 1 \text{ kJ mol}^{-1}$, $r_{\text{GdH(SS)}} = 3.8 \text{ \AA}$; ^d Activation energy, E .

by taking into account the contribution of two water molecules belonging to the SS and characterized by a rotational correlation time $\tau_{R(SS)}$ of 45 ps. This involves consequently a decrease in the global τ_R passing from 169 to 140 ps, a value that best fits the molecular size of the complex. The same value of τ_R was used in the analysis of the NMRD profile of $\text{Gd}_2\text{L2}$, obtaining the best result with the additional contribution of four SS water molecules with a $\tau_{R(SS)}$ of 60 ps. As it is clearly apparent from the plot of **Figure 5**, the SS contribution is rather small in the case of $\text{Gd}_2\text{L1}$, about 12% at 1.5 T and 310K, while it turns out to be very significant for $\text{Gd}_2\text{L2}$ as it can be attributed to it over 20% of the overall relaxivity measured. The greater weight of the SS contribution to $\text{Gd}_2\text{L2}$ is probably due to the presence of negative charges in the complex due to the deprotonation of the alcohol groups, in accordance with the CEST data.

MR Phantom Images

MR images of phantom containing glass capillaries filled with 1.5 mM water solutions of $\text{Gd}_2\text{L1}$, $\text{Gd}_2\text{L2}$, or GdHPDO3A were imaged at 7 T. T_{2w} and T_{1w} representative images are reported in **Figures 6A,B**, respectively. The Signal Intensity in T_{1w} image is higher in the two capillaries filled with dinuclear Gd-complexes (capillary 1 and 2 in **Figure 6**) with respect to that one filled with GdHPDO3A (capillary 3 in **Figure 6**). Furthermore, as expected, contrast enhancement provided by $\text{Gd}_2\text{L2}$ is visibly higher than that one provided by $\text{Gd}_2\text{L1}$.

Molecular Modeling on $\text{Gd}_2\text{L2}$

The geometry of isolated $\text{Gd}_2\text{L2}$ dimer was optimized at the DFT level, including a water molecule coordinated to each Gd^{3+} ion; to simulate the conditions at physiological pH, the

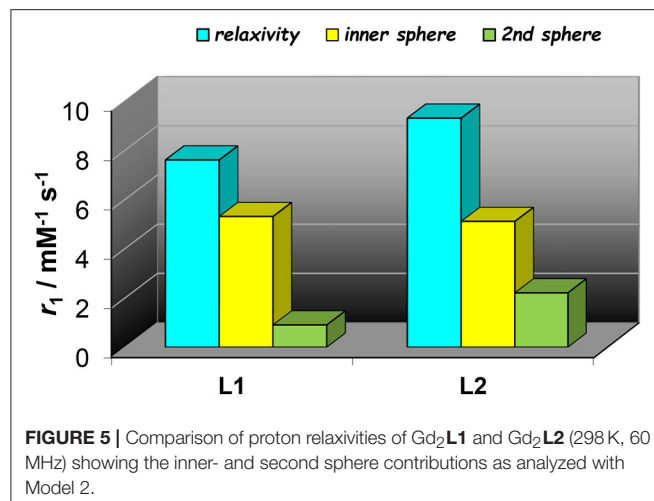


FIGURE 5 | Comparison of proton relaxivities of $\text{Gd}_2\text{L}1$ and $\text{Gd}_2\text{L}2$ (298 K, 60 MHz) showing the inner- and second sphere contributions as analyzed with Model 2.

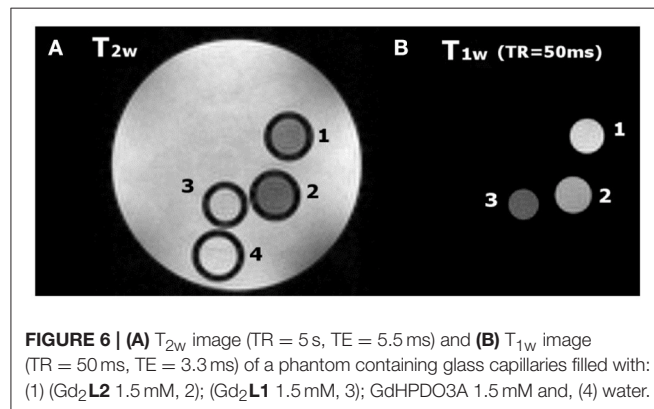


FIGURE 6 | (A) T_{2w} image ($TR = 5$ s, $TE = 5.5$ ms) and **(B)** T_{1w} image ($TR = 50$ ms, $TE = 3.3$ ms) of a phantom containing glass capillaries filled with: (1) ($\text{Gd}_2\text{L}2$ 1.5 mM), (2) ($\text{Gd}_2\text{L}1$ 1.5 mM), (3) GdHPDO3A 1.5 mM and, (4) water.

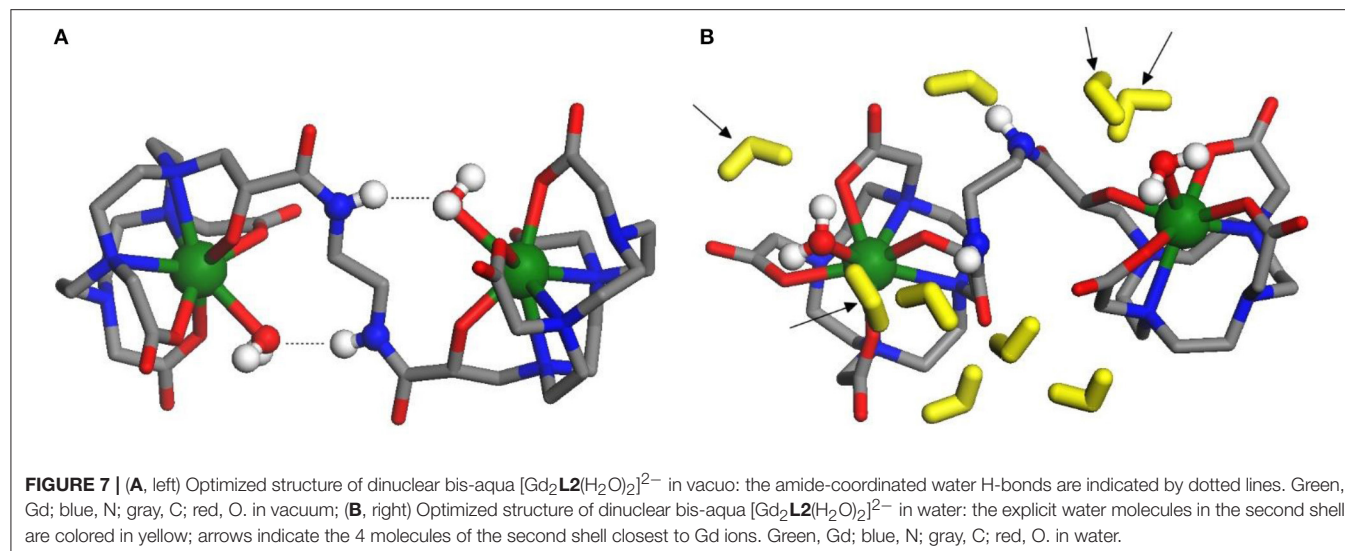
carboxylic and hydroxyl groups on both HPADO3A chelators were deprotonated, generating a double negative charge on the dimer. Then, the solvent (water) effects were included, re-optimizing the geometry with 9 water molecules in the second solvation shell and using the PCM model to account for the long range electrostatic interactions with the rest of the solvent. The optimized structures of the isolated and solvated dimer are depicted in Figures 7A,B, respectively. In both cases, one water molecule is coordinated to each metal ion: the complexation energies (obtained by removing one of the coordinated waters and recomputing the energy of the resulting dimer and of the water molecule alone) resulted -33.6 kJ/mol in vacuo and -22.0 kJ/mol in the solvent. Not surprisingly, solvent effects weaken the coordination bond since the separated fragments, especially the charged Gd^{III} complex, can be “surrounded” by the polarized continuum better than the initial structure, so their solvation energy is higher.

In the isolated dimer (Figure 7A), due to the H-bonds between amide groups and coordinated waters, the dihedral angle of the N-C-C-N branch connecting the two GdHPADO3A moieties is close to 180° , so that the $\text{Gd}-\text{H}_2\text{O}$ bond directions are almost opposite to each other. This arrangement changes when the solvent is added, since the amide groups prefer to

bind to water molecules in the second solvation shell, which are more free to move improving the H-bond stability: as a consequence, the dihedral angle is optimized around 104° and the $\text{Gd}-\text{H}_2\text{O}$ bonds are much more parallel than in the former case. The distance of the coordinated water hydrogen atoms from Gd is $2.8/2.9$ Å both in vacuo and in solution. In the latter structure, two water molecules of the second solvation shell are quite close to each GdHPDO3A moiety (indicated by arrows in Figure 7B): the distance of their hydrogens from Gd is $3.2-4.8$ Å, a range in fair agreement with the NMR relaxometric results above described. It is also interesting to compute the energy profile for the rotation of the GdHPDO3A ends around the N-C-C-N branch, since this parameter has been shown to be critical in assessing the relaxation efficacy. Thus, we have performed a rigid scan of the dinuclear $\text{Gd}_2\text{L}2$ complex with respect to this dihedral angle in vacuo (Figures S5) and in water (Figure S6): in the latter case, each second shell water molecule was attributed to the closer GdHPDO3A moiety and moved along with it during the scan. The energy curves along this rotation are quite different in vacuo and in the presence of solvent molecules. As discussed above, the isolated dimer is stabilized when the Gd-cages are oriented in opposite directions, and a barrier of around 40 kJ mol $^{-1}$ is required to break the intramolecular H-bonds and rotate the two units. On the other hand, more than one energy minimum is found for the solvated dimer, reflecting the larger number of intermolecular interactions available with the water molecules. The computed rotational barrier is higher, around 120 kJ mol $^{-1}$, although this result is likely overestimated for the presence of a limited number of solvent molecules, which do not describe the solvation shell for all the conformations with the same accuracy. In any case, we can safely conclude that a high rotational barrier is also expected in aqueous solution.

CONCLUSIONS

Dinuclear Gd^{III} and Eu^{III} complexes based on two well-established $q = 1$ monomeric chelates derived from the macrocyclic systems HPDO3A and DOTAMAP were successfully synthesized via a multi-step procedure. The macrocyclic structure of the complexes guarantees the excellent thermodynamic stability and kinetic inertness of the parent complexes. While the $\text{Ln}_2\text{L}1$ complexes are electrically neutral, with the propionamide moiety coordinating the Ln-center, from CEST measurements on the $\text{Eu}_2\text{L}2$ complex we could conclude that the hydroxyl groups of the ligand $\text{H}_2\text{L}2$ deprotonates around physiological pH and coordinate tightly the metal center; hence, the $\text{Ln}_2\text{L}2$ complexes are dianionic. This hypothesis finds further support on the ^1H and ^{17}O relaxometric data, which showed a fast water exchange rate in $\text{Gd}_2\text{L}2$, much faster than that found for the neutral GdHPDO3A, and a sizeable (ca. 20%) contribution of second sphere water molecules present in the surroundings of the GdHPADO3A cage. A model in which four SS water molecules at a relatively short distance from the Gd-center and with $\tau_{R(\text{SS})}$ of 60 ps was considered to account for the large relaxivity enhancement found for the dinuclear



$\text{Gd}_2\text{L}2$ with respect to the mononuclear GdHPDO3A ($r_1 = 9.5$ vs. $4.6 \text{ mM}^{-1}\text{s}^{-1}$, at 20 MHz and 298 K). This additional contribution was necessary because the relaxivity gain exceeds the increase in the molecular correlation time associated with the corresponding increase in molecular size. In the case of $\text{Gd}_2\text{L}1$, both models of analysis provide reasonable results, thus indicating the occurrence of a much lower SS contribution. The relaxometric results also confirm a high rigidity of both dinuclear complexes with a hindered or slow rotation through the linker connecting the two cages. These conclusions are further supported by the molecular modeling at the DFT level on $\text{Gd}_2\text{L}2$, which identifies a group of water molecules in well-defined positions around the metal center and at a distance quite comparable with that estimated from relaxometric data. In addition, the calculations highlight the occurrence of a high energy barrier for the rotation through the C-C bond of the ethylene linker.

These experimental results confirm that simple systems like dinuclear Gd-complexes afford optimal results in terms of relaxivity enhancement at high field strengths, as shown by the phantom MR-images at 7T, provided they are compact, stereochemically rigid, characterized by predominantly isotropic rotational motion. An additional relevant contribution arises from the presence of a well-defined second hydration sphere. $\text{Gd}_2\text{L}2$ features all these characteristics that provide an efficacy as relaxation agent over 110% higher (per Gd) than that of the clinically used MRI probes.

REFERENCES

- Aime, S., Botta, M., Ermondi, G., Fedeli, F., and Uggeri, F. (1992). Synthesis and NMRD studies of gadolinium(3+) complexes of macrocyclic polyamino polycarboxylic ligands bearing β -benzyloxy- α -propionic residues. *Inorg. Chem.* 31, 1100–1103. doi: 10.1021/ic00032a035
- Becke, A. D. (1993). Density functional thermochemistry. III. The role of exact exchange. *J. Chem. Phys.* 98, 5648–5652. doi: 10.1063/1.464913

ETHICS STATEMENT

As the study presented in the manuscript does not involve human or animal subjects, an ethics approval was not required as per institutional and national guidelines.

AUTHOR CONTRIBUTIONS

LL: performed chemical synthesis and relaxometric measurements; GF: performed the CEST experiments and the MR phantom Images. MC: performed the DFT study; LT, MB, and MC: performed interpretation of data and critically reviewed the manuscript; LT and MB: wrote the manuscript. All authors approved the final version of the manuscript.

ACKNOWLEDGMENTS

LT and MB acknowledge the support of the Università del Piemonte Orientale for (Research grant 2016). GF acknowledges Fondazione Italiana per la Ricerca sul Cancro (FIRC) for his fellowship.

SUPPLEMENTARY MATERIAL

The Supplementary Material for this article can be found online at: <https://www.frontiersin.org/articles/10.3389/fchem.2018.00158/full#supplementary-material>

- Bloembergen, N., and Morgan, L. O. (1961). Proton relaxation times in paramagnetic solutions. Effects of electron spin relaxation. *J. Chem. Phys.* 34, 842–850. doi: 10.1063/1.1731684
- Boros, E., Polasek, M., Zhang, Z., and Caravan, P. (2012). Gd(DOTAla): a single amino acid Gd-complex as a modular tool for high relaxivity MR contrast agent development. *J. Am. Chem. Soc.* 134, 19858–19868. doi: 10.1021/ja3019187m

- Botta, M. (2000). Second coordination sphere water molecules and relaxivity of gadolinium(III). *Eur. J. Inorg. Chem.* 2000, 399–407. doi: 10.1002/(SICI)1099-0682(200003)2000:3<399::AID-EJIC399>3.0.CO;2-B
- Botta, M., and Tei, L. (2012). Relaxivity enhancement in macromolecular and nanosized Gd^{III}-Based MRI contrast agents. *Eur. J. Inorg. Chem.* 1945–1960. doi: 10.1002/ejic.201101305
- Caravan, P., Cloutier, N. J., Greenfield, M. T., McDermid, S. A., Dunham, S. U., Bulte, J. W., et al. (2002). The interaction of MS-325 with human serum albumin and its effect on proton relaxation rates. *J. Am. Chem. Soc.* 124, 3152–3162. doi: 10.1021/ja017168k
- Caravan, P., Ellison, J. J., McMurry, T. J., and Lauffer, R. B. (1999). Gadolinium(III) Chelates as MRI contrast agents: structure, dynamics, and applications. *Chem. Rev.* 99, 2293–2352. doi: 10.1021/cr980440x
- Caravan, P., Farrar, C. T., Frullano, L., and Uppal, R. (2009). Influence of molecular parameters and increasing magnetic field strength on relaxivity of gadolinium- and manganese-based T1 contrast agents. *Contrast Media Mol. Imaging* 4, 89–100. doi: 10.1002/cmmi.267
- Cossi, M., Rega, N., Scalmani, G., and Barone, V. (2003). Energies, structures, and electronic properties of molecules in solution with the C-PCM solvation model. *J. Comp. Chem.* 24, 669–681. doi: 10.1002/jcc.10189
- Delli Castelli, D., Caligara, M. C., Botta, M., Terreno, E., and Aime, S. (2013). Combined high resolution NMR and ¹H and ¹⁷O relaxometric study sheds light on the solution structure and dynamics of the lanthanide(III) complexes of HPDO3A. *Inorg. Chem.* 52, 7130–7138. doi: 10.1021/ic400716c
- Delli Castelli, D., Ferrauto, G., Cutrin, J. C., Terreno, E., and Aime, S. (2014). *In vivo* maps of extracellular pH in murine melanoma by CEST-MRI. *Magn. Reson. Med.* 71, 326–332. doi: 10.1002/mrm.24664
- Dolg, M., Stoll, H., Savin, A., and Preuss, H. (1989). Energy-adjusted pseudopotentials for the rare earth elements. *Theor. Chim. Acta* 75, 173–194. doi: 10.1007/BF00528565
- Ferrauto, G., Aime, S., McMahon, M. T., Morrow, J. R., Snyder, E. M., Li, A., et al. (2017). “Chemical exchange saturation transfer (CEST) contrast agents,” in *Contrast Agents for MRI: Experimental Methods*, eds V. C. Pierre and M. J. Allen (Cambridge, UK: RSC Publishing), 243–317.
- Fontes, A., Karimi, S., Helm, L., Yulikov, M., Ferreira, P. M., and André J. P. (2015). Dinuclear DOTA-based Gd^{III} chelates – revisiting a straightforward strategy for relaxivity improvement. *Eur. J. Inorg. Chem.* 1579–1591. doi: 10.1002/ejic.201403159
- Freed, J. H. (1978). Dynamic effect of pair correlation functions on spin relaxation by translational diffusion in liquids. II. Finite jumps and independent t_1 processes. *J. Chem. Phys.* 69, 4034–4037. doi: 10.1063/1.436302
- Frisch, M. J., Trucks, G. W., Schlegel, H. B., Scuseria, G. E., Robb, M. A., Cheeseman, J. R., et al. (2016). *Gaussian 16, Revision A.03 Gaussian*. Wallingford, CT: Gaussian, Inc.
- Geraldes, C. F., and Laurent, S. (2009). Classification and basic properties of contrast agents for magnetic resonance imaging. *Contrast Media Mol. Imaging* 4, 1–23. doi: 10.1002/cmmi.265
- Grimme, S., Antony, J., Ehrlich, S., and Krieg, H. (2010). A consistent and accurate Ab initio parametrization of density functional dispersion correction (DFT-D) for the 94 elements H–Pu. *J. Chem. Phys.* 132:154104. doi: 10.1063/1.3382344
- Hay, P. J., and Wadt, W. R. (1985a). Ab initio effective core potentials for molecular calculations. Potentials for the transition metal atoms Sc to Hg. *J. Chem. Phys.* 82, 270–283.
- Hay, P. J., and Wadt, W. R. (1985b). Ab initio effective core potentials for molecular calculations. Potentials for K to Au including the outermost core orbitals. *J. Chem. Phys.* 82, 299–310. doi: 10.1063/1.448975
- Helm, L. (2010). Optimization of gadolinium-based MRI contrast agents for high magnetic-field applications. *Future Med. Chem.* 2, 385–396. doi: 10.4155/fmc.09.174
- Lawson, D., Barge, A., Terreno, E., Parker, D., Aime, S., and Botta, M. (2015). Optimizing the high-field relaxivity by selfassembling of macrocyclic Gd(III) complexes. *Dalton Trans.* 44, 4910–4917. doi: 10.1039/C4DT02971B
- Merbach, A. E., Helm, L., and Tóth, É. (2013). *The Chemistry of Contrast Agents in Medical Magnetic Resonance Imaging*, 2nd Edn. New York, NY: John Wiley & Sons.
- Nicholls, F. J., Ling, W., Ferrauto, G., Aime, S., and Modo, M. (2015). Simultaneous MR imaging for tissue engineering in a rat model of stroke. *Sci. Rep.* 5:14597 doi: 10.1038/srep14597
- Powell, D. H., Dhubghaill, O. M. N., Pubanz, D., Helm, L., Lebedev, Y. S., Schlaepfer, W., et al. (1996). Structural and dynamic parameters obtained from ¹⁷O NMR, EPR, and NMRD studies of monomeric and dimeric Gd³⁺ complexes of interest in magnetic resonance imaging: an integrated and theoretically self-consistent approach. *J. Am. Chem. Soc.* 118, 9333–9346. doi: 10.1021/ja961743g
- Pumphrey, A., Yang, Z., Ye, S., Powell, D. K., Thalman, S., Watt, D. S., et al. (2016). Advanced cardiac chemical exchange saturation transfer (cardioCEST) MRI for *in vivo* cell tracking and metabolic imaging. *NMR Biomed.* 29, 74–83. doi: 10.1002/nbm.3451
- Ranganathan, R. S., Fernandez, M. E., Kang, S. I., Nunn, A. D., and Ratsep, P. C., Pillai, K. M., et al. (1998). New multimeric magnetic resonance imaging agents. *Invest. Radiol.* 33, 779–797. doi: 10.1097/00004424-199811000-00002
- Rotz, M. W., Culver, K. S. B., Parigi, G., MacRenaris, K. W., Luchinat, C., Odom, T. W., et al. (2015). High relaxivity Gd(III)-DNA gold nanostars: investigation of shape effects on proton relaxation. *ACS Nano* 9, 3385–3396. doi: 10.1021/nn5070953
- Rudovský, J., Botta, M., Hermann, P., Koridze, A., and Aime, S. (2006). Relaxometric and solution NMR structural studies on ditopic lanthanide(III) complexes of a phosphinate analogue of DOTA with a fast rate of water exchange. *Dalton Trans.* 2323–2333. doi: 10.1039/b518147j
- Stancanello, J., Terreno, E., Delli Castelli, D., Cabella, C., Uggeri, F., and Aime, S. (2008). Development and validation of a smoothing-splines-based correction method for improving the analysis of CEST-MR images. *Contrast Media Mol. Imaging* 4, 136–149. doi: 10.1002/cmmi.240
- Swift, T. J., and Connick, R. E. J. (1962). NMR-relaxation mechanisms of O¹⁷ in aqueous solutions of paramagnetic cations and the lifetime of water molecules in the first coordination sphere. *J. Chem. Phys.* 37, 307–319. doi: 10.1063/1.1701321
- Tei, L., Baranyai, Z., Gaino, L., Forgács, A., Vágner, A., and Botta, M. (2015). Thermodynamic stability, kinetic inertness and relaxometric properties of monoamido derivatives of lanthanide(III) DOTA complexes. *Dalton Trans.* 44, 5467–5478. doi: 10.1039/C4DT03939D
- Tei, L., Gugliotta, G., Avedano, S., Giovenzana, G. B., and Botta, M. (2009a). Application of the Ugi four component reaction to the synthesis of ditopic bifunctional chelating agents. *Org. Biomol. Chem.* 7, 4406–4414 doi: 10.1039/b907932g
- Tei, L., Gugliotta, G., Baranyai, Z., and Botta, M. (2009b). A new bifunctional Gd^{III} complex of enhanced efficacy for MR-molecular imaging applications. *Dalton Trans.* 9712–9714. doi: 10.1039/b917566k
- Terreno, E., Stancanello, J., Longo, D., Delli Castelli, D., Milone, L., Sanders, H. M., et al. (2009). Methods for an improved detection of the MRI-CEST effect. *Contrast Media Mol. Imaging* 5, 237–247. doi: 10.1002/cmmi.290
- Tircsó, G., Kovacs, Z., and Sherry, A. D. (2006). Equilibrium and formation/dissociation kinetics of some Ln(III)PCTA complexes. *Inorg. Chem.* 45, 9269–9280. doi: 10.1021/ic0608750
- Vagner, A., Gianolio, E., Aime, A., Maiocchi, A., Toth, I., Baranyai, Z., et al. (2016). High kinetic 3¹S inertness of a bis-hydrated Gd-complex with a constrained AAZTA-like ligand. *Chem. Commun.* 52, 11235–11239. doi: 10.1039/C6CC04753J
- Wadt, W. R., and Hay, P. J. (1985). Ab initio effective core potentials for molecular calculations. Potentials for main group elements Na to Bi. *J. Chem. Phys.* 82, 284–298.

Conflict of Interest Statement: The authors declare that the research was conducted in the absence of any commercial or financial relationships that could be construed as a potential conflict of interest.

The reviewer, EC, and handling Editor declared their shared affiliation.

Copyright © 2018 Leone, Ferrauto, Cossi, Botta and Tei. This is an open-access article distributed under the terms of the Creative Commons Attribution License (CC BY). The use, distribution or reproduction in other forums is permitted, provided the original author(s) and the copyright owner are credited and that the original publication in this journal is cited, in accordance with accepted academic practice. No use, distribution or reproduction is permitted which does not comply with these terms.



Effect of the Nature of Donor Atoms on the Thermodynamic, Kinetic and Relaxation Properties of Mn(II) Complexes Formed With Some Trisubstituted 12-Membered Macrocyclic Ligands

OPEN ACCESS

Edited by:

Lorenzo Tei,
Università degli Studi del Piemonte
Orientale, Italy

Reviewed by:

Petr Hermann,
Charles University, Czechia
José Martins,
University of Minho, Portugal

***Correspondence:**

Ferenc K. Kálmán
kalman.ferenc@science.unideb.hu
Gyula Tircsó
gyula.tircso@science.unideb.hu

†Present Address:

Zsolt Baranyai,
Bracco Imaging Spa, Bracco
Research Centre, Colleretto Giacosa,
Italy

Specialty section:

This article was submitted to
Inorganic Chemistry,
a section of the journal
Frontiers in Chemistry

Received: 08 March 2018

Accepted: 31 May 2018

Published: 13 August 2018

Citation:

Garda Z, Molnár E, Kálmán FK,
Botár R, Nagy V, Baranyai Z,
Brücher E, Kovács Z, Tóth I and
Tircsó G (2018) Effect of the Nature of
Donor Atoms on the Thermodynamic,
Kinetic and Relaxation Properties of
Mn(II) Complexes Formed With Some
Trisubstituted 12-Membered
Macrocyclic Ligands.
Front. Chem. 6:232.
doi: 10.3389/fchem.2018.00232

Zoltán Garda¹, Enikő Molnár¹, Ferenc K. Kálmán^{1*}, Richárd Botár¹, Viktória Nagy¹,
Zsolt Baranyai^{1†}, Ernő Brücher¹, Zoltán Kovács², Imre Tóth¹ and Gyula Tircsó^{1*}

¹ Department of Inorganic and Analytical Chemistry, Faculty of Science and Technology, University of Debrecen, Debrecen, Hungary, ² Advanced Imaging Research Center, The University of Texas Southwestern Medical Center, Dallas, TX, United States

During the past few years increasing attention has been devoted to Mn(II) complexes as possible substitutes for Gd(III) complexes as contrast agents in MRI. Equilibrium ($\log K_{\text{MnL}}$ or pMn value), kinetic parameters (rates and half-lives of dissociation) and relaxivity of the Mn(II) complexes formed with 12-membered macrocyclic ligands were studied. The ligands were selected in a way to gain information on how the ligand rigidity, the nature of the donor atoms in the macrocycle (pyridine N, amine N, and etheric O atom), the nature of the pendant arms (carboxylates, phosphonates, primary, secondary and tertiary amides) affect the physicochemical parameters of the Mn(II) complexes. As expected, decreasing the denticity of DOTA (to afford DO3A) resulted in a drop in the stability and inertness of $[\text{Mn}(\text{DO3A})]^-$ compared to $[\text{Mn}(\text{DOTA})]^{2-}$. This decrease can be compensated partially by incorporating the fourth nitrogen atom into a pyridine ring (e.g., PCTA) or by replacement with an etheric oxygen atom (ODO3A). Moreover, the substitution of primary amides for acetates resulted in a noticeable drop in the stability constant (PC3AM^{H}), but it increased as the primary amides (PC3AM^{H}) were replaced by secondary ($\text{PC3AM}^{\text{Gly}}$) or tertiary amide ($\text{PC3AM}^{\text{Pip}}$) pendants. The inertness of the Mn(II) complexes behaved alike as the rates of acid catalyzed dissociation increased going from DOTA ($k_1 = 0.040 \text{ M}^{-1}\text{s}^{-1}$) to DO3A ($k_1 = 0.45 \text{ M}^{-1}\text{s}^{-1}$). However, the rates of acid catalyzed dissociation decreased from $0.112 \text{ M}^{-1}\text{s}^{-1}$ observed for the anionic Mn(II) complex of PCTA to $0.0107 \text{ M}^{-1}\text{s}^{-1}$ and $0.00458 \text{ M}^{-1}\text{s}^{-1}$ for the cationic Mn(II) complexes of PC3AM^{H} and $\text{PC3AM}^{\text{Pip}}$ ligands, respectively. In spite of its lower denticity (as compared to DOTA) the sterically more hindered amide complex ($[\text{Mn}(\text{PC3AM}^{\text{Pip}})]^{2+}$) displays surprisingly high conditional stability (pMn = 8.86 vs. pMn = 9.74 for $[\text{Mn}(\text{PCTA})]^-$) and excellent kinetic inertness. The substitution of phosphonates for the acetate pendant arms (DOTP and DO3P), however, resulted in a noticeable drop in the conditional

stability as well as dissociation kinetic parameters of the corresponding Mn(II) complexes ($[\text{Mn(DOTP)}]^{6-}$ and $[\text{Mn(DO3P)}]^{4-}$) underlining that the phosphonate pedant should not be considered as a suitable building block for further ligand design while the tertiary amide moiety will likely have some implications in this respect in the future.

Keywords: Mn(II) complexes, contrast agents for MRI, stability, inertness, relaxivity

INTRODUCTION

In the recent years, the research in the field of Mn(II) coordination chemistry has been intensified aiming to develop Mn(II) complexes suitable for *in vivo* application as magnetic resonance imaging (MRI) contrast agents (CA) (Drahos et al., 2012; Gale et al., 2015; Forgács et al., 2016; Garda et al., 2016). Gd(III) complexes are used as CAs in millions of doses. These agents had been assumed to be safe, however, nephrogenic systemic fibrosis (NSF), a devastating disease discovered in the late 90s has pointed out that they can cause serious health problems in patients with severe renal impairment (Idee et al., 2006). Thus, the design of safer CAs for MRI might be achieved by replacing the paramagnetic metal center with one that is better tolerated by the living systems (e.g., essential metal ions like Mn(II) or Fe(II)). The Mn(II) complexes are considered to be safe alternatives to Gd(III) in MRI as Mn(II) is an essential metal ion and therefore, biological systems can efficiently control its homeostasis (Murakami et al., 1996; Aime et al., 2002; Balogh et al., 2007; Drahos et al., 2011; Kálmán and Tircsó, 2012; Gale et al., 2015; Garda et al., 2016). However, the lack of ligand-field stabilization in high spin Mn(II) complexes results in lower thermodynamic stability compared to other divalent essential metal and the trivalent Gd(III) complexes. In addition, most Mn(II) chelates are kinetically labile. Due to these factors, the development of safe Mn(II) MRI CAs for *in vivo* applications remains challenging. We have shown 6 years ago that only *trans*-CDTA (*trans*-CDTA = *trans*-1,2-diaminocyclohexane-*N,N,N',N'*-tetraacetic acid) forms thermodynamically stable and kinetically inert Mn(II) chelate with acceptable relaxation enhancement out of several Mn(II) complexes of open-chain and AAZTA (AAZTA = 6-amino-6-methylperhydro-1,4-diazepine tetraacetic acid) ligands (Kálmán and Tircsó, 2012). This observation inspired the development of new open-chain ligands for Mn(II) complexation such as PyC3A, PhDTA, BEDIK (PyC3A = *N*-picolyl-*N,N',N'*-*trans*-1,2-cyclohexylenediamine-triacetate, PhDTA = *ortho*-phenylenediamine-*N,N,N',N'*-tetraacetic acid, BEDIK = 2-(aminomethyl)aniline-*N,N,N',N'*-tetraacetic acid), derivatives of 2,6-bis-aminomethyl pyridine and various open-chain ligands incorporating the picolinate moiety (Su et al., 2012; Forgács et al., 2015, 2017; Gale et al., 2015; Phukan et al., 2015; Wu et al., 2015; Póta et al., 2018) as well as redox activated Mn(II)-based MRI CA candidates (Loving et al., 2013). The design and synthesis of new bifunctional chelators (BFCs) derived from *trans*-1,2-diaminocyclohexane for targeted imaging applications has also been reported (Gale et al., 2015; Vanasschen et al., 2017).

Macrocyclic ligands have also been screened with the aim of finding a suitable macrocyclic platform for Mn(II) complexation. The investigated macrocyclic ligands were mostly the acetate, rarely the phosphonate and phosphinate derivatives of tacn (tacn = 1,4,7-triazacyclononane), cyclen and pyclen; efforts were also devoted to the investigation of some rigid pyridine-based 15-membered and other macrocyclic complexes formed with 9-, 12-, 14-, and 15-membered macrocyclic ligands (Dees et al., 2007; Drahos et al., 2010, 2011, 2012; Molnar et al., 2014; Forgács et al., 2016, 2017; Garda et al., 2016). The main goal of these studies was the development of a ligand platform that would allow a solvent molecule to be coordinated in the inner coordination sphere of the Mn(II) complexes, which is necessary to achieve appropriate relaxation enhancement. This was achieved in most cases; actually, some of the chelates, such as Mn(II) complexes of the rigid 15-PyaneN₅ (3,6,9,12,18-pentaazabicyclo[12.3.1]octadeca-1(18),14,16-triene) and 15-PyaneN₃O₂ (3,12,18-Triaaza-6,9-dioxabicyclo[12.3.1]octadeca-1(18),14,16-triene) was found to have not just one, but two bound water molecules. However, most of these complexes were kinetically too labile for *in vivo* applications. The only structures that represented an acceptable compromise between the apparently contradictory requirements (thermodynamic and redox stability/inertness/relaxivity) were the Mn(II) chelates of the *cis*-DO2A and the 15-PyaneN₃O₂ ligands (Dees et al., 2007; Drahos et al., 2010; Garda et al., 2016). The kinetic properties improved by the replacement of two carboxylate moieties with dimethylamide metal binding units (Forgács et al., 2016). The results obtained in our laboratory by studying monopicolimates of 9-, 12- and 14-membered macrocyclic ligands have also indicated that the best kinetic data were obtained for the Mn(II) complex of a 12-membered macrocyclic derivative, but further ligand optimization is required to identify the best candidates for *in vivo* applications (Molnar et al., 2014).

Since we have access to several 12-membered macrocyclic heptadentate ligands (DO3A, ODO3A, PCTA, DO3P, DO3AM, PC3AM^H, PC3AM^{Gly} PC3AM^{Pip}) from our previous studies performed with their Ln(III) complexes, we decided to study the stability and dissociation kinetic properties of the Mn(II) complexes formed with these chelators. We expected to gain more information on how the rigidity (DO3A vs. PCTA, or DO3AM^H vs. PC3AM^H), the nature of the donor atoms in the macrocycle (DO3A vs. ODO3A) and the nature of the pendant arms (DO3A vs. DO3P, i.e., replacement of acetate pendants by phosphonates), DO3A vs. DO3AM (replacement of acetate pendants by amides), or PCTA vs. PCTAM (replacement of acetate pendants by amides for rigidified macrocycle) and the nature of amide pendants (PC3AM^H vs. PC3AM^{Gly} or

PC3AM^{Pip} (replacement of primary amides by secondary and tertiary amides, respectively) affect the physicochemical properties of Mn(II) complexes. The goal of this project was to better understand how these (functional) modifications in the ligand structure affect equilibrium and kinetic behaviors of the corresponding Mn(II) complexes. Such data can help us to design ligands for improved Mn(II) complexation. It should be kept in mind, however, that some of these Mn(II) complexes would not be very efficient relaxation agents because of the lack of inner sphere water molecule. The formulae of the studied ligands are shown in **Figure 1**.

The stability constants of the Mn(II) complexes were determined by pH-potentiometry and/or ¹H relaxometry (measuring T_1 relaxation times and plotting $1/T_1$ values normalized to 1 mM paramagnetic substance as a function of pH). The kinetic inertness of the Mn(II) complexes have been evaluated by studying the acid catalyzed dissociation or metal/ligand exchange reactions occurring with Cu²⁺ (for [Mn(DOTAM)]²⁺, [Mn(DO3AM^H)]²⁺, [Mn(DO3A)]⁻, [Mn(PCTA)]⁻ and [Mn(ODO3A)]⁻ complexes), or transCDTA (as in the case of [Mn(DO3A)]⁻ chelate), or DTPA (as in the case of [Mn(DOTP)]⁶⁻ and [Mn(DO3P)]⁴⁻ chelates). Based on these data the half-lives were calculated at pH = 1 and 7.4 and compared to those of DO2A and DOTA derivatives published in the literature. The relaxivity values of some complexes were also determined in order to confirm that the relaxivity of the Mn(II) complexes formed with 12-membered heptadentate macrocyclic chelators is purely of outer-sphere in origin since the Mn(II) complexes of macrocyclic ligands with seven or more donor atoms are not expected to have an inner-sphere water molecule (Rocklage et al., 1989).

MATERIALS AND METHODS

Materials

The chemicals used in the experiments were of the highest analytical grade. The concentration of the MnCl₂, CuCl₂ and ZnCl₂ solutions was determined by using standardized Na₂H₂EDTA solution and eriochrome black T (Mn(II)), murexide (Cu(II)) and xylenolorange (Zn(II)) as indicator. The ligands were either prepared by following literature procedures (DOTAM, DO3A, DO3P, PCTA, ODO3A, PC3AM^{Gly}) (Amorim et al., 1988; Maumela et al., 1995; Aime et al., 1997; Siaugue et al., 2000; Sun et al., 2003; Rojas-Quijano et al., 2009; Nithyakumar and Alexander, 2016) or obtained from commercial sources (DO3AM^H - CheMatech, Dijon (France)). The PC3AM^H and PC3AM^{Pip} ligands were prepared by alkylating the pyclen macrocycle prepared according to literature description (Stetter et al., 1981) with a suitable bromoacetamide derivative (see the **Supplementary Material** for the detailed synthesis and analytical data) available from commercial sources or prepared by following literature synthesis (Kaupang and Bonge-Hansen, 2013).

Equilibrium Measurements

The concentration of the ligand solutions was determined by pH-potentiometric titration in the presence and absence of an excess (5–10 fold) of MnCl₂. For determining the protonation constants of the investigated ligands, pH-potentiometric titrations were

made by means of 0.2 M standardized NaOH in 2 and 3 mM ligand solutions in the pH-range of 1.75–11.85. All equilibrium measurements were performed at a constant 0.15 M NaCl ionic strength at 25 °C. The protonation and the stability constants of the Mn(II) complexes were determined by pH-potentiometric titrations (DOTP, DO3A, PCTA, ODO3A, DO3P) while owing to the slow formation rates of Mn(II) complexes formed with amide type ligands, the stability constants of DOTAM, DOTMA, DO3AM^H, PC3AM^H, PC3AM^{Gly}, PC3AM^{Pip} complexes were determined by out-of-cell pH-potentiometry in combination with ¹H relaxometry. The metal-to-ligand concentration ratio in the solutions was 1:1. For the calculation of protonation constants of the ligands and the log K_{MnL} and log K_{MnLH_i} values of the complexes, mL-pH data pairs (50–180), obtained in the pH range of 1.75–11.85 or r_{obs} -pH data pairs (10–15 batch samples) obtained in the pH range of 2–4.5 were used (the samples were equilibrated for 4–7 days). The equilibrium constants characterizing the deprotonation that occurs at basic pH were determined from the data obtained via direct pH-potentiometric titrations performed on the pre-formed complexes.

The pH-potentiometric titrations were carried out with a Metrohm 888 Titrando titration workstation using a Metrohm-6.0233.100 combined electrode. The samples (6.00 mL) were thermostated at 25 °C. The samples were stirred and kept under inert gas (N₂) to avoid the effect of CO₂. KH-phthalate (pH = 4.005) and borax (pH = 9.177) buffers were used for the pH-calibration. The method proposed by Irving et al. was used for the calculation of H⁺ concentrations from the measured pH values (Irving et al., 1967). A 0.01 M HCl (I = 0.15 M set with NaCl) solution was titrated with standardized NaOH solution of known concentration (approx. 0.2 M). The correction factor obtained as difference of calculated pH and measured pH values was used to calculate the [H⁺] in the samples. The ionic product of water was determined from the same titrations (HCl/NaOH) from the data collected in the pH range of 11.20–11.85.

The relaxometric data were collected using a Bruker Minispec MQ20 NMR relaxometer. The batch samples were equilibrated for 4–7 days (until no further change in the relaxivity was observed for the samples prepared in duplicates) and the T_1 values were measured multiple times. A datapoint plotted on figures represents an average of 5–6 T_1 measurements (**Figures S3–S9** in Supplementary Material). The data were fitted by using the molar r_{1p} relaxivity value of the MnCl₂ (7.92 M⁻¹s⁻¹ at 0.49 T and 25 °C). The equilibrium constants were calculated using the PSEQUAD program (Zékány and Nagypál, 1985).

Kinetic Measurements

The dissociation reactions were followed by UV-vis spectrophotometry at 269 nm for the pyclen derivatives or at 300 nm for other complexes in the pH range of 3.6–5.0 for the exchange reactions with Cu(II) and up to pH = 6.0 when Zn(II) was used as a ligand scavenger. The acid catalyzed dissociation reactions were performed in the HCl concentration range of 0.05–1.0 M. The concentration of the complexes in the samples was 0.25 mM, while the concentration of the exchanging metal ion in the metal initiated transchelation reactions was 10–40 times higher to ensure pseudo-first-order conditions. Relaxometry was used to follow the transchelation reactions

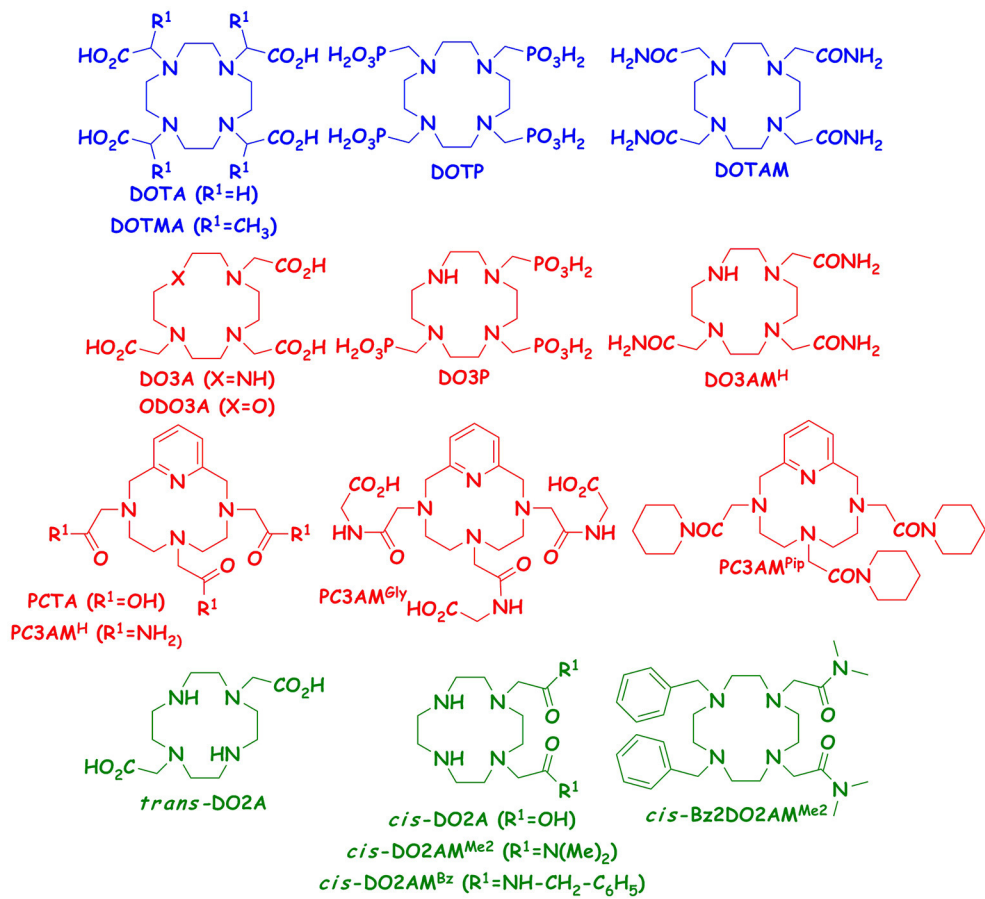


FIGURE 1 | Structures of hexa-, hepta- and octadente ligands studied and compared in this work.

of $[\text{Mn}(\text{DOTAM})]^{2+}$, $[\text{Mn}(\text{DO3AM}^H)]^{2+}$, $[\text{Mn}(\text{DO3A})]^-$, $[\text{Mn}(\text{PCTA})]^-$ and $[\text{Mn}(\text{ODO3A})]^-$ with Cu(II)/Zn(II) ions in the pH range of 3.6–5.5 (Figures S17–S19 in Supplementary Material). The concentration of the complexes in these samples was set to 1.0–2.0 mM to achieve relatively large change during the dissociation reaction. The relaxivity of the complexes is in the range of $1.00\text{--}1.44 \text{ mM}^{-1}\text{s}^{-1}$, which increases to $7.92 \text{ mM}^{-1}\text{s}^{-1}$ upon Zn(II) mediated decomplexation. The temperature was maintained at 25 °C and the ionic strength of the solutions was kept constant at 0.15 M with NaCl. *N,N'*-dimethyl- (DMP) and *N*-methyl-piperazine (NMP) buffers ($\log K_2^H = 4.18$ and 4.90 at 25 °C and $I = 0.15$ M NaCl, respectively) were used at 0.05 M concentration to keep the pH constant. The pseudo-first-order rate constants (k_{obs}) were calculated by fitting the absorbance or relaxivity-time data pairs to Equation (1)

$$X_t = (X_0 - X_e)e^{-k_{\text{obs}}t} + X_e \quad (1)$$

where X_t , X_0 , and X_e are the absorbance or relaxivity at time t , at the start and at equilibrium, respectively. The calculations were performed with the computer program Micromath Scientist, version 2.0 (Salt Lake City, UT, USA) using a standard least-squares procedure.

Relaxivity Measurements

The longitudinal water proton relaxation rates ($r_1 = 1/T_1 - 1/T_w$) were measured at 20 MHz with a Bruker Minispec MQ-20 relaxometer (Bruker Biospin, Germany). Samples were thermostated by using a circulating water bath at 25.0 ± 0.2 °C. The longitudinal relaxation times (T_1) were measured by the inversion-recovery method ($180^\circ - \tau - 90^\circ$), averaging 5–6 data points collected for each concentration point obtained from 14 different τ values (τ values ranging between 0 to at least 6 times the expected T_1). The relaxivity of the complexes was determined by titrating a nearly 1.0 mM ligand solution with a Mn(II) stock solution at pH = 7.22–7.43 (50 mM HEPES buffer, $I = 0.15$ M NaCl, 25 °C). Under these conditions, the only Mn(II) ion containing species present in solution is the $[\text{Mn}(L)]$, which was supported by the r_1 vs. pH profiles. The relaxivity of the complex was determined as the slope of the straight line obtained by plotting $1/T_{1p}$ values as a function of Mn(II) concentration for samples with $[\text{Ligand}] > [\text{Mn(II)}]$. The relaxivity of $[\text{Mn}(\text{DOTP})]^{6-}$ and $[\text{Mn}(\text{DO3P})]^{4-}$ was determined in the pH range of 10.0–11.0 and 8.5–9.3, respectively where mainly the $[\text{Mn}(\text{DO3P})]^{4-}$ and $[\text{Mn}(\text{DOTP})]^{6-}$ complex exists in solution (Figures S4 and S9 in Supplementary Material).

RESULTS AND DISCUSSION

Stability of the Mn(II) Complexes

The protonation and complexation equilibria of the macrocyclic ligands and their Mn(II) complexes have been studied by pH-potentiometric and relaxometric methods in the presence of 0.15 M NaCl whose ionic strength mimics the physiological conditions. The protonation constants of the ligands were evaluated by fitting the pH-V(mL) base data pairs collected in the pH-potentiometric titrations. The protonation equilibria of the ligands can be described by Equation (2). The log K^H values are listed in **Table 1**. (a comparison of previously published log K^H data available in the **Supplementary Material**) together with the constants of H₄DOTA, *cis*- and *trans*-H₂DO2A derivatives given for comparison.

$$K_i^H = \frac{[H_i L]}{[H_{i-1} L][H^+]}, i = 1, 2, \dots \quad (2)$$

As it has been stated before in several publications (Desreux et al., 1981), the first two protonations of these tetraazacyclododecane derivatives occur at the opposite ring nitrogen donor atoms followed by further protonation steps depending on the nature of donor groups incorporated into the pendant arms. The protonation sequence of PCTA and ODO3A and their derivatives differ slightly from that of DOTA and its derivatives owing to the asymmetric nature of the macrocyclic ligands (Aime et al., 1997). The first protonation in these ligands occurs at the nitrogen atom situated *trans* to the pyridine N or etheric O atom. The protonation of a *cis* nitrogen atom in the second step forces the first proton to shift to the other *cis* nitrogen of the macrocycle leaving the *trans* N atom unprotonated (Aime et al., 1997). The substitution of amides for the carboxylate groups (DO3AM^H, PC3AM^H, etc.) results in a significant decrease, while the introduction of phosphonate groups (e.g., DO3P) causes a notable increase in the total basicity of the ligands. Not only the value but also the number of the protonation constants is affected by these structural alterations. As it is seen from the data shown in **Table 1**, the sum of the first two protonation constants ($\Sigma \log \beta_2^H = \log K_1^H + \log K_2^H$) is significantly higher for the acetate derivatives than that for the amide derivative ligands because the number of the negatively charged sidearms decreases, which results in a weaker hydrogen bonding existing between the protonated donor atoms of the macrocycle and the amide group. On the other hand, the basicity of the macrocyclic nitrogen atoms in DO3P is higher than that in DO3A resulting in a noticeably higher ligand basicity. The ligand ODO3A, derived from DO3A by substituting an etheric O-atom for the macrocyclic NH, also displays a drop in the $\Sigma \log \beta_2^H$ value due to a change in the protonation sequence (Amorim et al., 1988).

In order to gain information on the thermodynamic stability of the Mn(II) complexes, samples containing the metal and ligand in 1 to 1 molar ratio were studied by pH potentiometry or ¹H-relaxometry and in some cases by a combination of the two methods. The titration data were fitted by assuming the existence of [M(L)] and some protonated species ([M(H_iL)]) at lower pH values. In some cases to fit the data obtained at higher pH, the formation of ternary hydroxido complexes ([M(L)(OH)]) were

also included in the equilibrium model. The stability constants (K_{ML}) and the various protonation forms (K_{MHL}) of ML metal chelates are defined by Equations (3)–(5). However, a comparison of the stabilities of different complexes solely on the basis of their stability constants might be misleading because of the differences in ligand basicities. Therefore, we have calculated the pMn values at pH 7.4 defined as $pMn = -\log [Mn^{2+}]_{free}$ with $c_{Mn} = c_L = 1 \times 10^{-5}$ M as suggested by Tóth and co-workers (Drahos et al., 2010). The pMn value accounts for the effect of proton competition (ligand basicity and complex protonation) on the stability constant essentially offering the same information as the conditional stability constant. Higher pMn values indicate a higher chelate stability at specified conditions. Considering the above mentioned conditions ($c_{Mn} = c_L = 1 \times 10^{-5}$ M, pH = 7.4), the minimum value of the pMn is 5, which corresponds to 0% complexation.

$$K_{ML} = \frac{[M(L)]}{[M][L]} \quad (3)$$

$$K_{MHL} = \frac{[M(H_i L)]}{[M(H_{i-1} L)][H^+]}, \text{ where } i = 1, 2, \dots \quad (4)$$

$$K_{MLOH} = \frac{[M(L)]}{[M(L)(OH)][H^+]} \quad (5)$$

The ligand DOTA is generally considered as the “gold standard” for metal based systems. The [Mn(DOTA)]²⁻ complex has a pMn value of 9.02 ($c_{Mn} = c_L = 1 \times 10^{-5}$ M at pH = 7.4) corresponding to $\log K_{MnL}$ of 19.44. As seen from the data shown in **Table 2**, the stability constants obtained for the complexes with phosphonate pendant arms ([Mn(DOTP)]⁶⁻ and [Mn(DO3P)]⁴⁻) are close to that of [Mn(DOTA)]²⁻; they are the highest among the complexes we studied. The pMn values however, indicate that the conditional stability of these complexes is the lowest among the studied systems. By analyzing the data shown in **Table 2** one can conclude that among the studied heptadentate ligands the Mn(II) complex formed with the rigid pyridine macrocyclic PCTA ligand has the highest conditional stability near to physiological conditions. It is higher than that of the [Mn(DO3A)]⁻ complex, although the number and nature of the donor atoms coordinating the Mn(II) ion are nearly the same (4N and 3O) in these ligands. The pMn value characterizing [Mn(PCTA)]⁻ is higher than that calculated for [Mn(DOTA)]²⁻ by 0.7 pM unit while the pMn values of the complexes formed with DO3A, ODO3A and amide derivatives of the rigidified pyclyl macrocycles PC3AM^{Gly} and PC3AM^{Pip} ligands are slightly lower than that of [Mn(DOTA)]²⁻ (with a perceptible increase from primary to secondary and to tertiary amide sidearms). These differences can be explained in terms of ligand protonation constants, as it is stated above. The first two protonation constants ($\log K_1^H$ and $\log K_2^H$) of DOTA and its derivatives (except for the DOTAM and DO3AM^H chelators) are greater than pH 7.4 meaning that the ligands are diprotonated above this pH value, which used in pMn calculations. In contrast, for PCTA and its derivatives only the $\log K_1^H$ value is higher than 7.4. In case of ODO3A the $\log K_2^H$ is slightly higher than 7.4 (**Table 1**) whereas for the DOTA and its derivatives the second protonation occurs above pH = 9.0 (25 °C and $I = 0.15$ M NaCl).

TABLE 1 | Protonation constants of the hexa-, hepta- and octadentate ligands ($I = 0.15 \text{ M NaCl}, 25^\circ\text{C}$).

	$\log K_1^{\text{H}}$	$\log K_2^{\text{H}}$	$\log K_3^{\text{H}}$	$\log K_4^{\text{H}}$	$\log K_5^{\text{H}}$	$\log K_6^{\text{H}}$	$\Sigma \log K_i^{\text{H}}$
DO3A	10.07 (5)	8.93 (6)	4.43 (9)	4.11 (7)	1.88 (7)	—	19.00
DO3AM ^H	9.40 (5)	6.28 (8)	—	—	—	—	15.68
DO3P	12.55 (2)	11.37 (1)	8.57 (2)	7.02 (2)	5.36 (2)	1.84 (2)	23.92
ODO3A	8.74 (2)	7.58 (2)	3.99 (3)	2.39 (3)	—	—	16.32
PCTA	9.97 (3)	6.73 (5)	3.22 (6)	1.40 (9)	—	—	16.70
PC3AM ^H	8.76 (3)	4.10 (4)	—	—	—	—	12.86
PC3AM ^{Gly}	8.85 (1)	4.55 (1)	3.81 (1)	3.21 (1)	2.80 (1)	1.38 (1)	13.40
PC3AM ^{Pip}	8.74 (1)	5.77 (2)	1.42 (9)	—	—	—	14.51
DOTA ^[c]	11.41	9.83	4.38	4.63	1.92	1.58	21.24
DOTMA ^[b]	11.72	9.06	4.74	5.59	1.92	—	20.78
DOTAM	7.31 (1)	6.07 (1)	—	—	—	—	13.38
DOTP	13.6 (2) ^[a]	12.23 (3)	8.63 (5)	7.45 (4)	5.84 (5)	5.02 (5)	25.83
trans-DO2A ^[d]	11.69	9.75	3.97	2.68	—	—	21.44
cis-DO2A ^[d]	11.44	9.51	4.14	1.55	—	—	20.95
cis-DO2AM ^{Me2,[e]}	10.14	8.38	—	—	—	—	18.52
cis-Bz2DO2AM ^{Me2,[f]}	11.11	8.22	—	—	—	—	19.33
cis-DO2AM ^{Bz2,[f]}	9.62	6.90	—	—	—	—	16.52

^[a]1H- and ³¹P-NMR; ^[b] $I = 0.1 \text{ M KCl}$ (Aime et al., 2011); ^[c] $I = 0.1 \text{ M KCl}$ (Takács et al., 2014); ^[d]Garda et al. (2016); ^[e] $I = 0.1 \text{ M KCl}$ (Forgács et al., 2016); ^[f] $I = 0.1 \text{ M KCl}$ (Forgács et al., 2017).

Consequently, these ligands exist in their diprotonated form near pH = 7.4 and so the proton competition is more significant in these systems.

Linear relationships between experimentally measured $\log K_{\text{M(L)}}$ values and ligand basicities were reported for more than 60 years ago (Martell and Calvin, 1952). Later Choppin proposed the inclusion of linear polyamino polycarboxylate systems and demonstrated a single linear correlation between $\log K_{\text{M(L)}}$ values and $\Sigma \log K_i^{\text{H}}$ for polydentate ligands that form five-membered chelate rings with Ln(III) cations (Choppin, 1985). More recently, such empirical relationships have been found for macrocyclic polyamino polycarboxylates as well (Kumar et al., 1995; Huskens et al., 1997). As the diversity of ligands has grown over the years, it has become apparent that a major uncertainty in establishing such relationships is the number of ligand protonation steps that should be included in the calculation of $\Sigma \log K_i^{\text{H}}$ (the basicity of amides, phosphinates, carboxylates and phosphonates differ considerably i.e., these correlations are expected to exist for structurally similar ligands). A similar empirical relationship between the stability ($\log K_{[\text{Cu(L)}]}$) and the sum of the first two $\log K_i^{\text{H}}$ values corresponding to the protonation of N-atoms has been shown to hold for Cu(II) complexes of several linear and macrocyclic ligands (Lukes et al., 2001). Even though this relationship ignores the basicity of the side-chain coordinating groups, an analogous approach for Gd(III) complexes with macrocyclic ligands (including 1,4,7-triazacyclonanane, 1,4,7,10-tetraazacyclododecane and 1,4,8,11-tetraazacyclotetradecane with carboxamide, carboxylate and methylenephosphonate pendant arms) gives an acceptable linear correlation with $R^2 = 0.86$ ($\log K_{\text{Gd(L)}} = 1.5 (\log K_1^{\text{H}} + \log K_2^{\text{H}}) - 9.7$) (Brücher et al., 2013). We applied a similar approach to the Mn(II) complexes studied in the current

work (Figure 2) This resulted in an unacceptable correlation ($R^2 = 0.63$) (Figure 2, red points: $\log K_{\text{MnL}} = 0.50 (\log K_1^{\text{H}} + \log K_2^{\text{H}}) + 6.22$). However, omission of the data corresponding to PCTA (positive deviation) and DO3AM^H (negative deviation) considerably improved the correlation ($\log K_{\text{MnL}} = 0.47 (\log K_1^{\text{H}} + \log K_2^{\text{H}}) + 6.68$ with $R^2 = 0.89$) while the numbers describing the correlation did not change significantly. Figure 2 shows how the weakness of one structural motif can be compensated in part by the strength of another when the effects of various structural features are combined. $[\text{Mn}(\text{PCTA})]^-$ has higher, whereas $[\text{Mn}(\text{DO3AM}^{\text{H}})]^{2+}$ has lower stability than expected based on the ligand basicity. Likewise, the Mn(II) complex of PCTA-tris(amide), (PC3AM^H) is less stable than expected while $[\text{Mn}(\text{PC3AM}^{\text{Gly}})]^-$ and $[\text{Mn}(\text{PC3AM}^{\text{Pip}})]^{2+}$ have stabilities higher than expected. Our data also indicate that Mn(II) complexes of all the bisamides of cis-DO2A reported in the literature have lower stability than expected on the basis of ligand basicity, highlighting the importance of further ligand design.

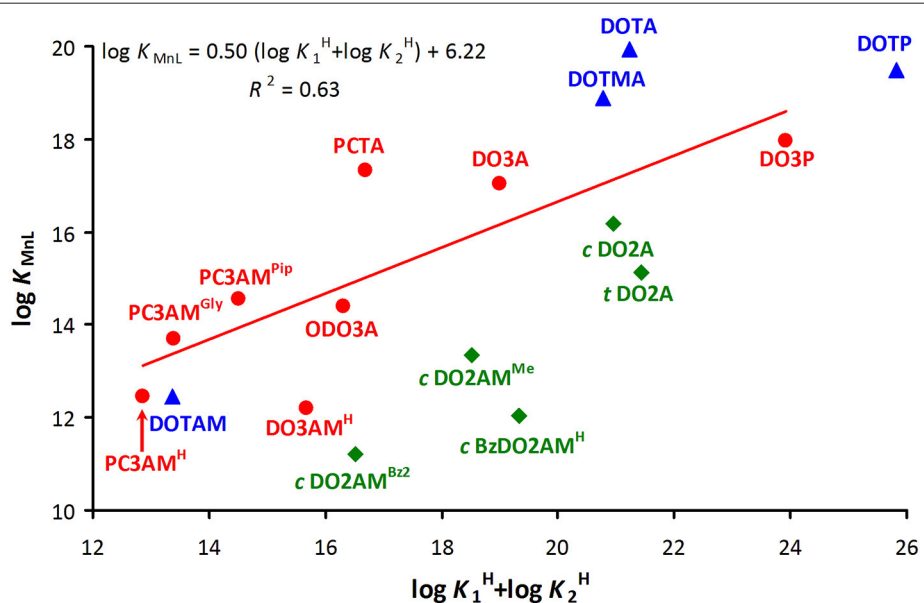
Demetallation of the Mn(II) Chelates

The kinetic inertness of the Mn(II) complexes is the other important parameter for the complexes considered for use *in vivo*. The inertness of Mn(II) complexes formed with trisubstituted 12-membered macrocyclic ligands were characterized either by studying the rates of acid catalyzed dissociation or by studying transmetallation reactions occurring between the complexes and a suitable exchanging metal ion such as Zn(II) or Cu(II). The demetallation reactions of labile complexes were performed at high pH by following the ligand exchange reactions with *trans*-CDTA and DTPA ligands. The demetallation reactions were studied in the presence of a large Cu(II)/Zn(II)/*trans*-CDTA/DTPA excess or by using high acid

TABLE 2 | Stability and protonation constants as well as pMn values for the Mn(II) complexes ($I = 0.15 \text{ M NaCl}$, 25°C).

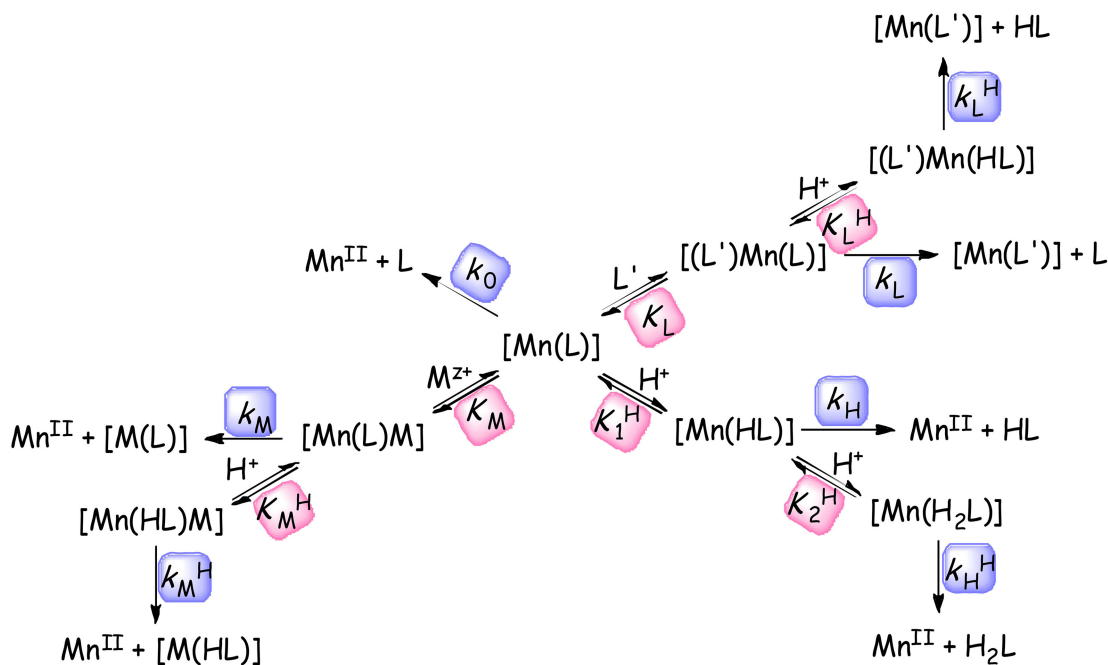
	$\log K_{ML}$	$\log K_{ML}^H$	$\log K_{MHL}^H$	$\log K_{MH2L}^H$	$\log K_{ML}^{OH}$	$\text{pMn}^{\text{[h]}}$
DO3A	16.55 (4)	4.26 (2)	—	—	—	8.66
DO3AM ^H	11.69 (2)	—	—	—	—	7.32
DO3P	17.45 (2)	8.06 (2)	7.05 (1)	5.31 (2)	—	6.43
ODO3A	13.88 (1)	2.77 (5)	—	—	—	8.57
PCTA	16.83 (1) 16.64 (7) ^[a]	1.96(1)	—	—	—	9.74
PC3AM ^H	11.94(3) 11.78 (8) ^[a]	—	—	—	10.90 (4)	7.77
PC3AM ^{Gly}	13.20 (1)	3.98 (1)	3.14 (1)	2.87 (1)	10.67 (2)	8.37
PC3AM ^{Pip}	14.05 (2)	—	—	—	11.63 (2)	8.86
DOTA ^[b]	19.44	3.96	—	—	—	9.02
DOTMA ^[c]	18.37 ^[a]	4.56 ^[a]	—	—	—	8.69
DOTAM	11.96 (1)	—	—	—	—	8.60
DOTP ^[d]	18.98 (1)	8.09 (1)	7.79 (1)	6.74 (1)	—	6.43
trans-DO2A ^[e]	14.64	4.40	—	—	—	6.52
cis-DO2A ^[e]	15.68	4.15	—	—	—	7.27
cis-DO2AM ^{Me2,[f]}	12.64	—	—	—	—	6.98
cis-Bz2DO2AM ^{Me2,[f]}	11.54	—	—	—	10.44	6.00
cis-DO2AM ^{Bz2,[g]}	10.72	—	—	—	9.44	6.69

^[a]1H-relaxometry; ^[b] $I = 0.1 \text{ M KCl}$ (Takács et al., 2014); ^[c]Tircsó and Woods (in preparation); ^[d]the 4th protonation constant of the complex is ($\log K_{MH3L}^H = 5.02$ (1)); ^[e]Garda et al. (2016); ^[f] $I = 0.1 \text{ M KCl}$ (Forgács et al., 2016); ^[g] $I = 0.1 \text{ M KCl}$ (Forgács et al., 2017); ^[h]The pMn values were calculated at pH = 7.4, $c_M = c_L = 10^{-5} \text{ M}$ by using the conditions as suggested by Drahos et al. (2010).

**FIGURE 2 |** Plot of stability constants ($I = 0.15 \text{ M NaCl}$ and 25°C) of Mn(II) complexes of 12-membered macrocyclic ligands vs. basicity of the macrocyclic nitrogen atoms ($\log K_1^H + \log K_2^H$) of the ligands (green: disubstituted, red: trisubstituted and blue: tetrasubstituted derivatives).

concentration in order to ensure pseudo-first-order conditions (Equation 6). **Scheme 1** outlines all the possible dissociation pathways for the Mn(II) complexes. **Scheme 1** shows that the dissociation may occur through exchange reactions with other M' metal ion or L' ligand by the assistance of protons. The reactions of the released Mn(II) and L ligand with the exchanging L' and M' reactants are assumed to be very rapid.

The rate constants k_0 , k_H , k_M^H , k_L^H , $k_{M'}^H$, and $k_{L'}^H$ characterize the rate of the spontaneous, proton-assisted, metal-assisted and proton-metal-assisted (when the exchanging metal attacks the protonated or the proton attacks the dinuclear complexes) ligand and proton-ligand reaction pathways, respectively. K_1^H , K_2^H , K_M^H , and K_L^H are the protonation constants of the [Mn(L)], [Mn(HL)], [Mn(L)M],



SCHEME 1 | Assumed reaction pathways for the dissociation of Mn(II) complexes in the presence of metal ions and ligands available for exchange reactions ($\text{M} = \text{Cu}(\text{II})$ or $\text{Zn}(\text{II})$, $\text{L}' = \text{trans-CDTA}$ or DTPA, the charges are omitted for clarity).

$[\text{Mn}(\text{L})(\text{L}')]$, and the stability constant of the dinuclear (K_M) $[\text{Mn}(\text{L})\text{M}]$ and ternary (K_L) $[\text{Mn}(\text{L})(\text{L}')]$ complexes, respectively.

The rate of dissociation can be expressed by the Equation (6), where k_{obs} is the pseudo-first-order rate constant and $[\text{Mn}(\text{L})]_t$ is the total concentration of the species containing $[\text{Mn}(\text{L})]$ complex. The $[\text{Mn}(\text{L})]_t$ will differ slightly depending on the experimental conditions (in the presence of a large metal or ligand excess). As $[\text{Mn}(\text{L})]_t = [\text{Mn}(\text{L})] + [\text{Mn}(\text{HL})] + [\text{Mn}(\text{H}_2\text{L})] + [\text{Mn}(\text{L})\text{M}] + [\text{Mn}(\text{L})(\text{L}')]$ for reactions performed at high pH (in the pH range of 3.0–5.0 often applied in Cu(II) exchange reactions) will involve fewer protonated species while the acid catalyzed dissociation reactions run in the strongly acidic media (0.1–1.0 M acid concentration range) predominantly contain protonated species ($[\text{Mn}(\text{L})]_t = [\text{Mn}(\text{L})] + [\text{Mn}(\text{HL})] + [\text{Mn}(\text{H}_2\text{L})]$).

$$-\frac{d[\text{MnL}]}{dt} = k_{\text{obs}}[\text{MnL}]_t \quad (6)$$

By taking into account the various complex species and the possible reaction pathways as well as the protonation and stability constants of the reactive intermediates, the following equation (Equation 7) can be derived to describe the rates of dissociation.

$$k_{\text{obs}} = \frac{k_0 + k_1[\text{H}^+] + k_2[\text{H}^+]^2 + k_3[\text{M}^{2+}] + k_4[\text{M}^{2+}][\text{H}^+] + k_5[\text{L}'] + k_6[\text{L}'][\text{H}^+]}{1 + K_1^{\text{H}}[\text{H}^+] + K_1^{\text{H}}K_2^{\text{H}}[\text{H}^+]^2 + K_M[\text{M}^{2+}] + K_M^{\text{H}}[\text{M}^{2+}][\text{H}^+] + K_{\text{L}'}[\text{L}'] + K_{\text{L}'}^{\text{H}}[\text{L}'][\text{H}^+]} \quad (7)$$

where $k_1 = k_{\text{H}} \cdot K_1^{\text{H}}$, $k_2 = K_1^{\text{H}} \cdot K_2^{\text{H}}$, $k_3 = k_M \cdot K_M$, $k_4 = K_M^{\text{H}} \cdot K_M^{\text{H}}$, $k_5 = k_{\text{L}'} \cdot K_{\text{L}'}$ and $k_6 = K_{\text{L}'}^{\text{H}} \cdot K_{\text{L}'}^{\text{H}}$. By fitting the experimental

k_{obs} data to Equation (7) resulted in the rate constants characterizing spontaneous (k_0 , s^{-1}), acid catalyzed (k_1 , $\text{M}^{-1}\text{s}^{-1}$ and k_2 , $\text{M}^{-2}\text{s}^{-1}$) and metal-assisted (k_3 , $\text{M}^{-1}\text{s}^{-1}$) dissociation for the Mn(II) complexes that are listed in Table 3. For the calculation we had to have some information about the importance of different reaction pathways. The role of the metal-proton-assisted (k_4 , $\text{M}^{-2}\text{s}^{-1}$), ligand (k_5 , $\text{M}^{-1}\text{s}^{-1}$) and ligand-proton-assisted (k_6 , $\text{M}^{-2}\text{s}^{-1}$) pathways in these demetallation reactions were negligible and in most cases the protonation and stability constants of the intermediates (K_1^{H} , K_2^{H} , K_M , and $K_{\text{L}'}^{\text{H}}$) could not be determined because of their very low values.

As an example, Figure 3 shows a representative plot of k_{obs} values as a function of acid concentration obtained for $[\text{Mn}(\text{PCTA})]^-$ during the Zn(II) induced transmetallation reactions in the pH range of 3.09–5.88 (some more data are included in the ESI). The rates of acid catalyzed dissociation reactions obtained for PCTA and its amide derivatives are shown in Figure 4.

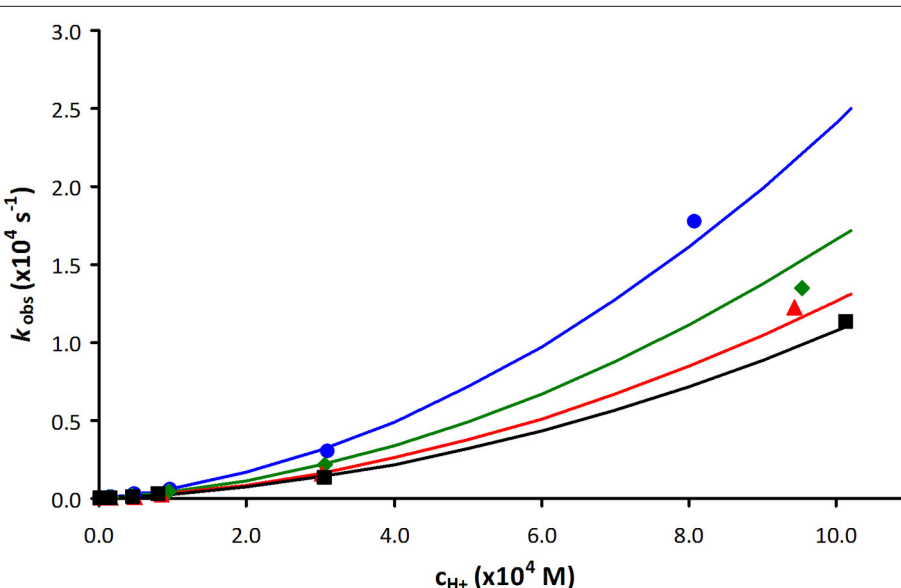
The k_{obs} values increase with increasing H^+ ion concentration in all cases (k_1 , k_2) and either increase (k_3) or remain unaffected by increasing the exchanging metal ion concentration. It is difficult to directly compare the rate constants that characterize the different reaction pathways. Therefore, the half-lives ($t_{1/2}$) of

the dissociation reactions of Mn(II) complexes were calculated under physiological conditions ($\text{pH} = 7.4$, $10 \mu\text{M}$ concentration

TABLE 3 | Rate constants of spontaneous (k_0), proton-assisted (k_1 and k_2), metal-ion-assisted (k_3) pathways and half-lives characterizing the dissociation of Mn(II) complexes ($I = 0.15 \text{ M NaCl}, 25^\circ\text{C}$).

	$k_0 (\text{s}^{-1})$	$k_1 (\text{M}^{-1}\text{s}^{-1})$	$k_2 (\text{M}^{-2}\text{s}^{-1})$	$k_3 (\text{M}^{-1}\text{s}^{-1})$	$t_{1/2} (\text{s}) 0.1 \text{ M HCl}$	$t_{1/2} (\text{h}) \text{ pH } 7.4$ $c_M = 10^{-5} \text{ M}$
[Mn(PCTA)] ⁻	$(7.0 \pm 0.1) \times 10^{-2}[\text{b}]$	$(8.2 \pm 0.7) \times 10^{-2}[\text{a}]$ $(1.09 \pm 0.01) \times 10^{-1}[\text{b}]$	$(3.5 \pm 0.4) \times 10^2[\text{a}]$	$(1.8 \pm 0.3) \times 10^{-6}[\text{a}]$	8.6	5.9×10^4
[Mn(PC3AM ^{H+}) ²⁺]	—	$(1.07 \pm 0.01) \times 10^{-2}$	—	—	6.5×10^2	4.5×10^5
[Mn(PC3AMGly)] ⁻	$(3.4 \pm 0.2) \times 10^{-4}[\text{c}]$	$(1.64 \pm 0.02) \times 10^{-2}[\text{c}]$	—	—	3.5×10^2	—
[Mn(PC3AM ^{Pip}) ²⁺]	—	$(4.64 \pm 0.04) \times 10^{-3}$	—	—	1.5×10^3	1.0×10^6
[Mn(DO3A)] ⁻	—	0.45 ± 0.03	$(3.2 \pm 0.3) \times 10^2$	—	0.21	1.1×10^4
[Mn(DO3AM ^{H+}) ²⁺]	—	0.94 ± 0.02	—	—	7.4	5.2×10^3
[Mn(DO3P)] ^{4- [e]}	—	$(2.4 \pm 0.2) \times 10^5$	$(2.2 \pm 0.3) \times 10^{14}$	—	—	3×10^{-3}
[Mn(ODO3A)] ^{- [d]}	—	27 ± 2	$(1.5 \pm 0.3) \times 10^5$	—	2.8×10^{-2}	1.8×10^2
[Mn(DOTP)] ^{6- [e]}	—	$(2.35 \pm 0.29) \times 10^5$	$(8.35 \pm 0.8) \times 10^{14}$	—	—	1.3×10^{-3}
[Mn(DOTAM)] ²⁺	—	$(1.6 \pm 0.03) \times 10^{-2}$	—	—	4.3×10^2	3.0×10^5
[Mn(DOTMA)] ^{2- [f]}	1.04×10^{-4}	3.96×10^{-5}	—	—	6.2×10^3	—
[Mn(DOTA)] ^{2- [g]}	1.8×10^{-7}	0.04	1.6×10^3	1.5×10^{-5}	4.3×10^{-2}	1.1×10^3
[Mn(<i>trans</i> -DO2A)] ^[h]	—	85	3.0×10^6	—	2.3×10^{-5}	48
[Mn(<i>cis</i> -DO2A)] ^[h]	—	100	1.6×10^6	—	4.3×10^{-5}	58
[Mn(<i>cis</i> -DO2AM ^{Me2}) ^{2+ [i]}]	—	8.7	—	—	0.79	556
[Mn(<i>cis</i> -BzDO2AM ^{H+}) ^{2+ [i]}]	—	36	—	—	0.19	136
[Mn(<i>cis</i> -DO2AM ^{Bz2}) ^{2+ [i]}]	—	38	—	—	0.18	126

^[a]relaxometry, the stability constant of the dinuclear intermediate (K_M) was found to be $38 \pm 6 \text{ M}^{-1}$; ^[b]stopped-flow in highly acidic condition where the k_0 is the spontaneous and k_1 is the proton-assisted dissociation of the [Mn(HL)] complex; ^[c]the k_0 is the spontaneous and k_1 is the proton-assisted dissociation of the [Mn(H₃L)] complex; ^[d]the K_1^H was fixed to 600 based determined by pH-potentiometry; ^[e]ligand exchange reaction with trans-CDTA⁴⁻ or DTPA⁵⁻ in the pH range 8–9.5, the stability constant of the protonated intermediate (K_1^H) was found to be $(2.0 \pm 0.4) \times 10^8$, the K_H was fixed to $10^{8.06}$; ^[f] Tircsó and Woods (*in preparation*) in 1.0 M KCl, where the k_0 is the spontaneous and k_1 is the proton-assisted dissociation of the [Mn(H₂L)] complex; ^[g]the stability constant of the [Mn(DOTA)Zn] dinuclear intermediate (K_M) was found to be 68 M^{-1} (Drahos et al., 2011); ^[h]Garda et al. (2016); ^[i] $I = 0.1 \text{ M KCl}$ (Forgács et al., 2016); ^[j] $I = 0.1 \text{ M KCl}$ (Forgács et al., 2017); ^[k]the half-life ($t_{1/2}$) corresponding to 0.1 M acid concentration were not calculated since the dissociation reactions were carried out at high pH (where [Mn(DO3P)]⁴⁻ and [Mn(DOTP)]⁶⁻ exist in multiple protonated forms up to pH = 9.0 and their dissociation is extremely fast), i.e., the rate constants were determined only for the fully deprotonated species; ^[l]the half-life ($t_{1/2}$) was not calculated since the dissociation reactions were carried out under acidic conditions where a protonated complex exists.

**FIGURE 3 |** Plot of the pseudo-first-order rate constants (k_{obs}) as a function of Zn(II) and H⁺ ion concentration for [Mn(PCTA)]⁻ (blue: 10-fold Zn(II) excess, green: 20-fold Zn(II) excess, red: 30-fold Zn(II) excess and black: 40-fold Zn(II) excess).

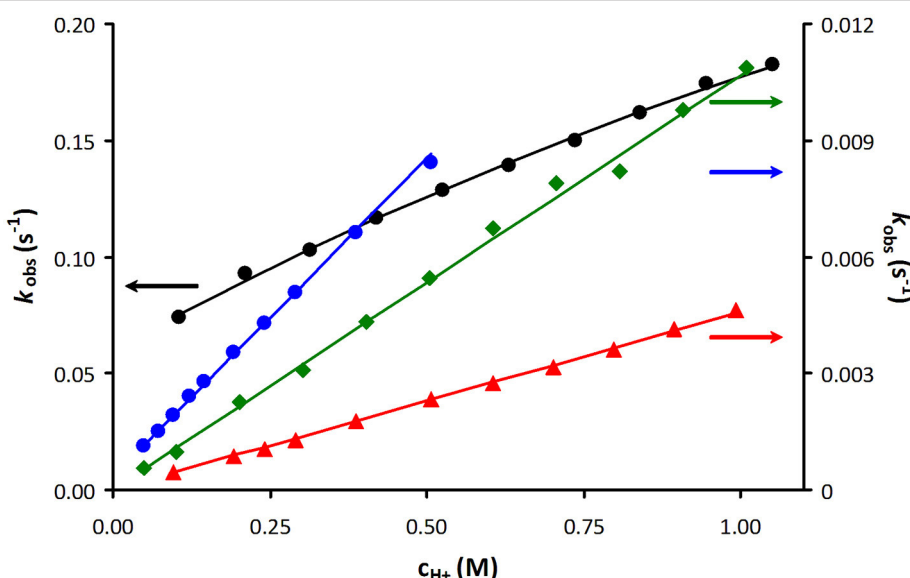


FIGURE 4 | Plot of the pseudo-first-order rate constants (k_{obs}) as a function of H^+ ion concentration for $[\text{Mn}(\text{PCTA})]^-$ (black), $[\text{Mn}(\text{PC3AM}^{\text{H}})]^{2+}$ (green), $[\text{Mn}(\text{PC3AM}^{\text{Gly}})]^-$ (blue) and $[\text{Mn}(\text{PC3AM}^{\text{Pip}})]^{2+}$ (red).

of the exchanging metal ion) and also for 0.1 M H^+ concentration since the most inert Mn(II) complexes were studied in acidic milieu (Table 3).

The comparison of the k_1 (rate constant characterizing the acid catalyzed dissociation) or half-live ($t_{1/2}$) values shows that the dissociation kinetics of the Mn(II) complexes of 12-membered macrocyclic ligands strongly depends on the rigidity of the macrocycles, the nature of donor atoms present in the macrocycle, as well as on the metal binding moieties attached to the nitrogen atoms of the macrocycles. For a class of very similar ligands (i.e., 12-membered macrocycles), the rate of acid catalyzed dissociation (k_1) was found to differ as much as eight orders of magnitude ($2.4 \times 10^5 \text{ M}^{-1}\text{s}^{-1}$ for DO3P vs. $4.64 \times 10^{-3} \text{ M}^{-1}\text{s}^{-1}$ for PC3AM^{Pip}), which underlines the importance of both the macrocyclic backbone and the metal binding sidearms in ligand design. As seen from the data shown in Table 3, the replacement of the secondary amine ($>\text{NH}$ in DO3A) in the macrocycle by etheric oxygen atom (-O- as in ODO3A) resulted in a 50 fold increase in the k_1 value of the Mn(II) complexes, which indicates that the given structural modification should not be considered for Mn(II) chelators. On the other hand, the incorporation of the secondary amine moiety ($>\text{NH}$) into a pyridine ring has a beneficial effect on the kinetic parameters as evidenced by the 5-fold decrease of the k_1 value of its Mn(II) complex. When analyzing the effect of the nature of pendant arms on the dissociation kinetic properties, it can be concluded that the inertness of Mn(II) complexes of amide derivatives is higher than that of Mn(II) complexes formed with ligands having acetate or especially, phosphonate sidearms. This behavior is clearly related to the decreased basicity of the amide based ligands as well as the hindered proton transfer from the protonation site to the

ring nitrogen donor atom(s), which is essential for the acid-assisted path. It was previously proved that the substitution of a phosphonate for the carboxylate group can facilitate the proton transfer to the macrocyclic nitrogen since the phosphonate groups (in acidic solutions) can be protonated even when they are metal-bound (Kálmán et al., 2008). The replacement of the acetates by primary amides resulted in noticeable increase in the kinetic inertness going from PCTA to its trisamide derivatives (PC3AMH). Further improvement was observed going from the primary (PC3AM^H) toward the tertiary amide (PC3AM^{Pip}) complexes (the k_1 values decrease from $0.109 \text{ M}^{-1}\text{s}^{-1}$ observed for the anionic PCTA complex to $0.0107 \text{ M}^{-1}\text{s}^{-1}$ and $0.00464 \text{ M}^{-1}\text{s}^{-1}$ for the cationic Mn(II) complexes of PC3AM^H and PC3AM^{Pip}, respectively). This tendency is analogous to the kinetic behavior of Ln(III) complexes of DOTA-tetraamides (Aime et al., 1999; Pasha et al., 2007). A break in this trend is apparent for the $[\text{Mn}(\text{PC3AM}^{\text{Gly}})]^-$ complex, which is due to the presence of charged (and protonatable) groups in this ligand. The sterically more hindered amide $[\text{Mn}(\text{PC3AM}^{\text{Pip}})]^{2+}$ complex displays surprisingly high kinetic inertness as evidenced by its k_1 rate constant, which is significantly lower than that of $[\text{Mn}(\text{DOTA})]^{2-}$ in spite of its lower denticity.

We have attempted to correlate the dissociation kinetic data and the stability or pMn values of the Mn(II) complexes by plotting the $-\log k_1$ values against the basicity of the nitrogen atoms of the ligands ($\log K_1^{\text{H}}$, $\log K_2^{\text{H}}$, and $\log K_1^{\text{H}} + \log K_2^{\text{H}}$). Plots of the $-\log k_1$ values against the first ($\log K_1^{\text{H}}$) and second ($\log K_2^{\text{H}}$) protonation constants are included in the supporting information (Figures S11–S14). Although no direct correlation is expected to exist between thermodynamic and kinetic parameters, we could observe a linear correlation when the $-\log k_1$ values were plotted as a function of pMn values

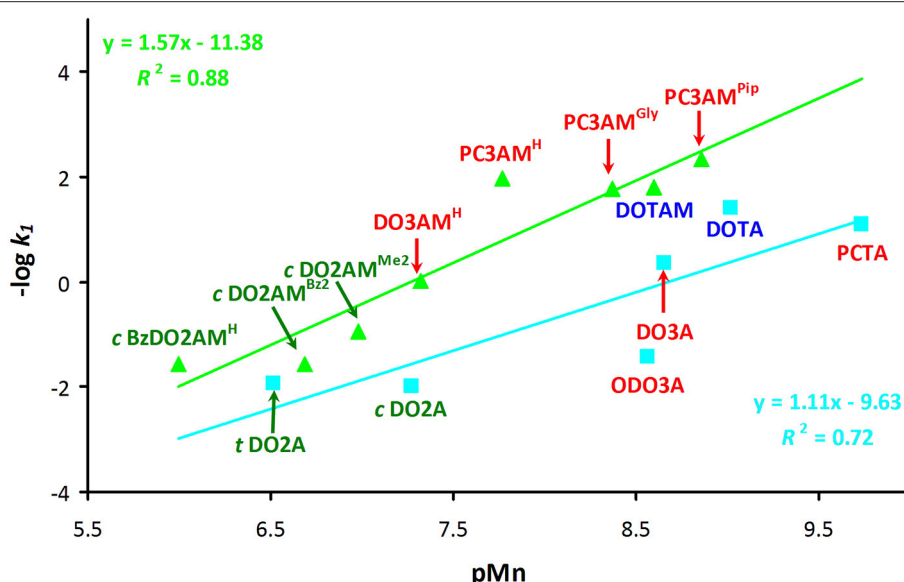


FIGURE 5 | Plot of $-\log k_1$ values (k_1 is the rate constant of the acid-assisted dissociation) as a function of pMn for acetate (light blue) and amide (light green) derivatives of 12-membered macrocycles ($I = 0.15 \text{ M NaCl}$ and 25°C). Disubstituted ligands are shown in green, trisubstituted derivatives are in red and tetrasubstituted derivatives are in blue.

(Figure 5). However, the acetate (blue line) and amide (green line) systems had to be considered separately, although it should be emphasized that we had very limited data to work with. The basicity of amide ligands weaker than that of the acetate derivatives, thus the Mn(II) complexes of the amide derivatives tend to dissociate more slowly via the proton assisted dissociation path. This is reflected by the fact that the correlation curve for the amide complexes runs above the line of the acetate derivatives and it has slightly larger slope. This observation strongly implies if one could design amide ligands that would form complexes with higher thermodynamic (and conditional) stability, then the kinetic inertness of such complexes is also expected to increase.

Relaxivity of the Mn(II) Complexes

The relaxivity (r_{1p} , $\text{mM}^{-1}\text{s}^{-1}$) is defined as the longitudinal water proton relaxation rate in a solution containing 1.0 mM concentration of the paramagnetic species. It characterizes the efficiency of a paramagnetic metal chelate to enhance the solvent proton relaxation rate at a given magnetic field (usually 20 MHz) and temperature. The inner-sphere contribution to relaxivity is directly proportional to the number of metal bound water molecules (q), and therefore, relaxivity values may provide some useful information on the hydration state of paramagnetic complexes of similar molecular weights and electronic relaxation times. As published in the literature, the Mn(II) complex formed with the heptadentate ligand DO3A does not possess a metal bound water molecule ($q = 0$), and therefore, it has low relaxivity ($1.30 \text{ mM}^{-1}\text{s}^{-1}$) originating solely from second and outer sphere contributions (Rolla et al., 2013). The r_{1p} values of the Mn(II) complexes formed with heptadentate 12-membered macrocyclic ligands were determined at 0.5 T field strength and 25°C and

reported in Table 4 along with some relaxivity data published for the complexes of hexa-, hepta- and octadentate ligands. The relaxivity of the $[\text{Mn}(\text{PCTA})]^{+}$ and $[\text{Mn}(\text{ODO3A})]^{+}$ complexes are indeed very similar to that of the $[\text{Mn}(\text{DO3A})]^{+}$ suggesting the absence of metal bound water molecules in these complexes as well. In fact, the X-ray crystal structure of the Mn(II) chelate formed with tris(ethyl ester) of PCTA confirms the absence of the metal bound solvent molecule in the $[\text{Mn}(\text{PCTA-OEt}_3)]^{2+}$ complex (Wen et al., 2012) suggesting that this is also true for the PCTA complex. The Mn(II) complexes of amide derivatives show even lower relaxivity, which can be explained by weaker second and outer sphere contributions (for example, X-ray crystallography has shown that $[\text{Mn}(\text{DO3AM}^{\text{H}})]^{2+}$ does not have an inner sphere water molecule) (Wang and Westmoreland, 2009) whereas increased second and outer sphere effects are likely responsible for the slight increase in the relaxivities observed for $[\text{Mn}(\text{DOTP})]^{6-}$ and $[\text{Mn}(\text{DO3P})]^{4-}$ in the pH ranges of $10.0\text{--}11.0$ and $8.5\text{--}9.3$, respectively, where the deprotonated complex exists in solution. Below these pH ranges the phosphonate moieties undergo protonation, which further increases the relaxivity ($2.60\text{--}2.90 \text{ mM}^{-1}\text{s}^{-1}$ values were observed near $\text{pH} = 7.4$, see Supplementary Material). Similar increase in the relaxivity (to $3.20 \text{ mM}^{-1}\text{s}^{-1}$ at 20 MHz , 37°C) is observed for the $[\text{Mn}(\text{DOTA})]^{2-}$ complex upon its protonation and formation of the thermodynamically stable diprotonated $[\text{Mn}(\text{H}_2\text{DOTA})]$ complex that exists as a non-hydrated chelate both in solution and in the solid state (Wang and Westmoreland, 2009). The relaxivity of the diprotonated species at $t \rightarrow 0$ time point was determined from the extrapolation of the relaxivity vs. time data collected after acidification of the samples containing the complexes. The X-ray crystallographic structure of $[\text{Mn}(\text{H}_2\text{DOTA})]$ indicates the protonation of two *trans*

TABLE 4 | Relaxivities (r_{1p}) determined for selected Mn(II) complexes (at 0.5 T field strength, 25 °C and pH = 7.4).

Chelate	r_{1p} ($\text{mM}^{-1}\text{s}^{-1}$)	Chelate	r_{1p} ($\text{mM}^{-1}\text{s}^{-1}$)
$[\text{Mn}(\text{PCTA})]^-$	1.50	$[\text{Mn}(\text{DOTP})]^{6-}$	2.37 ^[e]
$[\text{Mn}(\text{PC3AM}^{\text{H}})]^{2+}$	1.21	$[\text{Mn}(\text{DOTMA})]^{2+}$	1.11, 0.96 ^[f]
$[\text{Mn}(\text{PC3AM}^{\text{Gly}})]^-$	1.44	$[\text{Mn}(\text{DOTMA})]^{2-}$ / $[\text{Mn}(\text{H}_2\text{DOTMA})]$ ($q = 0$)	1.76/2.98 ^[g]
$[\text{Mn}(\text{PC3AM}^{\text{Pip}})]^{2+}$	1.28	$[\text{Mn}(\text{DOTA})]^{2-}$ / $[\text{Mn}(\text{H}_2\text{DOTA})]$ ($q = 0$)	1.25/3.20 ^[f]
$[\text{Mn}(\text{DO3A})]^-$	1.18- 1.31, 1.30 ^[a]	$[\text{Mn}(\text{trans-DO2A})]$	1.50 ^[a]
$[\text{Mn}(\text{DO3AM}^{\text{H}})]^{2+}$	1.33	$[\text{Mn}(\text{cis-DO2A})]$	2.10 ^[a]
$[\text{Mn}(\text{DO3P})]^{4-}$	2.23 ^[b]	$[\text{Mn}(\text{cis-DO2AM}^{\text{Me2}})]^{2+}$	2.50 ^[h]
$[\text{Mn}(\text{ODO3A})]^-$	1.40	$[\text{Mn}(\text{cis-BzDO2AM}^{\text{H}})]^{2+}$	3.80 ^[l]
$[\text{Mn}(\text{AAZTA})]^{2-}$, [c]	1.60 ^[d]	$[\text{Mn}(\text{cis-DO2AM}^{\text{Bz2}})]^{2+}$	3.50 ^[l]

^[a]Rolla et al. (2013); ^[b]determined in the pH range of 8.5–9.3 where mainly the $[\text{Mn}(\text{DO3P})]^{4-}$ complex exists in solution; ^[c]AAZTA = 6-amino-6-methylperhydro-1,4-diazepine tetraacetic acid; ^[d]Tai et al. (2011); ^[e]determined in the pH range of 10.0–11.0 where the deprototonated complex exists in solution; ^[f] Wang and Westmoreland (2009) measured at 0.5 T field strength and 37 °C; ^[g]Tircsó and Woods (in preparation); ^[h]Forgács et al. (2016); ^[l]Forgács et al. (2017).

carboxylate moieties (e.g., the coordination around the metal ion is similar to that observed in $[\text{Mn}(\text{trans-DO2A})]$ as determined by DFT calculations). Thus, the relaxivity of the diprotonated $[\text{Mn}(\text{H}_2\text{DOTA})]$ and $[\text{Mn}(\text{H}_2\text{DOTMA})]$ complexes is expected to be similar to that of $[\text{Mn}(\text{trans-DO2A})]$ (when $q = 0$). The value obtained by us is considerably higher, which highlights the importance of prototropic exchange as a useful tool to improve the relaxivity of the complexes (however, it has to be underlined that the protonation of the complex generally leads to a decrease in kinetic inertness). A similar relaxivity enhancing role of prototropic exchange was demonstrated for Gd(III) complexes of phosphonate derivatives such as ($[\text{Gd}(\text{DOTP})]^{5-}$ and $[\text{Gd}(\text{DOTA-4Amp})]^{5-}$) (Avecilla et al., 2003; Kálmann et al., 2007).

CONCLUSIONS

In this work, we summarized the results of our studies on the equilibrium and kinetic properties of Mn(II) complexes of several trisubstituted 12-membered macrocyclic ligands tested in our laboratory during the past 5–6 years. Originally, these ligands were intended for Ln(III) complexation. In this project, these structurally extremely diverse ligands were investigated for their Mn(II) chelating ability and we believe that the results presented here will help us to better understand the relationship that exists between the ligand structures and the thermodynamic/kinetic/relaxometric properties of their Mn(II)

complexes. The stability constants of the complexes were determined by pH-potentiometry and often supported by ^1H -relaxometry. As expected, decreasing the denticity and basicity of the parent ligand DOTA (i.e., removing one metal binding pendant arm to afford DO3A) resulted in a drop in the stability of the Mn(II) complex. This decrease can be compensated by incorporating the fourth (secondary) nitrogen atom into a pyridine ring (e.g., PCTA) or replacing the secondary amine with an etheric oxygen atom. The substitution of primary amides for the acetates also resulted in a drop in the stability constant (DO3AM^H or PC3AM^H), but the stability increased as the primary amides (PC3AM^H) were replaced by secondary (PC3AM^{Gly}) or tertiary amide (PC3AM^{Pip}) moieties. The ligands incorporating phosphonate pendant arms were found to form the most stable Mn(II) complexes but their conditional stability at pH = 7.4 was the lowest. Very similar conclusion was derived by analyzing the dissociation kinetics data. Among the studied complexes, $[\text{Mn}(\text{DO3P})]^{4-}$ was found to be the most labile while the Mn(II) complex of the rigid macrocycle (pyclen) based tertiary amide chelator PC3AM^{Pip} has the highest kinetic inertness whose acid catalyzed dissociation rate is nearly 8 orders of magnitude lower than that of $[\text{Mn}(\text{DO3P})]^{4-}$. By considering the structure of PC3AM^{Pip} it can be concluded that the rigidity of the macrocycle is one of the key structural features that determine the dissociation kinetic properties of Mn(II) complexes. Further improvements can be achieved by proper selection of the donor atoms in the metal binding sidearms attached to the nitrogen atoms of the macrocycles. The tertiary amide coordinating sidearm appears to be one of the best candidates in this respect. The Mn(II) complexes of the studied heptadentate ligands are poor T_1 relaxation agents because they do not have a metal bound water molecule. However, the trends observed for Gd(III) complexes seems to hold for the Mn(II) chelates as evidenced by the low relaxivity of the amide based systems or by the increase in the relaxivity due to accelerated prototropic exchange in $[\text{Mn}(\text{DOTP})]^{6-}$ and $[\text{Mn}(\text{DO3P})]^{4-}$.

AUTHOR CONTRIBUTIONS

The ligand synthesis was accomplished by ZK and GT. Equilibrium and relaxometric studies were performed by ZG, EM, FKK, RB, ZB, and GT while were analyzed with the help of IT and EB. Kinetic studies were performed by ZG, EM, FKK, and GT and the data were evaluated with the help of IT and EB. The manuscript was written through contributions of all authors. All authors have given approval to the final version of the manuscript.

ACKNOWLEDGMENTS

Authors are grateful for the support granted by the Hungarian National Research, Development and Innovation Office (NKFIH K-120224 project) and for the János Bolyai Research Scholarship of the Hungarian Academy of Sciences (GT and FKK). The research was also supported in a part by the EU and

co-financed by the European Regional Development Fund under the projects GINOP-2.3.2-15-2016-00008 and GINOP-2.3.3-15-2016-00004. This work was carried out within the frame of the COST CA15209 Action European Network on NMR Relaxometry.

REFERENCES

- Aime, S., Anelli, P. L., Botta, M., Brocchetta, M., Canton, S., Fedeli, F., et al. (2002). Relaxometric evaluation of novel manganese(II) complexes for application as contrast agents in magnetic resonance imaging. *J. Biol. Inorg. Chem.* 7, 58–67. doi: 10.1007/s007750100265
- Aime, S., Barge, A., Bruce, J. I., Botta, M., Howard, J. A. K., Moloney, J. M., et al. (1999). NMR, relaxometric, and structural studies of the hydration and exchange dynamics of cationic lanthanide complexes of macrocyclic tetraamide ligands. *J. Am. Chem. Soc.* 121, 5762–5771. doi: 10.1021/ja990225d
- Aime, S., Botta, M., Geninatti Crich, S., Giovenzana, G. B., Jommi, G., Pagliarin, R., et al. (1997). Synthesis and NMR studies of three pyridine-containing triaza macrocyclic triacetate ligands and their complexes with lanthanide ions. *Inorg. Chem.* 36, 2992–3000. doi: 10.1021/ic960794b
- Aime, S., Botta, M., Garda, Z., Kucera, B. E., Tircso, G., Young, V. G., et al. (2011). Properties, solution state behavior, and crystal structures of chelates of DOTMA. *Inorg. Chem.* 50, 7955–7965. doi: 10.1021/ic2012827
- Amorim, M. T., Delgado, R., da Silva, J. J., Cândida, M., Vaz, T. A., and Vilhena, M. F. (1988). Metal complexes of 1-oxa-4,7,10-triazacyclododecane-N,N',N''-triacetic acid. *Talanta* 35, 741–745. doi: 10.1016/0039-9140(88)0175-9
- Avecilla, F., Peters, J. A., and Geraldes, C. F. G. C. (2003). X-ray crystal structure of a sodium salt of $[Gd(DOTP)]^{5-}$: implications for its second-sphere relaxivity and the ^{23}Na NMR hyperfine shift effects of $[Tm(DOTP)]^{5-}$. *Chem. Eur. J.* 23, 4179–4186. doi: 10.1002/ejic.200300312
- Balogh, E., He, Z. J., Hsieh, W. Y., Liu, S., and Tóth, É. (2007). Dinuclear complexes formed with the triazacyclonane derivative ENOTA $^{4-}$: high-pressure ^{17}O NMR evidence of an associative water exchange on $[Mn_2^{II}(ENOTA)(H_2O)_2]$. *Inorg. Chem.* 46, 238–250. doi: 10.1021/ic0616582
- Brücher, E., Tircsó, G., Baranyai, Z., Kovács, Z., and Sherry, A. D. (2013). “The Chemistry of contrast agents in medical magnetic resonance imaging,” in *Stability and Toxicity of Contrast Agents*, 2nd Edn, eds A. Merbach, L. Helm, and E. Tóth (Chichester: John Wiley and Sons), 157–208. Available online at: <https://www.wiley.com/en-hu/The+Chemistry+of+Contrast+Agents+in+Medical+Magnetic+Resonance+Imaging,+2nd+Edition-p-9781119991762>
- Choppin, G. R. (1985). Thermodynamics of lanthanide-organic ligand complexes. *J. Less Common Met.* 112, 193–205. doi: 10.1016/0022-5088(85)90024-4
- Dees, A., Zahl, A., Puchta, R., Hommes, N. J., Heinemann, F. W., and Ivanović-Burmazović, I. (2007). Water exchange on seven-coordinate Mn(II) complexes with macrocyclic pentadentate ligands: insight in the mechanism of Mn(II) SOD mimetics. *Inorg. Chem.* 46, 2459–2470. doi: 10.1021/ic061852o
- Desreux, J. F., Merciny, E., and Loncin, M. F. (1981). Nuclear magnetic resonance and potentiometric studies of the protonation scheme of two tetraaza tetraacetic macrocycles. *Inorg. Chem.* 20, 987–991. doi: 10.1021/ic50218a008
- Drahos, B., Kotek, J., Hermann, P., Lukes, I., and Tóth, E. (2010). Mn $^{2+}$ complexes with pyridine-containing 15-membered macrocycles: thermodynamic, kinetic, crystallographic, and $^{1}H/^{17}O$ relaxation studies. *Inorg. Chem.* 49, 3224–3238. doi: 10.1021/ic9020756
- Drahos, B., Kubicek, V., Bonnet, C. S., Hermann, P., Lukes, I., and Toth, E. (2011). Dissociation kinetics of Mn $^{2+}$ complexes of NOTA and DOTA. *Dalton Trans.* 40, 1945–1951. doi: 10.1039/c0dt01328e
- Drahos, B., Lukes, I., and Toth, E. (2012). Manganese(II) complexes as potential contrast agents for MRI. *Eur. J. Inorg. Chem.* 12, 1975–1986. doi: 10.1002/ejic.201101336
- Forgács, A., Pujales-Paradela, R., Regueiro-Figueroa, M., Valencia, L., Esteban-Gómez, D., Botta, M., et al. (2017). Developing the family of picolinate ligands for Mn $^{2+}$ complexation. *Dalton Trans.* 46, 1546–1558. doi: 10.1039/C6DT04442E
- Forgács, A., Regueiro-Figueroa, M., Barriada, J. L., Esteban-Gómez, D., de Blas, A., Rodriguez-Bias, T., et al. (2015). Mono-, Bi-, and trinuclear bis-hydrated Mn $^{2+}$ complexes as potential MRI contrast agents. *Inorg. Chem.* 54, 9576–9587. doi: 10.1021/acs.inorgchem.5b01677
- Forgács, A., Tei, L., Baranyai, Z., Tóth, I., Zékány, L., and Botta, M. (2016). A bisamide derivative of $[Mn(1,4-DO2A)]$ – solution thermodynamic, kinetic, and NMR relaxometric studies. *Eur. J. Inorg. Chem.* 8, 1165–1174. doi: 10.1002/ejic.201501415
- Gale, E. M., Atanasova, I. P., Blasi, F., Ay, I., and Caravan, P. (2015). A manganese alternative to gadolinium for MRI contrast. *J. Am. Chem. Soc.* 137, 15548–15557. doi: 10.1021/jacs.5b10748
- Garda, Z., Forgács, A., Do, Q. N., Kálmann, F. K., Timári, S., Baranyai, Z., et al. (2016). Physico-chemical properties of Mn II complexes formed with *cis*- and *trans*-DO2A: thermodynamic, electrochemical and kinetic studies. *J. Inorg. Biochem.* 163, 206–213. doi: 10.1016/j.jinorgbio.2016.07.018
- Huskens, J., Torres, D. A., Kovacs, Z., André, J. P., Geraldes, C. F., and Sherry, A. D. (1997). Alkaline earth metal and lanthanide(III) complexes of ligands based upon 1,4,7,10-tetraazacyclododecane-1,7-bis(acetic acid). *Inorg. Chem.* 36, 1495–1503. doi: 10.1021/ic961131x
- Idee, J. M., Port, M., Raynal, I., Schaefer, M., Le Greneur, S., and Corot, C. (2006). Clinical and biological consequences of transmetallation induced by contrast agents for magnetic resonance imaging: a review. *Fund. Clin. Pharmacol.* 20, 563–576. doi: 10.1111/j.1472-8206.2006.00447.x
- Irving, H. M., Miles, M. G., and Pettit, L. D. (1967). A study of some problems in determining the stoichiometric proton dissociation constants of complexes by potentiometric titrations using a glass electrode. *Anal. Chim. Acta* 38, 475–488. doi: 10.1016/S0003-2670(01)80616-4
- Kálmann, F. K., Baranyai, Z., Tóth, I., Bánya, I., Király, R., Brücher, E., et al. (2008). Synthesis, potentiometric, kinetic, and NMR studies of 1,4,7,10-tetraazacyclododecane-1,7-bis(acetic acid)-4,10-bis(methylenephosphonic acid) (DO2A2P) and its complexes with Ca(II), Cu(II), Zn(II) and lanthanide(III) Ions. *Inorg. Chem.* 47, 3851–3862. doi: 10.1021/ic7024704
- Kálmann, F. K., and Tircsó, G. (2012). Kinetic inertness of the Mn $^{2+}$ complexes formed with AAZTA and some open-chain EDTA derivatives. *Inorg. Chem.* 51, 1006–10067. doi: 10.1021/ic300832e
- Kálmann, F. K., Woods, M., Caravan, P., Jurek, P., Spiller, M., Tircsó, G., et al. (2007). Potentiometric and relaxometric properties of a gadolinium-based MRI contrast agent for sensing tissue pH. *Inorg. Chem.* 46, 5260–5270. doi: 10.1021/ic0702926
- Kaupang, Å., and Bonge-Hansen, T. (2013). α -Bromodiazoacetamides – a new class of diazo compounds for catalyst-free, ambient temperature intramolecular C–H insertion reactions. *Beilstein J. Org. Chem.* 9, 1407–1413. doi: 10.3762/bjoc.9.157
- Kumar, K., Tweedle, M. F., Malley, M. F., and Gougoutas, J. Z. (1995). Synthesis, stability, and crystal structure studies of some Ca $^{2+}$, Cu $^{2+}$, and Zn $^{2+}$ complexes of macrocyclic polyamino carboxylates. *Inorg. Chem.* 34, 6472–6480. doi: 10.1021/ic00130a012
- Loving, G. S., Mukherjee, S., and Caravan, P. (2013). Redox-activated manganese-based MR contrast agent. *J. Am. Chem. Soc.* 135, 4620–4623. doi: 10.1021/ja312610j
- Lukes, I., Kotek, J., Vojtisek, P., and Hermann, P. (2001). Complexes of tetraazacycles bearing methylphosphinic/phosphonic acid pendant arms with copper(II), zinc(II) and lanthanides(III). A comparison with their acetic acid analogues. *Coord. Chem. Rev.* 216–217, 287–312. doi: 10.1016/S0013-0854(01)00336-8
- Martell, A. E., and Calvin, M. (1952). *Chemistry of Metal Chelate Compounds*. New York, NY: Prentice Hall.
- Maumela, H., Hancock, R. D., Carlton, L., Reibenspies, J. H., and Wainwright, K. P. (1995). The amide oxygen as a donor group. metal ion complexing properties

SUPPLEMENTARY MATERIAL

The Supplementary Material for this article can be found online at: <https://www.frontiersin.org/articles/10.3389/fchem.2018.00232/full#supplementary-material>

- of tetra-N-acetamide substituted cyclen: a crystallographic, NMR, molecular mechanics, and thermodynamic study. *J. Am. Chem. Soc.* 117, 6698–6707. doi: 10.1021/ja00130a008
- Molnar, E., Camus, N., Patinec, V., Rolla, G. A., Botta, M., Tircso, G., et al. (2014). Picolinate-containing macrocyclic Mn²⁺ complexes as potential MRI contrast agents. *Inorg. Chem.* 53, 5136–5149. doi: 10.1021/ic500231z
- Murakami, T., Baron, R. L., Peterson, M. S., Oliver, J. H., Davis, L., Confer, R., et al. (1996). Hepatocellular carcinoma: MR imaging with mangafodipir trisodium (Mn-DPD). *Radiology* 200, 69–77. doi: 10.1148/radiology.200.1.8657947
- Nithyakumar, A., and Alexander, V. (2016). A tri- (Ru^{II}-Gd₂^{III}) and tetrานuclear (Ru^{II}-Gd₃^{III}) d-f heterometallic complexes as potential bmodal imaging probes for mri and optical imaging *New J. Chem.* 40, 4606–4616. doi: 10.1039/C5NJ03393D
- Pasha, A., Tircsó, G., Tircsóné Benyó, E., Brücher, E., and Sherry, A. D. (2007). Synthesis and characterization of DOTA-(amide)(4) derivatives: equilibrium and kinetic behavior of their lanthanide(III) complexes. *Eur. J. Inorg. Chem.* 27, 4340–4349. doi: 10.1002/ejic.200700354
- Póta, K., Garda, Z., Kálmán, F. K., Barriada, J. L., Esteban-Gómez, D., Platas-Iglesias, C., et al. (2018). Taking the next step toward inert Mn²⁺ complexes of open-chain ligands: the case of the rigid PhDTA ligand. *New J. Chem.* 42, 8001–8011. doi: 10.1039/C8NJ00121A
- Phukan, B., Patel, A. B., and Mukherjee, C. (2015). A water-soluble and water-coordinated Mn(II) complex: synthesis, characterization and phantom MRI image study. *Dalton Trans.* 44, 12990–12994. doi: 10.1039/C5DT01781E
- Rocklage, S. M., Chacheris, W. P., Quay, S. C., Hahn, F. E., and Raymond, K. N. (1989). Manganese(II) N,N'-dipyridoxylethylenediamine-N,N'-diacetate 5,5'-bis(phosphate). Synthesis and characterization of a paramagnetic chelate for magnetic resonance imaging enhancement. *Inorg. Chem.* 28, 477–485. doi: 10.1021/ic00302a019
- Rojas-Quijano, F. A., Tircsóné Benyó, E., Tircsó, G., Kálmán, F. K., Baranyai, Z., Aime, S., et al. (2009). Lanthanide(III) complexes of tris(amide) PCTA derivatives as potential bimodal magnetic resonance and optical imaging Agents. *Chem. Eur. J.* 15, 13188–13200. doi: 10.1002/chem.200901095
- Rolla, G. A., Platas-Iglesias, C., Botta, M., Tei, L., and Helm, L. (2013). ¹H and ¹⁷O NMR relaxometric and computational study on macrocyclic Mn(II) complexes. *Inorg. Chem.* 52, 3268–3279. doi: 10.1021/ic302785m
- Siaugue, J.-M., Segat-Dioury, F., Favre-Reguillon, A., Madic, C., Foos, J., and Guy, A. (2000). An efficient synthesis of pyridine containing triaza-macrocyclic triacetate ligand and luminescence properties of its europium(III) complex. *Tetrahedron Lett.* 41, 7443–7446. doi: 10.1016/S0040-4039(00)1272-7
- Stetter, H., Frank, W., and Mertens, R. (1981). Darstellung und komplexbildung von polyazacycloalkan-N-essigsäuren. *Tetrahedron*, 37, 767–772. doi: 10.1016/S0040-4020(01)97695-1
- Su, H., Wu, C., Zhu, J., Miao, T., Wang, D., Xia, C., et al. (2012). Rigid Mn(II) chelate as efficient MRI contrast agent for vascular imaging. *Dalton Trans.* 41, 14480–14483. doi: 10.1039/c2dt31696j
- Sun, X., Wuest, M., Kovacs, Z., Sherry, A. D., Motekaitis, R., Wang, Z., et al. (2003). *In vivo* behavior of copper-64-labeled methanephosphonate tetraaza macrocyclic ligands. *J. Biol. Inorg. Chem.* 8, 217–225. doi: 10.1007/s00775-002-0408-5
- Takács, A., Napolitano, R., Purgel, M., Bényei, A. C., Zékány, L., Brücher, E., et al. (2014). Solution structures, sFilities, kinetics, and dynamics of DO3A and DO3A-sulphonamide complexes. *Inorg. Chem.* 53, 2858–2872. doi: 10.1021/ic4025958
- Tei, L., Gugliotta, G., Fekete, M., Kálmán, F. K., and Botta, M. (2011). Mn(II) complexes of novel hexadentate AAZTA-like chelators: a solution thermodynamics and relaxometric study. *Dalton Trans.* 40, 2025–2032. doi: 10.1039/c0dt01114b
- Vanasschen, C., Molnár, E., Tircsó, G., Kálmán, F. K., Tóth, É., Brandt, M., et al. (2017). Novel CDTA-based, bifunctional chelators for stable and inert MnII complexation: synthesis and physicochemical characterization. *Inorg. Chem.* 56, 7746–7760. doi: 10.1021/acs.inorgchem.7b00460
- Wang, S., and Westmoreland, T. D. (2009). Correlation of relaxivity with coordination number in six-, seven-, and eight-coordinate Mn(II) complexes of pendant-arm cyclen derivatives. *Inorg. Chem.* 48, 719–727. doi: 10.1021/ic8003068
- Wen, J., Geng, Z., Yin, Y., and Wang, Z. (2012). A mononuclear Mn²⁺ complex based on a novel tris-(ethyl acetate) pendant-armed tetraazamacrocycle: Effect of pyridine on self-assembly and weak interactions. *Inorg. Chem. Commun.* 21, 16–20. doi: 10.1016/j.inoche.2012.03.042
- Wu, C., Li, D., Yang, L., Lin, B., Zhang, H., Xu, Y., et al. (2015). Multivalent manganese complex decorated amphiphilic dextran micelles as sensitive MRI probes. *J. Mater. Chem. B* 3, 1470–1473. doi: 10.1039/C4TB02036G
- Zékány, L., and Nagypál, I. (1985). “PSEQUAD,” in *Computational Methods for the Determination of Formation Constants*, ed D. Leggett (Springer), 291–353.

Conflict of Interest Statement: The authors declare that the research was conducted in the absence of any commercial or financial relationships that could be construed as a potential conflict of interest.

Copyright © 2018 Garda, Molnár, Kálmán, Botár, Nagy, Baranyai, Brücher, Kovács, Tóth and Tircsó. This is an open-access article distributed under the terms of the Creative Commons Attribution License (CC BY). The use, distribution or reproduction in other forums is permitted, provided the original author(s) and the copyright owner(s) are credited and that the original publication in this journal is cited, in accordance with accepted academic practice. No use, distribution or reproduction is permitted which does not comply with these terms.



Synthesis, Characterization, and Handling of Eu^{II}-Containing Complexes for Molecular Imaging Applications

Lina A. Basal and Matthew J. Allen*

Department of Chemistry, Wayne State University, Detroit, MI, United States

Considerable research effort has focused on the *in vivo* use of responsive imaging probes that change imaging properties upon reacting with oxygen because hypoxia is relevant to diagnosing, treating, and monitoring diseases. One promising class of compounds for oxygen-responsive imaging is Eu^{II}-containing complexes because the Eu^{II/III} redox couple enables imaging with multiple modalities including magnetic resonance and photoacoustic imaging. The use of Eu^{II} requires care in handling to avoid unintended oxidation during synthesis and characterization. This review describes recent advances in the field of imaging agents based on discrete Eu^{II}-containing complexes with specific focus on the synthesis, characterization, and handling of aqueous Eu^{II}-containing complexes.

OPEN ACCESS

Edited by:

Zsolt Baranyai,
Bracco Imaging S.p.a., Italy

Reviewed by:

Mark Woods,
Portland State University,
United States

Jean-Claude Georges Bunzli,
École Polytechnique Fédérale de
Lausanne, Switzerland

*Correspondence:

Matthew J. Allen
mallen@chem.wayne.edu

Specialty section:

This article was submitted to
Inorganic Chemistry,
a section of the journal
Frontiers in Chemistry

Received: 16 January 2018

Accepted: 28 February 2018

Published: 19 March 2018

Citation:

Basal LA and Allen MJ (2018)
Synthesis, Characterization, and
Handling of Eu^{II}-Containing
Complexes for Molecular Imaging
Applications. *Front. Chem.* 6:65.
doi: 10.3389/fchem.2018.00065

INTRODUCTION

Divalent europium is a paramagnetic ion with photophysical and electrochemical properties that can be modulated with coordination chemistry (Gansow et al., 1977; Yee et al., 1980, 1983; Sabbatini et al., 1982, 1984; Antonio and Soderholm, 1996; Jiang et al., 1998; Shipley et al., 1999; Burai et al., 2000; Soderholm et al., 2002; Botta et al., 2003; Christoffers and Starynowicz, 2008; Gamage et al., 2010; Pan et al., 2011; Garcia and Allen, 2012a,b; Gál et al., 2013; Kelly et al., 2015; Kuda-Wedagedara et al., 2015; Regueiro-Figueroa et al., 2015; Allen, 2016; Ekanger et al., 2016a, 2017; Jin et al., 2016; Vanek et al., 2017a,b; Burnett et al., 2017; Kawasaki et al., 2017; Corbin et al., 2018; Jenks et al., 2018). Because of these tunable properties, divalent europium complexes have potential use as molecular-imaging probes that sense O₂, which is important because O₂ imbalances are often correlated with disease (Shweiki et al., 1992; Barnham et al., 2004; Mattson, 2004; Lin and Beal, 2006; Park et al., 2008; Facciabene et al., 2011). One promising technique to investigate oxygenation is contrast-enhanced magnetic resonance imaging (MRI) with Eu^{II}-containing complexes. Divalent europium was proposed as a *p*O₂ sensor for MRI (Burai et al., 2000) because divalent europium acts as a T₁-shortening contrast agent for MRI until it is oxidized to Eu^{III}, which shows no measurable T₁-shortening ability at imaging-relevant concentrations and field strengths (≤ 6 mM) (Ekanger et al., 2016a; Basal et al., 2017b). Recently, the first example of *in vivo* imaging using a Eu^{II}-containing contrast agent was reported (Ekanger et al., 2015), and other *in vivo* examples followed (Ekanger et al., 2016b; Funk et al., 2016; Basal et al., 2017a). The recent advancement of Eu^{II}-containing complexes as O₂ sensors for molecular imaging and the unique experimental challenges of characterizing and handling air-sensitive Eu^{II}-containing

complexes inspired this review. Unlike Gd^{III}, which is a commonly studied ion for MRI, Eu^{II} is air-sensitive and requires careful handling techniques because Eu^{II} oxidizes to Eu^{III} when exposed to O₂. Many researchers who might be interested in Eu^{II} likely have experience with Gd^{III}. However, because of the crucial differences in preparation and handling between Eu^{II} and Gd^{III}, this review focuses on the synthesis, handling, and characterization of identity and purity of Eu^{II}-containing complexes relevant to molecular imaging (**Figure 1**). For measurements of molecular-imaging-relevant properties for MRI, readers are referred elsewhere (Caravan et al., 1999; Burai et al., 2000, 2002; Tóth et al., 2001; Botta et al., 2003; Garcia et al., 2011, 2012; Garcia and Allen, 2012b; Ekanger et al., 2014, 2015, 2016a,b; Basal et al., 2017a,b; Lenora et al., 2017; Pierre et al., 2018). Because this review is focused on techniques for handling and characterizing discrete, air-sensitive Eu^{II}-containing complexes for molecular imaging, we do not describe other divalent lanthanide complexes, nanoparticles, imaging probes, or nonaqueous Eu^{II}-containing complexes. Readers are referred elsewhere for details of those subjects (Evans, 2000; Dorenbos, 2003; Bochkarev, 2004; Bottrill et al., 2006; le Masne de Chermont et al., 2007; Kuda-Wedagedara and Allen, 2014; Pierre et al., 2014; Ekanger and Allen, 2015; Angelovski, 2016; Edelmann, 2016; Wang et al., 2017).

SYNTHESIS OF Eu^{II}-CONTAINING COMPLEXES

In this section, we describe procedures for the preparation of Eu^{II}-containing complexes using the ligands depicted in **Figure 2**. These procedures are divided into two general strategies (**Figure 3**): (1) chemical or electrochemical reduction of Eu^{III}-containing complexes or mixtures of Eu^{III} salts and ligands and (2) metalation of ligands with Eu^{II} salts. Depending on the route used to generate Eu^{II}-containing complexes, different techniques are appropriate to evaluate the identity and purity of the resulting complexes. These characterization techniques and strategies for effectively handling solutions of Eu^{II}-containing complexes for analyses are described in the handling section of this article.

Reduction of Eu^{III} to Produce Eu^{II}-containing Complexes

In the process of forming Eu^{II}-containing complexes, Eu^{III} is often reduced using electrochemical or chemical methods. Transient formation of detectable amounts of Eu^{II}-containing complexes can be achieved using cyclic voltammetry, and isolable Eu^{II}-containing complexes can be obtained through electrochemical or chemical reduction of either Eu^{III}-containing complexes or mixtures of Eu^{III} with ligands. The most favorable route to form a Eu^{II}-containing complex should be determined based upon the ligand and the type of analysis that is needed.

Transient Formation of Eu^{II}-Containing Complexes From Cyclic Voltammetry

To obtain information about the reduction and oxidation potentials of Eu^{II}-containing complexes, several research groups have formed Eu^{II}-containing complexes transiently using cyclic voltammetry. A description of air-free electrochemical techniques used for cyclic voltammetry or bulk electrolysis to form Eu^{II}-containing complexes is described in the handling section of this review. When reducing Eu^{III} to form Eu^{II}, two routes are commonly taken: the corresponding Eu^{III}-containing complexes are synthesized and purified before electrolysis, such as in the case of Eu-containing complexes of **8, 20, 21, 25, 26, 27, 31–34, and 39** (Gansow et al., 1977; Yee et al., 1980, 1983; Burai et al., 2003; Vanek et al., 2016; Basal et al., 2017a; Burnett et al., 2017). Alternatively, Eu^{III} salts—such as Eu(OTf)₃, EuCl₃, or Eu(NO₃)₃—are dissolved in the presence of ligands, enabling the formation of complexes upon electrolysis of Eu^{III} to Eu^{II}, such in the case of Eu-containing complexes of **1–8, 10, 11, 13–15, 20–23, 28–30, and 35–38** (Yee et al., 1980, 1983; Sabbatini et al., 1984; Burai et al., 2002, 2003; Botta et al., 2003; Gamage et al., 2010; Gál et al., 2013; Regueiro-Figueroa et al., 2015). In these experiments, cyclic voltammetry peaks that are different than the peaks for Eu^{II/III}_{aqua} or the ligand (if the ligand is redox active in the potentials spanned by the voltammogram) are attributed to the formation of Eu^{II/III}-containing complexes (**Figure 4**).

For the selection of an appropriate route, consideration of ligand structure and solubility is necessary. For example, ligands that readily form complexes with Eu^{II} upon reduction

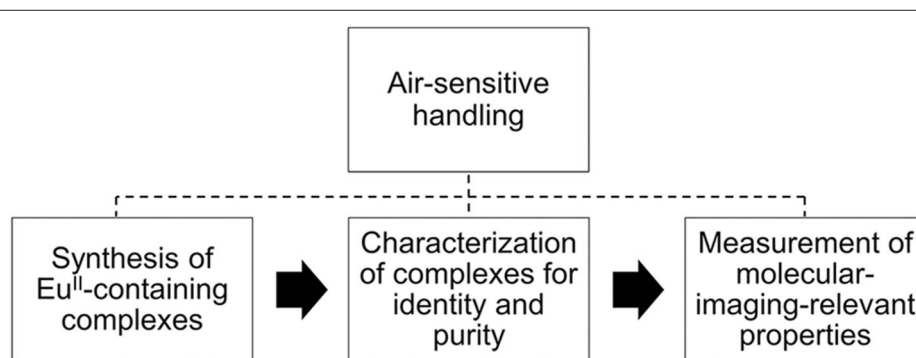
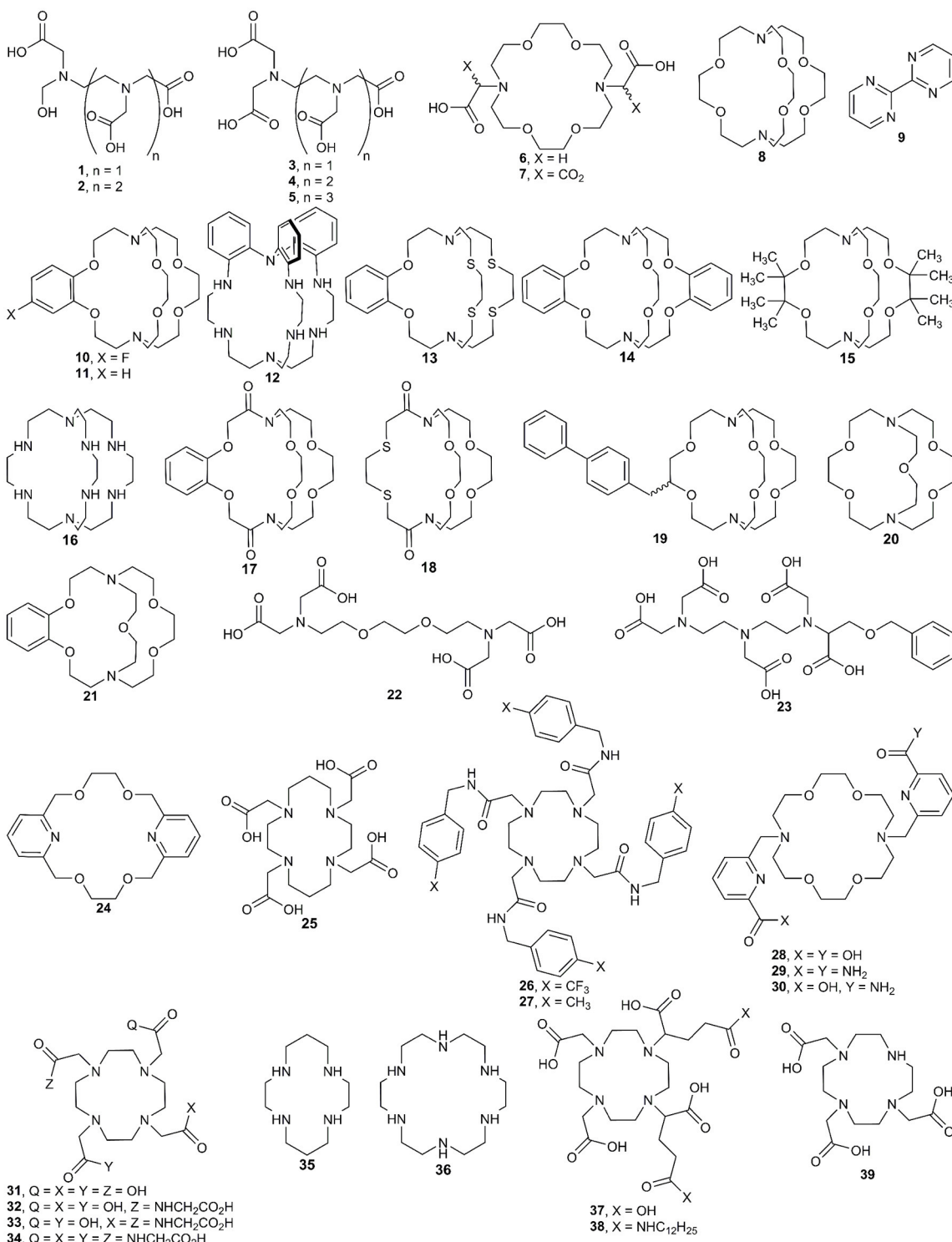
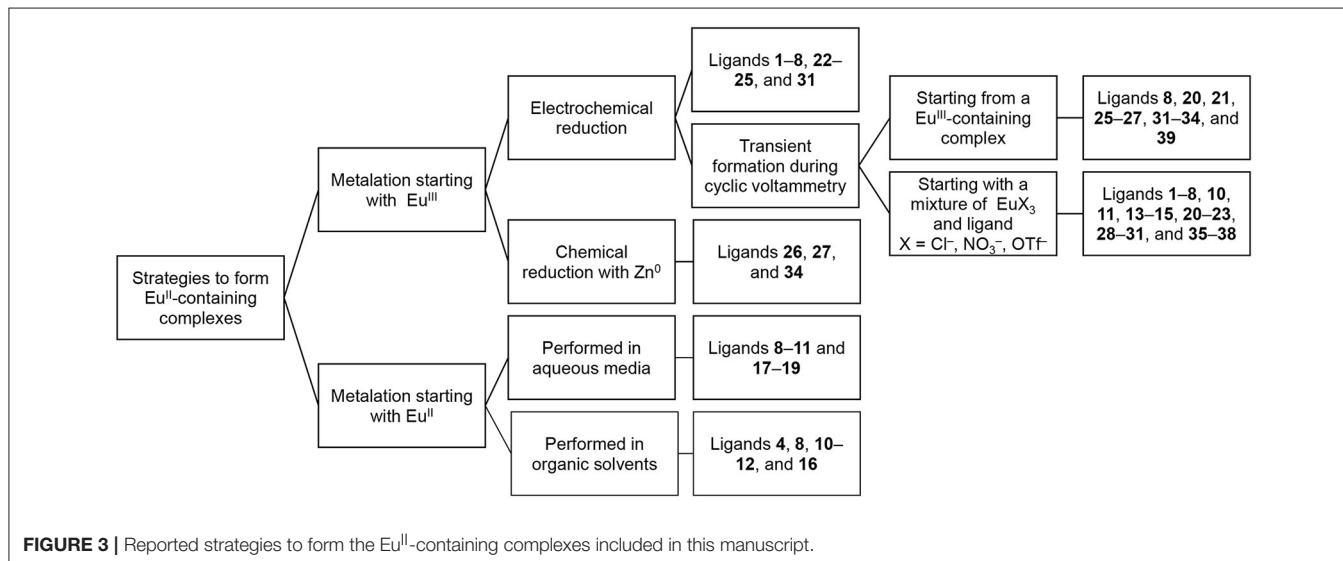


FIGURE 1 | Pathway for Eu^{II}-containing complexes that have applications in molecular imaging.



from Eu^{III}, like cryptands **8**, **20**, and **21**, produce the same electrochemical profiles whether starting with a mixture of Eu^{III} and ligand or a Eu^{II}-containing complex (Yee et al., 1980,

1983). When solubility differences exist between ligands and their corresponding complexes, such as if the ligand is not soluble but the complex is, then one must ensure complexation prior



to CV analysis. If the complex is insoluble in aqueous media, then organic solvents can be employed with the caveat that the measured standard electrode potential might not reflect the potential under aqueous conditions.

Producing Eu^{II}-Containing Complexes via Electrochemical Reduction of Eu^{III}

Beyond the transient reduction of Eu^{III} on the surface of electrodes during cyclic voltammetry, Eu^{III} can be reduced on an isolable scale electrochemically using bulk electrolysis in oxygen-free solvent under an atmosphere of inert gas. Reduction via bulk electrolysis involves holding a sufficiently negative potential to reduce Eu^{III} to Eu^{II}. The electrochemical potential used to reduce a Eu^{III}-containing complex is often 0.1–0.5 V more negative than the $E_{1/2}$ of the target complex (Burai et al., 2002, 2003; Botta et al., 2003); however, the reduction potential of the ligand functional groups should be considered before selecting this technique to avoid the possibility of reducing redox-active ligands. Bulk electrolysis was used to obtain Eu^{II}-containing complexes of **1–8, 22–25, and 31** (Sabbatini et al., 1982, 1984; Burai et al., 2000, 2002; Christoffers and Starynowicz, 2008). In these studies, solutions containing both Eu^{III} salts and ligands were held at the appropriate potential, typically in a two-compartment glass cell with a fritted glass separator with sparging of inert gas (Bard and Faulkner, 2000). The resulting Eu^{II}-containing complexes can be used for further analysis of molecular-imaging-relevant properties, including UV-visible and luminescence spectroscopy, relaxivity measurements, ¹⁷O-NMR spectroscopy, and NMRD measurements (Sabbatini et al., 1984; Burai et al., 2000, 2002; Christoffers and Starynowicz, 2008). Bulk electrolysis of a solution of metal and ligand can provide enough material to obtain crystals for X-ray diffraction: for example, bulk electrolysis of Eu^{III} to Eu^{II} in the presence of ligand **24** followed by slow evaporation or cooling under inert atmosphere resulted in crystals of Eu^{II}**24** (Christoffers and Starynowicz, 2008). Bulk electrolysis to produce isolable Eu^{II}-containing complexes is appropriate when the potential

needed to reduce a Eu^{III}-containing complex to a Eu^{II}-containing complex does not overlap with the redox-activity of the ligand, when the desired Eu^{II} salt is unavailable, or when the standard potential or pH of the complex in solution is incompatible with chemical reductants.

Chemical Reduction of Eu^{III}-Containing Complexes to Form Eu^{II}-Containing Complexes

In addition to bulk electrolysis, chemical reductants are used to generate Eu^{II}-containing complexes. Depending on the standard potential of the Eu^{III}-containing complex to be reduced, different reducing agents will be appropriate. For example, the reduction potential of Zn ($Zn^{II} + 2e^- \rightarrow Zn^0$) is -0.960 V vs Ag/AgCl (saturated KCl) (Bard and Faulkner, 2000); therefore, complexes that have standard electrode potentials more positive than -0.960 V vs Ag/AgCl should, thermodynamically, be reduced by Zn⁰. Eu^{III}-containing complexes were reduced using Zn⁰ to form Eu^{II}**26**, Eu^{II}**27**, and Eu^{II}**34** (Ekanger et al., 2016a; Basal et al., 2017a,b). In these studies, the Eu^{III}-containing complexes were dissolved in water in the presence of zinc metal dust, and the pH was adjusted between 4 and 6.5 to expose Zn⁰, resulting in the reduction of Eu^{III} to Eu^{II}. To date, only amalgamated Zn and Zn⁰ have been used to chemically reduce Eu^{III}-containing complexes to Eu^{II}-containing complexes in water (McCoy, 1935; Ekanger et al., 2016a; Basal et al., 2017a,b). However, other chemical reductants, which have been used to reduce other Ln^{III} ions to Ln^{II} ions (Teprovich et al., 2008; MacDonald et al., 2013; Fieser et al., 2015), could be used if the low pH required for the use of zinc metal is undesirable or if the standard electrode potential of the Eu-containing complex is more negative than that of Zn⁰.

Complex Formation by Direct Mixing of Eu^{II} Salts and Ligands

Another technique to synthesize Eu^{II}-containing complexes is mixing Eu^{II} halide salts with ligands. Eu^{II} chloride, bromide,

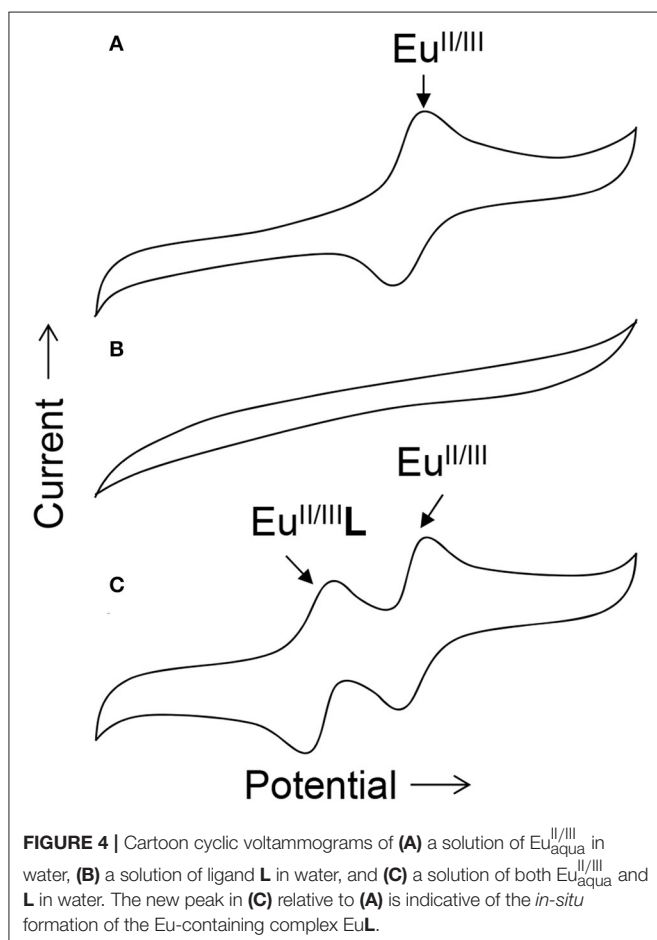


FIGURE 4 | Cartoon cyclic voltammograms of (A) a solution of $\text{Eu}_{\text{aqua}}^{\text{II/III}}$ in water, (B) a solution of ligand **L** in water, and (C) a solution of both $\text{Eu}_{\text{aqua}}^{\text{II/III}}$ and **L** in water. The new peak in (C) relative to (A) is indicative of the *in-situ* formation of the Eu-containing complex EuL .

and iodide salts are available commercially. When mixing Eu^{II} and ligands, often a slight excess of a Eu^{II} halide salt (1.1–1.2 equivalents) is mixed with a water-soluble ligand (1 equivalent) in water. Complexes tend to be easier to purify from an excess of Eu^{II} relative to an excess of ligand: the addition of phosphate buffer precipitates excess Eu^{II} from solution as phosphate salts that can be removed with a small (0.2 micrometer) hydrophilic filter to yield a buffered solution of Eu^{II}-containing complex (Garcia and Allen, 2012b). This technique was used to synthesize Eu^{II}-containing complexes of **8–11** and **17–19** (Zucchi et al., 2010; Garcia and Allen, 2012b; Garcia et al., 2012; Ekanger et al., 2014, 2015, 2016b, 2017; Lenora et al., 2017).

When a ligand is not water-soluble but the resulting complex is, aqueous solutions of Eu^{II}-containing complexes can be prepared by mixing Eu^{II} salts with ligands in an organic solvent and then separating the resulting complex from the organic solvent. Purification by precipitation or crystallization results in solids that are soluble in water for imaging. For an example of purification by precipitation, Eu^{II}**16** was synthesized in tetrahydrofuran: EuI₂ and **16** are soluble in tetrahydrofuran, but Eu^{II}**16** is not, enabling isolation of Eu^{II}**16** by precipitation (Kuda-Wedagedara et al., 2015). For an example of purification by crystallization, crystals were grown of cryptates Eu^{II}**4**, Eu^{II}**8**, Eu^{II}**10**, Eu^{II}**11**, Eu^{II}**12**, and Eu^{II}**16** from slow evaporation of

a mixture of ligand and Eu^{II} halide in acetone, methanol, or methanol/tetrahydrofuran (Burai et al., 2000; Ekanger et al., 2015; Kuda-Wedagedara et al., 2015; Jin et al., 2016; Lenora et al., 2017).

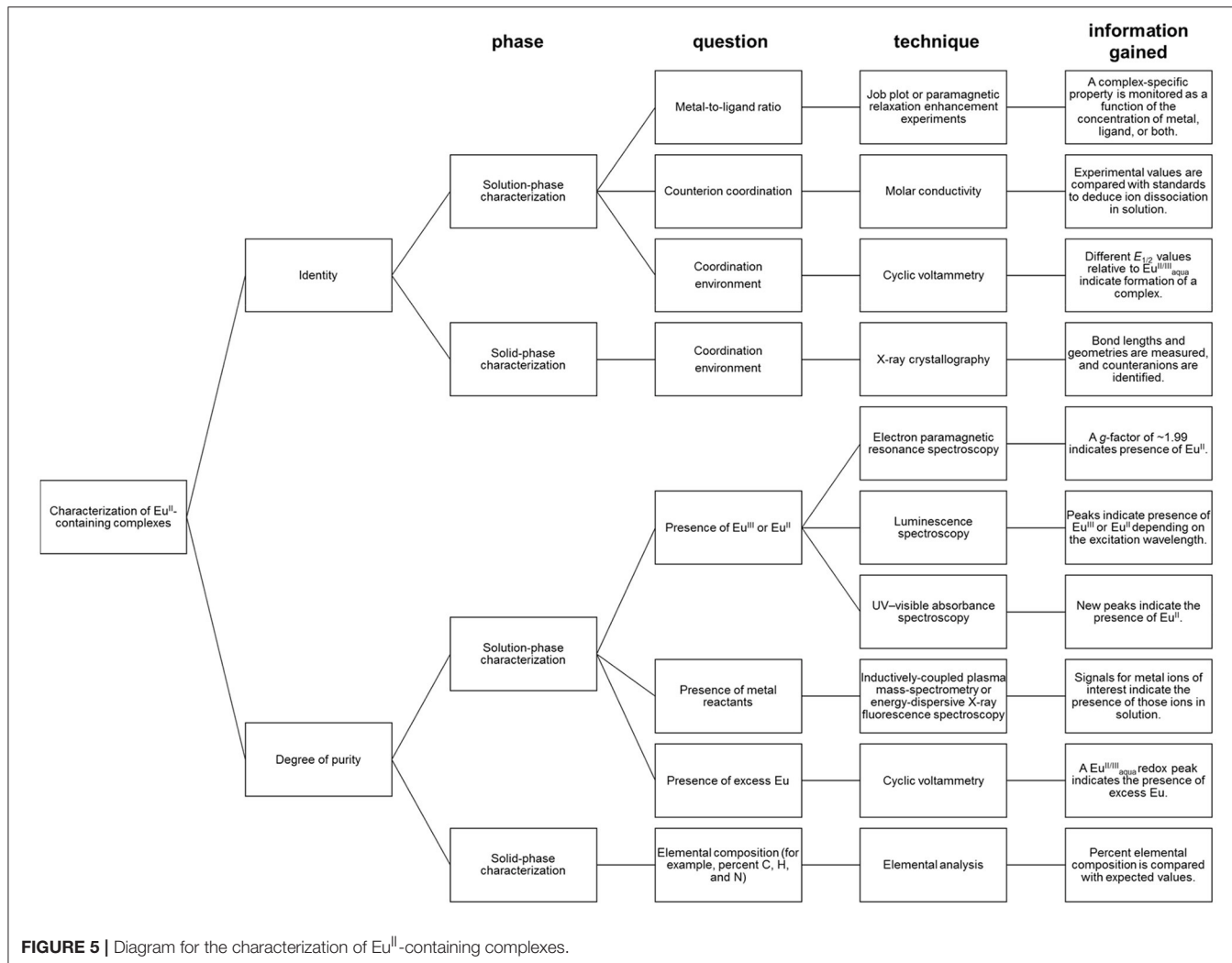
CHARACTERIZATION FOR IDENTITY AND PURITY IN AQUEOUS MEDIA

Depending on the route chosen to form Eu^{II}-containing complexes, different techniques for the characterization of identity and purity of Eu^{II}-containing complexes must be used (Figure 5). Assessment of identity of Eu^{II}-containing complexes includes evidence for the oxidation state of Eu, coordination environment, and metal-to-ligand ratio. Assessment of the purity of Eu^{II}-containing complexes includes the detection of Eu^{II} or Eu^{III}, ligand, reactants, or byproducts.

When Eu^{II}-containing complexes are generated *in situ* via cyclic voltammetry, purity with respect to excess $\text{Eu}_{\text{aqua}}^{\text{II}}$ can be assessed by observation of a peak for $\text{Eu}_{\text{aqua}}^{\text{II/III}}$. The minimum detectable concentration of europium by cyclic voltammetry, and hence the boundary of usefulness for this technique, is influenced by multiple experimental parameters including concentration of supporting electrolyte, the identity of the buffer and solvent, and choice of reference electrode (Bard and Faulkner, 2000). With these parameters in mind, minimum detectable concentrations can be determined experimentally (Harris, 2003). Unlike Eu^{II/III}, if a ligand is not redox-active, cyclic voltammetry does not provide evidence for the presence of uncomplexed ligand. Therefore, the usefulness of cyclic voltammetry for detection of excess ligand is situationally dependent.

Regarding the identity of the complex that is formed during the course of cyclic voltammetry, formation of a Eu-containing complex can be validated by comparing the standard electrode potential of the new complex with the standard electrode potential of a sample of the Eu-containing complex (Tables 1, 2). For example, Eu^{II}-containing complexes of **8**, **20**, and **21** were synthesized and found to produce the same $E_{1/2}$ whether starting with a mixture of Eu^{III} and ligand or an already-synthesized Eu^{II}-containing complex (Yee et al., 1980, 1983). However, the standard electrode potential is influenced by the same experimental parameters that are listed for consideration of purity using cyclic voltammetry; therefore, care must be taken to note experimental parameters when comparing standard electrode potentials.

In the case where Eu^{III}-containing complexes are reduced chemically with zinc, such as $2\text{Eu}^{2+}\text{Cl}_3 + \text{Zn}^0 \rightarrow 2\text{Eu}^{2+}\text{Cl}_2 + \text{ZnCl}_2$, a combination of spectroscopic techniques can be used to provide evidence of the oxidation state and degree of purity. For evidence that Zn^{II} was removed from solution post-reduction, the concentration of Zn^{II} (down to parts-per-billion levels) can be monitored with inductively coupled plasma-mass spectrometry (Ekanger et al., 2016a). For evidence of the reduction of Eu^{III}, a lack of overlap of the excitation bands of Eu^{II}- and Eu^{III}-containing species enables monitoring of the presence of Eu^{III} (down to micromolar levels) by luminescence spectroscopy when excitation is performed with a Eu^{III}-specific wavelength (Ekanger et al., 2016a; Basal et al., 2017a). Evidence



for the generation of Eu^{II} is obtained using electron paramagnetic resonance (EPR) spectroscopy. In its ground state, Eu^{III} has no net magnetic moment (Cullity and Graham, 2009) despite having six unpaired electrons. The magnetic moment (μ_{eff}) of lanthanides is calculated using the total angular momentum (J), unlike the magnetic moments of 3dⁿ transition metals that take into account the number of unpaired electrons (Cotton, 2006; Layfield et al., 2015). This difference is due to the quenching of orbital angular momentum by ligands for 3d orbitals but not for the shielded 4f orbitals. Therefore, the Eu^{III} ground state would not be expected to be observed in EPR spectroscopy (Abragam and Bleaney, 1970). However, Eu^{II} is paramagnetic and characterized by a signal in EPR spectroscopy with a g factor of ~1.99 (Abragam and Bleaney, 1970; Caravan et al., 1999). Also, Eu^{II}-containing complexes can be colored yellow or orange and give rise to broad and relatively intense UV-visible absorptions and emissions that are distinct from the corresponding Eu^{III}-containing species (Burai et al., 2003; Kuda-Wedagedara et al., 2015; Ekanger et al., 2016a). For example, a combination of spectroscopic techniques were used to monitor the formation of

Eu^{II}-containing complexes Eu22, Eu26, and Eu34 (Ekanger et al., 2016a; Basal et al., 2017a).

In the case where the formation of a complex was achieved by mixing EuCl₂ with ligands, evidence of 1:1 complex formation in solution was determined by measuring the change in relaxivity as a function of Eu^{II}-to-ligand ratio, a technique known as proton relaxation enhancement (Lauffer, 1987; Lenora et al., 2017). Another solution-phase technique to monitor complex formation is a Job plot where both ligand and metal ratios are varied, and a unique property of the complex, such as a complex-specific emission, is monitored (Renny et al., 2013; Kuda-Wedagedara et al., 2015). The choice of spectral feature to monitor in a Job plot is complex-dependent. Typically, Eu^{II}-based emission is largely quenched in aqueous media due to the abundance of OH oscillators (Jiang et al., 1998); therefore, luminescence spectroscopy is not suitable to characterize the formation of every Eu^{II}-containing complex. Other features to monitor as a function of metal-to-ligand ratio include complex-specific absorbance peaks, relaxivity, or cyclic voltammetry peaks.

TABLE 1 | Midpoint potentials of Eu^{II/III}-containing complexes more negative than aqua ions.

Ligand	$E_{1/2}$ (V) ^[a]	$E_{1/2}$ (V)	Reference electrode	pH	References
5	-1.417	-1.373	saturated calomel	4	Botta et al., 2003
4	-1.386	-1.342	saturated calomel	4	Botta et al., 2003
23	-1.375	-1.331	saturated calomel	4	Botta et al., 2003
4	-1.356	-1.356	Ag/AgCl	6.5	Gál et al., 2013
2	-1.356	-1.312	saturated calomel	4	Botta et al., 2003
4	-1.35	-1.35	Ag/AgCl	nr ^[b]	Burai et al., 2000
38	-1.331	-1.331	Ag/AgCl	6.5	Gál et al., 2013
37	-1.291	-1.291	Ag/AgCl	6.5	Gál et al., 2013
31	-1.241	-1.241	Ag/AgCl	6.5	Gál et al., 2013
39	-1.18	-1.18	Ag/AgCl	7	Vanek et al., 2016
22	-1.164	-1.120	saturated calomel	4	Botta et al., 2003
3	-1.153	-1.109	saturated calomel	4	Botta et al., 2003
31	-1.135	-1.135	Ag/AgCl	nr ^[b]	Burai et al., 2003
1	-1.125	-1.081	Saturated calomel	4	Botta et al., 2003
32	-1.1105	-1.1105	Ag/AgCl	7	Burnett et al., 2017
33	-1.0680	-1.0680	Ag/AgCl	7	Burnett et al., 2017
36	-1.052	-1.052	Ag/AgCl	6.5	Gál et al., 2013
25	-0.996	-0.996	Ag/AgCl	nr ^[b]	Burai et al., 2003
34	-0.9710	-0.9710	Ag/AgCl	7	Burnett et al., 2017
6	-0.92	-0.92	Ag/AgCl	nr ^[b]	Burai et al., 2000
34	-0.903	-0.903	Ag/AgCl	7	Ekanger et al., 2016a
34	-0.879	-0.879	Ag/AgCl	4	Ekanger et al., 2016a
7	-0.82	-0.82	Ag/AgCl	nr ^[b]	Burai et al., 2000
35	-0.817	-0.817	Ag/AgCl	6.5	Gál et al., 2013
28	-0.753	-0.753	Ag/AgCl	7	Regueiro-Figueroa et al., 2015
26	-0.727	-0.727	Ag/AgCl	na ^[c]	Basal et al., 2017a
27	-0.720	-0.720	Ag/AgCl	na ^[c]	Basal et al., 2017a

^[a]converted to V vs. Ag/AgCl by subtracting 0.044 V from the saturated calomel values (Bard and Faulkner, 2000); ^[b]nr, not reported; ^[c]na, not applicable, solvent is dimethylformamide.

In the case where single crystals of a Eu^{II}-containing complex are obtained, X-ray diffraction combined with elemental analysis provides information regarding identity and purity. X-ray diffraction provides information about the oxidation state and coordination environment of the Eu^{II} ion in the solid state, including bond distances and number and identity of counter ions (Zucchi et al., 2010; Ekanger et al., 2015; Kuda-Wedagedara et al., 2015; Jin et al., 2016; Basal et al., 2017a; Lenora et al., 2017). Elemental analysis provides information about elemental composition as an indication of purity. However, it is important to note that for molecular-imaging applications, solution-phase characterization is often more important than solid-phase analysis of solids because solid-state properties do not necessarily

TABLE 2 | Midpoint potentials of Eu^{II/III}-containing aqua complexes and complexes more positive than aqua ions.

Ligand	$E_{1/2}$ (V) ^[a]	$E_{1/2}$ (V)	Reference electrode	pH	References
aqua	-0.67	-0.67	Ag/AgCl	6.5	Gál et al., 2013
aqua	-0.668	-0.624	saturated calomel	4	Botta et al., 2003
aqua	-0.664	-0.620	saturated calomel	3	Yee et al., 1979
aqua	-0.648	-0.648	Ag/AgCl	na ^[d]	Basal et al., 2017a
aqua	-0.6365	-0.6365	Ag/AgCl	7	Burnett et al., 2017
aqua	-0.63	-0.63	Ag/AgCl	nr ^[e]	Burai et al., 2000
30	-0.61	-0.61	Ag/AgCl	7	Regueiro-Figueroa et al., 2015
aqua	-0.585	-0.585	Ag/AgCl	nr ^[e]	Burai et al., 2003
aqua	-0.554	-0.554	Ag/AgCl	2.08	Anderson and Macero, 1963
aqua	-0.549	-0.7645 ^[b]	Fc/Fc ⁺ ^[c]	7.5	Gamage et al., 2010
20	-0.479	-0.435	saturated calomel	2–7	Yee et al., 1980
29	-0.453	-0.453	Ag/AgCl	7	Regueiro-Figueroa et al., 2015
21	-0.41	-0.37	saturated calomel	nr ^[e]	Yee et al., 1980
8	-0.259	-0.215	saturated calomel	nr ^[e]	Yee et al., 1980
8	-0.141	-0.3669 ^[b]	Fc/Fc ⁺ ^[c]	7.5	Gamage et al., 2010
[P ₅ W ₃₀ O ₁₁₀] ¹⁵⁻	0.11	0.11	Ag/AgCl	0	Antonio and Soderholm, 1996
14	-0.100	-0.2996 ^[b]	Fc/Fc ⁺ ^[c]	7.5	Gamage et al., 2010
11	-0.068	-0.2769 ^[b]	Fc/Fc ⁺ ^[c]	7.5	Gamage et al., 2010
10	0.016	-0.2324 ^[b]	Fc/Fc ⁺ ^[c]	7.5	Gamage et al., 2010
13	0.083	-0.2123 ^[b]	Fc/Fc ⁺ ^[c]	7.5	Gamage et al., 2010
16	0.13	0.13	Ag/AgCl	9.7	Kuda-Wedagedara et al., 2015

^[a]converted to V vs. Ag/AgCl by subtracting 0.044 V from the saturated calomel values (Bard and Faulkner, 2000) or by adding $|E_{pa(Ag/AgCl)} - E_{pa(ferrocene/ferrocenium)}|$ to the reported $E_{1/2}$ values vs. ferrocene/ferrocenium (Gamage et al., 2010); ^[b]average of the anodic and cathodic peak potentials; ^[c]Fc/Fc⁺, ferrocene/ferrocenium; ^[d]na, not applicable, solvent is dimethylformamide; ^[e]nr, not reported.

reflect solution-phase behavior or coordination environment. For example, Eu^{II}-containing complexes Eu10, Eu11, and Eu16, crystallize with one chloride counteranion bound to Eu^{II}. In the case of Eu16, solution-phase characterization suggests that the counteranion remains coordinated to Eu^{II} in solution (Kuda-Wedagedara et al., 2015); however, for Eu10 and Eu11, molar-conductivity data suggests that counteranions dissociate in solution (Ekanger et al., 2015; Lenora et al., 2017).

HANDLING Eu^{II}-CONTAINING SAMPLES TO PREVENT OXIDATION

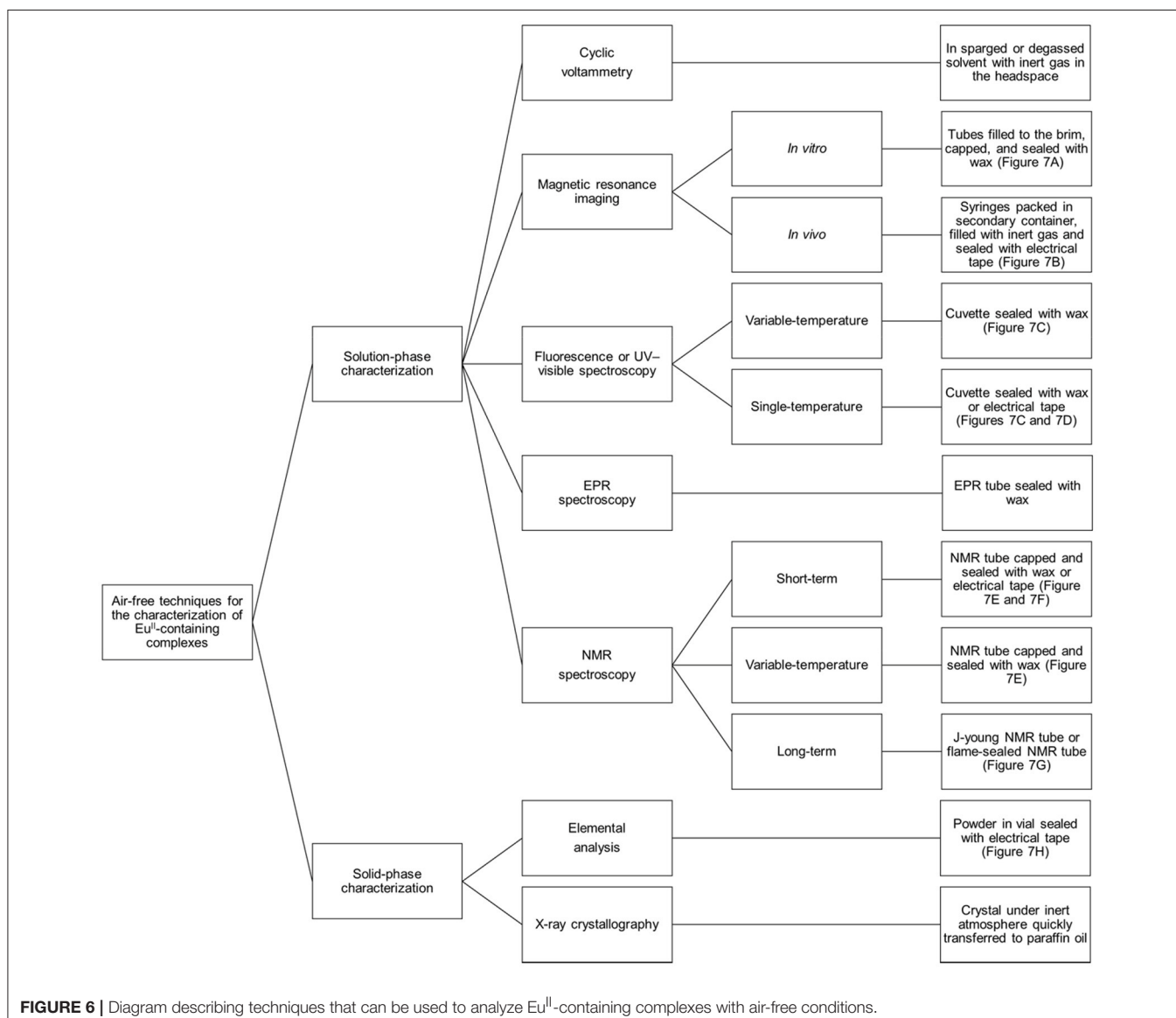
Preventing Eu^{II}-containing complexes from oxidizing over the course of analyses is critical for the collection of accurate data: Eu^{III} and Eu^{II} have different properties, and misinterpretation

of experimental results can occur if care is not taken to prevent unintentional oxidation of Eu^{II}. Rigorous techniques must be used in the synthesis and handling of Eu^{II}-containing complexes. This section describes apparatuses and techniques that were successfully used to study Eu^{II}-containing complexes (**Figures 6, 7**).

Cyclic voltammetry or bulk electrolysis performed either inside or outside of a glovebox should use solvents that have been degassed (under reduced pressure, for example, on a Schlenck line) or well-sparged (≥ 5 min of vigorous bubbling with an inert gas for volumes of ~ 3 mL in a capped vessel that contains a vent needle). To ensure that there is no detectable dissolved oxygen in solution, cyclic voltammetry of degassed solvents should not show peaks for O₂ (Green, 2018). If outside of a glovebox, the inert-gas source should be retracted to the head-space of the vessel once sparging is complete prior to cyclic voltammetry or bulk electrolysis. Inside the glovebox, there is no need for

an inert gas line in the headspace because the atmosphere is O₂-free. If outside of a glovebox, transfer of solutions of Eu^{II} from bulk electrolysis for crystal growth or other analyses must be performed using air-free techniques (Shriver and Drezdzon, 1986).

For other routes to synthesize and handle Eu^{II}-containing complexes in aqueous media, air-free handling is achieved using Shlenck techniques, a wet (water allowed but no molecular oxygen) glovebox, or a combination of both. During the synthesis of Eu^{II}-containing complexes in a glovebox, the glovebox atmosphere must not be contaminated with oxygen. Either a commercial oxygen sensor or chemical indicator can be used to monitor the atmosphere. One suitable chemical indicator for this purpose is dicyclopentadienyltitanium(IV) dichloride (Ti^{IV}Cp₂Cl₂) (Burgmayer, 1998). When the titanium metallocene is dissolved in acetonitrile in the presence of zinc metal, a deep blue solution is obtained. An aliquot of this solution



is filtered through celite or a hydrophilic filter and diluted with acetonitrile to yield a diffuse, blue solution caused by the presence of $\text{Ti}^{\text{III}}\text{Cp}_2(\text{NCCH}_3)_2$. If the solution remains blue upon evaporation, $\text{Ti}^{\text{III}}\text{Cp}_2(\text{NCCH}_3)_2$ is unoxidized, indicating that the atmosphere is good (<5 ppm O₂) (Shriver and Drezdzon, 1986). A color change to green is caused by formation of a dimeric species or some oxidation of Ti^{III} to Ti^{IV}. A color change to yellow is indicative of near-complete oxidation to $\text{Ti}^{\text{IV}}\text{Cp}_2(\text{NCCH}_3)_2$. Either green or yellow suggests a bad atmosphere with respect to O₂, and steps to address the quality of the atmosphere should be taken prior to working with Eu^{II}. If the indicator persists as green or yellow after refreshing the glovebox atmosphere by purging the glovebox with inert gas, then the oxygen-removing catalyst should be replaced or regenerated. Ideally, the atmosphere of a wet glovebox should be checked at least daily, and the atmosphere should be purged with inert gas before and after each use. All liquids to be used in a wet glovebox should be rigorously degassed before transport into the glovebox. Solids to be brought into a glovebox can be placed in an open vial and brought into the antechamber if the solids do not sublime at the temperature and pressure of the glovebox antechamber. To prevent loss of solid from bumping or the vial accidentally

tipping, the top of the vial can be covered with tissue that is secured with a rubber band (**Figure 7I**). If solids sublime at the temperature and pressure of the antechamber, then the solids should be placed under an inert atmosphere in a sealed container prior to being brought into the glovebox.

Solution-phase characterization of Eu^{II}-containing samples, including NMR spectroscopy, MRI, and fluorescence or UV-visible absorbance spectroscopy, requires that samples be sealed to prevent oxygen contamination that would interfere with the integrity of the results. For NMR spectroscopy, J-young NMR tubes with Teflon seals or flame-sealed NMR tubes are appropriate for long term studies (**Figure 7G**). Alternatively, NMR tubes capped with a plastic cap and sealed with paraffin wax or electrical tape suffice for studies that last a few hours (**Figures 7E,F and Video S1**). For samples that must be shipped, samples can be loaded into NMR tubes that are subsequently flame-sealed (Lenora et al., 2017). For MRI, tubes (for example, glass vials that have a 400 μL capacity) can be filled to the brim with solution (to avoid bubbles), capped, dipped in wax, and loaded into an apparatus that is then covered in paraffin wax (**Figure 7A**) (Garcia and Allen, 2012b; Garcia et al., 2012; Basal et al., 2017a,b). For *in-vivo* injections, syringes with rubber-tip

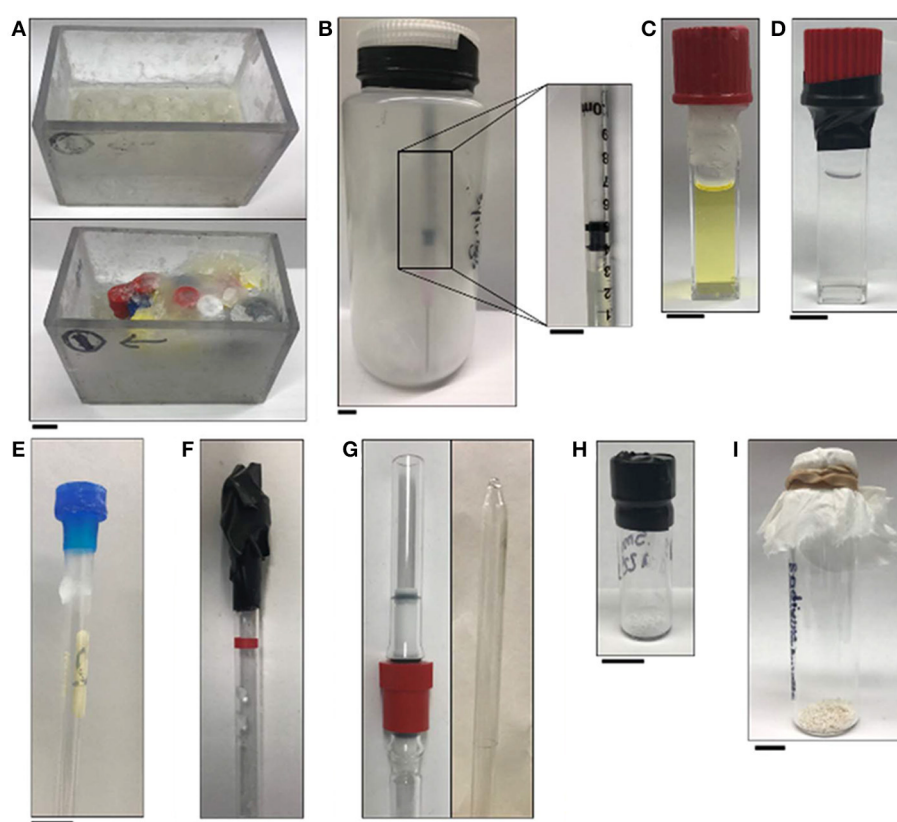


FIGURE 7 | Pictures of apparatuses included in the handling section of this manuscript: **(A)** empty tube holder (top) and tube holder with tubes that are covered in wax (bottom); **(B)** jar sealed with electrical tape that contains glass wool and syringes of Eu^{II}-containing complexes packed under an inert atmosphere and (inset) a plastic 1 mL syringe with a rubber tip on the plunger that contains a solution of a Eu^{II}-containing complex; **(C)** wax-sealed cuvette; **(D)** electrical-tape-sealed cuvette; **(E)** wax-sealed NMR tube; **(F)** electrical-tape-sealed NMR tube; **(G)** J-young NMR tube (left) and flame-sealed NMR tube (right); **(H)** electrical-tape-sealed vial containing a solid sample; and **(I)** glass vial that contains solid sample covered with a tissue that is secured with a rubber band. All scale bars represent 1 cm.

plungers can be loaded with sample, packaged in a bottle that is under an atmosphere of N₂ or Ar, and sealed with electrical tape (**Figure 7B**; Basal et al., 2017a). Packed this way, the integrity of samples is sufficient for shipping with glass wool included in the bottle to minimize vibrations during shipping. For samples in cuvettes (for example, samples for emission or absorbance spectroscopy that must be removed from the glovebox), quartz cuvettes with Teflon caps can be sealed with paraffin wax (**Figure 7C**) or electrical tape (**Figure 7D**) (Kuda-Wedagedara et al., 2015; Ekanger et al., 2016a; Jin et al., 2016; Basal et al., 2017a). For samples that will undergo temperature changes (heating or cooling), we have observed that paraffin wax is more reliable than electrical tape.

To ensure that a technique or apparatus successfully seals Eu^{II} from air over the course of an experiment, the relaxivity, UV-visible absorption, or luminescence spectra of the Eu^{II}-containing complex can be measured immediately after sample preparation and after the analyses are complete, if the analyses are nondestructive. Another way to assess the air-free environment and handling of a Eu^{II}-containing sample is to measure a spectral feature of the Eu^{II}-containing complex as a function of time at different concentrations of europium. Time-dependent measurements can reveal the presence of oxidizing impurities (Burai et al., 2002). For example, the oxidation half-life ($t_{1/2}$), which is the time at which half of the complex has oxidized, was measured for Eu6 by monitoring the intensity of a complex-specific UV-visible absorbance peak as a function of time (Burai et al., 2002). For a 5 mM solution of Eu6, the $t_{1/2}$ was found to be 10 days. However, $t_{1/2}$ increased as a function of concentration of europium (>1 month for Eu6 at 100 mM), suggesting that the $t_{1/2}$ reported at 5 mM was influenced by the presence of oxidizing impurities such as O₂. Oxygen can be avoided using the techniques described in this section.

If a Eu^{II}-containing sample cannot be monitored to check the effectiveness of an air-free technique, then another way to assess if an apparatus is sealed from air is to monitor the color change of a solution of Ti^{III}Cp₂Cl₂ sealed in parallel to the sample to

be measured (Burgmayer, 1998). The use of Ti^{III}Cp₂Cl₂ as an indicator provides information regarding the technique used to seal the solution from air. However, a limitation of this method is that it does not provide direct information about the Eu^{II}-containing complex being analyzed.

CONCLUSIONS AND OUTLOOK

The unique and tuneable properties of Eu^{II} make Eu^{II}-containing complexes promising molecular imaging agents. The synthesis, characterization, and handling of Eu^{II} require care with respect to the use of air-free techniques and characterization of oxidation states because Eu^{II} and Eu^{III} have different molecular imaging properties that confound results if the ions are inadvertently comingled within a sample. We expect that the techniques described in this review will guide the future synthesis, characterization, and handling of Eu^{II}-containing complexes for molecular imaging.

AUTHOR CONTRIBUTIONS

LB and MA: Contributed to the manuscript and approved the final version.

ACKNOWLEDGMENTS

MA gratefully acknowledges support from the National Institutes of Health (R01EB013663), and LB was supported by a Rumble fellowship from Wayne State University.

SUPPLEMENTARY MATERIAL

The Supplementary Material for this article can be found online at: <https://www.frontiersin.org/articles/10.3389/fchem.2018.00065/full#supplementary-material>

Video S1 | Video demonstration of the sealing of an NMR sample with paraffin wax.

REFERENCES

- Abragam, A., and Bleaney, B. (1970). *Electron Paramagnetic Resonance of Transition Ions*. Belfast: Oxford University Press.
- Allen, M. J. (2016). Aqueous lanthanide chemistry in asymmetric catalysis and magnetic resonance imaging. *Synlett* 27, 1310–1317. doi: 10.1055/s-0035-1561363
- Anderson, L. B., and Macero, D. J. (1963). The formal reduction potential of the europium(III)-europium(II) system. *J. Phys. Chem.* 67, 1942–1942. doi: 10.1021/j100803a520
- Angelovski, G. (2016). What we can really do with bioresponsive MRI contrast agents. *Angew. Chem. Int. Ed.* 55, 7038–7046. doi: 10.1002/anie.201510956
- Antonio, M. R., and Soderholm, L. (1996). Redox behavior of europium in the Preyssler heteropolyanion [EuP₅W₃₀O₁₁₀]¹²⁻. *J. Clust. Sci.* 7, 585–591. doi: 10.1007/BF01165803
- Bard, A. J., and Faulkner, L. R. (2000). *Electrochemical Methods: Fundamentals and Applications*, 2nd Edn. New York, NY: John Wiley & Sons, Inc.
- Barnham, K. J., Masters, C. L., and Bush, A. I. (2004). Neurodegenerative diseases and oxidative stress. *Nat. Rev. Drug Discov.* 3, 205–214. doi: 10.1038/nr01330
- Basal, L. A., Bailey, M. D., Romero, J., Ali, M. M., Kurenbekova, L., Yustein, J., et al. (2017a). Fluorinated Eu^{II}-based multimodal contrast agent for temperature- and redox-responsive magnetic resonance imaging. *Chem. Sci.* 8, 8356–8350. doi: 10.1039/C7SC03142D
- Basal, L. A., Yan, Y., Shen, Y., Haacke, E. M., Mehrmohammadi, M., and Allen, M. J. (2017b). Oxidation-responsive, Eu^{II/III}-based, multimodal contrast agent for magnetic resonance and photoacoustic imaging. *ACS Omega* 2, 800–805. doi: 10.1021/acsomega.6b00514
- Bochkarev, M. N. (2004). Molecular compounds of “new” divalent lanthanides. *Coord. Chem. Rev.* 248, 835–851. doi: 10.1016/j.ccr.2004.04.004
- Botta, M., Ravera, M., Barge, A., Bottaro, M., and Osella, D. (2003). Relationship between ligand structure and electrochemical and relaxometric properties of acyclic poly(aminocarboxylate) complexes of Eu(II). *Dalton Trans.* 1628–1633. doi: 10.1039/b211533f
- Bottrill, M., Kwok, L., and Long, N. J. (2006). Lanthanides in magnetic resonance imaging. *Chem. Soc. Rev.* 35, 557–571. doi: 10.1039/b516376p
- Burai, L., Scopelliti, R., and Tóth, É. (2002). Eu^{II}-cryptate with optimal water exchange and electronic relaxation: a synthon for potential pO₂ responsive macromolecular MRI contrast agents. *Chem. Commun.* 2366–2367. doi: 10.1039/B206709A

- Burai, L., Tóth, É., Moreau, G., Sour, A., Scopelliti, R., and Merbach, A. E. (2003). Novel macrocyclic Eu^{II} complexes: fast water exchange related to an extreme M—O_{water} distance. *Chem. Eur. J.* 9, 1394–1404. doi: 10.1002/chem.200390159
- Burai, L., Tóth, E., Seibig, S., Scopelliti, R., and Merbach, A. E. (2000). Solution and solid-state characterization of Eu^{II} chelates: a possible route towards redox responsive MRI contrast agents. *Chemistry* 6, 3761–3770. doi: 10.1002/1521-3765(20001016)6:20<3761::AID-CHEM3761>3.0.CO;2-6
- Burgmayer, S. J. N. (1998). Use of a titanium metallocene as a colorimetric indicator for learning inert atmosphere techniques. *J. Chem. Ed.* 75, 460–460. doi: 10.1021/ed075p460
- Burnett, M. E., Adebesin, B., Funk, A. M., Kovacs, Z., Sherry, A. D., Ekanger, L. A., et al. (2017). Electrochemical investigation of Eu^{3+/2+} redox couple in complexes with variable numbers of glycaminide and acetate pendant arms. *Eur. J. Inorg. Chem.* 2017, 5001–5005. doi: 10.1002/ejic.201701070
- Caravan, P., Tóth, É., Rockenbauer, A., and Merbach, A. E. (1999). Nuclear and electronic relaxation Eu²⁺_(aq): an extremely labile aqua ion. *J. Am. Chem. Soc.* 121, 10403–10409. doi: 10.1021/ja992264v
- Christoffers, J., and Starynowicz, P. (2008). A europium(II) complex with bis-pyridino-18-crown-6. *Polydron* 27, 2688–2692. doi: 10.1016/j.poly.2008.05.028
- Corbin, B. A., Hovey, J. L., Thapa, B., Schlegel, H. B., and Allen, M. J. (2018). Luminescence differences between two complexes of divalent europium. *J. Organomet. Chem.* 857, 88–93. doi: 10.1016/j.jorgchem.2017.09.007
- Cotton, S. (2006). *Lanthanide and Actinide Chemistry*. Chichester: John Wiley & Sons Ltd.
- Cullity, B. D., and Graham, C. D. (2009). *Introduction to Magnetic Materials*, 2nd Edn. Hoboken, NJ: John Wiley & Sons, Inc.
- Dorenbos, P. (2003). f → d transition energies of divalent lanthanides in inorganic compounds. *J. Phys. Condens. Matter* 15, 575–594. doi: 10.1088/0953-8984/15/3/322
- Edelmann, F. T. (2016). Lanthanides and actinides: annual survey of their organometallic chemistry covering the year 2015. *Coord. Chem. Rev.* 318, 29–130. doi: 10.1016/j.ccr.2016.04.001
- Ekanger, L. A., Ali, M. M., and Allen, M. J. (2014). Oxidation-responsive Eu^{2+/3+}-liposomal contrast agent for dual-mode magnetic resonance imaging. *Chem. Commun.* 50, 14835–14838. doi: 10.1039/C4CC07027E
- Ekanger, L. A., and Allen, M. J. (2015). Overcoming the concentration-dependence of responsive probes for magnetic resonance imaging. *Metalomics* 7, 405–421. doi: 10.1039/C4MT00289J
- Ekanger, L. A., Basal, L. A., and Allen, M. J. (2017). The role of coordination environment and pH in tuning the oxidation rate of europium(II). *Chem. Eur. J.* 23, 1145–1150. doi: 10.1002/chem.201604842
- Ekanger, L. A., Mills, D. R., Ali, M. M., Polin, L. A., Shen, Y., Haacke, E. M., et al. (2016a). Spectroscopic characterization of the 3+ and 2+ oxidation states of europium in a macrocyclic tetraglycinate complex. *Inorg. Chem.* 55, 9981–9988. doi: 10.1021/acs.inorgchem.6b00629
- Ekanger, L. A., Polin, L. A., Shen, Y., Haacke, E. M., and Allen, M. J. (2016b). Evaluation of Eu^{II}-based positive contrast enhancement after intravenous, intraperitoneal, and subcutaneous injections. *Contrast Media Mol. Imaging* 11, 299–303. doi: 10.1002/cmmi.1692
- Ekanger, L. A., Polin, L. A., Shen, Y., Haacke, E. M., Martin, P. D., and Allen, M. J. (2015). A Eu^{II}-containing cryptate as a redox sensor in magnetic resonance imaging of living tissue. *Angew. Chem. Int. Ed.* 54, 14398–14401. doi: 10.1002/anie.201507227
- Evans, W. J. (2000). Perspectives in reductive lanthanide chemistry. *Coord. Chem. Rev.* 206–207, 263–283. doi: 10.1016/S0010-8545(00)00267-8
- Facciabene, A., Peng, X., Hagemann, I. S., Balint, K., Barchetti, A., Wang, L.-P., et al. (2011). Tumour hypoxia promotes tolerance and angiogenesis via CCL28 and T_{reg} cells. *Nature* 475, 226–230. doi: 10.1038/nature10169
- Fieser, M. E., MacDonald, M. R., Krull, B. T., Bates, J. E., Ziller, J. W., Furche, F., et al. (2015). Structural, spectroscopic, and theoretical comparison of traditional vs recently discovered Ln²⁺ ions in the [K(2,2,2-cryptand)][(C₅H₄SiMe₃)₃Ln] complexes: the variable nature of Dy²⁺ and Nd²⁺. *J. Am. Chem. Soc.* 137, 369–382. doi: 10.1021/ja510831n
- Funk, A. M., Clavijo Jordan, V., Sherry, A. D., Ratnakar, S. J., and Kovacs, Z. (2016). Oxidative conversion of a europium(II)-based T₁ agent into a europium(III)-based paraCEST agent that can be detected *in vivo* by magnetic resonance imaging. *Angew. Chem. Int. Ed.* 55, 5024–5027. doi: 10.1002/anie.201511649
- Gál, M., Kielar, F., Sokolová, R., Ramešová, Š., and Kolivoška, V. (2013). Electrochemical study of Eu^{III}/Eu^{II} redox properties of complexes with potential MRI ligands. *Eur. J. Inorg. Chem.* 2013, 3217–3223. doi: 10.1002/ejic.201300252
- Gamage, N. D., Mei, Y., Garcia, J., and Allen, M. J. (2010). Oxidatively stable, aqueous europium(II) complexes through steric and electronic manipulation of cryptand coordination chemistry. *Angew. Chem. Int. Ed.* 49, 8923–8925. doi: 10.1002/anie.201002789
- Gansow, O. A., Kausar, A. R., Triplett, K. M., Weaver, M. J., and Yee, E. L. (1977). Synthesis and chemical properties of lanthanide cryptates. *J. Am. Chem. Soc.* 99, 7087–7089. doi: 10.1021/ja00463a065
- Garcia, J., and Allen, M. J. (2012a). Developments in the coordination chemistry of europium(II). *Eur. J. Inorg. Chem.* 2012, 4550–4563. doi: 10.1002/ejic.201200159
- Garcia, J., and Allen, M. J. (2012b). Interaction of biphenyl-functionalized Eu²⁺-containing cryptate with albumin: implications to contrast agents in magnetic resonance imaging. *Inorg. Chim. Acta* 393, 324–327. doi: 10.1016/j.ica.2012.07.006
- Garcia, J., Kuda-Wedagedara, A. N. W., and Allen, M. J. (2012). Physical properties of Eu²⁺-containing cryptates as contrast agents for ultrahigh-field magnetic resonance imaging. *Eur. J. Inorg. Chem.* 2012, 2135–2140. doi: 10.1002/ejic.201101166
- Garcia, J., Neelavalli, J., Haacke, E. M., and Allen, M. J. (2011). Eu^{II}-containing cryptates as contrast agents for ultra-high field strength magnetic resonance imaging. *Chem. Commun.* 47, 12858–12860. doi: 10.1039/c1cc15219j
- Green, K. (2018). *Cyclic Voltammetry (CV)*. Cambridge, MA: JoVE Science Education Database. Analytical Chemistry. JoVE.
- Harris, D. C. (2003). *Quantitative Chemical Analysis*, 6th Edn. New York, NY: W. H. Freeman and Company.
- Jenks, T. C., Bailey, M. D., Hovey, J. L., Fernando, S., Basnayake, G., Cross, M. E., et al. (2018). First use of a divalent lanthanide for visible-light-promoted photoredox catalysis. *Chem. Sci.* 9, 1273–1278. doi: 10.1039/C7SC02479G
- Jiang, J., Higashiyama, N., Machiida, K., and Adachi, G., (1998). The luminescent properties of divalent europium complexes of crown ethers and cryptands. *Coord. Chem. Rev.* 170, 1–29. doi: 10.1016/S0010-8545(98)00070-8
- Jin, G. X., Bailey, M. D., and Allen, M. J. (2016). Unique Eu(II) coordination environments with a janus cryptand. *Inorg. Chem.* 55, 9085–9090. doi: 10.1021/acs.inorgchem.6b01659
- Kawasaki, K., Sugiyama, R., Tsuji, T., Iwasa, T., Tsunoyama, H., Mizuhata, Y., et al. (2017). A designer ligand field for blue-green luminescence of organoeuropium(II) sandwich complexes with cyclononetetraenyl ligands. *Chem. Commun.* 53, 6557–6560. doi: 10.1039/C7CC03045B
- Kelly, R. P., Bell, T. D. M., Cox, R. P., Daniels, D. P., Deacon, G. B., Jaroscik, F., et al. (2015). Divalent tetra- and penta-phenylcyclopentadienyl europium and samarium sandwich and half-sandwich complexes: synthesis, characterization, and remarkable luminescence properties. *Organometallics* 34, 5624–5636. doi: 10.1021/acs.organomet.5b00842
- Kuda-Wedagedara, A. N., and Allen, M. J. (2014). Enhancing magnetic resonance imaging with contrast agents for ultra-high field strengths. *Analyst* 139, 4401–4410. doi: 10.1039/C4AN00990H
- Kuda-Wedagedara, A. N., Wang, C., Martin, P. D., and Allen, M. J. (2015). Aqueous Eu(II)-containing complex with bright yellow luminescence. *J. Am. Chem. Soc.* 137, 4960–4963. doi: 10.1021/jacs.5b02506
- Lauffer, R. B. (1987). Paramagnetic metal complexes as water proton relaxation agents for NMR imaging: theory and design. *Chem. Rev.* 87, 901–927. doi: 10.1021/cr00081a003
- Layfield, R. A., and Murugesu, M., (eds.). (2015). *Lanthanides and Actinides in Molecular Magnetism*. Weinheim: Wiley-VCH Verlag GmbH & Co.
- le Masne de Chermont Q., Chanéac, C., Seguin, J., Pellé, F., Maitrejean, S., Jolivet, J. P., et al. (2007). Nanoprobes with near-infrared persistent luminescence for *in vivo* imaging. *Proc. Natl. Acad. Sci. U.S.A.* 104, 9266–9271. doi: 10.1073/pnas.0702427104
- Lenora, C. U., Carniato, F., Shen, Y., Latif, Z., Haacke, E. M., Martin, P. D., et al. (2017). Structural features of Eu^{II}-containing cryptates that influence relaxivity. *Chem. Eur. J.* 23, 15404–15414. doi: 10.1002/chem.201702158
- Lin, M. T., and Beal, M. F. (2006). Mitochondrial dysfunction and oxidative stress in neurodegenerative diseases. *Nature* 443, 787–795. doi: 10.1038/nature05292

- MacDonald, M. R., Bates, J. E., Ziller, J. W., Furche, F., and Evans, W. J. (2013). Completing the series of +2 ions for the lanthanide elements: synthesis of molecular complexes of Pr²⁺, Gd²⁺, Tb²⁺, and Lu²⁺. *J. Am. Chem. Soc.* 135, 9857–9868. doi: 10.1021/ja403753j
- Mattson, M. P. (2004). Pathways towards and away from Alzheimer's disease. *Nature* 430, 631–639. doi: 10.1038/nature02621
- McCoy, H. N. (1935). The separation of europium from other rare earths. *J. Am. Chem. Soc.* 57:1756. doi: 10.1021/ja01312a506
- Pan, C. L., Pan, Y. S., Wang, J., and Song, J. F. (2011). A heterometallic sandwich complex of europium(II) for luminescent studies. *Dalton Trans.* 40, 6361–6363. doi: 10.1039/c1dt0635j
- Park, L., Zhou, P., Pitstick, R., Capone, C., Anrather, J., Norris, E. H., et al. (2008). Nox2-Derived radicals contribute to neurovascular and behavioral dysfunction in mice overexpressing the amyloid precursor protein. *Proc. Natl. Acad. Sci. U.S.A.* 105, 1347–1352. doi: 10.1073/pnas.0711568105
- Pierre, V. C., and Allen, M. J. (eds.). (2018). *Contrast Agents for MRI: Experimental Methods*. Cambridge: Royal Society of Chemistry.
- Pierre, V. C., Allen, M. J., and Caravan, P. (2014). Contrast agents for MRI: 30+ years and where are we going? *J. Biol. Inorg. Chem.* 19, 127–131. doi: 10.1007/s00775-013-1074-5
- Regueiro-Figueroa, M., Barriada, J. L., Pallier, A., Esteban-Gómez, D., Blas, A., Rodríguez-Blas, T., et al. (2015). Stabilizing divalent europium in aqueous solution using size-discrimination and electrostatic effects. *Inorg. Chem.* 54, 4940–4952. doi: 10.1021/acs.inorgchem.5b00548
- Renny, J. S., Tomasevich, L. L., Tallmadge, E. H., and Collum, D. B. (2013). Method of continuous variations: applications of job plots to the study of molecular associations in organometallic chemistry. *Angew. Chem. Int. Ed.* 52, 11998–12013. doi: 10.1002/anie.201304157
- Sabbatini, N., Ciano, M., Dellonte, S., Bonazzi, A., and Balzani, V. (1982). Absorption and emission properties of a europium(II) cryptate in aqueous solution. *Chem. Phys. Lett.* 90, 265–268. doi: 10.1016/0009-2614(82)83236-3
- Sabbatini, N., Ciano, M., Dellonte, S., Bonazzi, A., Bolletta, F., and Balzani, V. (1984). Photophysical properties of europium(II) cryptates. *J. Phys. Chem.* 88, 1534–1537. doi: 10.1021/j150652a018
- Shipley, C. P., Capecchi, S., Salata, O. V., Etchells, M., Dobson, P. J., and Christou, V. (1999). Orange electroluminescence from a divalent europium complex. *Adv. Mater.* 11, 533–536. doi: 10.1002/(SICI)1521-4095(199905)11:7;3.0.CO;2-U
- Shriver, D. F., and Drezdzon, M. A. (1986). *The Manipulation of Air-Sensitive Compounds*. New York, NY: John Wiley & Sons, Inc.
- Shweiki, D., Itin, A., Soffer, D., and Keshet, E. (1992). Vascular endothelial growth factor induced by hypoxia may mediate hypoxia-initiated angiogenesis. *Nature* 359, 843–845. doi: 10.1038/359843a0
- Soderholm, L., Antonio, M. R., Skanthakumar, S., and Williams, C. W. (2002). Correlated electrons in the Eu-exchanged Preissler anion [EuP₅W₃₀O₁₁₀]ⁿ⁻. *J. Am. Chem. Soc.* 124, 7290–7291. doi: 10.1021/ja025821d
- Teprovich, J. A. Jr., Antharjanam, P. K. S., Prasad, E., Pesciotta, E. N., and Flowers, R. A. II. (2008). Generation of Sm^{II} reductants using high intensity ultrasound. *Eur. J. Inorg. Chem.* 2018, 5015–5019. doi: 10.1002/ejic.200800876
- Tóth, É., Burai, L., and Merbach, A. E. (2001). Similarities and differences between the isoelectronic Gd^{III} and Eu^{II} complexes with regard to MRI contrast agent applications. *Coord. Chem. Rev.* 216–217, 363–382. doi: 10.1016/S0010-8545(01)00312-5
- Vanek, J., Smrká, F., Lubal, P., Trísková, I., and Trnková, L. (2016). Dual carbonate sensor based on Eu(III) complex of DO3A ligand. *Monatsh. Chem.* 147, 925–934. doi: 10.1007/s00706-016-1722-x
- Wang, J., Ma, Q., Wang, Y., Shen, H., and Yuan, Q. (2017). Recent progress in biomedical applications of persistent luminescence nanoparticles. *Nanoscale* 9, 6204–6218. doi: 10.1039/C7NR01488K
- Yee, E. L., Cave, R. J., Guyer, K. L., Tyma, P. D., and Weaver, M. J. (1979). A survey of ligand effects upon the reaction entropies of some transition metal redox couples. *J. Am. Chem. Soc.* 101, 1131–1137. doi: 10.1021/ja00499a013
- Yee, E. L., Gansow, O. A., and Weaver, M. J. (1980). Electrochemical studies of europium and ytterbium cryptate formation in aqueous solution. Effects of varying the metal oxidation state upon cryptate thermodynamics and kinetics. *J. Am. Chem. Soc.* 102, 2278–2285. doi: 10.1021/ja00527a024
- Yee, E. L., Hupp, J. T., and Weaver, M. J. (1983). The nonadiabicity question for Europium(III/II): outer-sphere reactivities of Europium (III/II) cryptates. *Inorg. Chem.* 22, 3465–3470. doi: 10.1021/ic00165a020
- Zucchi, G., Thuéry, P., Rivière, E., and Ephritikhine, M. (2010). Europium(II) compounds: simple synthesis of a molecular complex in water and coordination polymers with 2,2'-bipyrimidine-mediated ferromagnetic interactions. *Chem. Commun.* 46, 9143–9145. doi: 10.1039/c0cc02539a

Conflict of Interest Statement: The authors declare that the research was conducted in the absence of any commercial or financial relationships that could be construed as a potential conflict of interest.

Copyright © 2018 Basal and Allen. This is an open-access article distributed under the terms of the Creative Commons Attribution License (CC BY). The use, distribution or reproduction in other forums is permitted, provided the original author(s) and the copyright owner are credited and that the original publication in this journal is cited, in accordance with accepted academic practice. No use, distribution or reproduction is permitted which does not comply with these terms.



ParaCEST Agents Encapsulated in Reverse Nano-Assembled Capsules (RACs): How Slow Molecular Tumbling Can Quench CEST Contrast

Annah Farashishiko¹, Jacqueline R. Slack¹, Mauro Botta² and Mark Woods^{1,3*}

¹ Department of Chemistry, Portland State University, Portland, OR, United States, ² Dipartimento di Scienze e Innovazione Tecnologica, Università del Piemonte Orientale “Amedeo Avogadro”, Alessandria, Italy, ³ Advanced Imaging Research Center, Oregon Health and Science University, Portland, OR, United States

OPEN ACCESS

Edited by:

Carlos Lodeiro,
Faculdade de Ciências e Tecnologia
da Universidade Nova de Lisboa,
Portugal

Reviewed by:

Dario Livo Longo,
Università degli Studi di Torino, Italy
Zoltan Kovacs,
University of Texas Southwestern
Medical Center, United States

*Correspondence:

Mark Woods
mark.woods@pdx.edu;
woodsmar@ohsu.edu

Specialty section:

This article was submitted to
Inorganic Chemistry,
a section of the journal
Frontiers in Chemistry

Received: 22 January 2018

Accepted: 20 March 2018

Published: 06 April 2018

Citation:

Farashishiko A, Slack JR, Botta M and Woods M (2018) ParaCEST Agents Encapsulated in Reverse Nano-Assembled Capsules (RACs): How Slow Molecular Tumbling Can Quench CEST Contrast. *Front. Chem.* 6:96.
doi: 10.3389/fchem.2018.00096

Although paraCEST is a method with immense scope for generating image contrast in MRI, it suffers from the serious drawback of high detection limits. For a typical discrete paraCEST agent the detection limit is roughly an order of magnitude higher than that of a clinically used relaxation agent. One solution to this problem may be the incorporation of a large payload of paraCEST agents into a single macromolecular agent. Here we report a new synthetic method for accomplishing this goal: incorporating a large payload of the paraCEST agent DyDOTAM³⁺ into a Reverse Assembled nano-Capsule. An aggregate can be generated between this chelate and polyacrylic acid (PAA) after the addition of ethylene diamine. Subsequent addition of polyallylamine hydrochloride (PAH) followed by silica nanoparticles generated a robust encapsulating shell and afforded capsule with a mean hydrodynamic diameter of 650 ± 250 nm. Unfortunately this encapsulation did not have the effect of amplifying the CEST effect per agent, but quenched the CEST altogether. The quenching effect of encapsulation could be attributed to the effect of slowing molecular tumbling, which is inevitable when the chelate is incorporated into a nano-scale material. This increases the transverse relaxation rate of chelate protons and a theoretical examination using Solomon Bloembergen Morgan theory and the Bloch equations shows that the increase in the transverse relaxation rate constant for the amide protons, in even modestly sized nano-materials, is sufficient to significantly quench CEST.

Keywords: CEST quenching, assembled nano-capsules, NMR relaxation, molecular tumbling, contrast agents

INTRODUCTION

In the nearly two decades since it was first demonstrated (Ward et al., 2000), exogenous Chemical Exchange Saturation Transfer (CEST) has become a topic of intense research interest. As a method of generating contrast in MRI scans, the use of exogenous CEST agents has several advantages over the more conventional relaxation agents used in clinical radiology. CEST agents can be turned on and off post-administration (Zhang et al., 2003), they can be selectively imaged even in the presence of another CEST agent (Aime et al., 2005), they can also be used to ratiometrically sense the concentration of biologically relevant species such as pH, lactate concentration, temperature or

enzyme activity (Olatunde et al., 2015; Pavuluri and McMahon, 2017; Sinharay et al., 2017; Zhang et al., 2017a,b). But for all these advantages CEST still suffers from one very serious drawback: exogenous CEST agents have inherently high detection limits.

As its name suggests CEST occurs when a pre-saturation pulse is applied to protons that are asynchronous but exchange with the solvent water. If exchange is sufficiently slow, the saturation effect will be transferred to the solvent water, reducing its signal intensity. It is this change that is registered as increased contrast in an MRI scan. The original report on exogenous CEST examined diamagnetic agents (Ward et al., 2000). The resonance frequency of the exchanging protons on these diamagnetic agents cannot be more than a few thousand Hz at the very most from that of water and this introduces two limitations. Firstly, it limits the exchange regime; since exchange must be slow for CEST a small resonance frequency difference means that slower exchange kinetics are demanded. Intuitively it is clear that the faster the permitted exchange kinetics the more saturation will be transferred to the solvent water, increasing the amount of contrast. For this reason, larger resonance frequency differences are to be preferred. Secondly, when the resonance frequency of protons on the CEST agent is close to that of solvent water a significant amount of off-resonance direct saturation can occur. This undesirable effect interferes with the observation of CEST but can be minimized by increasing the shift separation between the two exchanging pools (Zhang et al., 2003; Woods et al., 2006). It was established shortly after the development of exogenous CEST that paramagnetic lanthanide complexes could afford CEST agents that have very large resonance frequency differences and exchange kinetics in the slow exchange regime (Zhang et al., 2001). Commonly tetraamide derivatives of DOTA, such as DOTAM (**Figure 1**) are used, exploiting the exchange of either the coordinated water molecule or the amide protons (Woods et al., 2006). Depending upon the particular lanthanide that is employed in the agent the shift of exchanging protons can range from a few to a few hundred ppm from water (Sherry et al., 2005). These paramagnetic CEST agents are commonly referred to as paraCEST agents.

In an effort to reduce the detection limits of exogenous CEST agents to practical levels a number of strategies have

been investigated that would increase the number of exchanging protons per agent. Typically, these strategies have involved one of two approaches: either encapsulating a large volume of water within a semi-permeable membrane (such as a liposome) and using a paramagnetic shift reagent to shift the resonance frequency of the encapsulated water (Ferrauto et al., 2016); or construct a system that will carry a large payload of lower molecular weight CEST agents. In the context of paraCEST this latter strategy has the potential advantage of maintaining the large resonance frequency difference between the two exchanging proton pools. This is in contrast to lipoCEST, which has the advantage that extremely large exchanging pools can be generated. But, despite the use of a paramagnetic shift reagent, the resonance frequency difference between the two exchanging pools is quite small, comparable only to that of a diamagnetic agent (Ferrauto et al., 2017).

Reports of systems designed to carry large payloads of a low molecular weight paraCEST agent are comparatively sparse. Oligomers of Eu³⁺ based paraCEST agents have been prepared and afford the opportunity to increase the number of exchanging protons by a factor of 15–20 (Wu et al., 2008, 2010). Higher payloads have been achieved by decorating the surface of PAMAM dendrimers with paraCEST agents (Ali et al., 2009, 2012). This strategy, like that of the oligomeric agents, has two major limitations: the maximum payload of a single agent is not that high (only a few hundred at most, depending up which generation of dendrimer is used) and the chelate requires significant synthetic modifications to be undertaken before it can be incorporated into the final imaging agent. In recognition of these limitations 55 nm amine functionalized silica nanoparticles (SNPs) have been used as payload delivery system (Evbuomwan et al., 2012). The amine functionalization could be used to couple directly to carboxylic acid substituents on a Eu³⁺ DOTA-tetraamide derivative. This method permitted the incorporation of a very large payload of paraCEST agents. The problem with this system was that upon incorporation into the nano-structure the CEST effect of the Eu³⁺ chelate was quenched.

We have previously demonstrated that a range of Gd³⁺ chelates with different overall negative charges can be encapsulated into different types of nano-scale capsules affording high payload delivery systems (Farashishiko et al., 2016). The benefit of this approach is that capsules are easily made from charged chelates and no expensive or laborious alterations to the chelate structure are necessary. In previous systems, a polyanionic Gd³⁺ chelate was added to a cationic polymer, such as polyallylamine hydrochloride (PAH), resulting in formation of a charge driven aggregate. A robust shell could then be added to the aggregate through either: addition of a SNPs to form Nano-Assembled Capsules (NACs) (Plush et al., 2009; Farashishiko et al., 2016); or through crosslinking with a dicarboxylic acid and peptide coupling reagent to form Cross-linked nano-Assembled Capsules (CACs) (Farashishiko et al., 2017). It was discovered that both of these approaches lead to significant improvements in the performance of the Gd³⁺ chelate as a *T*₁-shortening contrast agent as well as the encapsulation of a massive payload of chelate (Farashishiko et al.,

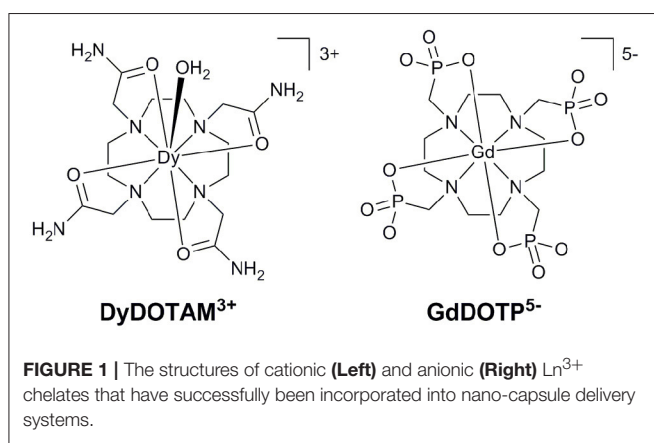


FIGURE 1 | The structures of cationic (**Left**) and anionic (**Right**) Ln³⁺ chelates that have successfully been incorporated into nano-capsule delivery systems.

2016, 2017). This observation indicates that the capsule shell in both of these systems is highly permeable to water—suggesting that either system may be amenable to modification for the delivery of high payloads of paraCEST agents.

EXPERIMENTAL

General Remarks

Polyacrylic acid (PAA) (100,000 MW ~1,389 acrylic acid units per molecule, 35 wt % in water) and PAH (56,000 MW ~596 allylamine units per molecule) were purchased from Sigma-Aldrich. Ethylene diamine was purchased from J.T. Baker. A suspension of SiO₂ NP (Snowtex-O type, 20.3 wt % SiO₂ NP and pH 3.5) was purchased from Nissan chemicals and the pH adjusted to 5.5 using 150 mM NaOH prior to use. Deionized water (18.2 MΩ) was used throughout.

Reverse NAC Preparation

An aqueous solution of PAA (215 μL, 5 mg/mL) was added to an aqueous solution of DyDOTAM(Cl)₃ (535 μL, 40 mM) in a 1.5 mL Eppendorf centrifuge tube and vortexed to mix the solutions for 10 s at low speed. This ratio of reactants afforded a charge ratio $R = 0.5$ (Equation 1). A solution of ethylene diamine (215 μL, 110 mM) was added and the mixture immediately turned turbid, indicating the formation of PAA-DyDOTAM aggregates. The reaction mixture was vortexed at a very low speed for 5 s and then aged for 10 s. An aqueous solution of PAH (20 μL, 89 μM) was added to the turbid solution and vortexed at a low speed for 10 s and aged for 15 s. An aqueous suspension of SNPs (535 μL; concentration of 2.0 wt %) was added. The resulting mixture was then stirred vigorously at a medium speed for 10 s and aged for 2 h. Finally, the RACs were purified by filter centrifugation using a 10 kDa MWCO filter centrifuge tube. The RACs so obtained were characterized in terms of size and morphology by DLS and SEM as previously described (Farashishiko et al., 2016).

CEST Experiments

CEST spectra were acquired on a Bruker Avance IIa operating at 400.13 MHz using a broadband observe (BBO) probe. Spectra were acquired with a 1 ppm spectral resolution and a relaxation delay of 10 s. Samples were prepared in a 10 M CsCl solution in H₂O at 40 mM (Dy³⁺) and pH 6.5. The use of CsCl was to ensure that RACs did not settle during the acquisition of the CEST spectrum.

RESULTS AND DISCUSSION

Capsule Preparation

The attraction of NACs and CACs as high payload delivery systems is the ease with which Gd³⁺ chelates are incorporated into the nano-materials. Incorporating a CEST agent in a nano-capsule presents a rather different set of challenges. It is a relatively simple matter to select a Gd³⁺ chelate as a T_1 -shortneing agent that can be incorporated into a nano-capsule—the only prerequisite seems to be that the overall negative charge of chelate be two or greater (Farashishiko et al., 2016). The

effort required to prepare a polyanionic CEST agent would be significant and would off-set the synthetic advantages of using a nano-capsule based delivery system. ParaCEST agents are commonly derived from neutral ligands, such as the tetraamide derivatives of DOTA, and are therefore intrinsically positively charged unless strategies are employed to alter the overall charge. In this context we asked the question: can the electrostatic charges that hold these nano-capsule systems be reversed to permit the delivery of a large payload of polycationic (rather than polyanionic) chelates?

Two major hurdles blocked the seemingly simple path toward the preparation of nano-capsules loaded with a polycationic chelate. Previous results (Plush et al., 2009; Farashishiko et al., 2016, 2017) would seem to indicate that a charge driven aggregate could be produced by the simple expedient of mixing a tricationic chelate with an anionic polymer. However, when DyDOTAM³⁺ (a paraCEST agent) was added to PAA in aqueous solution at pH 7 with $R = 0.5$ the solution became only weakly turbid indicating that the aggregates that formed were only weakly charge associated. The charge ratio (R) is defined in Equation (1). Solution turbidity (interpreted as more robust aggregates) could be increased by addition of several equivalents of ethylene diamine to the mixture of PAA and DyDOTAM³⁺. Once aggregates have been formed in this manner, the next hurdle to overcome was developing a method for producing an encapsulating shell. Attempts to develop a cross-linked shell using EDC and polyamines such as ethylene diamine, butylene diamine and even PAH proved unsuccessful. In light of these results encapsulation strategies focused on the use of small nanoparticles (Bagaria and Wong, 2011; Bagaria et al., 2011) to form a charge driven coating, *c.f.* NACs (Farashishiko et al., 2016). The use of SNPs directly with the PAA/DyDOTAM³⁺ aggregates was, unsurprisingly, not successful. Under the prevailing reaction conditions both the aggregates and the SNPs are expected to be negatively charged, and this would account for the failure of SNPs to generate stable nano-capsules in this system. To overcome this problem an intermediate step was introduced—the negatively charge aggregates were coated with a cationic polymer layer. PAH was added to the turbid mixture after formation of the PAA/DyDOTAM³⁺ aggregate. Modification of the aggregate surface charge through addition of PAH was found to facilitate formation of an encapsulating shell using SNPs. The synthetic procedure that successfully allowed the preparation of Reversed nano-Assembled Capsules (RACs) with $R = 0.5$ is described schematically in Figure 2.

$$R = \frac{|[chelate]z^+|}{|[polymer]z^-|} \quad (1)$$

The capsules produced from this synthetic method were found to be quite large—the average hydrodynamic volume determined by dynamic light scattering was 650 ± 250 nm. The morphology of RACs as seen in the scanning electron micrograph (Figure 3) is very similar to that observed previously for both NACs and CACs (Farashishiko et al., 2016, 2017). It is significant to note that the rate at which water molecules were able to diffuse between

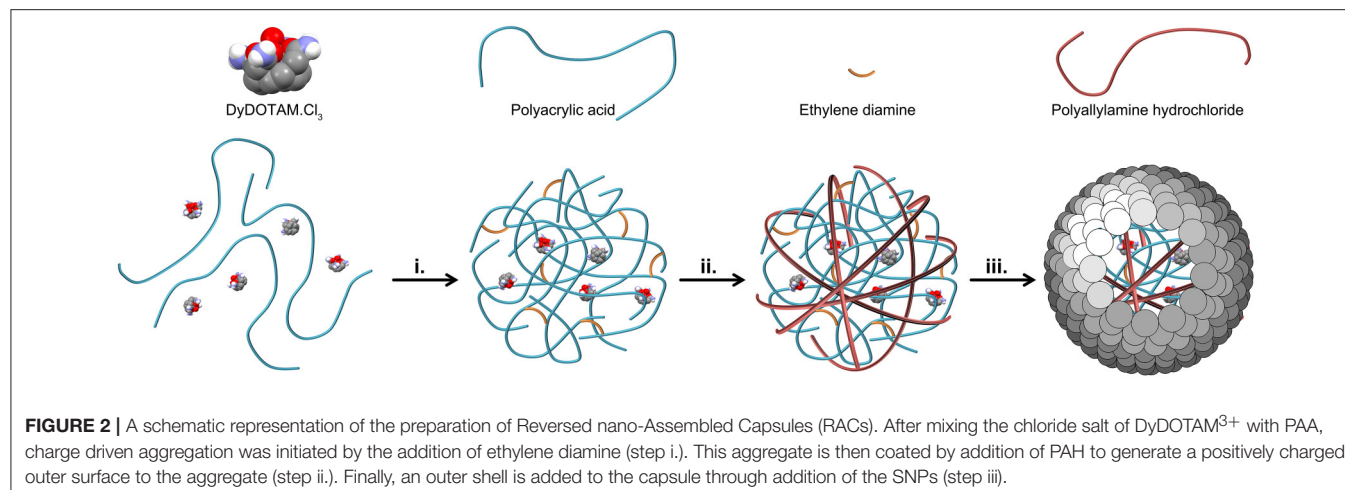


FIGURE 2 | A schematic representation of the preparation of Reversed nano-Assembled Capsules (RACs). After mixing the chloride salt of DyDOTAM³⁺ with PAA, charge driven aggregation was initiated by the addition of ethylene diamine (step i.). This aggregate is then coated by addition of PAH to generate a positively charged outer surface to the aggregate (step ii.). Finally, an outer shell is added to the capsule through addition of the SNPs (step iii.).

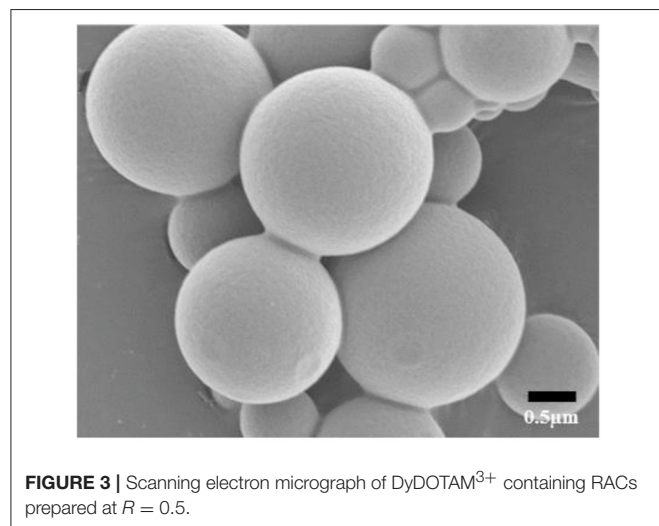


FIGURE 3 | Scanning electron micrograph of DyDOTAM³⁺ containing RACs prepared at $R = 0.5$.

the solvent and the capsule interior was found to decrease with increasing size for both NACs and CACs (Farashishiko et al., 2016, 2017). The RACs formed here are comparable in size to their NAC counterparts also formed with $R = 0.5$ (although larger than the corresponding CACs), it seems reasonable to presume that the rate at which water exchanges in and out of these capsules is comparably rapid (Farashishiko et al., 2016).

Evaluation of CEST Properties

Previously reported systems for delivering large payloads of CEST agent (Wu et al., 2008, 2010; Ali et al., 2009, 2012; Ebuomwan et al., 2012) have tended to focus on the effect arising from exchange of water coordinated to Eu³⁺. In the context of this work the most interesting effect is that arising from exchange of the amide protons of DyDOTAM³⁺. Since DyDOTAM³⁺ has eight amide protons vs. two for a coordinated water molecule, exploiting amide based paraCEST already affords a potential four-fold increase in detectability over Eu³⁺-bound water based paraCEST. Also, because the Dy³⁺ ion induces an extremely large

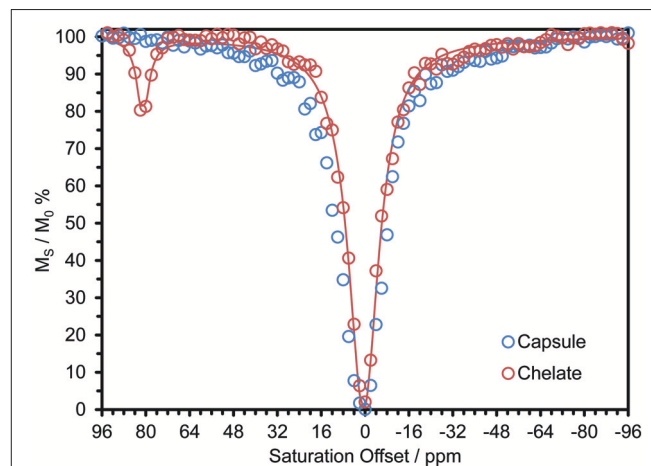


FIGURE 4 | CEST spectra of 40 mM solution of DyDOTAM³⁺ at pH 6.5 and 298 K in 10 M CsCl, as discrete chelates (red, the line is a fit to the data using a 2-site exchange model of the Bloch equations Zhang et al., 2003. Fitting parameters are: $\tau_{NH} = 1.51$ ms, $T_{1NH} = 6$ ms, $T_{1W} = 2.3$ s, $T_{2NH} = 5$ ms, $T_{2W} = 0.31$ s) and incorporated into RACs (blue) – CW irr. time = 10 s, $B_0 = 400$ MHz, $\gamma B_1 = 1000$ Hz.

hyperfine shift, the resonance frequency of the amide protons of DyDOTAM³⁺ is even farther from the solvent water ($\sim +80$ ppm) than the coordinated water of Eu³⁺ ($\sim +50$ ppm). The CEST spectrum of a 40 mM solution of DyDOTAM³⁺ at pH 6.5 demonstrates this with a clear CEST peak at about +80 ppm (Figure 4).

CEST spectra take some time to acquire and so when acquiring the CEST spectrum of nano-scale materials such as these it is necessary to ensure that the nano-material does not settle during acquisition. After experimentation it was determined that a 10 M solution of CsCl would suspend the capsules long enough to permit the acquisition of a CEST spectrum without appreciable settling of the nano-materials. The effect of even a high concentration of a chaotropic salt, such a CsCl, can be

seen to be negligible from previously published data (Conte, 2015; Payne et al., 2017). Accordingly, all CEST data were recorded under identical conditions for comparative purposes. Despite these precautions, the CEST spectrum of DyDOTAM³⁺ encapsulated in RACs shows no CEST arising from the amide protons (**Figure 4**).

Several explanations may be offered as to why DyDOTAM³⁺, once incorporated into RACs, does not exhibit CEST arising from the amide protons. As a result of the observation that no CEST was obtained from either this nano-scale system or the Eu³⁺-loaded SNPs (Evbuomwan et al., 2012), we were motivated to probe one possible explanation in particular. Is it possible that rapid nuclear relaxation is having a quenching effect on CEST?

As the saturation pulse equalizes the populations of the α and β states, longitudinal relaxation will act to return the system to the Boltzmann distribution (Woods et al., 2006). Consequently, more rapid longitudinal relaxation will reduce the amount of CEST obtained. Although paramagnetic ions do shorten T_1 , the Ln³⁺ ions capable of inducing large hyperfine shifts (those of interest for paraCEST) have anisotropic f -shells that result in rapid electronic relaxation. Because electronic relaxation is very fast ($\sim 0.1\text{--}1$ ps) in these ions their shortening effect on proton T_1 (their relaxivity, r_1) is small (Bertini et al., 1993). However, if a paramagnetic ion tumbles more slowly in solution (long rotational correlation time, τ_R) then relaxivity can increase as a consequence of Curie nuclear spin relaxation (Banci et al., 1991). But, in the context of CEST, it is important to recognize that this effect is highly field dependent and as B_0 increases the effect of increasing τ_R decreases such that, at the fields typically used for evaluating CEST agents (9.4 T and above), τ_R has virtually no effect on r_1 ($\omega_H \tau_R \gg 1$). It is therefore not expected that coupling a paraCEST agent to a nano-scale system will alter proton T_1 s in a way that will adversely affect CEST.

The effect of increasing τ_R on transverse relaxation stands in marked contrast to that observed for longitudinal relaxation. As predicted by theory (Banci et al., 1991), the transverse relaxivity (r_2) of a paramagnetic ion with a long τ_R does not disperse as B_0

increases (as r_1 does), but continues to increase with the square of the magnetic field. Therefore, at high fields a paramagnetic ion that tumbles slowly could have a significantly large transverse relaxivity. Simulating the CEST spectrum of DyDOTAM³⁺ using the Bloch equations and increasingly shorter and shorter T_2 values for the amide protons (T_{2NH}) shows that a paramagnetic ion with a very substantial T_2 -shortening effect could potentially adversely affect CEST (**Figure 5A**). Note that this simulation does not take into account any T_2 -shortening that might occur to the solvent water protons. In the present case, the effect that DyDOTAM³⁺ has on the solvent water T_2 will be highly dependent upon the rate of water exchange in and out of the RAC. Given the size of the RACs, exchange of water between the interior and solvent water is likely to be rapid which means that the T_2 of solvent water is also likely to undergo a shortening effect.

Is it possible that, with slowed molecular tumbling, the T_{2NH} DyDOTAM³⁺ could be shortened to the extent necessary to negatively impact CEST? Using the equations of paramagnetic relaxation in a form suitable for lanthanide(III) ions (Bertini et al., 2017), T_{2NH} was calculated for DyDOTAM³⁺ at three different τ_R values: 100 ps (approximately the value of a low molecular weight chelate), and 1 and 10 ns reflecting a range of values that could be taken by smaller nanoscale materials (**Figure 5B**). From these calculations it can be seen that R_{2NH} remains very low across the plotted field range when tumbling is fast ($\tau_R = 100$ ps)—it never exceeds 10^3 s⁻¹. The effect of R_{2NH} on the CEST arising from a rapidly tumbling chelate is negligible. However, as rotation slows the effect on R_{2NH} is dramatic at higher fields. For the most slowly tumbling system ($\tau_R = 10$ ns) R_{2NH} increases substantially with increasing field—at 400 MHz R_{2NH} is calculated to be about 2×10^4 s⁻¹, in good agreement with literature values (Bertini et al., 2017). Given the considerable size of the RACs it is likely that τ_R for the encapsulated DyDOTAM³⁺ will be longer than the 10 ns used in this calculation, which will in turn further increase the value of R_{2NH} —conceivably by as much as an order of magnitude. Nonetheless, these calculations provide a good basis

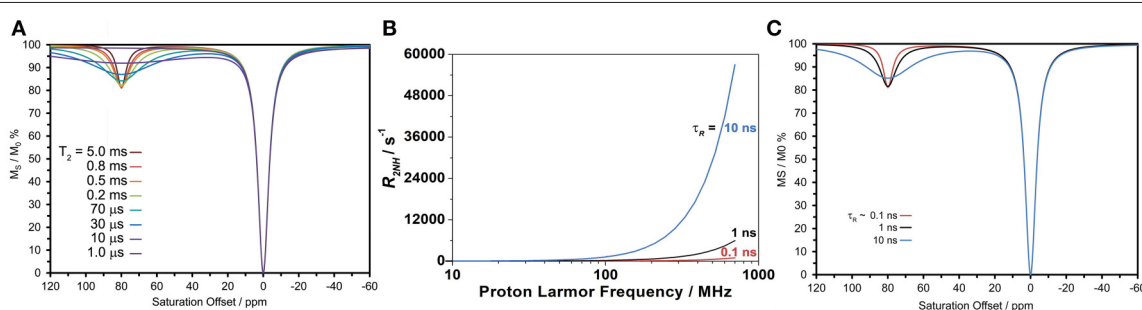


FIGURE 5 | Calculated properties of DyDOTAM³⁺ under different conditions. **(A)** Simulations of CEST arising from the amide protons using the Bloch equations to assess the potential effect of shortening T_{2NH} , generated fixing all parameters to similar values to those obtained from fitting the experimental spectrum in **Figure 4** ($B_0 = 400$ MHz, $\gamma B_1 = 1000$ Hz, $T_1^{\text{bulk}} = 2$ s, $T_2^{\text{bulk}} = 1$ s, $T_{1NH} = 40$ ms, $k_{\text{ex}} = 650$ s⁻¹). **(B)** Simulations of the amide proton transverse relaxation rate constant as a function of field for different values of τ_R assuming a distance of 5 Å and an electronic relaxation time of 0.1 ps. **(C)** Simulations of CEST arising from the amide protons using the Bloch equations, the same parameters used in **(A)** and R_{2NH} values determined for the different τ_R values in **(B)**.

to conservatively examine the effect that such rapid transverse relaxation could have on CEST.

Figure 5C shows simulations of CEST spectra for the amide protons of DyDOTAM³⁺ at 400 MHz using the $R_{2\text{NH}}$ values obtained by calculation in **Figure 5B** for τ_R values of 0.1, 1, and 10 ns. It can be seen that the simulated CEST spectrum of the freely tumbling chelate ($\tau_R = 0.1$ ns) closely resembles that obtained experimentally (**Figure 4**). As τ_R increases the CEST peak at 80 ppm broadens and decreases in intensity such that when $\tau_R = 10$ ns the CEST peak is already becoming broad and less distinct. As noted earlier $\tau_R = 10$ ns represents a conservatively rapid rate of tumbling for RACs with a hydrodynamic volume averaging 650 nm. If τ_R is longer, as seems likely, then $R_{2\text{NH}}$ will be larger and the detrimental effect on CEST increased. Slow molecular tumbling in a Dy³⁺ chelates could be responsible for entirely quenching CEST in systems such as these RACs.

Not only will the amount of CEST produced by these slowly tumbling systems be reduced, but it will also be increasingly difficult to extract the CEST. Because the CEST peak is now very broad, a significant bandwidth is required of the pre-saturation pulse. In practice, this means that the power of this pulse must be high. The CEST spectrum of the DyDOTAM³⁺ loaded RACs was acquired using a healthy 1 kHz of γB_1 power, affording a reasonable pulse bandwidth. In practice a pre-saturation power equivalent to $\gamma B_1 = 1$ kHz is too high for practical MRI applications. Lower pulse powers, with their correspondingly narrower bandwidths, will be able to saturate only a small fraction of the amide proton resonance, also contributing to a quenching of CEST in these slowly tumbling systems.

CONCLUSIONS

If the rate of proton exchange across the RAC shell was unduly slow then it would also act to quench the CEST arising from the amide protons of the encapsulated DyDOTAM³⁺. The possibility of slow water exchange kinetics can largely be ruled out by comparison with the previously reported NACs (Farashishiko et al., 2016). The encapsulating shell of both RACs and NACs are made up of electrostatically associated SNPs. This shell has a comparatively high water permeability coefficient as demonstrated by the fact that relaxivity (which demands very rapid water exchange kinetics) is not limited by water exchange

until the capsules become very large, much larger than the RACs studied here. The high relaxivity of $R = 0.5$ NACs, which are similar in size to the RACs reported here, is a clear indication that that water exchange in and out of the capsule does not limit the relaxivity and is therefore rapid enough that it will not quench CEST.

It is evident from our simulations that a substantial increase in τ_R does have a strong negative impact on the CEST properties of a nano-scale paraCEST material based on later Ln³⁺ ions. Slow molecular tumbling can increase the rate of transverse relaxation to such an extent that it out competes CEST and effectively quenches (or reduces) the observed CEST effect. This effect will almost certainly arise when Ln³⁺ ions, in particular the heavy late lanthanides, have large magnetic moments. These ions induce large Curie relaxation contributions and thus more rapid transverse relaxation of proximate protons. In contrast, the lighter early lanthanides have smaller magnetic moments and would therefore be less likely to induce such rapid transverse relaxation even when τ_R becomes long (Bertini et al., 2017). This means that the effect of long τ_R values are unlikely to explain the CEST quenching observed by Sherry and co-workers or Pagel and co-workers for Eu³⁺-based CEST agents (Wu et al., 2008, 2010; Ali et al., 2009, 2012; Ebvoumwan et al., 2012).

In summary, cationic paraCEST agents can be incorporated into nano-scale capsules through the expedient of reversing the charges. When the paraCEST agent relies upon a late Ln³⁺ ion with a large magnetic moment, the significant increase in R_2 that accompanies the increase in τ_R results can result in quenching of CEST. It remains to be seen whether the encapsulation of paraCEST agents based on early Ln³⁺ ions, such as Pr³⁺ or Eu³⁺, would permit the development of high payload CEST systems.

AUTHOR CONTRIBUTIONS

All authors listed have made a substantial, direct and intellectual contribution to the work, and approved it for publication.

FUNDING

Financial support was provided by Portland State University, the National Institute of General Medical Sciences: GM118964 (MW) and the University of Piemonte Orientale (Ricerca locale 2016) (MB).

REFERENCES

- Aime, S., Carrera, C., Delli Castelli, D., Geninatti Crich, S., and Terreno, E. (2005). Tunable imaging of cells labeled with MRI-PARACEST agents. *Angew. Chem. Int. Ed.* 44, 1813–1815. doi: 10.1002/anie.200462566
- Ali, M. M., Bhuiyan, M. P., Janic, B., Varma, N. R., Mikkelsen, T., Ewing, J. R., et al. (2012). A nano-sized PARACEST-fluorescence imaging contrast agent facilitates and validates *in vivo* CEST MRI detection of glioma. *Nanomedicine* 7, 1827–1837. doi: 10.2217/nnm.12.92
- Ali, M. M., Yoo, B., and Pagel, M. D. (2009). Tracking the relative *in vivo* pharmacokinetics of nanoparticles with PARACEST MRI. *Mol. Pharm.* 6, 1409–1416. doi: 10.1021/mp900040u
- Bagaria, H. G., Kadali, S. B., and Wong, M. S. (2011). Shell thickness control of nanoparticle/polymer assembled microcapsules. *Chem. Mater.* 23, 301–308. doi: 10.1021/cm102472h
- Bagaria, H. G., and Wong, M. S. (2011). Polyamine-salt aggregate assembly of capsules as responsive drug delivery vehicles. *J. Mater. Chem.* 21, 9454–9466. doi: 10.1039/c1jm10712g
- Banci, L., Bertini, I., and Luchinat, C. (1991). *Nuclear and Electron Relaxation. The Magnetic Nucleus Unpaired Electron Coupling in Solution*. Weinheim: Wiley VCH.
- Bertini, I., Capozzi, F., Luchinat, C., Nicastro, G., and Xia, Z. (1993). Water proton relaxation for some lanthanide aqua ions in solution. *J. Phys. Chem.* 97, 6351–6354.

- Bertini, I., Luchinat, C., Parigi, G., and Ravera, E. (2017). *Solution NMR of Paramagnetic Molecules*, 2nd Edn. Amsterdam: Elsevier Science.
- Conte, P. (2015). Effects of ions on water structure: a low-field ^1H T_1 NMR relaxometry approach. *Magn. Reson. Chem.* 53, 711–718. doi: 10.1002/mrc.4174
- Evbuomwan, O. M., Merritt, M. E., Kiefer, G. E., and Dean Sherry, A. (2012). Nanoparticle-based PARACEST agents: the quenching effect of silica nanoparticles on the CEST signal from surface-conjugated chelates. *Contrast Media Mol. Imag.* 7, 19–25. doi: 10.1002/cmmi.459
- Farashishiko, A., Chacón, K. N., Blackburn, N. J., and Woods, M. (2016). Nano assembly and encapsulation; a versatile platform for slowing the rotation of polyanionic Gd^{3+} -based MRI contrast agents. *Contrast Media Mol. Imag.* 11, 154–159. doi: 10.1002/cmmi.1676
- Farashishiko, A., Plush, S. E., Maier, K. B., Dean Sherry, A., and Woods, M. (2017). Crosslinked shells for nano-assembled capsules: a new encapsulation method for smaller Gd^{3+} -loaded capsules with exceedingly high relaxivities. *Chem. Commun.* 53, 6355–6358. doi: 10.1039/C7CC00123A
- Ferrauto, G., Delli Castelli, D., Di Gregorio, E., Terreno, E., and Aime, S. (2016). LipoCEST and cellCEST imaging agents: opportunities and challenges. *Wiley Interdiscip. Rev. Nanomed. Nanobiotechnol.* 8, 602–618. doi: 10.1002/wnan.1385
- Ferrauto, G., Di Gregorio, E., Ruzza, M., Catanzaro, V., Padovan, S., and Aime, S. (2017). Enzyme-responsive LipoCEST agents: assessment of MMP-2 activity by measuring the intra-liposomal water ^1H NMR shift. *Angew. Chem. Int. Ed.* 56, 12170–12173. doi: 10.1002/anie.201706271
- Olatunde, A. O., Bond, C. J., Dorazio, S. J., Cox, J. M., Benedict, J. B., Daddario, M. D., et al. (2015). Six, seven or eight coordinate FeII, CoII or NiII complexes of amide-appended tetraazamacrocycles for ParaCEST thermometry. *Chem. Eur. J.* 21, 18290–18300. doi: 10.1002/chem.201503125
- Pavuluri, K., and McMahon, M. T. (2017). pH Imaging using Chemical Exchange Saturation Transfer (CEST) MRI. *Isr. J. Chem.* 57, 862–879. doi: 10.1002/ijch.201700075
- Payne, K. M., Wilds, J. M., Carniato, F., Botta, M., and Woods, M. (2017). On water and its effect on the performance of T_1 -shortening contrast agents. *Isr. J. Chem.* 57, 880–886. doi: 10.1002/ijch.201700037
- Plush, S. E., Woods, M., Zhou, Y.-F., Kadali, S. B., Wong, M. S., and Sherry, A. D. (2009). Nanoassembled capsules as delivery vehicles for large payloads of high relaxivity Gd^{3+} agents. *J. Am. Chem. Soc.* 131, 15918–15923. doi: 10.1021/ja906981w
- Sherry, A. D., Zhang, S., and Woods, M. (2005). “Water exchange is the key parameter in the design of next generation MRI agents,” in *ACS Symposium Series 903, Medicinal Inorganic Chemistry*, eds J. L. Sessler, S. R. Doctrow, T. J. McMurray, and S. J. Lippard (Washington, DC: American Chemical Society), 151–165.
- Sinharay, S., Howison, C. M., Baker, A. F., and Pagel, M. D. (2017). Detecting *in vivo* urokinase plasminogen activator activity with a catalyCEST MRI contrast agent. *NMR Biomed.* 30, 1–8. doi: 10.1002/nbm.3721
- Ward, K. M., Aletras, A. H., and Balaban, R. S. (2000). A new class of contrast agents for MRI based on proton chemical exchange dependent saturation transfer (CEST). *J. Magn. Reson.* 143, 79–87. doi: 10.1006/jmre.1999.1956
- Woods, M., Woessner, D. E., and Sherry, A. D. (2006). Paramagnetic lanthanide complexes as PARACEST agents for medical imaging. *Chem. Soc. Rev.* 35, 500–511. doi: 10.1039/b509907m
- Wu, Y., Carney, C. E., Denton, M., Hart, E., Zhao, P., Streblow, D. N., et al. (2010). Polymeric PARACEST MRI contrast agents as potential reporters for gene therapy. *Org. Biomol. Chem.* 8, 5333–5338. doi: 10.1039/c0ob0087f
- Wu, Y., Zhou, Y., Ouari, O., Woods, M., Zhao, P., Soesbe, T. C., et al. (2008). Polymeric PARACEST agents for enhancing MRI contrast sensitivity. *J. Am. Chem. Soc.* 130, 13854–13855. doi: 10.1021/ja805775u
- Zhang, L., Martins, A. F., Zhao, P., Tieu, M., Esteban-Gómez, D., McCandless, G. T., et al. (2017a). Enantiomeric recognition of D- and L-Lactate by CEST with the aid of a paramagnetic shift reagent. *J. Am. Chem. Soc.* 139, 17431–17437. doi: 10.1021/jacs.7b08292
- Zhang, L., Martins, A. F., Zhao, P., Wu, Y., Tircsó, G., and Sherry, A. D. (2017b). Lanthanide-based $T_{2\text{ex}}$ and CEST complexes provide insights into the design of pH sensitive MRI Agents. *Angew. Chem. Int. Ed.* 56, 16626–16630. doi: 10.1002/anie.201707959
- Zhang, S., Merritt, M., Woessner, D. E., Lenkinski, R. E., and Sherry, A. D. (2003). PARACEST agents: modulating MRI contrast via water proton exchange. *Acc. Chem. Res.* 36, 783–790. doi: 10.1021/ar020228m
- Zhang, S., Winter, P., Wu, K., and Sherry, A. D. (2001). A Novel Europium(III)-based MRI contrast agent. *J. Am. Chem. Soc.* 123, 1517–1518. doi: 10.1021/ja005820q

Conflict of Interest Statement: The authors declare that the research was conducted in the absence of any commercial or financial relationships that could be construed as a potential conflict of interest.

Copyright © 2018 Farashishiko, Slack, Botta and Woods. This is an open-access article distributed under the terms of the Creative Commons Attribution License (CC BY). The use, distribution or reproduction in other forums is permitted, provided the original author(s) and the copyright owner are credited and that the original publication in this journal is cited, in accordance with accepted academic practice. No use, distribution or reproduction is permitted which does not comply with these terms.



Fluorinated Paramagnetic Complexes: Sensitive and Responsive Probes for Magnetic Resonance Spectroscopy and Imaging

Katie L. Peterson¹, Kriti Srivastava² and Valérie C. Pierre^{2*}

¹ Department of Chemistry, Bemidji State University, Bemidji, MN, United States, ² Department of Chemistry, University of Minnesota, Minneapolis, MN, United States

OPEN ACCESS

Edited by:

Lorenzo Tei,
Università degli Studi del Piemonte
Orientale, Italy

Reviewed by:

Francesca Garello,
Università degli Studi di Torino, Italy
Amnon Bar-Shir,
Weizmann Institute of Science, Israel
Lothar Helm,
École Polytechnique Fédérale de
Lausanne, Switzerland

*Correspondence:

Valérie C. Pierre
pierre@umn.edu

Specialty section:

This article was submitted to
Inorganic Chemistry,
a section of the journal
Frontiers in Chemistry

Received: 27 February 2018

Accepted: 20 April 2018

Published: 23 May 2018

Citation:

Peterson KL, Srivastava K and
Pierre VC (2018) Fluorinated
Paramagnetic Complexes: Sensitive
and Responsive Probes for Magnetic
Resonance Spectroscopy and
Imaging. *Front. Chem.* 6:160.
doi: 10.3389/fchem.2018.00160

Fluorine magnetic resonance spectroscopy (MRS) and magnetic resonance imaging (MRI) of chemical and physiological processes is becoming more widespread. The strength of this technique comes from the negligible background signal in *in vivo* ¹⁹F MRI and the large chemical shift window of ¹⁹F that enables it to image concomitantly more than one marker. These same advantages have also been successfully exploited in the design of responsive ¹⁹F probes. Part of the recent growth of this technique can be attributed to novel designs of ¹⁹F probes with improved imaging parameters due to the incorporation of paramagnetic metal ions. In this review, we provide a description of the theories and strategies that have been employed successfully to improve the sensitivity of ¹⁹F probes with paramagnetic metal ions. The Bloch-Wangsness-Redfield theory accurately predicts how molecular parameters such as internuclear distance, geometry, rotational correlation times, as well as the nature, oxidation state, and spin state of the metal ion affect the sensitivity of the fluorine-based probes. The principles governing the design of responsive ¹⁹F probes are subsequently described in a “how to” guide format. Examples of such probes and their advantages and disadvantages are highlighted through a synopsis of the literature.

Keywords: fluorine, lanthanide, iron, magnetic resonance imaging, magnetic resonance spectroscopy, contrast agent, molecular probe, responsive probe

FLUORINE MRS AND MRI

Fluorine magnetic resonance imaging (MRI) was first reported in 1977, just four years after the development of ¹H MRI, by Holland who acquired phantom images of NaF and perfluorotributylamine (Holland et al., 1977). In 1985, McFarland obtained the first ¹⁹F *in vivo* MR images of a rat using a fluorinated probe which accumulates in the liver, Fluosol-DA (McFarland et al., 1985). These pioneering studies demonstrated the key advantages of fluorine nuclei for magnetic resonance spectroscopy (MRS) and imaging (MRI). Today, these advantages are still exploited for monitoring a variety of biological analytes and processes.

The fluorine nuclei (^{19}F , $I = \frac{1}{2}$) is attractive due to its 100% abundance and high receptivity (83% that of ^1H). These attributes make it comparable to the ^1H nuclei (Knight et al., 2011; Ruiz-Cabello et al., 2011). Further, the similar gyromagnetic ratios (γ) of ^{19}F and ^1H allow images to be collected on broadband ^1H MRI scanners provided broadband amplifiers and dedicated radiofrequency coils are employed to accommodate the slower Larmor frequency of ^{19}F (Stares et al., 2018). The primary advantage of ^{19}F probes over ^1H MRI contrast agents is that the background signal in ^{19}F MRI is negligible. The body contains low amounts of fluorine that are primarily embedded in the solid matrices of bones and teeth. As a result, those fluorines have very short transverse relaxation times (T_2) and very broad signals that are easily removed with appropriate pulse sequences (Yu et al., 2013a). On the other hand, T_1 (longitudinal relaxation times) and T_2 -based ^1H MRI contrast agents, which are primarily gadolinium- and iron oxide nanoparticle-based, generate contrast by modulating the relaxation rates of the naturally-occurring water molecules. The significant background from the endogenous water can render certain imaging more difficult. In addition, ^{19}F nuclei have a large chemical shift range, >300 ppm, that readily allows for the design of fluorine probes featuring two distinct resonances that can be independently imaged if they are sufficiently separated. As will be discussed later, this property is advantageous in the design of ratiometric responsive ^{19}F MRI probes. Ratiometric probes can independently map the distribution of the probe and target analyte *in vivo* and enable tracking of different cell types or monitoring of multiple markers simultaneously.

IMPROVING THE SENSITIVITY OF ^{19}F PROBES

Despite the advantages of ^{19}F MRS and MRI, this field is limited by its low sensitivity that requires the use of high concentrations of probe, typically between 10 and 50 mM. In comparison, Gd-based T_1 contrast agents can be readily detected *in vivo* at substantially lower concentrations (0.1 μM) (Helm et al., 2018). This low sensitivity is due in part to the fact that only the ^{19}F nuclei of the probe are detected. Those nuclei are inherently less concentrated than the ^1H of H_2O used in ^1H MRI, hence the lower sensitivity. This issue is usually addressed by increasing the local concentration of ^{19}F nuclei. A second underlying problem of ^{19}F probes, and particularly diamagnetic ones, is the long T_1 relaxation times of ^{19}F , typically 0.5–3 s for small diamagnetic compounds, which necessitate long image acquisition times in order to obtain sufficient signal-to-noise ratio (SNR). This issue is best addressed via the incorporation of appropriate paramagnetic metal ions that shorten the relaxation rates of the ^{19}F nuclei.

Increasing Sensitivity by Increasing the Density of ^{19}F Nuclei

The most straightforward approach to increasing ^{19}F MRS/MRI signal intensity is simply to increase the local concentration of ^{19}F nuclei. This is most often accomplished by increasing the number of ^{19}F nuclei on the probe. Complications of this approach are

attributed to the hydrophobicity of fluorine which decreases the solubility of a probe in water and affects biodistribution and clearance. Nonetheless, many perfluorocarbons have successfully been used as ^{19}F MRS/MRI oximetry sensors and ^{19}F cell tracking agents provided they are injected as stable emulsions formulated to optimize clearance (Janjic and Ahrens, 2009; Ruiz-Cabello et al., 2011). Highly fluorinated molecules are mostly inert and considered non-toxic, which has facilitated their use *in vivo* and translation to humans. For instance, fluorinated nano-emulsions are undergoing a phase I clinical trial for ^{19}F MRI cell tracking applications (Ahrens and Zhong, 2013; Ahrens et al., 2014). However, not all fluorinated compounds can be assumed to be entirely non-toxic, especially at the high concentrations required for ^{19}F MRS/MRI. For instance, perfluoroctane sulfonate (PFOS) and perfluoroctanoic acid (PFOA) are both known to affect the function of the pancreas, thyroid, and liver (Chang et al., 2014; Kamendulis et al., 2014).

An often overlooked complication of perfluorinated probes arise when their ^{19}F nuclei are not chemically equivalent. Non-equivalent ^{19}F nuclei of a probe that have small frequency differences between the ^{19}F resonances result in blurry MR images that are the result of incomplete overlap of the images resulting from each ^{19}F resonance (Janjic et al., 2008). This substantially complicates image acquisition, can lead to artifacts, and decreases SNR. It is thus best to increase the number of fluorines in such a way that they remain chemically equivalent.

One of the most efficient ways to ensure that each ^{19}F nuclei is chemically equivalent is to incorporate high molecular symmetry in the design. Transition metal and lanthanide complexes with C_3 or C_4 symmetry are ideally suited for this application if the ligands are fluorinated appropriately. The macrocyclic DOTA (1,4,7,10-tetraazacyclododecane-1,4,7,10-tetraacetic acid) ligand, for instance, adopts a pseudo C_4 symmetry in which the acetate arms are arranged in a propeller-like fashion above the plane of the coordinating nitrogen atoms. Four possible isomers exist for this system based on the combination of two macrocyclic ring configurations (square prismatic or square antiprismatic) and the two possible arrangements of the acetate arms (Caravan et al., 1999; Benetollo et al., 2003). The substituents on the acetate arms and the Ln^{III} ion both influence the ratio of isomers observed by NMR such that one isomer can be favored over the others (Parker et al., 2002). The judicious choice of the macrocycle's arms has a notable impact on the ^{19}F NMR spectra of this class of macrocycles and on their effectiveness to function as ^{19}F MRS/MRI probes. $\text{Ln}(\text{F-DOTPME})^-$ (1,4,7,10-tetraazacyclododecane-1,4,7,10-tetrakis(methanephosphonic acid mono(2',2',2'-trifluoroethyl ester)), the lanthanide complex of the tetra trifluoroethyl-substituted DOTMP (1,4,7,10-tetraazacyclododecane-1,4,7,10-tetracyl-tetrakis(methylphosphonic acid)) analog (**1**, **Figure 1**; Kim et al., 1997), for instance, exists in solution at room temperature as a mixture of all eight isomers, which results in the presence of eight distinct ^{19}F peaks within a 12 (Yb^{III}) to 70 ppm (Tm^{III}) range. As discussed above, the presence of these different isomers limits the efficacy of these complexes to function as ^{19}F MR probes. The metal complexes of the tetra substituted DOTA with aryl- CF_3 groups (**11**, **Figure 1**; Chalmers et al., 2010)

exist primarily as one isomer, whose proportion depends on the nature of the lanthanide ion. This ligand is therefore better suited for ^{19}F MRI applications. The problem of multiple isomers is not limited to tetra-substituted macrocyclic derivatives. In fact, many DOTA analogs with only one or two fluorinated arms are present in solution as more than one isomer (2–4), the percentage of which varies according to the lanthanide (Kenwright et al., 2008; Chalmers et al., 2010; Placidi et al., 2013; Cakic et al., 2016).

Substitution of one or more carboxylate arms with bulky phosphinate groups or the introduction of substituent at the α -position to the ring nitrogen affects this dynamic process. For instance, Chalmers et al. reported two DOTA derivatives incorporating two trifluoroaryl groups and either two carboxylic acid or two glutaric acid substituents at the α -position to the ring nitrogen (5 and 6, **Figure 1**) (Chalmers et al., 2011a,b). In solution the carboxylic acid derivative, unlike the glutamic acid one, favors one major isomer which accounts for 80% of the ^{19}F NMR spectrum. The selectivity for one isomer can also be improved via the use of a phosphinate arm. For instance, all lanthanide complexes of 7 exist primarily (>87%) as one isomer. In extreme cases, a single isomer of a DOTA analog fluorinated on a single arm can be obtained, as for compounds 8–10 (**Figure 1**) (Jiang et al., 2011; Davies et al., 2015).

A single isomer for a tetra-substituted DOTA complex which exploits the symmetry of the ligand in order to maximize the number of equivalent fluorines can nonetheless be obtained. Examples include M-DOTAm-F12 (2,2',2'',2'''-(1,4,7,10-tetraazacyclododecane-1,4,7,10-tetrayl)tetraakis(N-(2,2',2-trifluoroethyl)acetamide)) (12, **Figure 1**; Srivastava et al., 2017a,b) and more recently the redox-responsive Eu-complex 39 (**Figure 9**) (Basal et al., 2017). Both of these complexes contain 12 ^{19}F nuclei linked to the macrocycle via four amide arms. Importantly, they both exist as a single isomer for which all 12 ^{19}F nuclei remain chemically equivalent. This increases the sensitivity of the ^{19}F MR probe and the resolution of the images that can be obtained with it. The high symmetry of the DOTA scaffold can also be exploited with certain transition metals. The unusual but stable 8-coordinate structure of the Fe^{II} -DOTAm-F12 maintains a high symmetry and chemical equivalency for its 12 fluorine nuclei (Srivastava et al., 2017a). The higher solubility in water of the M-DOTAm-F12, >100 mM, renders it particularly promising for further development and imaging applications. In summary, the C_3 or C_4 symmetry of metal complexes can be exploited to increase the number of chemically equivalent ^{19}F nuclei on a probe, but the drawback of multiple stable isomers in solution remains a challenge.

Increasing Sensitivity With Paramagnetic Metal Ions

Increasing the number of ^{19}F nuclei per agent can only go so far in terms of increasing the sensitivity of ^{19}F probes. Ultimately, there is a limit to the number of ^{19}F nuclei that can be added to a molecule in such a way that they are chemically equivalent all the while maintaining sufficient water solubility for *in vivo* applications. A complementary approach to increasing the number of ^{19}F nuclei that is often used simultaneously is to

decrease the T_1 of the ^{19}F nuclei. Diamagnetic molecules typically have T_1 of ^{19}F nuclei in the range of 0.5–3 s. For *in vivo* imaging applications, that are limited by time, the long T_1 of diamagnetic fluorine probes hinders their sensitivity (Harvey et al., 2012b). It is thus preferential to decrease the T_1 of the ^{19}F nuclei of fluorine probes. This is best achieved by incorporating paramagnetic metal ions such as lanthanides(III) or iron(II). The metal should be selected with care as different paramagnetic metal ions have different effects on the relaxation of nearby nuclei.

The effect of a paramagnetic metal ion on the T_1 and T_2 of a ^{19}F nuclei is described by the Bloch-Wangsness-Redfield theory. A ^{19}F nuclei adjacent to a paramagnetic center in a magnetic field can relax via five different mechanisms: (1) chemical shift anisotropy, (2) inter-nuclear dipole-dipole interaction, (3) electron-nucleus contact interaction, (4) electron-nucleus dipole-dipole interaction, and (5) Curie relaxation (Chalmers et al., 2010). Of these, chemical shift anisotropy is negligible for a single ^{19}F nuclei or CF_3 group, and inter-nuclear dipole-dipole mechanisms are minimal, accounting for <1% of the total relaxation. The electron-nucleus contact interaction is also negligible since ligand geometries generally locate the ^{19}F nuclei further than 4.5–7.5 Å away from the metal ion, resulting in coupling values of zero. Thus, only the electron-nucleus dipole-dipole and Curie relaxation processes contribute significantly to the relaxation of the ^{19}F nuclei. Given this, the longitudinal ($R_1 = 1/T_1$) and transverse ($R_2 = 1/T_2$) relaxation rates of ^{19}F nuclei in paramagnetic metal complexes are described by Equations (1) and (2), respectively (Chalmers et al., 2010).

$$R_1 = \frac{2}{15} \left(\frac{\mu_0}{4\pi} \right)^2 \frac{\gamma_F^2 \mu_{\text{eff}}^2}{d^6} \left(\frac{7\tau_{R+e}}{1 + \omega_e^2 \tau_{R+e}^2} + \frac{3\tau_{R+e}}{1 + \omega_F^2 \tau_{R+e}^2} \right) + \frac{2}{5} \left(\frac{\mu_0}{4\pi} \right)^2 \frac{\omega_F^2 \mu_{\text{eff}}^4}{(3kT)^2 d^6} \frac{3\tau_R}{1 + \omega_F^2 \tau_R^2} \quad (1)$$

$$R_2 = \frac{1}{15} \left(\frac{\mu_0}{4\pi} \right)^2 \frac{\gamma_F^2 \mu_{\text{eff}}^2}{d^6} \left(4\tau_{R+e} + \frac{3\tau_{R+e}}{1 + \omega_e^2 \tau_{R+e}^2} + \frac{13\tau_{R+e}}{1 + \omega_F^2 \tau_{R+e}^2} \right) + \frac{1}{5} \left(\frac{\mu_0}{4\pi} \right)^2 \frac{\omega_F^2 \mu_{\text{eff}}^4}{(3kT)^2 d^6} \left(4\tau_R + \frac{3\tau_R}{1 + \omega_F^2 \tau_R^2} \right) \quad (2)$$

where

$$\mu_{\text{eff}}^2 = g_J^2 \mu_B^2 J(J+1) \quad (3)$$

$$\omega_e = \left(\frac{g_J \mu_B}{\hbar} \right) B_0 \quad (4)$$

$$\tau_{R+e} = (\tau_R^{-1} + T_{1e}^{-1}) \quad (5)$$

In these equations, d is the distance separating the ^{19}F nuclei from the paramagnetic metal ion, μ_0 is the permeability of vacuum, γ_F is the gyromagnetic ratio of the ^{19}F nuclei, T is the temperature in K, k is Boltzmann's constant, and ω_F is the Larmor angular frequency of ^{19}F . The effective magnetic moment, μ_{eff} , is proportional to the effective electron g-factor (g_J), the Bohr magneton (μ_B), and the electron angular momentum, $J(J+1)$ according to Equation (3). The electron angular frequency (ω_e) is a function of the magnetic field strength (B_0) according to Equation (4) in which \hbar is the reduced Planck's constant. The τ_{R+e} term is dependent on the rotational correlation time

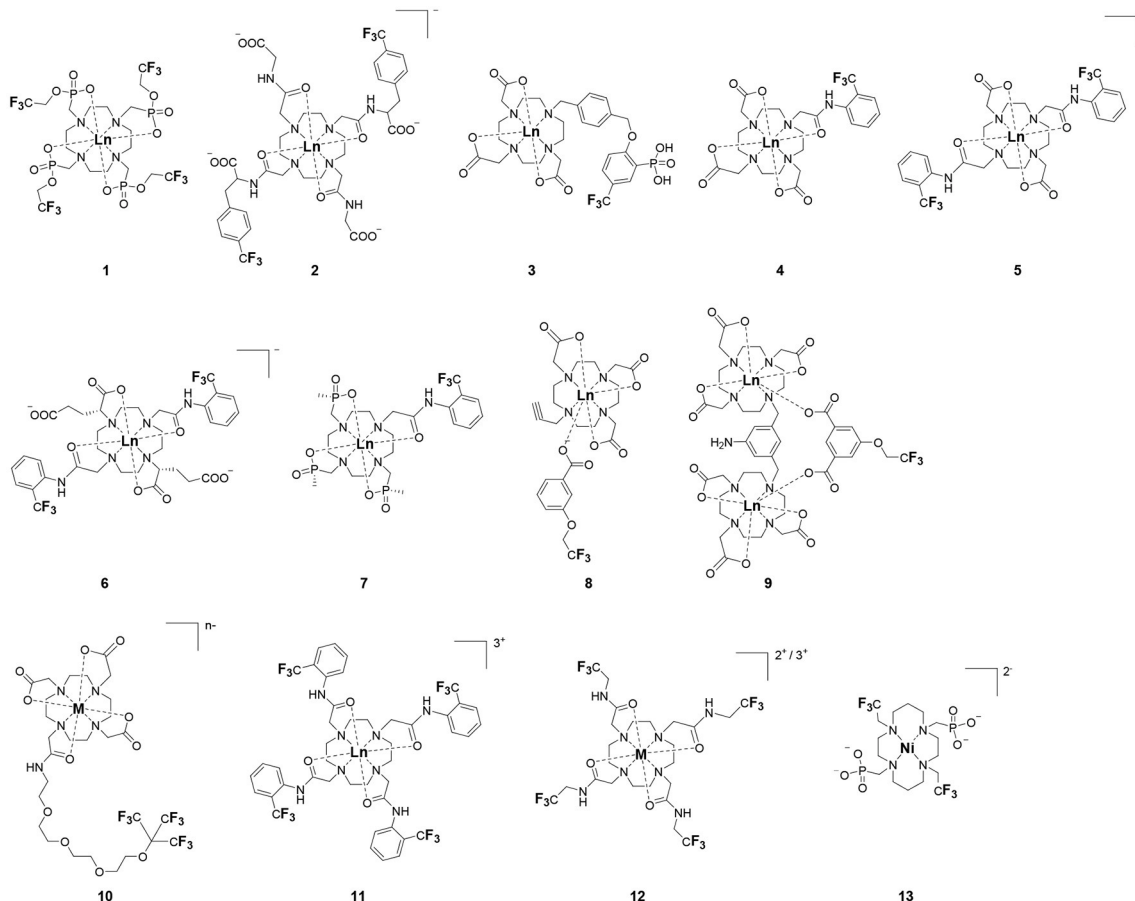


FIGURE 1 | Chemical structures of non-responsive paramagnetic ^{19}F probes (**1**, Kim et al., 1997; **2**, Cakic et al., 2016; **3**, Placidi et al., 2013; **4**, Chalmers et al., 2010; **5–6**, Chalmers et al., 2011a; **7**, Chalmers et al., 2011a,b; **8–9**, Davies et al., 2015; **10**, Jiang et al., 2011; **11**, Chalmers et al., 2010; **12**, Srivastava et al., 2017a,b; **13**, Blahut et al., 2016, 2017).

(τ_{R}) and the electron spin longitudinal relaxation time (T_{1e}) according to Equation (5).

In Equations (1) and (2), the first term represents the dipolar relaxation characterized by the stochastic electron magnetization of the electron-nucleus dipole-dipole interaction. The second term is the Curie relaxation arising from the interaction between the fluorine nuclear spin and the magnetic dipole induced by the applied magnetic field. Together, they relate R_1 and R_2 to the effective magnetic moment (μ_{eff}) of the paramagnetic metal, the ^{19}F -metal distance (d), the rotational correlation time (τ_{R}), the applied magnetic field strength (B_0), and the temperature (T). Optimizing the sensitivity of ^{19}F MRS/MRI probes requires understanding each of these relationships.

Dependence on the Nature of the Metal Ion

The effective magnetic moment (μ_{eff}) of the paramagnetic metal affects both the electron-nucleus dipole-dipole interaction and, to a greater extent, the Curie relaxation mechanism. The effective magnetic moment of transition metal complexes is a function of

both their oxidation state and their ligand fields. Each lanthanide ion has a characteristic μ_{eff} value (Table 1).

The effect of the nature of the transition or lanthanide ion on the relaxation rates of the ^{19}F nuclei of fluorinated complexes and the sensitivity of the resulting fluorine probe has been explored via a series of non-responsive probes. Several fluorinated ligands have been investigated, which enables a more in-depth evaluation of the influence of the structure of the ligand on the ^{19}F relaxation rates of the probe (Figure 1, Table 2). Studies by Parker and coworkers focused on a DOPA ([4,7-di[[hydroxymethyl]phosphoryl]methyl]-10-([2-(trifluoromethyl)phenyl]carbamoyl)methyl)-1,4,7,10-tetraazacyclododecan-1-yl)methyl](methyl)phosphinic acid ligand monosubstituted with *ortho* aryl-CF₃ (7) and DOTA ligand scaffold tetra substituted with aryl-CF₃ groups (11) (Chalmers et al., 2010, 2011a). In this scaffold, *ortho* substitution of the CF₃ group lead to a greater decrease in relaxation times due to the shorter distance separating the ^{19}F nuclei from the lanthanide ion (Senanayake et al., 2007; Chalmers et al., 2010). In agreement with the Bloch-Wangsness-Redfield theory, this first study demonstrated that paramagnetic lanthanide ions

TABLE 1 | Magnetic and relaxation properties of lanthanide(III) ions.

Lanthanide ion	Ground state term	μ_{eff} (B.M.) ^a	μ_{eff} (exp) ^b	Bleany Constant (C_j) ^c	Electron relaxation time (T_{1e})/ 10^{-13} s ^d
Ce ^{III}	$^2F_{5/2}$	2.56	2.55	-6.3	0.90
Pr ^{III}	3H_4	3.62	3.47	-11.0	0.57
Nd ^{III}	$^4I_{9/2}$	3.68	3.69	-4.2	1.15
Pm ^{III}	5I_4	2.68	2.41	2.0	Unknown
Sm ^{III}	$^6H_{5/2}$	1.55–1.65	1.58	-0.7	0.45
Eu ^{III}	7F_0	3.40–3.51	3.4	4.0	0.09
Eu ^{II}	$^8S_{7/2}$	7.6–8.0		0	10^4 e
Gd ^{III}	$^8S_{7/2}$	7.94	7.63	0	10^4 – 10^5 f
Tb ^{III}	7F_6	9.7	9.8	-86	2.03
Dy ^{III}	$^6H_{15/2}$	10.6	10.3	-100	2.99
Ho ^{III}	5I_8	10.6	10.4	-39	1.94
Er ^{III}	$^4H_{15/2}$	9.6	9.4	33	2.38
Tm ^{III}	3H_6	7.6	7.6	53	3.69
Yb ^{III}	$^2F_{7/2}$	4.5	4.3	22	1.37

^a(Gysling and Tsutsui, 1971; Tilley et al., 1980; Garcia and Allen, 2012).^b(Gysling and Tsutsui, 1971; Bertini et al., 1993a; Chalmers et al., 2010).^c(Bleaney, 1972).^daqua ion, 2.1 T (Alsaadi et al., 1980).^evalue for Eu^{II} was calculated using formula in Burai et al. (2003).^fBertini et al. (1993b).

can increase the R_1 by up to two orders of magnitude, with the greatest change observed with those metal ions with the highest μ_{eff} , notably, Tb^{III}, Dy^{III}, Ho^{III}, and Er^{III} (Table 2). Unfortunately, the poor solubility of the tetra substituted complexes in water limited further *in vivo* studies.

Recently, our lab reported the relaxation properties of the Fe^{II} and Ln^{III} complexes of another macrocyclic ligand, DOTAm-F12 (12) (Srivastava et al., 2017a,b). Complexes of this series, including the Fe^{II} complex, have a number of advantageous properties for ¹⁹F imaging. The complexes each contain 12 fluorine nuclei that are chemically equivalent, resulting in a single ¹⁹F resonance. As discussed above, a high number of fluorine nuclei and their equivalency are two necessary components in the design of sensitive ¹⁹F probes for MR imaging. The complexes are also highly soluble in water; they can be dissolved in concentrations of up to 100 mM, a necessity for any biological applications. The Fe^{II} complex is notable as it is stable both in air and water and is a rare example of an eight coordinate iron complex (Srivastava et al., 2017a). Importantly, for both the Fe^{II} and the Ln^{III} complexes, the structure of the macrocycle places the fluorine nuclei from 5.22 to 6.84 Å from the metal ion. As will be discussed later, this is an optimum distance since it minimizes the effect of the shortened T_2 of the ¹⁹F nuclei. As in Parker's study, the paramagnetic metal ions decrease the T_1 of the ¹⁹F nuclei by up to two orders of magnitude with the greatest decrease observed with those metal ions having the highest μ_{eff} , namely Tb^{III}, Dy^{III}, Ho^{III}, and Fe^{II}. Paramagnetic Ni^{II} cyclam complexes featuring *trans*-trifluoroethyl groups were also recently reported by Blahut et al. (2016, 2017). The *trans*-[Ni(te2f2p)]²⁻ (13, Figure 1) with phosphate ligands has a ¹⁹F-Ni distance of ~5 Å which facilitates a nearly 180-fold reduction in T_1 vs. the free ligand (Table 2). This Ni^{II} complex and

Fe^{II}-DOTAm-F12 (12) exemplify that the diverse electronic and structural parameters of transition metal complexes can also be exploited to optimize ¹⁹F paramagnetic relaxation enhancement (PRE).

The sensitivity of an agent, estimated by comparing SNR of solutions of complexes at the same concentration, is dependent not only on T_1 but also on T_2 . The line-broadening characteristic of the shorter T_2 of the fluorines of certain paramagnetic complexes significantly affect the sensitivity of the probe. An extreme example being the Gd^{III} complex of DOTAm-F12 that has such a short T_2 that the complex could not be observed by MRI. Note that for such complexes with rapid transverse relaxation, the use ultrashort TE (UTE) and zero TE (ZTE) acquisition pulse sequences can sometimes increase the SNR in ¹⁹F-MRI (Kislukhin et al., 2016).

Not all paramagnetic metals affect T_2 to the same degree as T_1 . Therefore, the most sensitive metal-based probes are not those whose metal ions have the highest μ_{eff} , but those whose ¹⁹F have the highest T_2/T_1 ratio. For M-DOTAm-F12 in water, these are Fe^{II}, Ho^{III}, Tm^{III}, and Yb^{III}. Importantly, the media also has a substantial effect on the relaxation times, and particularly on the transverse one. The T_2 of all M-DOTAm-F12 complexes decrease substantially in blood. This affects the sensitivity of all metal complexes. Ho^{III}-DOTAm-F12, for instance, is the most sensitive probe in water, yet it could not be detected in blood. The lower T_2 value of M-DOTAm-F12 complexes in blood in comparison to water could be due to different parameters. Coordination to albumin or other serum proteins and the resulting increase in rotational correlation time can affect both T_1 and T_2 . Blood is also more viscous than water, and this increase in viscosity also affects τ_R , T_1 , and T_2 . One should therefore not assume that a probe that is sensitive in water is necessarily appropriate for *in*

TABLE 2 | ^{19}F chemical shift and relaxation properties for non-responsive paramagnetic fluorine probes.

Ligand (\mathbf{B}_0)	Ln^{III}	δ (ppm)	$\Delta\delta$ (ppm)	R_1 (Hz)	T_1 (ms)	R_2 (Hz)	T_2 (ms)	T_2/T_1
2 (7.0 T) ^a	Eu ^{III}	-61.8	n.d.	1.4	714	18 ^h	56	0.078
	Gd ^{III}	-61.4		1.4	714	19 ⁱ	53	0.074
	Tb ^{III}	-61.6	n.d.	182	5.5	385	2.6	0.47
	Tb ^{III}	-65.2	n.d.	32 ^h	31	48 ^h	21	0.68
		-55.6		12 ^j	83	28 ⁱ	36	0.43
3 (7.0 T) ^b	Ligand	-61.24	n.d.	n.d.	n.d.	n.d.	n.d.	n.d.
	Gd ^{III}	-60.45	n.d.	322.6	3.1	500	2.0	0.65
	Yb ^{III}	-60.54	n.d.	3.7	273	238	4.2	0.015
4 (9.4 T) ^{c*}	Y ^{III}	-62	0	n.d.	n.d.	n.d.	n.d.	n.d.
	Tb ^{III}	-51.9	10.1	116	8.62	119	8.4	0.975
	Dy ^{III}	-64.9	-2.9	139	7.19	220	4.55	0.632
	Ho ^{III}	-64.2	-2.2	109	9.17	151	6.62	0.722
	Er ^{III}	-64.8	-2.8	65	15.38	157	6.37	0.414
	Tm ^{III}	-77.4	-15.4	51	19.61	91	10.99	0.56
5 (9.4 T) ^{c*}	Tb ^{III}	-61.9	n.d.	2.8	357.14	132	7.58	0.021
	Dy ^{III}	-99.8	n.d.	158	6.33	213	4.69	0.742
	Ho ^{III}	-57.7	n.d.	91	10.99	159	6.29	0.572
	Er ^{III}	-58.6	n.d.	81	12.35	164	6.10	0.494
	Tm ^{III}	-68.2	n.d.	56	17.86	102	9.80	0.549
7 (9.4 T) ^c	Y ^{III}	-61.2	0			15	66.7	
	Tb ^{III}	-47.7	13.5	147	6.8	267	3.75	0.55
	Dy ^{III}	-63.6	-2.4	185	5.41	251	3.98	0.737
	Ho ^{III}	-61.5	-0.3	120	8.33	143	6.99	0.839
	Er ^{III}	-72.6	-11.4	109	9.17	138	7.25	0.79
	Tm ^{III}	-89.5	-28.3	63	15.87	84	11.9	0.75
10 (11.7 T) ^d	ligand	-71.2		0.752	1330	1.43	701	0.53
	Y ^{III}	-71.1	0	0.66	1514	1.28	783	0.52
	Gd ^{III}	-66.6	-4.5	236	4.24	602	1.66	0.39
	Tb ^{III}	-63.3	-7.8	13.8	72.6	24.0	41.7	0.57
11 (9.4 T) ^e	Y ^{III}	-61.6	0	0.78	1282	2.9	345	0.27
	Tb ^{III}	-53.9	7.7	185	5.41	n.d.	n.d.	n.d.
	Ho ^{III}	-59	2.6	192	5.21	n.d.	n.d.	n.d.
	Er ^{III}	-63.5	-1.9	109	9.17	n.d.	n.d.	n.d.
	Tm ^{III}	-65.1	-3.5	59.7	16.8	n.d.	n.d.	n.d.

(Continued)

TABLE 2 | Continued

Ligand (B_0)	Ln^{III}	δ (ppm)	$\Delta\delta$ (ppm)	R_1 (Hz)	T_1 (ms)	R_2 (Hz)	T_2 (ms)	T_2/T_1
12 (7.0 T) ^f	ligand	-72.7		1.1	880	1.5	680	0.77
	La ^{III}	-72.1	0	1.8	570	2.5	400	0.70
	Eu ^{III}	-72.4	-0.3	2.8	360	24	41	0.11
	Gd ^{III}	-72.0	0.1	83	12	7100	0.14	0.01
	Tb ^{III}	-54.1	18.0	160	6.3	770	1.3	0.21
	Dy ^{III}	-52.4	19.7	170	5.9	450	2.2	0.37
	Ho ^{III}	-61.8	10.3	130	7.6	190	5.4	0.71
	Er ^{III}	-76.5	-4.4	71	14	110	8.8	0.63
	Tm ^{III}	-83.3	-11.2	39	26	63	16	0.62
	Yb ^{III}	-75.9	-3.8	7.7	130	18	55	0.42
	Fe ^{II}	-70.1	2.0	180	5.7	180	5.6	0.98
13 (7.0 T) ^g	ligand	-68.9		2000	0.5	20	50	0.1
	Ni ^{II}	-26	n.d.	357	2.8	1111	0.9	0.32

^aData listed for major isomers in solution.^b(Cakic et al., 2016).^c(Placidi et al., 2013).^d(Chalmers et al., 2011a).^e(Jiang et al., 2011).^f(Chalmers et al., 2010).^g(Srivastava et al., 2017b).^h(Blahut et al., 2016).ⁱMajor isomer.^jMinor isomer.

vivo applications where it will accumulate in blood or tissues. It is therefore recommended that the sensitivity of probes be evaluated not only in water but also in the media in which they are intended to be used. Also note that the greatest effect is not necessarily obtained with lanthanide ions. In blood, the most sensitive probe is Fe^{II}-DOTAm-F12 whose limit of detection (300 μ M) is more than an order of magnitude lower than that of small diamagnetic probes.

Similar trends have been observed with other lanthanide complexes, such as **2–5**, **7**, and **10–12** (Figure 1, Table 2). In general, the stronger relaxing metals with the higher μ_{eff} near 10, Tb^{III}, Dy^{III}, and Ho^{III} decrease both T_1 and T_2 the most. Lanthanides such as Er^{III}, Tm^{III}, and in the extreme case Gd^{III}, have lower T_2/T_1 ratio and hence lower sensitivity (Table 2) (Chalmers et al., 2010, 2011a,b; Jiang et al., 2011; Harvey et al., 2012b; Placidi et al., 2013; Blahut et al., 2016; Cakic et al., 2016; Srivastava et al., 2017b). Do note that the PRE effect is determined by other parameters beyond the μ_{eff} of the metal ion; it is also dependent on the magnetic field strength and on the distance separating the ¹⁹F nuclei and the paramagnetic metal ion (Equation 1–5). As mentioned above, transition metals such as Fe^{II} ($\mu_{eff} \sim 5$) and Ni^{II} ($\mu_{eff} \sim 3$) (complexes **12** and **13**, respectively) can also generate high ¹⁹F MRI SNR ratios of 20–30 despite their lower magnetic moments.

Even at greater ¹⁹F–M distances, the effect of the paramagnetic metal ion on the relaxation rates of the fluorine nuclei

can be notable. The fluorinated complex of Jiang (**10**, Figure 1) is a DOTA-based complex containing three equivalent trifluoromethyl groups separated by a polyethylene glycol linker that positions the ¹⁹F nuclei more than 10 Å away from the paramagnetic metal ion. Despite this great distance, paramagnetic metals such as Tb^{III}, Dy^{III}, Ho^{III}, Er^{III}, Gd^{III}, Fe^{III}, Ni^{II}, and Cu^{II} reduce T_1 and T_2 by >95% (Jiang et al., 2011). A noteworthy conclusion of this study is that the ¹⁹F relaxation times of these paramagnetic metal complexes are relatively constant (<5% change) with respect to environmental fluctuations in pH, temperature, and the concentration of either O₂ or bovine serum albumin (BSA) (Jiang et al., 2011). It is thus the identity of the paramagnetic metal ion that is the primary contributor to both the chemical shift and the relaxation rates of the fluorines. This observation is important for the development of responsive probes (*vide infra*).

Dependence on the ¹⁹F-M Distance

From the Bloch-Wangsness-Redfield Equations (1–5) given above, both the R_1 and the R_2 of the fluorine nuclei have a steep dependence on the distance d separating the ¹⁹F nuclei from the metal ion. The ¹⁹F–M distance is a key parameter in determining the sensitivity of metal-based fluorine probes. The effect of the paramagnetic metal ion on R_2 extends to longer distances than that of R_1 . Both too long and too short a distance can be detrimental. Too long a ¹⁹F–M distance and the effect

of the paramagnetic metal ion on the relaxation times of the fluorine nuclei is severely diminished. Too short a distance, and the substantial shortening of T_2 decreases the sensitivity of the fluorine probe. A higher T_2/T_1 ratio and thus a more sensitive fluorine probe is obtained if the ^{19}F nuclei are positioned between 4.5 and 7.5 Å from the metal ion (Harvey et al., 2012b).

Within this range, even minor changes in $^{19}\text{F}-\text{M}$ ion distance can have an impact on the relaxation rates of fluorine nuclei and the sensitivity of the agent. One such example are the lanthanide complexes containing a single aryl-CF₃ moiety positioned either on an acetate-based DOTA (**4**, Figure 1) or a phosphinate-based DOPA (**7**, Figure 1) scaffold. The DOTA complexes (**4**) exists in solution as a mixture of multiple isomers with the primary species representing only 50% of the fluorine signal intensity by NMR. On the other hand, the principal isomer of the phosphinate analog (**7**) accounts for 87% of the total ^{19}F signal intensity (Chalmers et al., 2011a). The R_1 and R_2 of lanthanide complexes of these two ligands are different. The R_1 of complexes of DOPA scaffold are 10–67% greater than those of the DOTA scaffold (Table 2). However, the R_2 of complexes (Ho^{III}, Er^{III}, and Tm^{III}) of DOPA scaffold are 5–12% smaller than those of DOTA scaffold with an exception of Tb^{III} and Dy^{III} being 14–124% greater than those of DOTA complexes. Global fitting of the relaxation rates collected at multiple field strengths to the Bloch-Wangness-Redfield theory determined that the differences in R_1 and R_2 are due to a 0.3 Å shorter $^{19}\text{F}-\text{Ln}$ distance in the DOPA complex than in the DOTA one (Chalmers et al., 2010, 2011a). Interestingly, the highest T_2/T_1 ratio with the DOTA-based scaffold was obtained with Tb^{III}. For the DOPA-based scaffold, it was instead Ho^{III} (0.84), Er^{III} (0.79), Tm (0.75), and Dy (0.74) that yielded the highest T_2/T_1 ratio. As is apparent from this example, the best metal ion for one fluorinated ligand is not necessarily the same for another one.

The effect that such minor modifications of the ligand and the structure of the complex have on the T_2/T_1 ratio and the sensitivity of the probe has been observed with other complexes. The Yb^{III}-DO3A (1,4,7,10-tetraazacyclododecane-1,4,7-tris(acetic acid))-based complex with a fluorinated aryl phosphonate of Angelovski, (**3**, Figure 1) positions the ^{19}F nuclei 7 Å from the metal, a $^{19}\text{F}-\text{Yb}$ distance 0.7 Å greater than in Yb-DOTAm-F12 (Placidi et al., 2013). At 7 T, the T_1 of 273 ms is nearly twice that in Yb^{III}-DOTAm-F12. More noticeably, the very short T_2 of the fluorines of this complex, 4.2 ms, results in a much smaller T_2/T_1 ratio and hence a much less sensitive probe than Yb^{III}-DOTAm-F12.

Supramolecular self-assembly enables more facile synthesis of paramagnetic fluorine probes via the formation of ternary complexes. Given the hardness of lanthanide ions, fluorinated carboxylate ligands are particularly well-suited for this approach (**8** and **9**, Figure 1) (Davies et al., 2015). These assemblies also decrease the relaxation times of the fluorine to a similar degree as observed in the complexes discussed above, although the relatively weak affinity of the carboxylate ligand for the lanthanide ($\log K_a \sim 4.9$) may result in decomplexation of the fluorinated moiety under biological conditions.

Similarly, paramagnetic metals have also been employed to increase the relaxation rates of fluorine nuclei in perfluorinated

emulsions. Perfluorocarbon-based emulsions present an advantage over monomolecular complexes in that they contain a higher density of fluorine nuclei which increases their sensitivity. The design and application of perfluorocarbon tracers for ^{19}F MRI have been reviewed elsewhere. (Knight et al., 2011; Tirotta et al., 2015) Here, the role of Gd^{III} and Fe^{III} in enhancing the relaxation rates of fluorine nuclei in nanoemulsions is explored. Neubauer et al. first reported a paramagnetic fluorinated emulsion containing a liquid perfluoro-15-crown-5 ether core encased in a lipid layer surface-coated with Gd-DTPA-BOA (6,9-bis(carboxymethyl)-3-(2-(((E)-octadec-9-en-1-yl)amino)-2-oxoethyl)-11-oxo-3,6,9,12-tetraazatriacont-21-enoic acid) complexes (**14**, Figure 2) (Neubauer et al., 2008). The relaxation rates of the fluorine nuclei in this paramagnetic emulsion increases according to an outer-sphere mechanism which requires the perfluorocarbons within the core of the nanoparticle to diffuse close to the Gd^{III} ions on the surface of the lipid monolayer. In this 200 nm assembly, the R_1 and R_2 of the fluorine nuclei located ~15 Å away from the Gd^{III} ion increase 4- and 8-fold, respectively. This, in turn, increases the sensitivity of the emulsion 2-fold (Neubauer et al., 2008). Further calculations on how the size of the nanoparticles, the $^{19}\text{F}-\text{Gd}$ distance (d), and the diffusion coefficient of the perfluorocarbon affect the R_1 and R_2 of the ^{19}F enabled further improvement of the assembly (Hu et al., 2011). A 4-fold relaxation enhancement was observed with a perfluoro-15-crown-5 ether and Gd-DTPA-BOA (**14**) compared to non-metallated perfluorocarbon. Additionally, a shorter linker between the Gd and the perfluorocarbon core of the DTPA complexes (**14** and **15**) vs. the Gd-DOTA chelate (**16**) further increased the fluorine relaxation rates (Hu et al., 2011). Subsequent work by de Vries et al. compared assemblies comprising DOTA-based Gd^{III} complexes to those containing Gd^{III} DTPA analogs (de Vries et al., 2014). Interestingly, Gd-DTPA-BSA (6,9-bis(carboxymethyl)-3-(2-(octadecylamino)-2-oxoethyl)-11-oxo-3,6,9,12-tetraazatriacontanoic acid) (**17**, $R_1 = 1.45 \text{ s}^{-1}$) had a greater impact on the relaxation rates of the fluorines than Gd-DOTA-DSPE (2,2',2''-(10-(2-((2-(((R)-2,3-bis(palmitoyloxy)propoxy)(hydroxy)phosphoryl)oxy)ethyl)amino)-2-oxoethyl)-1,4,7,10-tetraazacyclododecane-1,4,7-triyl) triacetic acid) (**18**, $R_1 = 1.05 \text{ s}^{-1}$) and Gd-DOTA-C6-DSPE (2,2',2''-(10-(2-((6-((2-((2-(((R)-2,3-bis(palmitoyloxy)propoxy)(hydroxy)phosphoryl)oxy)ethyl)amino)-6-oxohexyl)amino)-2-oxoethyl)-1,4,7,10-tetraazacyclododecane-1,4,7-triyl) triacetic acid) (**19**, Figure 2). This difference was attributed to a shorter $^{19}\text{F}-\text{Gd}$ distance in the emulsions containing the Gd-DTPA complex. As predicted from the Bloch-Wangness-Redfield theory, Gd^{III} has a limited effect on R_1 of nearby fluorines above 6 T. This highlights the limitations of paramagnetic complexes at high field (Neubauer et al., 2008; Hu et al., 2011; de Vries et al., 2014).

These previous examples positioned the paramagnetic metal ions on the surface of the nanoparticles and, thus, a significant distance away from the ^{19}F nuclei. To resolve this issue Kislyukhin et al. designed nanoparticles that incorporated the paramagnetic metal ions directly into the fluorous core, thereby decreasing the $^{19}\text{F}-\text{M}$ distance (Kislyukhin et al., 2016). Despite the electronegativity of the fluorine atoms that reduce the basicity

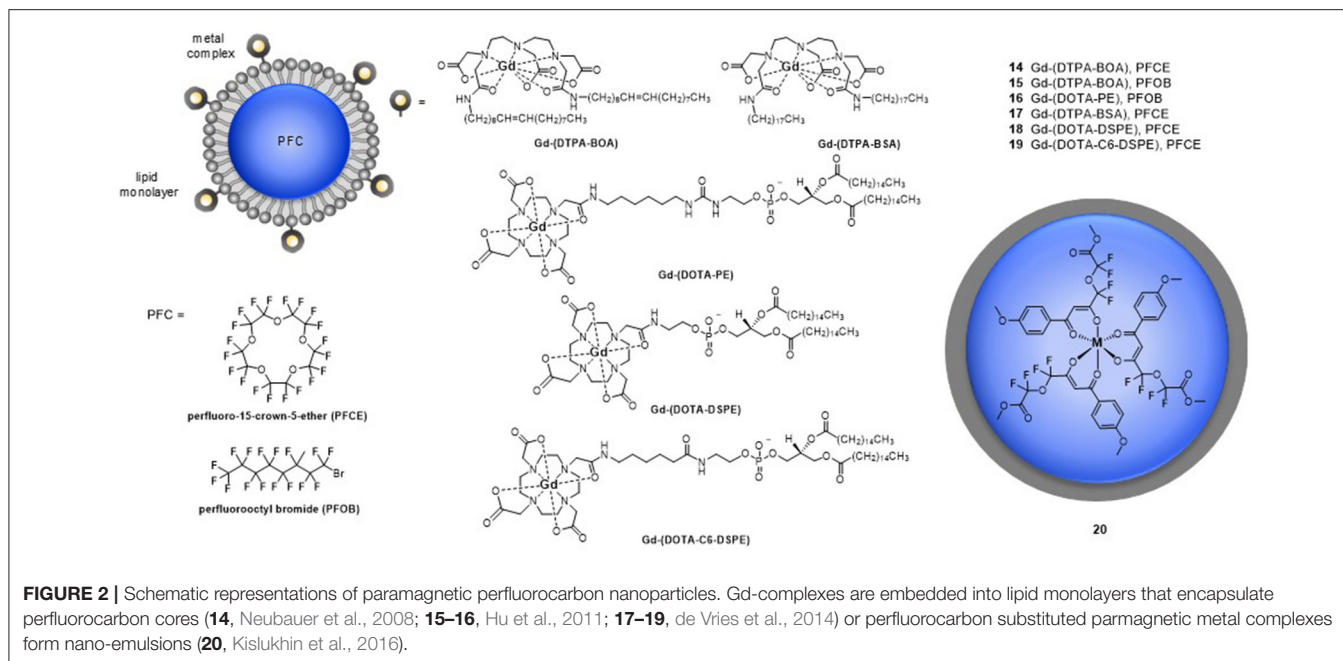


FIGURE 2 | Schematic representations of paramagnetic perfluorocarbon nanoparticles. Gd-complexes are embedded into lipid monolayers that encapsulate perfluorocarbon cores (**14**, Neubauer et al., 2008; **15–16**, Hu et al., 2011; **17–19**, de Vries et al., 2014) or perfluorocarbon substituted paramagnetic metal complexes form nano-emulsions (**20**, Kislyukhin et al., 2016).

of the ligand, fluorinated β -diketone ligands form neutral, hydrophobic complexes that are sufficiently stable and dispersible in the perfluorocarbon core (**20**, Figure 2). Three different paramagnetic metal ions were evaluated: Fe^{III} , Mn^{II} , and Gd^{III} . Of these, Fe^{III} had the greater impact on the R_1 of the ^{19}F nuclei, increasing it 13-fold, and the sensitivity of the nanoparticles, increasing it 5-fold. In comparison, Mn^{II} and Gd^{III} increased R_1 7- and 5-fold, respectively. Both Mn^{II} and Gd^{III} induced severe line broadening which decreased the sensitivity of the assembly. Advantageously, these nanoparticles are readily taken up by glioma cells. Since the nanoparticles also have low cytotoxicity (they reduce the viability of glioma cells by only 20%), they can be used to track cells *in vivo* 24 h post injection in mice. Do note, though, that it is not possible to distinguish between live and dead cells labeled with fluorine probes 24 h post injection, especially if the cells are engrafted subcutaneously.

Dependence on the Magnetic Field Strength

As the Bloch-Wangsness-Redfield theory indicates, both the R_1 and R_2 of fluorine nuclei depend on the strength of the magnetic field (Figures 3A,B, respectively). The magnetic field dependencies of R_1 and R_2 are also a function of the μ_{eff} of the metal ion and as such, different metal ions are better suited for either low field or high field experiments. A steeper increase in R_1 with respect to magnetic field strength is observed for Dy^{III} and Ho^{III} complexes of para-hydroxyl derivative of **4** than for its Tm^{III} and Tb^{III} , and Er^{III} complexes (Chalmers et al., 2010; Harvey et al., 2012b). For this ligand scaffold, the stronger relaxing ions such as Ho^{III} are thus more appropriate for experiments performed at lower magnetic field strengths, whereas the weaker Tm^{III} and Er^{III} provide adequate relaxation enhancement above 7 T (Chalmers et al., 2010; Harvey et al., 2012b).

The higher relaxation rates of fluorine nuclei of paramagnetic complexes allow for the collection of more data per unit time. Consequently, PRE increases both the spectral sensitivity and the SNR of paramagnetic fluorine agents compared to their diamagnetic analogs. Chalmers et al. demonstrated that the Dy^{III} of fluorinated DOPA complex (**7**) increased the image SNR \sim 13-fold compared to the diamagnetic Y^{III} analog (Chalmers et al., 2011a,b). The improved SNR correlates with a T_2/T_1 ratio closer to 1. With such a ratio, the benefit of increased R_1 is not diminished by the increased signal broadening due to rapid transverse relaxation. Similar conclusions were drawn with complexes of DOTAm-F12 (Srivastava et al., 2017b). In theory, sensitivity gains of 15–20 times that of diamagnetic analogs can be achieved with fluorinated lanthanide complexes between 1.5 and 9.4 T, the magnetic fields of clinical relevance (Harvey et al., 2012b). The use of paramagnetic metal ions is thus the most effective strategy to increase the sensitivity of probes for ^{19}F MRS/MRI, enabling imaging of sub-millimolar concentrations of probe in <15 min with adequate SNR (>4) (Chalmers et al., 2011a,b).

The Effect of the Rotational Correlation Time, τ_R

Both the R_1 and R_2 of fluorine nuclei are affected by their rotational correlation time (τ_R) as well as by the field strength of the instrument (B_0) and the temperature of the sample. Both R_1 and R_2 increase as the magnetic field strength (B_0) increases. This increase is far more significant if the rotational correlation time, τ_R , is also optimized. Macromolecules, which tumble more slowly (longer τ_R), have higher R_2 . As can be seen in Figure 3B, R_2 increases drastically for ^{19}F nuclei with $\tau_R > 1,000$ ps, especially at high magnetic field (>7 T). The resulting extreme line broadening explains why fluorines embedded in bones and teeth in the body are not visible by MRI. The effect

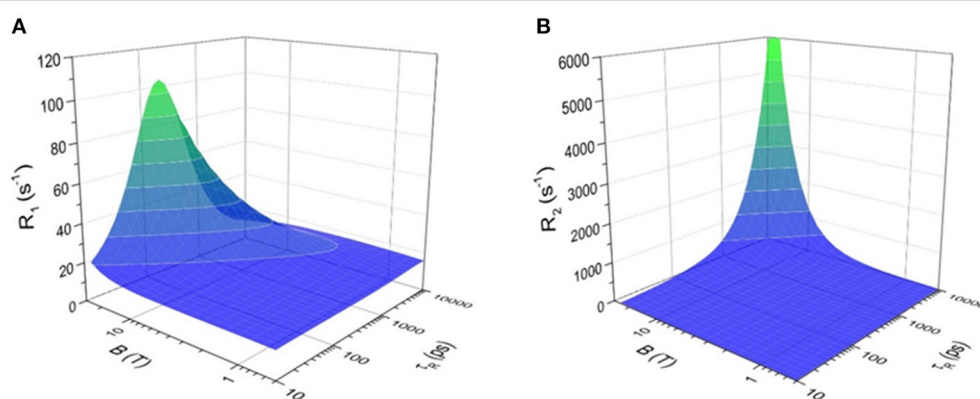


FIGURE 3 | Effect of applied magnetic field, B , and the rotational correlation time, τ_R on (A) longitudinal relaxation rate (R_1) and (B) transverse relaxation rate (R_2) of ^{19}F nuclei in $[\text{Tm-DOTAm-F12}]^{3+}$. The analysis is based on Equation (1) for R_1 or (2) for R_2 and is done at 37°C using the mean $^{19}\text{F}-\text{Tm}^{\text{III}}$ distance determined from X-ray crystallography (6.26 Å), assuming a magnetic moment, μ_{eff} , of 7.6 BM and an electronic relaxation time, τ_e , of 0.20 ps, values typical of Tm^{III} complexes.

of τ_R on R_1 is more complicated (Figure 3A). R_1 increases to a maximum when the tumbling rate of the M- ^{19}F vector (τ_R^{-1}) equals the Larmor frequency of the ^{19}F nuclei; i.e., when $\omega_F^2 \tau_R^2 = 1$ (Modo and Bulte, 2007). Monomolecular lanthanide complexes, such as those discussed in this review, have rotational correlation times on the order of 200–350 ps (Chalmers et al., 2010; Harvey et al., 2012b). Unlike for R_2 , there is an optimal τ_R beyond which R_1 decreases sharply especially at high magnetic field. The optimal τ_R is a function of the μ_{eff} of the paramagnetic metal ion. For Tm, an optimal τ_R of 200 ps increases R_1 substantially, particularly at high magnetic field. Unlike for Gd^{III} -based T_1 contrast agents (Caravan et al., 1999), there is not much advantage to macromolecular paramagnetic fluorine probes with longer τ_R .

There are limited examples in the literature of macromolecular fluorinated probes that feature a paramagnetic center. They are mostly used to increase the number of ^{19}F nuclei per unit. For example, the polymeric Dy^{III} -chitosan conjugate, 21 (Figure 4), increases the relaxation rates of the fluorines via the PRE effect (De Luca et al., 2014). As for the small molecules described earlier in this section, the aryl trifluoro groups are advantageously positioned close, but not too close (6.5 Å) from the lanthanide ion. This macromolecular complex features 10 trifluoro groups of equivalent ^{19}F nuclei appended to glycol chitosan, a linear polysaccharide selected for its biocompatibility. The increase in τ_R from 83 ps to 8 ns due to polymerization of the chitosan was evaluated with Gd^{III} -complexes similarly conjugated to the chitosan monomer (22) and polymer (23) (De Luca et al., 2014). In this case, the R_1 of the fluorine nuclei of the Dy chitosan conjugate 21 remained constant before and after polymerization (186 s $^{-1}$ at 9.4 T), whereas the R_2 decreased from 440 to 367 s $^{-1}$, which is unusual for a polymer (De Luca et al., 2014). Of note, this polymer is a rare example of a metallic fluorine probe that was successfully used *in vivo* to image tumors in mice. Although a dose of 0.54 g/kg was used in this study—a dose higher than typically used with Gd-based contrast agents—the sensitivity of the probe remained poor and a very long imaging time of 7 h was required to have sufficient SNR

(De Luca et al., 2014). Although this probe was more sensitive than small molecule fluorine probes, the very long imaging time remains a significant hurdle to the application of ^{19}F probes.

One should note that although macromolecular paramagnetic fluorine probes are rare, their diamagnetic analogs are more common. Several macromolecular structures based on hyperbranched polymers, dendrimers, or nanoparticles that incorporate a high number of ^{19}F nuclei have been described (Du et al., 2008; Criscione et al., 2009; Jiang et al., 2009; Peng et al., 2009; Ogawa et al., 2010a,b; Thurecht et al., 2010), and recently reviewed (Yu, 2013; Zhu et al., 2013). A macromolecular architecture is more advantageous for diamagnetic fluorine probes than for paramagnetic ones: the increase in τ_R decreases T_1 , and, if designed correctly, can increase the solubility of the probe in water as well as its *in vivo* retention time.

EXPLOITING THE METAL ION TO DESIGN RESPONSIVE FLUORINE PROBES

Applications of the Bloch-Wangsness-Redfield Theory to the Design of Responsive Fluorine Probes

Advantageously, a paramagnetic metal ion that alters T_1 and T_2 of the fluorine nuclei can also modulate their chemical shift ($^{19}\text{F}\Delta\delta$). Since variations in each of these three variables can readily be observed both by MRS and by MRI, paramagnetic fluorine complexes offer unique mechanisms for the development of responsive MR probes that often yield much greater response than their purely organic analogs (Yu et al., 2013a). Two different effects of paramagnetic metals can be exploited to design responsive molecular probes. The first is the PRE effect. It is governed by the Bloch-Wangsness-Redfield theory, affects both relaxation times (T_1 and T_2) and is a function primarily of the nature of the paramagnetic metal ion and the distance d separating it from the fluorine nuclei. The second is the lanthanide induced shift (LIS) effect. It is just as readily be observed with ^{19}F than with ^1H nuclei and

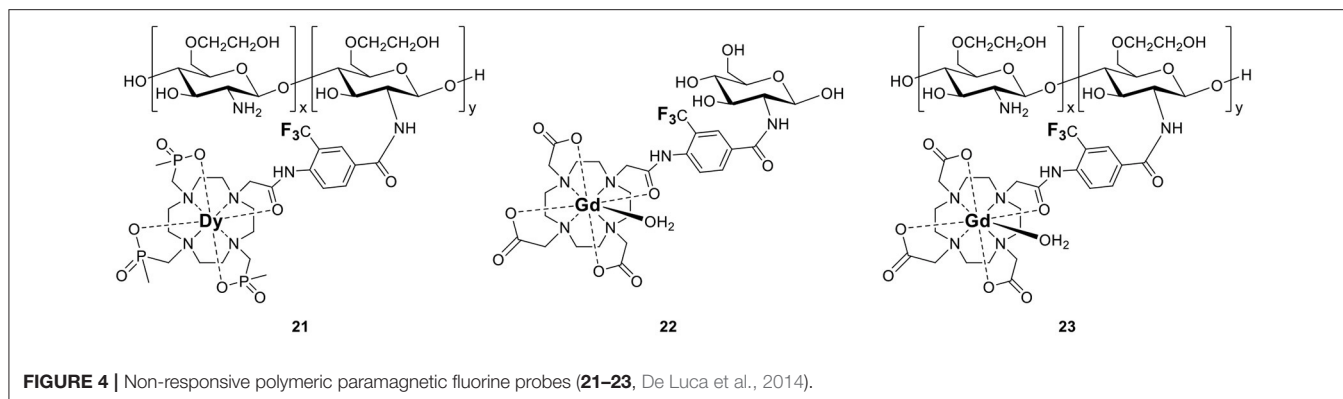


FIGURE 4 | Non-responsive polymeric paramagnetic fluorine probes (21–23, De Luca et al., 2014).

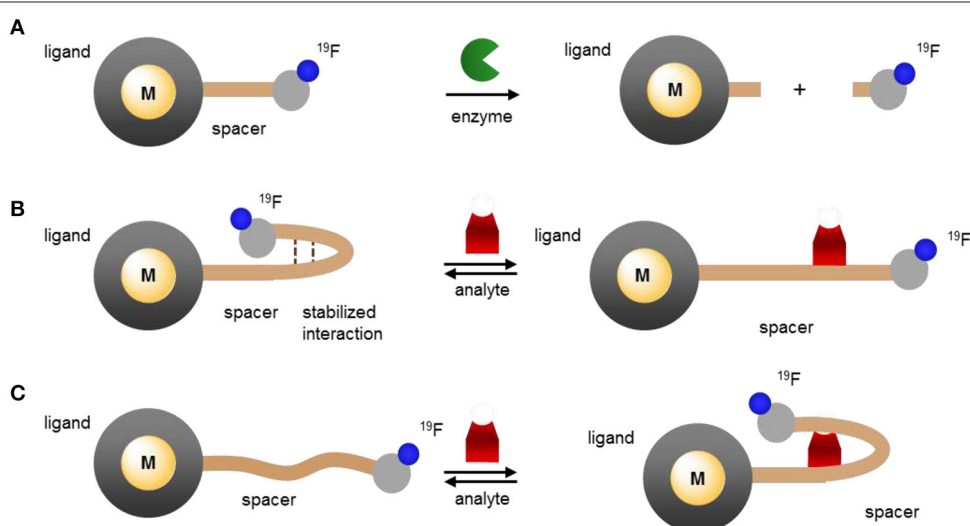


FIGURE 5 | Modulating the response of ^{19}F -paramagnetic metal probes by altering the distance separating the lanthanide ion from the ^{19}F nuclei: **(A)** cleavage of the ^{19}F -M distance spacer by the analyte and release of the fluorinated moiety; **(B,C)** analyte-triggered conformational change of the probe upon binding or reacting with the spacer.

is governed by the McConnell-Robertson theory. Unlike PRE, LIS is affected not only by the nature of the paramagnetic lanthanide ion and the distance d separating it from the fluorine nuclei, but also by the second order crystal field coefficient of the complex, B_2^0 , and the angle θ between the metal-fluorine vector and the principle magnetic dipolar axis of the lanthanide. Coupling either of these effects with the extensive range of chemical shifts available to ^{19}F offers valuable opportunity to design ratiometric responsive MR probes that can distinguish between changes in signal intensity due to the presence of an analyte vs. that due to a change in the concentration of the probe.

The PRE effect described in the previous section of this review is the basis for the improved sensitivity on a per ^{19}F basis of paramagnetic probes as compared to their organic counterparts. It is the substantial shorter T_1 and higher T_2/T_1 ratio of paramagnetic fluorinated complexes that enables more scans to be acquired in the same amount of time thereby yielding

higher SNR both by ^{19}F MRS and MRI. Analysis of the Bloch-Wangsness-Redfield Equations (1–5) indicate that at constant applied magnetic field (the same scanner) and for the same metal ion, T_1 and T_2 are a function of primarily one parameter: the distance d separating the ^{19}F nuclei from the metal ion. This parameter can be altered significantly by binding to or reacting with a substrate. Herein lies a substantial advantage of paramagnetic metal ions in fluorine probes: they readily enable the design of responsive and ratiometric molecular probes.

The dependence of T_1 and T_2 on the distance separating the fluorine nuclei from the lanthanide ion has already been applied to the design of responsive paramagnetic fluorine probes. As depicted in Figure 5, this distance can be altered either by reacting with a target or by induced conformational change upon binding to the desired analyte. The former approach yields an irreversible response, although one that can enable the detection of targets such as enzymes that are present at lower concentrations. The latter approach can lead to a reversible

response but given the enduring limits in the sensitivity of fluorine probes, it is more appropriate for biological analytes present at substantially higher concentrations such as pH or certain small molecules or metal ions.

Current examples of this class of responsive probes use for the most part Gd^{III}. As described in the previous section, Gd^{III} has a notable effect on the T_1 of nearby nuclei, and, importantly, a substantially more pronounced one on T_2 . Indeed, among the lanthanides, Gd^{III} typically offers the lowest T_2/T_1 ratio (**Table 2**). As a result of this very low ratio, the peaks of ¹⁹F nuclei near Gd^{III} ions broaden to the point of no longer being observable neither by MRS nor by MRI. Increasing the distance between the ¹⁹F nuclei and the Gd^{III} increases T_2 ; this enables the ¹⁹F signal to reappear.

A greater effect will be observed if the linker separating the ¹⁹F nuclei from the Gd^{III} ion is completely cleaved by the target (**Figure 5A**). As the fluorinated moiety diffuses away from the Gd^{III} complex, its relaxation times increase by orders of magnitude and, consequently, so does the ¹⁹F signal intensity. This approach is particularly well-suited for the detection of enzymes that cleave peptides or sugars. Indeed, the first example reported by Kikuchi and coworkers targeted caspase 3 (**24**, **Figure 6**). Adroit positioning of the ¹⁹F nuclei on the amino acid substrate of the enzyme that was directly tethered to the Gd^{III} complex resulted in a complete off/on response (Mizukami et al., 2008). This first probe, and its dual ¹⁹F MRI/fluorescence analog (**25**, **Figure 6**) (Mizukami et al., 2009), exemplified a distinct advantage of ¹⁹F molecular probes over both Gd^{III}- and nanoparticle-based responsive contrast agents: a substantial response with zero background such that presence of a signal can only result from co-localization of both the MR probe and the enzyme target. In comparison, ¹H MRI contrast agents have to contend with the intrinsic high ¹H background signal due to the high concentration of water of the biological milieu. With these agents, an increase in signal intensity does not necessarily correlate with the presence of the target; an identical response can simply result from higher local concentration of the contrast agent. Do note, however, that since such agents are not ratiometric they do not eliminate the possibility of false negative. That is, they cannot distinguish between a lack of signal due to a lack of enzyme as opposed to a lack of ¹⁹F probe.

This approach was recently extended by both the Kikuchi and the Engelmann groups to other enzymes, β -galactosidase (**26** and **27**) (Keliris et al., 2011, 2012; Mizukami et al., 2011), β -lactamase (**28**) (Matsushita et al., 2012), and matrix metalloprotease-2 (**29**, **Figure 6**; Yue et al., 2014, 2017) thereby opening the possibility of directly imaging gene expression by MRI. In each case, hydrolysis of the enzyme's substrate generates a self-immolative linker that releases the fluorinated moiety from the Gd^{III} probe thereby turning on the ¹⁹F MR signal. This approach is not limited to enzymes and cleavable linkers. Similar responses can be obtained with an analyte-induced conformational changes that either increase (turn on) or decrease (turn off) the ¹⁹F-Gd distance (**Figure 5B,C**, respectively). Fujimoto and coworkers used this approach to the PRE effect to extend the traditional molecular beacon motif commonly used to detect DNA (or RNA) by luminescence to that by ¹⁹F NMR (**30**, **Figure 6**

(Sakamoto et al., 2011). Hybridization with the target nucleotide sequence causes the stem loop of the probe to unfold, thereby increasing d and thus also the T_2 and signal intensity of the ¹⁹F nuclei.

Similar responses can be obtained with paramagnetic transition metals. Yu and Mason reported three fluorinated probes for β -galactosidase that use the same principle but in the opposite direction (**31–33**, **Figure 7**) (Yu et al., 2012, 2013b). Hydrolysis of the sugar moiety by β -galactosidase releases a fluorinated Fe^{III} chelator. The T_2 of this ligand decreases substantially upon subsequent coordination to the transition metal. As opposed to Kikuchi's and Engelman's examples, in this case the ¹⁹F signal of the probe is turned off by the enzyme. The practicality of such probes for *in vivo* imaging, however, is likely limited given that iron is tightly regulated in the body and is essentially unavailable (Raymond et al., 2003).

The same approach readily leads to the development of fluorine probes for paramagnetic metal ions. An example for Mn^{II} is **34** developed by Datta and coworkers (**Figure 7B**) (Sarkar et al., 2017). Coordination of Mn^{II} results in a 101-fold decrease of T_2 and, therefore, significant line broadening which decreases the signal intensity of the ¹⁹F nuclei.

By extension, this strategy can readily be adjusted to design probes that signal the redox potential of their surroundings. If the metal is chosen correctly, a change in its oxidation state enables it to switch between a diamagnetic and a paramagnetic state (**Figure 8**). In the paramagnetic state, the metal attenuates the ¹⁹F signal by substantially decreasing their T_2 . Conversion to the diamagnetic state lengthens T_2 resulting in a "turn on" response. Early examples that utilize metal redox state to modulate the relaxation of ¹⁹F nuclei, and in turn signal intensity, were reported by Chujo's lab (Tanaka et al., 2009; Kitamura et al., 2012). Their probes, Fc-POSS (**35**) and Cu-POSS (**36**) contain either a redox sensitive ferrocene or a Cu complex with a bis(2-pyridylmethyl)amino ligand (PMEA) along with trifluoromethyl groups appended to a cubic polyhedral oligomeric silsesquioxane (POSS) for water solubility (**Figure 9A**). The oxidation of Fe^{II} in **35** reduces the ¹⁹F signal intensity 3-fold due to the shortened relaxation time. The nitroxyl (HNO) mediated reduction of paramagnetic Cu^{II} in **36** to diamagnetic Cu^I modestly increased T_1 (from 1180 ms to 1460 ms) and T_2 (from 420 to 540 ms) causing a 3-fold increase in signal intensity. Thus, their work demonstrates the ability to apply PRE to the design of ¹⁹F redox sensitive responsive probes. Que's laboratory utilized this strategy and the PRE of Cu^{II} to detect cellular hypoxia by ¹⁹F MR (Xie et al., 2016). Reduction of CuATSM-F₃ (**37**, **Figure 9A**) from Cu^{II} (d⁹, paramagnetic) to Cu^I (d¹⁰, diamagnetic) and subsequent ligand dissociation increases T_2 of the ¹⁹F and restores their signal intensity. A second generation version of this probe (**38**) was designed to be more sensitive (Xie et al., 2017). It includes a higher density of ¹⁹F nuclei, a polyethylene glycol linker that increases the hydrophilicity of the probe and positions the ¹⁹F nuclei at an optimal distance from the copper ion. With a ¹⁹F-Cu distance of ~18 Å, the ¹⁹F signal is attenuated but remains visible by NMR when the probe is in the Cu^{II} state. Reduction to Cu^I generates a sharp signal which is 6-fold more intense, leading to a 4.5-fold increase in SNR in the ¹⁹F MRI images obtained at 7 T.

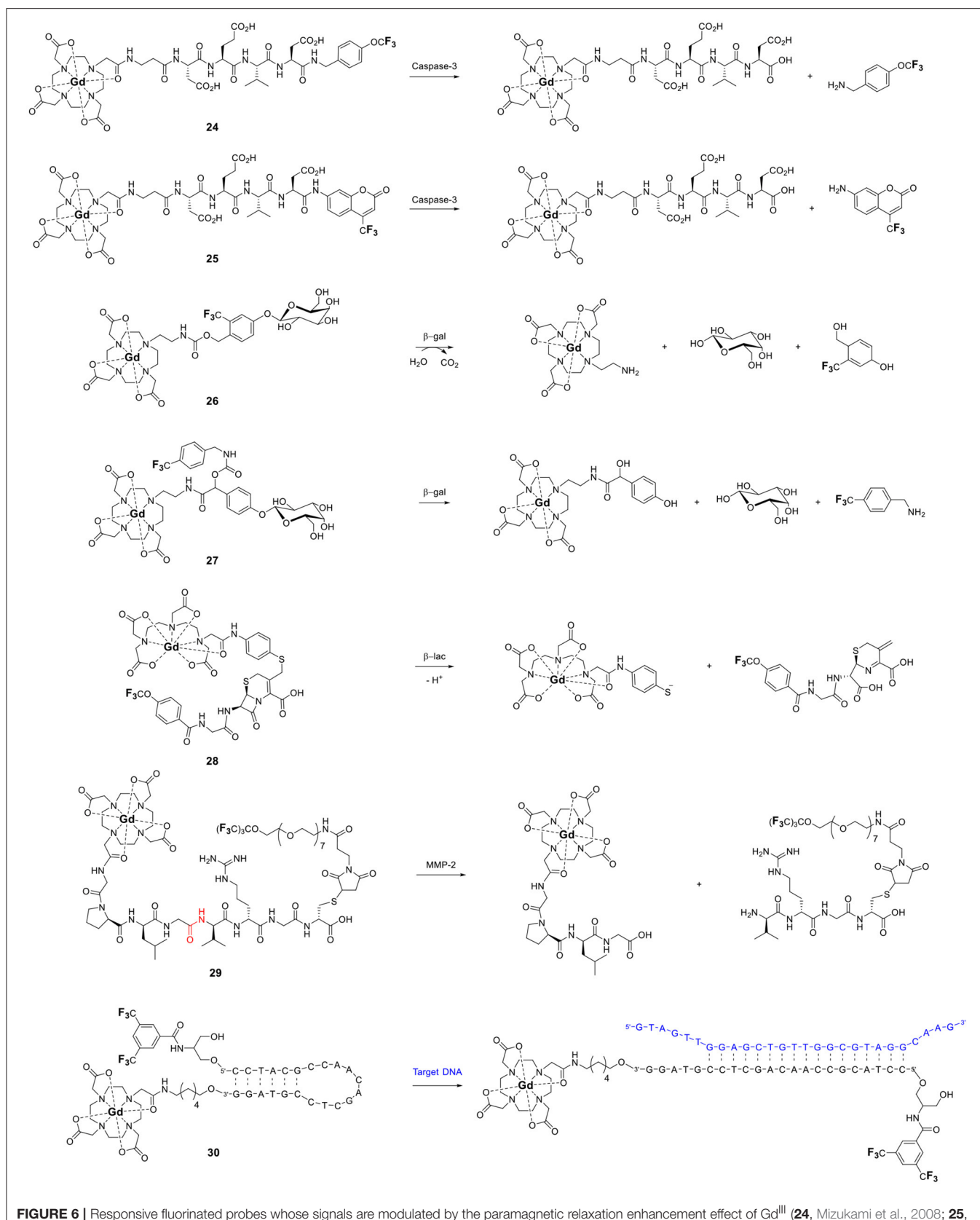
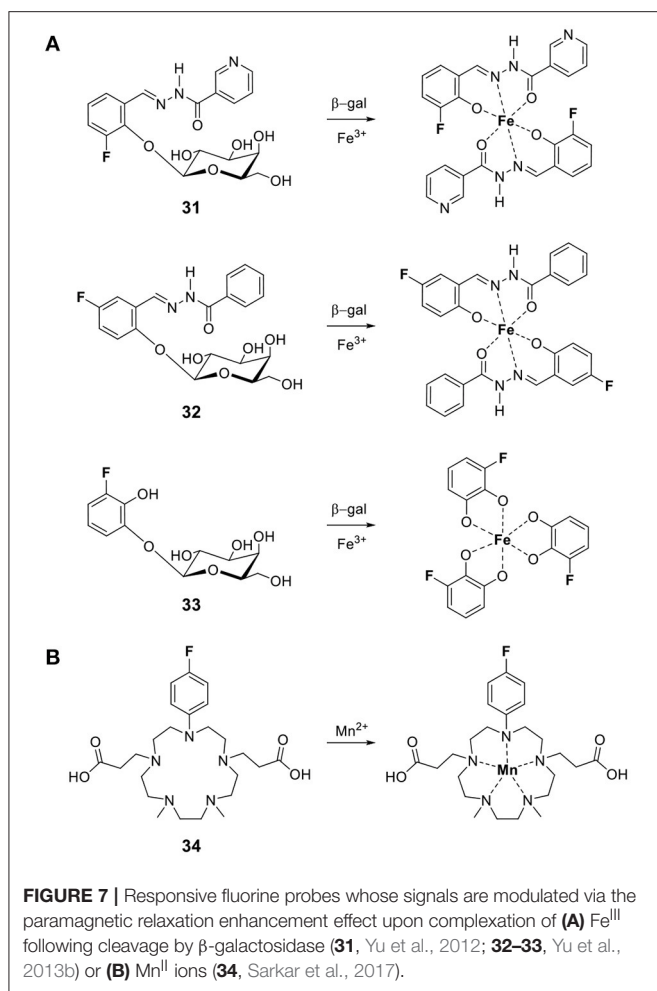


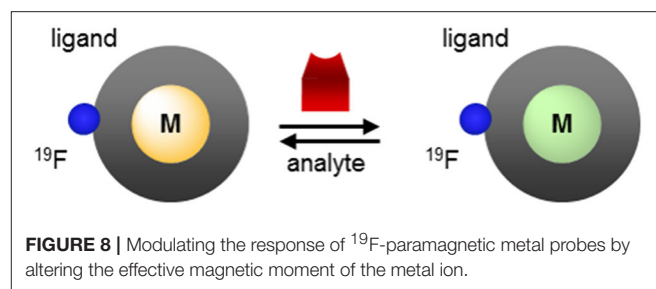
FIGURE 6 | Responsive fluorinated probes whose signals are modulated by the paramagnetic relaxation enhancement effect of Gd^{III} (**24**, Mizukami et al., 2008; **25**, Mizukami et al., 2009; **26**, Mizukami et al., 2011; **27**, Keliris et al., 2012; **28**, Matsushita et al., 2012; **29**, Yue et al., 2014, 2017; **30**, Sakamoto et al., 2011).



The large differences in relaxation times between the two species allow them to be independently imaged using short ($\text{TE} = 10 \text{ ms}$ for Cu^{II}) or long ($\text{TE} = 100 \text{ ms}$ for Cu^{I}) echo pulse sequences (Xie et al., 2017).

Allen's laboratory used an analogous approach with Eu in the design of their temperature and redox responsive ^{19}F probe (39, Figure 9A). This Eu-DOTAm (1,4,7,10-tetrakis(carbamoylmethyl)-1,4,7,10-tetraazacyclododecane) complex with a *p*-trifluoromethylphenyl arm, has 12 equivalent fluorine nuclei (Basal et al., 2017). In its +2 oxidation state, Eu significantly shortens the T_2 of the ^{19}F and hence quenches their signal. In its +3 oxidation state, Eu^{III} has a much lower μ_{eff} (3.40–3.51 B.M.) than Eu^{II} (7.6–8.0 B.M.; Tilley et al., 1980; Garcia and Allen, 2012) (Table 1) and thus a limited effect on the relaxation times of the fluorine which consequently reappear. In ^{19}F MRI images, oxidation of Eu^{II} to Eu^{III} results in a 6-fold increase in SNR. This responsive probe was successfully used to image non-hypoxic regions *in vivo* by ^{19}F MRI.

This approach also enables direct detection of reactive oxygen species. Oxidation of Co-NODA-CF₃ (2,2'-(7-(2-oxo-2-((2,2,2-trifluoroethyl)amino)ethyl)-1,4,7-triazonane-1,4-diyl)diamino acid) (40, Figure 9A) with H₂O₂ from paramagnetic Co^{II} (d⁷)



to diamagnetic Co^{III} (d⁶) shifts the ^{19}F signal by 3.6 ppm and increases the T_1 and T_2 of the ^{19}F nuclei 60- and 121-fold, respectively (Yu et al., 2016). This, in turn, results in a 23-fold increase in signal intensity in spin-density weighted ^{19}F MR images. Although the oxidation of the probe is reversible, the long (2 h) reaction time and the low sensitivity of the probe compared to *in vivo* levels of H₂O₂ still limit the application of this probe to *in vivo* imaging.

There are two main disadvantages to using paramagnetic metals that primarily affect T_2 in the design of responsive fluorine probes. The first, as mentioned above, is that such probes are not ratiometric. A lack of signal can be attributed both to a lack of target and to a lack of probe. Similarly, signal intensity is not a direct measure of the concentration of the target as it is equally affected by the concentration of the probe. The second disadvantage is that upon release, the organic fluorine moiety regains its very long T_1 . Such probes are thus plagued by the same sensitivity issue as the purely organic fluorinated probes (Yu et al., 2005, 2013a). Their T_1 of 0.4–5 s are 10- to 500-fold longer than their paramagnetic counterparts, which greatly limits the number of scans that can be acquired per amount of time. The low sensitivity of such probes practically restricts the markers that they could measure *in vivo*. In theory, both of these problems can be resolved with the use of a paramagnetic ion that has a more limited effect on T_2 and maintain as high a T_2/T_1 ratio as possible. Fe^{II}, Tm^{III}, and Ho^{III} are particularly well-suited for this approach (Srivastava et al., 2017b), but examples are not represented in the literature.

Applications of the McConnell-Robertson Theory to the Design of Responsive Fluorine Probes

One of the first applications of lanthanides in NMR spectroscopy was as induced shift reagents (Sanders et al., 1972). This application has surprisingly rarely been applied to ^{19}F NMR spectroscopy. Yet the same theory and equations developed for ^1H apply to ^{19}F and as such they can readily be exploited for the rational design of paramagnetic ^{19}F shift reagents. Lanthanide induced shift (LIS) is traditionally defined as the difference in chemical shift, $\Delta\delta$, between a paramagnetic complex and its diamagnetic analog ($\Delta\delta = \delta_{\text{para}} - \delta_{\text{dia}}$). In terms of responsive paramagnetic fluorine probes, the induced shift, $^{19}\text{FLIS}$, is defined as the difference between the chemical shift of a ^{19}F nuclei in the presence and absence of the probe's analyte

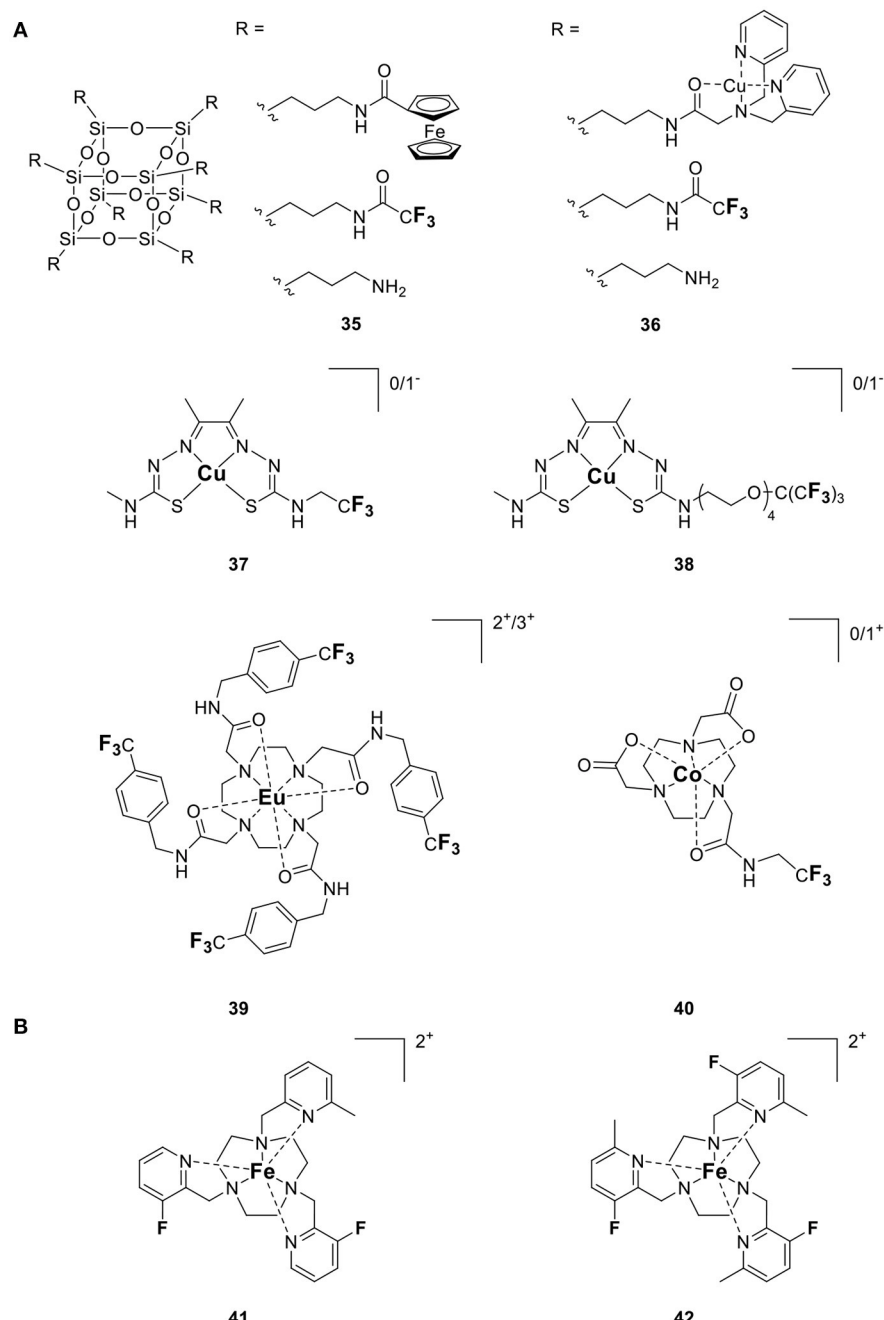


FIGURE 9 | Responsive fluorine probes which function by altering either **(A)** the oxidation state of a redox active metal (**35**, Tanaka et al., 2009; **36**, Kitamura et al., 2012; **37**, Xie et al., 2016; **38**, Xie et al., 2017; **39**, Basal et al., 2017; **40**, Yu et al., 2016) or **(B)** the spin state of Fe^{II} (**41–42**, Thorarinsdottir et al., 2017).

(Equation 6).

$$^{19}\text{F LIS} = ^{19}\text{F} \Delta \delta = \delta_{\text{probe + analyte}} - \delta_{\text{probe}} \quad (6)$$

This shift is the sum of the contributions from the contact shift, δ^c , and the pseudocontact shift, δ^{pc} (Peters et al., 1996; Allegrozzi et al., 2000; Harvey et al., 2012b). If the fluorine nuclei is kept 5 Å or more from the paramagnetic metal center, the contribution

from the contact shift is negligible, and the observed $^{19}\text{F LIS}$ is primarily due to the pseudocontact shift. This pseudocontact shift, δ^{pc} , is the result of the dipolar interaction between the ^{19}F nuclei and the unpaired electrons on the metal ion that experiences a Curie magnetization in the applied magnetic field. Thus, an anisotropic metal ion can amplify the chemical shift inequivalence between a fluorine nucleus in the presence and absence of the probe's analyte, resulting in greater resonance

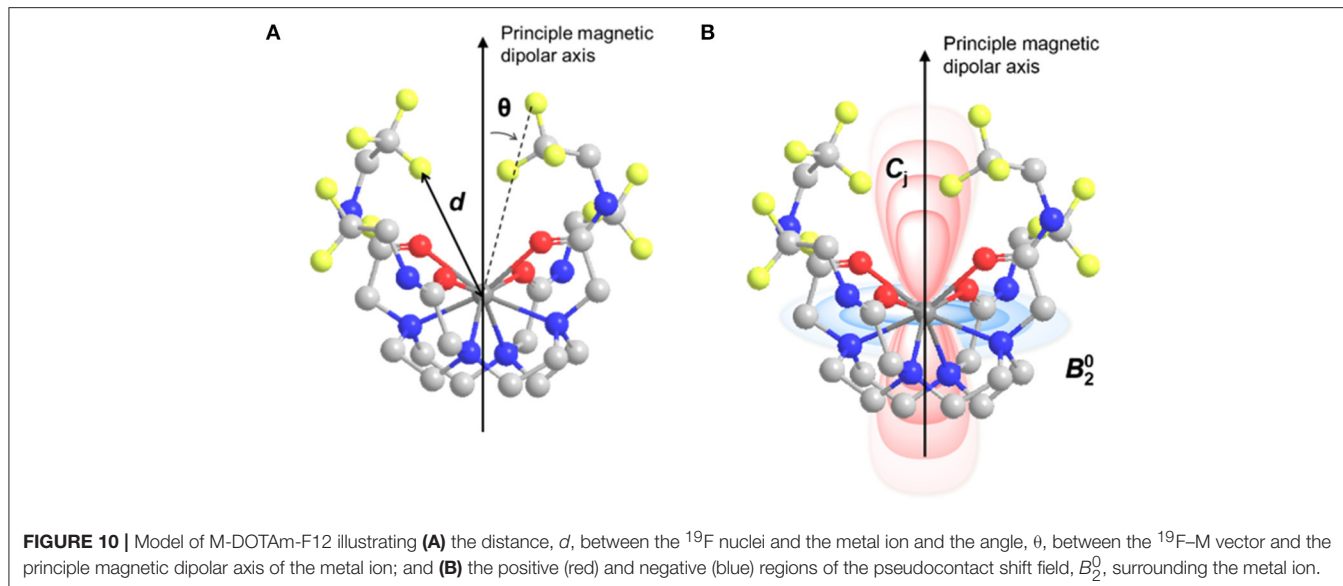


FIGURE 10 | Model of M-DOTAm-F12 illustrating **(A)** the distance, d , between the ^{19}F nuclei and the metal ion and the angle, θ , between the ^{19}F -M vector and the principle magnetic dipolar axis of the metal ion; and **(B)** the positive (red) and negative (blue) regions of the pseudocontact shift field, B_2^0 , surrounding the metal ion.

shift that are ultimately necessary for each nuclei to be imaged independently by MRI. Under the condition that the ^{19}F nuclei is at least 5 Å away from the metal ion, the pseudocontact shift is a function of the nature of the metal, its coordination environment, and the metal ion (**Figure 10**). This relationship is defined by the McConnell-Robertson equation (Equation 7) (Harvey et al., 2012b)

$$^{19}\text{FLIS} = \delta^{pc} = C_j \frac{\beta^2}{60(kT)^2} \frac{(3 \cos^2\theta - 1)}{d^3} B_2^0 \quad (7)$$

Where d is the ^{19}F -metal distance, θ is the angle between the principal magnetic dipolar axis of the metal ion and ^{19}F nuclei, B_2^0 is the second order crystal field coefficient that is dependent on the coordination environment of the metal ion, and C_j is the Bleaney coefficient for the specific metal. Both the direction and magnitude of the shift are dependent on the identity of the metal ion as denoted by its Bleaney coefficient (**Table 1**). One can thus rank metals by relative pseudocontact shift (PCS) strength, which in turn indicates their efficacy as ^{19}F LIS agents. Dy^{III} and Tb^{III} are undeniably excellent shift agents. However, given the necessity to maintain as high a T_2/T_1 ratio as possible to maximize ^{19}F sensitivity (see above), Tm^{III} and Ho^{III} are the best choices in the design of ^{19}F LIS probes for MRI.

According to the McConnell-Robertson equation, the design of responsive fluorinated lanthanide MR probes can be based on three parameters: the distance separating the ^{19}F nuclei from the metal ion, d (**Figure 5**), the angle θ between the main dipolar magnetic axis of the metal and the metal— ^{19}F vector (**Figure 11A**), and the second order crystal field coefficient, B_2^0 , which is a function of the direct coordination environment of the metal (**Figures 11B,C**).

The second order crystal field coefficient, B_2^0 , which is a function of the direct coordination environment of the lanthanide or transition metal, has been used in the design of responsive fluorine probes. Advantageously, this approach

enables the use of ligands of similar chemical structure as those used with gadolinium-based responsive contrast agents. Swapping Gd^{III} for Tm^{III} , Ho^{III} , or Dy^{III} and adding a fluorinated moiety within 4–7 Å of the metal is often all that is necessary. For example, the Parker group developed citrate-responsive ^{19}F probes, which are essentially fluorinated versions of Ln-DO3A (**43** and **44**, **Figure 12A**) (Harvey et al., 2012a). Coordination of citrate to a Tm^{III} complex results in the displacement of the two inner-sphere water molecules; the resulting change in B_2^0 causes a $^{19}\text{FLIS}$ of 4.7 ppm. Such ^{19}F probes are unfortunately marked with the same selectivity problem as the gadolinium responsive contrast agents that function by varying the number of inner-sphere water molecules (q -based responsive contrast agents) (Pierre et al., 2018). The selectivity of **43** and **44** for citrate over other hard anions that also have good affinity for the oxophilic lanthanides, such as bicarbonate, phosphate and lactate, is rather poor. The efficacy of the probe in blood and in cells is thus likely limited.

The same approach was used to design the Ca^{II} responsive fluorine probes **45** and **46** (**Figure 12A**). These probes are derivatives of a Gd^{III} -based responsive contrast agent which displays a change in longitudinal proton relaxivity, r_1 , in the presence of calcium (Harvey et al., 2012a). For **45** and **46** to bind Ca^{II} , one of the amide arms of the macrocycle must release the lanthanide. In doing so, it is replaced by a water molecule. The resulting change in B_2^0 causes a $^{19}\text{FLIS}$ of 3.0 or 3.9 ppm depending on the lanthanide ion (Dy^{III} or Tm^{III} , respectively) (Harvey et al., 2012a). Seemingly minor modifications on the structure of the probe can thus result in a substantial difference in its response.

The Parker group used a similar approach to develop four pH responsive probes. In **47** and **48** (**Figure 12B**) (Senanayake et al., 2007; Kenwright et al., 2008), protonation of a sulfonamide group coordinating the lanthanide at pH < 5 breaks the N-Ln bond, which opens up a coordination site for a water molecule. The resulting change in B_2^0 due to the differing coordination

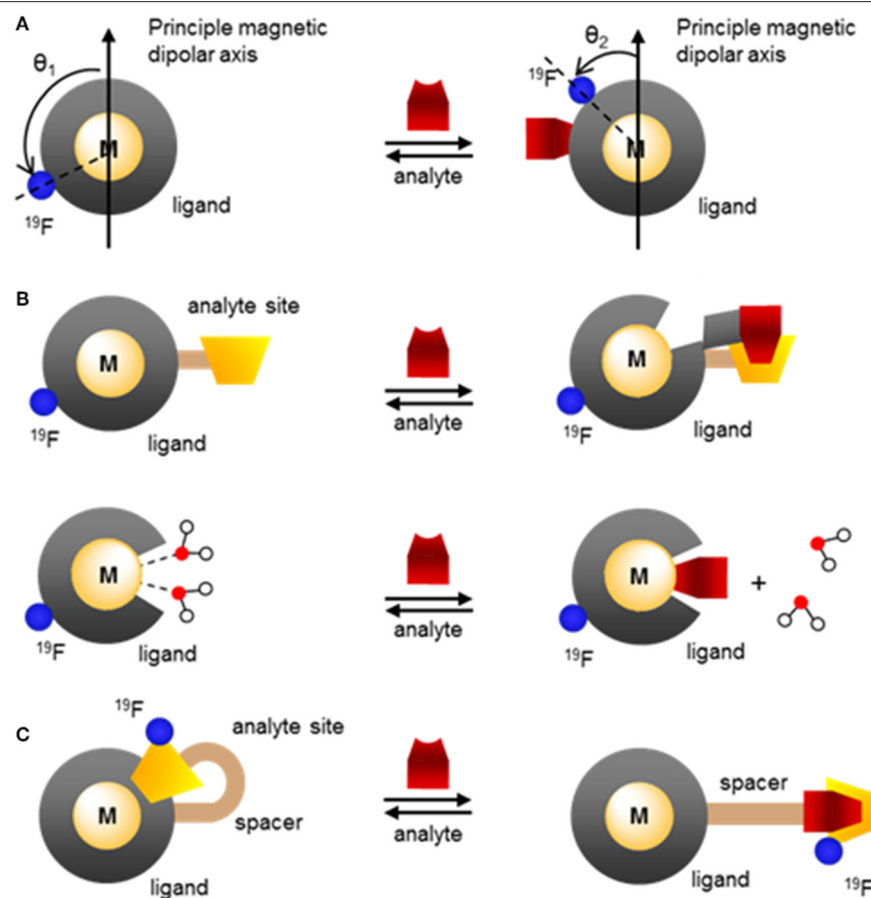


FIGURE 11 | Modulating the response of fluorinated paramagnetic probes by altering **(A)** the angle θ between the ^{19}F -M vector and the principle magnetic dipolar axis of the metal ion, **(B)** the lanthanide coordinating environment and thus the second order crystal field coefficient, B_2^0 through chelation of the analyte that partially decomplexes the metal or direct coordination of the analyte onto the lanthanide that displaces one or more water molecules, **(C)** the angle θ , B_2^0 , and the ^{19}F -M distance, d , through analyte induced changes in the coordination environment.

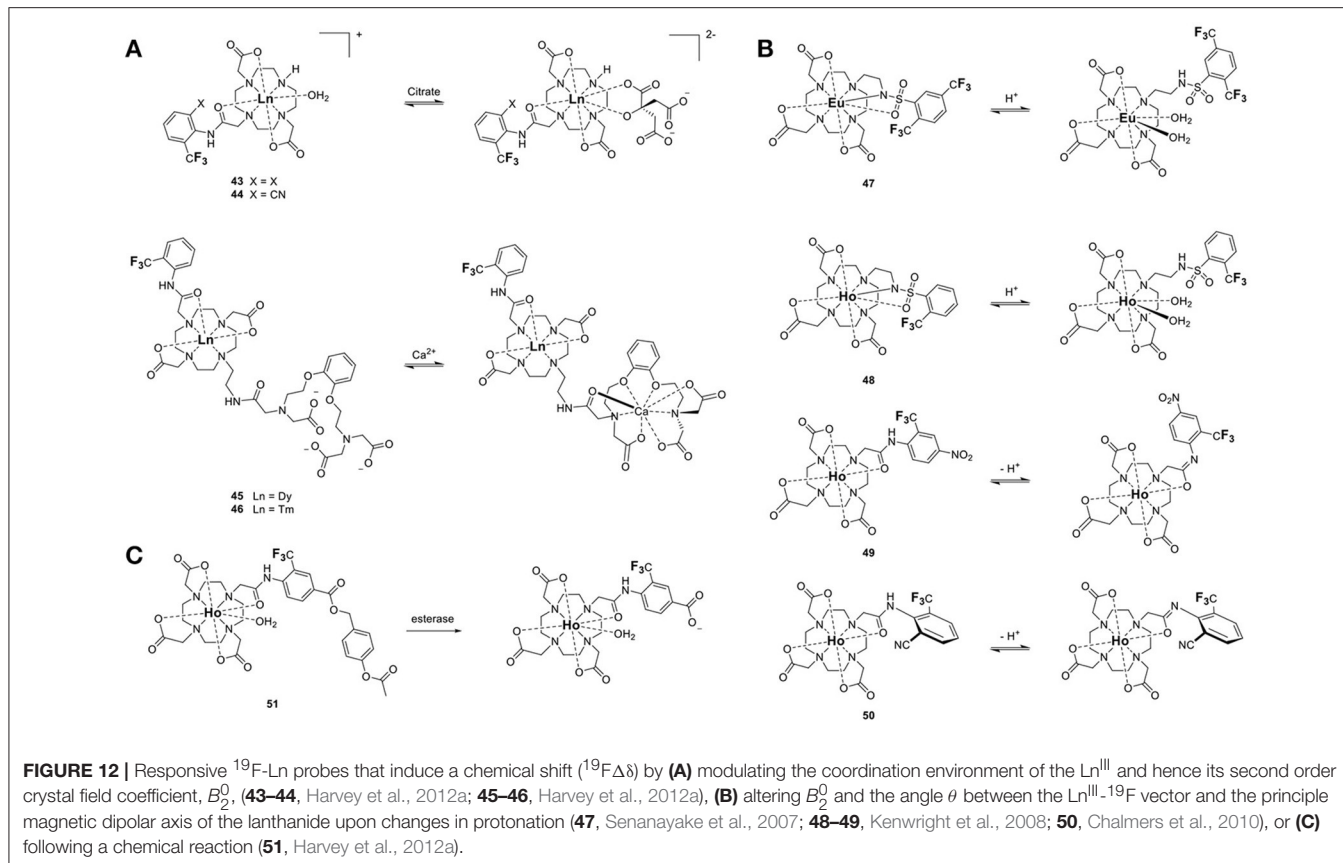
environment of the lanthanide ion, and in the angle θ due to conformational change through rotation of the arm, cause a $^{19}\text{FLIS}$ of -6 and $+2$ ppm between pH 8.5 and 4.2 for the two inequivalent ^{19}F in the Eu^{III} complex **47**. The ^{19}F resonance of the related Ho probe, **48**, shifts upfield by 40 ppm upon deprotonation (Chalmers et al., 2010). Note the greater $^{19}\text{FLIS}$ for Ho^{III} , which has a Bleany's coefficient of greater magnitude, than for Eu^{III} .

The other two pH probes, **49** and **50**, also rely on protonation of a coordinating arm, but in these cases the aryl amide does not release the lanthanide at acidic pH (Figure 12B) (Kenwright et al., 2008; Chalmers et al., 2010). Instead, deprotonation of the amide changes both B_2^0 and θ between the $\text{Ln}^{+}-^{19}\text{F}$ vector and the principal magnetic dipolar axis of the Ln^{III} ion. The latter is due to the differing conformation of the arm. The combination of these two effects result in a substantial $^{19}\text{FLIS}$ of 18 and 23 ppm for **49** and **50**, respectively.

The chemical shift of fluorine nuclei can also be modulated by altering the spin state of the metal ion. A recent example exploits the temperature induced transition of Fe^{II} from low spin ($S = 0$) to high spin ($S = 2$) in hexadentate triazacyclonone ligands with fluorinated 2-picoly substituents (41 and 42, Figure 9B) to image temperature by ^{19}F MRI (Thorarinsson et al., 2017). In these probes, the ^{19}F are positioned at an optimal distance away from the Fe^{II} center so as to maximize $^{19}\text{F}\Delta\delta$. Increasing the temperature from 4 to 60°C, causes the ^{19}F resonances of **41** to shift downfield 28.3–24.6 ppm. The single resonance of **42** instead shifts 12 ppm upfield. On a per °C basis, **41** is therefore a more sensitive probe than **42**. Importantly, the response of these two probes to temperature is nearly identical in water and fetal bovine serum (FBS), which bodes well for future *in vivo* applications.

The standard approaches that are used in the design of diamagnetic fluorine probes can also be applied to their paramagnetic analogs. An example is the α -chymotrypsin esterase probe **51** (Figure 12C). Hydrolysis of the ester, followed by self-immolation of the linker, yields a carboxylated fluorine moiety whose ^{19}F nuclei signal is positioned 6.2 ppm away from the starting material (Harvey et al., 2012a). These probes function essentially like their purely organic analogs recently

described by our group (Harvey et al., 2012b). The use of paramagnetic fluorine probes in *in vivo* imaging is currently limited by the lack of a suitable MRI scanner that can image fluorine. However, the development of such a scanner would revolutionize the field of medical imaging, providing a non-invasive way to monitor biological processes in real time.



reviewed by Mason (Yu et al., 2005). The advantage of the paramagnetic version resides in the sensitivity of the probe (see section Improving the Sensitivity of ^{19}F Probes). In this case, the lanthanide ion functions only to increase the sensitivity of the probe. Ho^{III} shortens the T_1 and T_2 of the fluorine, thereby significantly increasing the number of scans that can be recorded in a given amount of time, and thus improving the SNR of the probe.

Although this review has focused on ^{19}F MR imaging, a significant advantage of ^{19}F probes is their ability to also function in other modalities. Fluorinated polyaminocarboxylate-based complexes, for instance, can also be effective chemical exchange saturation transfer (CEST) MR contrast agents. Such dual-modalities are particularly well-suited for the design of ratiometric agents. False negatives are more readily avoided if one of the two modalities is responsive to the targeted marker while the other one is not. This enables the distribution of the contrast agent to be mapped independently of that of the marker. Two examples of dual ^{19}F -CEST agents have been reported. A fluorinated Eu-DOTAm-Gly complex with two *trans* trifluoromethyl groups (2, Figure 1) generated sufficient ^{19}F and CEST contrast *in vitro* despite multiple isomers in solution (Cakic et al., 2016). Unfortunately, the contrast agent was not detected *in vivo* by ^{19}F MRI, possibly due to interactions with tissues that substantially reduced T_2 . This first dual-modality ^{19}F contrast agent is not responsive.

Fe-DOTAm-F12 which was developed in our lab, has 12 equivalent fluorine nuclei and one isomer in solution (12, Figure 1). It functions both as a ^{19}F MR probe and a paraCEST contrast agent. Importantly, whereas the ^{19}F signal intensity is independent of pH, the CEST signal is modulated by pH. The % saturation transfer of the complexes increases 5-fold between pH 4 and 6.2. The complex accurately determines the pH independently of the concentration of the contrast agent between pH 6.9 and 7.4, a range that is relevant to cancer diagnosis. Advantageously, the similar sensitivity of the agent in both modalities facilitates ratiometric determination of pH.

OUTLOOK

The development of paramagnetic fluorine probes over the last decade mirrors, in many ways, that of paraCEST agents, the paramagnetic derivatives of CEST contrast agents. The introduction of paramagnetic metal ions in the design of fluorine probes, most notably lanthanides, iron, and cobalt, offer several advantages. Those include increased sensitivity of the fluorine probes due to decreased R_1 of the fluorine nuclei and increased chemical shift spectral window due to the paramagnetic induced shift.

Advantageously, both the effects on relaxation rates and chemical shift offer new approaches to the development of responsive fluorine probes that are not available with their diamagnetic counterparts, and these strategies lead to a

significantly greater response. Indeed, paramagnetic fluorinated complexes can be readily designed such that the chemical shifts and/or the relaxation times T_1 and T_2 of the fluorine nuclei change substantially upon binding to or reacting with a desired analyte. This causes either the appearance, disappearance or notable chemical shift of the ^{19}F peaks. Moreover, the absence of background signal in ^{19}F MRI is an added advantage of this class of probes over the more common Gd-based and iron oxide nanoparticle-based contrast agents which have to contend with the signal of endogenous water. The recent work published on paramagnetic fluorine probes, backed by accurate theoretical models, enable scientists to design molecules with maximum sensitivity by optimizing the nature, specially the oxidation and spin state, of the paramagnetic ion and its distance from the fluorine nuclei all while maximizing the number of chemically equivalent ^{19}F nuclei. Those same parameters are used in the design and optimization of responsive probes. Notably, the large spectral windows of paramagnetic fluorine probes enable the design of ratiometric responsive probes which can independently report on both the distribution of a probe and that of its targeted analyte. Paramagnetic fluorine probes are also uniquely suited to multicolor, or multifrequency, imaging, which enables the tracking of different types of cells.

Paramagnetic fluorine probes have drawbacks too that should be kept in mind. The increase in sensitivity due to lower R_1 induced by the paramagnetic ion is minimal at high magnetic fields. These probes are better suited for use with scanners of low and medium magnetic field strengths, below 6 T. The structure and conformation of the probe in solution, parameters

that can be more difficult to predict, have a significant impact on the properties of the probe. Complexes existing as a single isomer in solution with all fluorine nuclei chemically equivalent are more sensitive and easier to image, but many lanthanide complexes exist in solution as interconverting isomers. The potential toxicity of the complex should also be kept in mind, especially given the high concentrations of probes required for *in vivo* imaging. Although the toxicity and pharmacological properties of this new class of probes has not yet been evaluated, conclusions drawn from Gd-based contrast agents are likely to extend to paramagnetic fluorine probes. Kinetically labile lanthanide complexes, for instance, are expected to present higher toxicity. Nonetheless, we foresee that these first generation of paramagnetic fluorine probes will open avenues for many more applications for *in vivo* imaging. In particular, the ability of these probes to track different cells and biomarkers, and their response to different stimuli, render them particularly promising for molecular imaging.

AUTHOR CONTRIBUTIONS

VP, KP, and KS: searched and analyzed the literature; VP, KP, and KS: co-wrote the manuscript.

ACKNOWLEDGMENTS

This work was supported by the National Science Foundation Grant CAREER 1151665 and NSF INFEWS N/P/H2O:SusChEM CHE-1610832.

REFERENCES

- Ahrens, E. T., Helfer, B. M., O'Hanlon, C. F., and Schirda, C. (2014). Clinical cell therapy imaging using a perfluorocarbon tracer and fluorine-19 MRI. *Magn. Reson. Med.* 72, 1696–1701. doi: 10.1002/mrm.25454
- Ahrens, E. T., and Zhong, J. (2013). *In vivo* MRI cell tracking using perfluorocarbon probes and fluorine-19 detection. *NMR Biomed.* 26, 860–871. doi: 10.1002/nbm.2948
- Allegrozzi, M., Bertini, I., Janik, M. B. L., Lee, Y. M., Lin, G. H., and Luchinat, C. (2000). Lanthanide-induced pseudocontact shifts for solution structure refinements of macromolecules in shells up to 40 angstrom from the metal ion. *J. Am. Chem. Soc.* 122, 4154–4161. doi: 10.1021/ja993691b
- Alsaadi, B. M., Rossotti, F. J. C., and Williams, R. J. P. (1980). Hydration of complexone complexes of lanthanide cations. *J. Chem. Soc. Dalton Trans.* 2151–2154. doi: 10.1039/dt9800002151
- Basal, L. A., Bailey, M. D., Romero, J., Ali, M., Kurenbekova, L., Yustein, J., et al. (2017). Fluorinated EuII-based multimodal contrast agent for temperature- and redox-responsive magnetic resonance imaging. *Chem. Sci.* 8, 8345–8350. doi: 10.1039/C7SC03142D
- Benetollo, F., Bombieri, G., Calabi, L., Aime, S., and Botta, M. (2003). Structural variations across the lanthanide series of macrocyclic DOTA complexes: insights into the design of contrast agents for magnetic resonance imaging. *Inorg. Chem.* 42, 148–157. doi: 10.1021/ic025790n
- Bertini, I., Capozzi, F., Luchinat, C., Nicastro, G., and Xia, Z. C. (1993a). Water proton relaxation for some lanthanide aqua ions in solution. *J. Phys. Chem.* 97, 6351–6354.
- Bertini, I., Turano, P., and Vila, A. J. (1993b). Nuclear Magnetic resonance of paramagnetic metalloproteins. *Chem. Rev.* 93, 2833–2932.
- Blahut, J., Bernášek, K., Gálisová, A., Herynek, V., Číšarová, I., Kotek, J., et al. (2017). Paramagnetic ^{19}F relaxation enhancement in nickel(II) complexes of N-trifluoroethyl cyclam derivatives and cell labeling for ^{19}F MRI. *Inorg. Chem.* 56, 13337–13348. doi: 10.1021/acs.inorgchem.7b02119
- Blahut, J., Hermann, P., Galisova, A., Herynek, V., Číšarová, I., Tosner, Z., et al. (2016). Nickel(II) complexes of N-CH₂CF₃ cyclam derivatives as contrast agents for ^{19}F magnetic resonance imaging. *Dalton Trans.* 45, 474–478. doi: 10.1039/C5DT04138D
- Bleaney, B. (1972). Nuclear magnetic resonance shifts in solution due to lanthanide ions. *J. Magn. Reson.* 8, 91–100. doi: 10.1016/0022-2364(72)90027-3
- Burai, L., Tóth, É., Moreau, G., Sour, A., Scopelliti, R., and Merbach, A. E. (2003). Novel macrocyclic EuII complexes: fast water exchange related to an extreme M?Owater distance. *Chem. Eur. J.* 9, 1394–1404. doi: 10.1002/chem.200390159
- Cakic, N., Savic, T., Stricker-Shaver, J., Truffault, V., Platas-Iglesias, C., Mirkes, C., et al. (2016). Paramagnetic lanthanide chelates for multicontrast MRI. *Chem. Commun.* 52, 9224–9227. doi: 10.1039/C6CC04011J
- Caravan, P., Ellison, J. J., McMurry, T. J., and Lauffer, R. B. (1999). Gadolinium(III) chelates as MRI contrast agents: structure, dynamics, and applications. *Chem. Rev.* 99, 2293–2352. doi: 10.1021/cr980440x
- Chalmers, K. H., Botta, M., and Parker, D. (2011a). Strategies to enhance signal intensity with paramagnetic fluorine-labelled lanthanide complexes as probes for F-19 magnetic resonance. *Dalton Trans.* 40, 904–913. doi: 10.1039/C0DT01232G
- Chalmers, K. H., De Luca, E., Hogg, N. H. M., Kenwright, A. M., Kuprov, I., Parker, D., et al. (2010). Design principles and theory of paramagnetic fluorine-labelled lanthanide complexes as probes for F-19 magnetic resonance: a proof-of-concept study. *Chem. Eur. J.* 16, 134–148. doi: 10.1002/chem.200902300
- Chalmers, K. H., Kenwright, A. M., Parker, D., and Blamire, A. M. (2011b). 19F-lanthanide complexes with increased sensitivity for ^{19}F -MRI: optimization of the MR acquisition. *Magn. Reson. Med.* 66, 931–936. doi: 10.1002/mrm.22881
- Chang, E. T., Adami, H.-O., Boffetta, P., Cole, P., Starr, T. B., and Mandel, J. S. (2014). A critical review of perfluoroctanoate and perfluoroctanesulfonate

- exposure and cancer risk in humans. *Crit. Rev. Toxicol.* 44, 1–81. doi: 10.3109/10408444.2014.905767
- Criscione, J. M., Le, B. L., Stern, E., Brennan, M., Rahner, C., Papademetris, X., et al. (2009). Self-assembly of pH-responsive fluorinated dendrimer-based particulates for drug delivery and noninvasive imaging. *Biomaterials* 30, 3946–3955. doi: 10.1016/j.biomaterials.2009.04.014
- Davies, G.-L., Brown, A., Blackburn, O., Tropiano, M., Faulkner, S., Beer, P. D., et al. (2015). Ligation driven 19F relaxation enhancement in self-assembled Ln(III) complexes. *Chem. Commun.* 51, 2918–2920. doi: 10.1039/C4CC09952D
- De Luca, E., Harvey, P., Chalmers, K., Mishra, A., Senanayake, P. K., Wilson, J. I., et al. (2014). Characterisation and evaluation of paramagnetic fluorine labelled glycol chitosan conjugates for 19F and 1H magnetic resonance imaging. *J. Biol. Inorg. Chem.* 19, 215–227. doi: 10.1007/s00775-013-1028-y
- de Vries, A., Moonen, R., Yildirim, M., Langereis, S., Lamerichs, R., Pikkemaat, J. A., et al. (2014). Relaxometric studies of gadolinium-functionalized perfluorocarbon nanoparticles for MR imaging. *Contrast Media Mol. Imaging* 9, 83–91. doi: 10.1002/cmmi.1541
- Du, W., Nystrom, A. M., Zhang, L., Powell, K. T., Li, Y., Cheng, C., et al. (2008). Amphiphilic hyperbranched fluoropolymers as nanoscopic (19)F magnetic resonance imaging agent assemblies. *Biomacromolecules* 9, 2826–2833. doi: 10.1021/bm800595b
- Garcia, J., and Allen, M. J. (2012). Developments in the coordination chemistry of europium(II). *Eur. J. Inorg. Chem.* 2012, 4550–4563. doi: 10.1002/ejic.201200159
- Gysling, H., and Tsutsui, M. (1971). Organolanthanides and organoactinides. *Adv. Organomet. Chem.* 9, 361–395. doi: 10.1016/S0065-3055(08)60054-4
- Harvey, P., Chalmers, K. H., De Luca, E., Mishra, A., and Parker, D. (2012a). Paramagnetic 19F chemical shift probes that respond selectively to calcium or citrate levels and signal ester hydrolysis. *Chem. Eur. J.* 18, 8748–8757. doi: 10.1002/chem.201200737
- Harvey, P., Kuprov, I., and Parker, D. (2012b). Lanthanide complexes as paramagnetic probes for 19F magnetic resonance. *Eur. J. Inorg. Chem.* 2012, 2015–2022. doi: 10.1002/ejic.201100894
- Helm, L., Morrow, J. R., Bond, C. J., Carniato, F., Botta, M., Braun, M., et al. (2018). “Chapter 2: Gadolinium-based contrast agents,” in *Contrast Agents for MRI: Experimental Methods*, eds V. C. Pierre and M. J. Allen (Croydon: The Royal Society of Chemistry), 121–242.
- Holland, G. N., Bottomley, P. A., and Hinshaw, W. S. (1977). 19F magnetic resonance imaging. *J. Magn. Reson.* 28, 133–136. doi: 10.1016/0022-2364(77)90263-3
- Hu, L., Zhang, L., Chen, J., Lanza, G. M., and Wickline, S. A. (2011). Diffusional mechanisms augment the fluorine MR relaxation in paramagnetic perfluorocarbon nanoparticles that provides a “relaxation switch” for detecting cellular endosomal activation. *J. Magn. Reson. Imaging* 34, 653–661. doi: 10.1002/jmri.22656
- Janjic, J. M., and Ahrens, E. T. (2009). Fluorine-containing nanoemulsions for MRI cell tracking. *Wiley Interdiscipl. Rev. Nanomed. Nanobiotechnol.* 1, 492–501. doi: 10.1002/wnan.35
- Janjic, J. M., Srinivas, M., Kadayakkara, D. K. K., and Ahrens, E. T. (2008). Self-delivering nanoemulsions for dual fluorine-19 MRI and fluorescence detection. *J. Am. Chem. Soc.* 130, 2832–2841. doi: 10.1021/ja077388j
- Jiang, Z.-X., Feng, Y., and Yu, Y. B. (2011). Fluorinated paramagnetic chelates as potential multi-chromic 19F tracer agents. *Chem. Commun.* 47, 7233–7235. doi: 10.1039/c1cc11150g
- Jiang, Z.-X., Liu, X., Jeong, E.-K., and Yu, Y. B. (2009). Symmetry-guided design and fluorous synthesis of a stable and rapidly excreted imaging tracer for (19)F MRI. *Angew. Chem. Int. Ed.* 48, 4755–4758. doi: 10.1002/anie.200901005
- Kamendulis, L. M., Wu, Q., Sandusky, G. E., and Hocevar, B. A. (2014). Perfluoroctanoic acid exposure triggers oxidative stress in the mouse pancreas. *Toxicol. Rep.* 1, 513–521. doi: 10.1016/j.toxrep.2014.07.015
- Keliris, A., Mamedov, I., Hagberg, G. E., Logothetis, N. K., Scheffler, K., and Engelmann, J. (2012). A smart 19F and 1H MRI probe with self-immolative linker as a versatile tool for detection of enzymes. *Contrast Media Mol. Imaging* 7, 478–483. doi: 10.1002/cmmi.1470
- Keliris, A., Ziegler, T., Mishra, R., Pohmann, R., Sauer, M. G., Ugurbil, K., et al. (2011). Synthesis and characterization of a cell-permeable bimodal contrast agent targeting beta-galactosidase. *Bioorg. Med. Chem.* 19, 2529–2540. doi: 10.1016/j.bmc.2011.03.023
- Kenwright, A. M., Kuprov, I., De Luca, E., Parker, D., Pandya, S. U., Senanayake, P. K., et al. (2008). (19)F NMR based pH probes: lanthanide(III) complexes with pH-sensitive chemical shifts. *Chem. Commun.* 2514–2516. doi: 10.1039/b802838a
- Kim, W. D., Kiefer, G. E., Huskens, J., and Sherry, A. D. (1997). NMR studies of the lanthanide(III) complexes of 1,4,7,10-tetraazacyclododecane-1,4,7,10-tetrakis(methanephosphonic acid mono(2',2',2'-trifluoroethyl) ester). *Inorg. Chem.* 36, 4128–4134. doi: 10.1021/ic970169m
- Kislukhin, A. A., Xu, H., Adams, S. R., Narsinh, K. H., Tsien, R. Y., and Ahrens, E. T. (2016). Paramagnetic fluorinated nanoemulsions for sensitive cellular fluorine-19 magnetic resonance imaging. *Nat. Mater.* 15, 662–668. doi: 10.1038/nmat4585
- Kitamura, N., Hiraoka, T., Tanaka, K., and Chujo, Y. (2012). Reduced glutathione-resisting 19F NMR sensors for detecting HNO. *Bioorg. Med. Chem.* 20, 4668–4674. doi: 10.1016/j.bmc.2012.06.013
- Knight, J. C., Edwards, P. G., and Paisley, S. J. (2011). Fluorinated contrast agents for magnetic resonance imaging: a review of recent developments. *RSC Adv.* 1, 1415–1425. doi: 10.1039/c1ra00627d
- Matsushita, H., Mizukami, S., Mori, Y., Sugihara, F., Shirakawa, M., Yoshioka, Y., et al. (2012). F-19 MRI monitoring of gene expression in living cells through cell-surface beta-lactamase activity. *ChemBioChem* 13, 1579–1583. doi: 10.1002/cbic.201200331
- McFarland, E., Koutcher, J. A., Rosen, B. R., Teicher, B., and Brady, T. J. (1985). *In vivo* 19F NMR imaging. *J. Comput. Assist. Tomogr.* 9, 8–15. doi: 10.1097/00004728-198501000-00002
- Mizukami, S., Matsushita, H., Takikawa, R., Sugihara, F., Shirakawa, M., and Kikuchi, K. (2011). 19F MRI detection of [small beta]-galactosidase activity for imaging of gene expression. *Chem. Sci.* 2, 1151–1155. doi: 10.1039/c1sc00071c
- Mizukami, S., Takikawa, R., Sugihara, F., Hori, Y., Tochio, H., Wälchli, M., et al. (2008). Paramagnetic relaxation-based 19F MRI probe to detect protease activity. *J. Am. Chem. Soc.* 130, 794–795. doi: 10.1021/ja077058z
- Mizukami, S., Takikawa, R., Sugihara, F., Shirakawa, M., and Kikuchi, K. (2009). Dual-function probe to detect protease activity for fluorescence measurement and 19F MRI. *Angew. Chem. Int. Ed.* 48, 3641–3643. doi: 10.1002/anie.200806328
- Modo, M. M. J., and Bulte, J. W. M. (2007). *Molecular and Cellular MR Imaging*. Boca Raton, FL: CRC Press.
- Neubauer, A. M., Myerson, J., Caruthers, S. D., Hockett, F. D., Winter, P. M., Chen, J., et al. (2008). Gadolinium-modulated 19F signals from perfluorocarbon nanoparticles as a new strategy for molecular imaging. *Magn. Reson. Med.* 60, 1066–1072. doi: 10.1002/mrm.21750
- Ogawa, M., Nitahara, S., Aoki, H., Ito, S., Narazaki, M., and Matsuda, T. (2010a). Fluorinated polymer nanoparticles as a Novel F-19 MRI contrast agent prepared by dendrimer-initiated living radical polymerization. *Macromol. Chem. Phys.* 211, 1369–1376. doi: 10.1002/macp.200900672
- Ogawa, M., Nitahara, S., Aoki, H., Ito, S., Narazaki, M., and Matsuda, T. (2010b). Synthesis and evaluation of water-soluble fluorinated dendritic block-copolymer nanoparticles as a F-19-MRI contrast agent. *Macromol. Chem. Phys.* 211, 1602–1609. doi: 10.1002/macp.201000100
- Parker, D., Dickins, R. S., Puschmann, H., Crossland, C., and Howard, J. A. K. (2002). Being excited by lanthanide coordination complexes: aqua species, chirality, excited-state chemistry, and exchange dynamics. *Chem. Rev.* 102, 1977–2010. doi: 10.1021/cr010452+
- Peng, H., Blakey, I., Dargaville, B., Rasoul, F., Rose, S., and Whittaker, A. K. (2009). Synthesis and evaluation of partly fluorinated block copolymers as MRI imaging agents. *Biomacromolecules* 10, 374–381. doi: 10.1021/bm801136m
- Peters, J. A., Huskens, J., and Raber, D. J. (1996). Lanthanide induced shifts and relaxation rate enhancements. *Prog. Nucl. Magn. Reson. Spectrosc.* 28, 283–350. doi: 10.1016/0079-6565(95)01026-2
- Pierre, V. C., Harris, S. M., and Pailloux, S. L. (2018). Comparing strategies in the design of responsive contrast agents for magnetic resonance imaging: a case study with copper and zinc. *Acc. Chem. Res.* 51, 342–351. doi: 10.1021/acs.accounts.7b00301
- Placidi, M. P., Botta, M., Kálmán, F. K., Hagberg, G. E., Baranyai, Z., Krenzer, A., et al. (2013). Aryl-phosphonate lanthanide complexes and their fluorinated derivatives: investigation of their unusual relaxometric behavior and potential application as dual frequency 1H/19F MRI probes. *Chem. Eur. J.* 19, 11644–11660. doi: 10.1002/chem.201300763

- Raymond, K. N., Dertz, E. A., and Kim, S. S. (2003). Enterobactin: an archetype for microbial iron transport. *Proc. Natl. Acad. Sci. U.S.A.* 100, 3584–3588. doi: 10.1073/pnas.0630018100
- Ruiz-Cabello, J., Barnett, B. P., Bottomley, P. A., and Bulte, J. W. M. (2011). Fluorine (F-19) MRS and MRI in biomedicine. *NMR Biomed.* 24, 114–129. doi: 10.1002/nbm.1570
- Sakamoto, T., Shimizu, Y. K., Sasaki, J., Hayakawa, H., and Fujimoto, K. (2011). Signal turn-on probe for nucleic acid detection based on 19F nuclear magnetic resonance. *Bioorg. Med. Chem. Lett.* 21, 303–306. doi: 10.1016/j.bmcl.2010.11.013
- Sanders, J. K. M., Hanson, S. W., and Williams, D. H. (1972). Paramagnetic shift reagents. Nature of the interactions. *J. Am. Chem. Soc.* 94, 5325–5335. doi: 10.1021/ja00770a031
- Sarkar, A., Biton, I. E., Neeman, M., and Datta, A. (2017). A macrocyclic F-19-MR based probe for Mn²⁺ sensing. *Inorg. Chem. Commun.* 78, 21–24. doi: 10.1016/j.inoche.2017.02.008
- Senanayake, P. K., Kenwright, A. M., Parker, D., and van der Hoorn, S. K. (2007). Responsive fluorinated lanthanide probes for 19F magnetic resonance spectroscopy. *Chem. Commun.* 2923–2925. doi: 10.1039/b705844f
- Srivastava, K., Ferrauto, G., Young, V. G., Aime, S., and Pierre, V. C. (2017a). Eight-coordinate, stable Fe(II) complex as a dual 19F and CEST contrast agent for ratiometric pH imaging. *Inorg. Chem.* 56, 12206–12213. doi: 10.1021/acs.inorgchem.7b01629
- Srivastava, K., Weitz, E. A., Peterson, K. L., Marjanska, M., and Pierre, V. C. (2017b). Fe- and Ln-DOTAm-F12 are effective paramagnetic fluorine contrast agents for MRI in water and blood. *Inorg. Chem.* 56, 1546–1557. doi: 10.1021/acs.inorgchem.6b02631
- Stares, E., Rho, J., Ahrens, E. T., Foster, P., Li, A., and Bartha, R. (2018). “Chapter 6: Fluorine-based contrast agents,” in *Contrast Agents for MRI: Experimental Methods*, eds V. C. Pierre and M. J. Allen (Croydon: The Royal Society of Chemistry), 479–498.
- Tanaka, K., Kitamura, N., Takahashi, Y., and Chujo, Y. (2009). Reversible signal regulation system of 19F NMR by redox reactions using a metal complex as a switching module. *Bioorg. Med. Chem.* 17, 3818–3823. doi: 10.1016/j.bmcr.2009.04.039
- Thorarinsson, A. E., Gaudette, A. I., and Harris, T. D. (2017). Spin-crossover and high-spin iron(II) complexes as chemical shift 19F magnetic resonance thermometers. *Chem. Sci.* 8, 2448–2456. doi: 10.1039/C6SC04287B
- Thurecht, K. J., Blakey, I., Peng, H., Squires, O., Hsu, S., Alexander, C., et al. (2010). Functional hyperbranched polymers: toward targeted *in vivo* 19F magnetic resonance imaging using designed macromolecules. *J. Am. Chem. Soc.* 132, 5336–5337. doi: 10.1021/ja100252y
- Tilley, T. D., Andersen, R. A., Spencer, B., Ruben, H., Zalkin, A., and Templeton, D. H. (1980). Divalent lanthanide chemistry. Bis (pentamethylcyclopentadienyl) europium(II) and -ytterbium(II) derivatives: crystal structure of bis (pentamethylcyclopentadienyl) (tetrahydrofuran ytterbium(II)) -hemitoluene at 176 K. *Inorg. Chem.* 19, 2999–3003.
- Tirotta, I., Dichiarante, V., Pigliacelli, C., Cavallo, G., Terraneo, G., Bombelli, F. B., et al. (2015). 19F magnetic resonance imaging (MRI): from design of materials to clinical applications. *Chem. Rev.* 115, 1106–1129. doi: 10.1021/cr500286d
- Xie, D., Kim, S., Kohli, V., Banerjee, A., Yu, M., Enriquez, J. S., et al. (2017). Hypoxia-responsive F-19 MRI probes with improved redox properties and biocompatibility. *Inorg. Chem.* 56, 6429–6437. doi: 10.1021/acs.inorgchem.7b00500
- Xie, D., King, T. L., Banerjee, A., Kohli, V., and Que, E. L. (2016). Exploiting copper redox for 19F magnetic resonance-based detection of cellular hypoxia. *J. Am. Chem. Soc.* 138, 2937–2940. doi: 10.1021/jacs.5b13215
- Yu, J.-X., Hallac, R. R., Chiguru, S., and Mason, R. P. (2013a). New frontiers and developing applications in F-19 NMR. *Prog. Nucl. Magn. Reson. Spectrosc.* 70, 25–49. doi: 10.1016/j.pnmrs.2012.10.001
- Yu, J. X., Kodibagkar, V. D., Cui, W. N., and Mason, R. P. (2005). F-19: a versatile reporter for non-invasive physiology and pharmacology using magnetic resonance. *Curr. Med. Chem.* 12, 819–848. doi: 10.2174/0929867053507342
- Yu, J.-X., Kodibagkar, V. D., Hallac, R. R., Liu, L., and Mason, R. P. (2012). Dual 19F/1H MR gene reporter molecules for *in vivo* detection of β-galactosidase. *Bioconjugate Chem.* 23, 596–603. doi: 10.1021/bc200647q
- Yu, J.-X., Kodibagkar, V. D., Liu, L., Zhang, Z., Liu, L., Magnusson, J., et al. (2013b). 19F-MRS/1H-MRI dual-function probe for detection of [small beta]-galactosidase activity. *Chem. Sci.* 4, 2132–2142. doi: 10.1039/C3SC21099E
- Yu, M., Xie, D., Phan, K. P., Enriquez, J. S., Luci, J. J., and Que, E. L. (2016). A CoII complex for 19F MRI-based detection of reactive oxygen species. *Chem. Commun.* 52, 13885–13888. doi: 10.1039/C6CC08207F
- Yu, Y. B. (2013). Fluorinated dendrimers as imaging agents for F-19 MRI. *Wiley Interdiscipl. Rev. Nanomed. Nanobiotechnol.* 5, 646–661. doi: 10.1002/wnnan.1239
- Yue, X., Wang, Z., Zhu, L., Wang, Y., Qian, C., Ma, Y., et al. (2014). Novel 19F activatable probe for the detection of matrix metalloprotease-2 activity by MRI/MRS. *Mol. Pharm.* 11, 4208–4217. doi: 10.1021/mp500443x
- Yue, X., Wang, Z., Zhu, L., Wang, Y., Qian, C., Ma, Y., et al. (2017). Correction to “Novel 19F activatable probe for the detection of matrix metalloprotease-2 activity by MRI/MRS”. *Mol. Pharm.* 14, 1317–1318. doi: 10.1021/acs.molpharmaceut.7b00150
- Zhu, Q., Qiu, F., Zhu, B., and Zhu, X. (2013). Hyperbranched polymers for bioimaging. *RSC Adv.* 3, 2071–2083. doi: 10.1039/C2RA22210H

Conflict of Interest Statement: The authors declare that the research was conducted in the absence of any commercial or financial relationships that could be construed as a potential conflict of interest.

Copyright © 2018 Peterson, Srivastava and Pierre. This is an open-access article distributed under the terms of the Creative Commons Attribution License (CC BY). The use, distribution or reproduction in other forums is permitted, provided the original author(s) and the copyright owner are credited and that the original publication in this journal is cited, in accordance with accepted academic practice. No use, distribution or reproduction is permitted which does not comply with these terms.



Sonosensitive MRI Nanosystems as Cancer Theranostics: A Recent Update

Francesca Garello and Enzo Terreno *

Molecular and Preclinical Imaging Centers, Department of Molecular Biotechnology and Health Sciences, University of Torino, Torino, Italy

In the tireless search for innovative and more efficient cancer therapies, sonosensitive Magnetic Resonance Imaging (MRI) agents play an important role. Basically, these systems consist of nano/microvesicles composed by a biocompatible membrane, responsive to ultrasound-induced thermal or mechanical effects, and an aqueous core, filled up with a MRI detectable probe and a therapeutic agent. They offer the possibility to trigger and monitor in real time drug release in a spatio-temporal domain, with the expectation to predict the therapeutic outcome. In this review, the key items to design sonosensitive MRI agents will be examined and an overview on the different approaches available so far will be given. Due to the extremely wide range of adopted ultrasound settings and formulations conceived, it is hard to compare the numerous preclinical studies reported. However, in general, a significantly better therapeutic outcome was noticed when exploiting ultrasound triggered drug release in comparison to traditional therapies, thus paving the way to the possible clinical translation of optimized sonosensitive MRI agents.

OPEN ACCESS

Edited by:

Zsolt Baranyai,
Bracco Imaging S.p.A., Italy

Reviewed by:

Ahmed El-Fiqi,
Dankook University, South Korea
István Bányai,
University of Debrecen, Hungary

***Correspondence:**

Enzo Terreno
enzo.terreno@unito.it

Specialty section:

This article was submitted to
Medicinal and Pharmaceutical
Chemistry,
a section of the journal
Frontiers in Chemistry

Received: 05 February 2018

Accepted: 19 April 2018

Published: 07 May 2018

Citation:

Garello F and Terreno E (2018)
Sonosensitive MRI Nanosystems as
Cancer Theranostics: A Recent
Update. *Front. Chem.* 6:157.
doi: 10.3389/fchem.2018.00157

INTRODUCTION

New insights in cancer biology, along with the advances in early detection and treatment, led to increased life expectancy, and reduced cancer related deaths. However, there is still a strong need for more efficient, precise, and safer therapies. To decrease the systemic toxicity of some chemotherapeutic agents, drug encapsulation into biocompatible nanovesicles, named liposomes, has been envisaged. The FDA approval of Doxil®/Caelyx® in 1995, a doxorubicin liposomal formulation, for the treatment of Kaposi sarcoma, metastatic breast cancer and recurrent ovarian cancer (Barenholz, 2012), boosted the research for optimizing liposomal preparations. Liposomes are highly versatile nanovesicles consisting of a phospholipid bilayer surrounding an aqueous core; these vesicles can vary in size, shape, and lipid composition (Sessa and Weissmann, 1968). Basically, liposomes can carry drugs and/or other molecules, such as imaging or targeting agents, both in their aqueous core and/or in the lipidic membrane. Liposomes are designed to prevent drug extravasation into healthy tissues, prolong blood circulation time, improve drug accumulation, and enhance bioavailability at the target site (Blanco et al., 2015). The accumulation of liposomes into solid tumors is mostly due to peculiarities of the cancerous tissue, namely increased blood supply, enhanced endothelial permeability and reduced lymphatic drainage, resulting into the Enhanced Permeability and Retention (EPR) effect (Maeda et al., 2000).

Once accumulated in the tumor, the drug needs to be released from the carrier. For the nanomedicines currently approved in clinics, this crucial step occurs spontaneously, i.e., following the natural degradability of the nanocarrier interacting with tissue components (Rizzitelli et al., 2015). However, to better control this process, liposomes sensitive to endogenous (e.g., pH, redox potential, enzymatic activity) or exogenous (e.g., heat, light, pressure) stimuli can be designed (Guo and Szoka, 2003). Among different possibilities, in the last decade, considerable attention has been devoted to the use of ultrasounds (US) (Pong et al., 2006), as they are already clinically approved tools for imaging and therapy. Moreover, they can be modulated in terms of frequency and intensity according to the specific goal to be achieved. In addition, in view of personalized medicine based approaches, co-encapsulation of an imaging agent inside the vesicle could be envisaged in order to follow the release process and predict the therapeutic outcome. In this respect, Magnetic Resonance Imaging (MRI), due to its outstanding spatial resolution, low invasiveness and absence of limits in tissue penetration could be regarded as the optimal imaging technique. Small paramagnetic molecules can be loaded into liposomes in order to spatio-temporally track drug delivery and/or drug release. In the next paragraphs an overview on the different sonosensitive MRI agents will be presented, with a focus on ultrasound-based trigger mechanisms. Finally, some examples of successful preclinical applications in this field will be reported.

ULTRASOUND TRIGGERED DRUG RELEASE

Ultrasound is a form of mechanical energy characterized by an acoustic pressure wave at frequencies beyond the upper limit of the normal human sound range, which is from 20 to 20,000 Hz. Basically, US are produced by a sound source vibrating sinusoidally along time, back and forth in space (Xin et al., 2016). In practice US are often produced by means of a ceramic disk endowed with a piezoelectric effect and a specific radius. The disk is inserted within a transducer linked to a waveform function generator. The produced ultrasounds vary in frequency, amplitude, intensity, and speed of propagation. Frequency is the number of cycles of compressions and rarefactions in a

Abbreviations: CEST, Chemical Exchange Saturation Transfer; DOPE, 1,2-dioleoyl-sn-glycero-3-phosphoethanolamine; DPPE, 1,2-Dipalmitoyl-sn-glycero-3-phosphoethanolamine; Gd-DOTP, Gadolinium-1,4,7,10-tetraazacyclododecane-N,N',N'',N'''-tetrakis(methylenephosphonic acid); Gd-DTPA, Gadolinium-diethylenetriamine pentaacetic acid; Gd-DTPA-BMA, Gadolinium-di-ethylenetriaminopentaacetic acid-bis(methylamide); Ln-HPD03A, Lanthanide-1,4,7-triscarboxymethyl-1,4,7,10-tetraazacyclododecane; DSPE, 1,2-distearoyl-sn-glycero-3-phosphoethanolamine; DSPE-PEG2000, 1,2-distearoyl-sn-glycero-3-phosphoethanolamine-N-[methoxy(polyethylene glycol)-2000] (ammonium salt); DPPC, 1,2-dipalmitoyl-sn-glycero-3-phosphocholine; DSPC, 1,2-distearoyl-sn-glycero-3-phosphocholine; HIFU, High Intensity Focused Ultrasound; MPPC, 1-palmitoyl-2-hydroxy-sn-glycero-3-phosphocholine; MRI, Magnetic Resonance Imaging; NMR, Nuclear Magnetic Resonance; pLINFU, Pulsed Low Intensity Non Focused Ultrasounds; PP, Packing Parameter; PRFS, Proton Resonance Frequency Shift; SPIO, SuperParamagnetic Iron Oxide; T_m , Transition Temperature; TSL, Thermosensitive Liposomes; US, Ultrasounds; USPIO, Ultrasmall Iron Oxide Particles.

sound wave per second. Ultrasounds can be classified according to frequency into low (20–200 kHz), medium (0.7–3.0 MHz), or high (1–20 MHz) frequency waves. Low frequency US are characterized by deeper tissue penetration. Moreover, US can be further grouped according to intensity, defined as the quantity of energy in the US beam area, into low intensity ($<3\text{ W/cm}^2$) or high intensity ultrasound ($3\text{--}10,000\text{ W/cm}^2$) (ter Haar, 1999). Low intensity ultrasounds are already clinically approved to promote transdermal drug delivery, while high intensity US are mainly used for thermal ablation of uterine fibroids, kidney stone shattering, and palliative treatments. The possibility of using pulsed or continuous waves, over a variable time range, as well as focusing US by means of specific transducers, makes this technique extremely versatile. Ultrasounds can induce drug release in two different ways, namely by the mechanical or thermal route.

US Mechanical Effect

The US mechanical effect is based upon a combination of micromassage, cavitation and acoustic streaming. Micromassage refers to US induced cell vibrations, likely affecting tissue fluid interchange and tissue mobility. Cavitation is defined as the phenomena of the formation, growth, and subsequent collapse of microbubbles (Frenkel, 2008). Newly formed microbubbles or administered sonosensitive vesicles can oscillate stably (stable cavitation), inducing a constant fluid flow around the bubble, called microstreaming, that induces stress on cell membranes, and may enhance cell permeability. While, if the bubbles increase more than twofold their size, they violently collapse (inertial cavitation) causing microstreaming, formation of liquid jets and ultrasound shock wave emission, able to disrupt membranes of adjacent cells and create pores in capillary walls (Khokhlova et al., 2015). As cavitation phenomena can induce severe cytotoxic effects, a cavitation level sufficient to release drug from nanovesicles and permeabilize cell membranes but without killing cells should be induced (Pitt et al., 2004). To exploit this wide range of mechanical effects, specific US responsive nano-microsystem have been designed, mainly microbubbles (Hernot and Klibanov, 2008), and liposomes (Schroeder et al., 2007). More details about these systems are provided in section Sonosensitive Systems.

US Thermal Effect

The thermal effect, recently reviewed by T. Boissenot et al. (2016), is strictly linked to the application of high intensity US. More in details by focusing the US beam in a small area of a target tissue, the power per cross section area becomes extremely high, leading to significant absorption of thermal energy from the beam by the tissue and consequently resulting in local temperature rise. Resulting hyperthermia could be mild (39–42°C) or high (>43°C). Mild hyperthermia is generally employed to trigger drug release, as it will be discussed in paragraph Thermosensitive Systems. Whereas, high hyperthermia is mainly exploited to kill or ablate tissues (Diederich and Hyynnen, 1999): uterine fibroids, prostate, breast, pancreatic, and liver cancers have been safely and successfully treated with High Intensity Focused Ultrasound (HIFU). In this regard, precise,

and constant temperature monitoring of the heated area is of paramount importance; it can be obtained by means of invasive thermocouples or by MRI thermometry.

ULTRASOUND RESPONSIVE AND MRI DETECTABLE PROBES

So far, a number of reports has been published about the synthesis and optimization of ultrasound responsive and MRI detectable probes. The key components to design such systems are: (i) a lipidic membrane stable in physiological conditions, able to release its content selectively upon US exposure; (ii) a MRI agent, encapsulated within the system, able to report on drug release; (iii) an entrapped drug, that, upon release, carries out the therapeutic effect (**Figure 1**).

Sonosensitive Systems

Initially invented as contrast agent for ultrasound imaging and lately reconsidered for drug and gene delivery purposes, microbubbles are micron sized systems made of an external

shell encapsulating an inner gas core. These systems display a strong tendency to undergo stable or inertial cavitation upon US exposure. The shell could be made up of lipids, polymers or proteins. The inner core could also be filled with liquid perfluoropropane, then triggered to the gaseous phase when stimulated with acoustic energy. Theranostic microbubbles were prepared by Fan et al. bearing a phospholipidic shell, endowed with a complex of SuperParamagnetic Iron Oxide (SPIO) nanoparticles and doxorubicin, and filled with perfluoropropane (Fan et al., 2016). Similar, nanosized, probes were developed by Cavalli et al. (2015). Palmitic acid was the surfactant of choice to be included in the shell in order to entrap the MRI agent Gd-DOTP. Prednisolone phosphate (PLP) was added as therapeutic agent, while pluronic F68 was used as stabilizing agent. Both the preparations, however, were characterized by limited stability over time (1–3 h).

To this regard, liposomes appear promising systems, but, in order to be sonosensitive, special attention has to be dedicated to their membrane composition. TJ Evjen (2011) highlighted the important role played by the phospholipid Packing Parameter (PP). Non-bilayer forming lipids with large hydrophobic cross section as compared to the polar headgroup ($PP > 1$), like DOPE or DSPE, significantly promote liposome sonosensitivity (Evjen et al., 2013). This effect is associated to a DOPE/DSPE restructuring process: upon US exposure, a transformation from lamellar to reversed hexagonal phase occurs, inducing the formation of pores and/or tubular aggregates, through which the drug can readily leak out (Kang et al., 2014). In order to form liposomes, DOPE (or other phospholipids bearing $PP < 1$) must be mixed with phospholipids displaying natural tendency to form bilayers ($PP \sim 1$), cholesterol, useful to induce mechanical stability by tightening the membrane, and stealth moieties, to prolong blood circulation time. While the amount of cholesterol, saturated phospholipids, and polymers should be limited as they increase membrane stiffness and decrease the tendency to drug leakage, stealth moieties, like DSPE-PEG2000 seems to enhance sonosensitivity by the so called “antenna effect,” favoring the interactions between acoustic waves and the vesicles. Finally, Giustetto et al. demonstrated that also shape, size, and intravesicular composition of liposomes may influence US triggered drug release (Giustetto et al., 2013).

Thermosensitive Systems

In 1978, Yatvin et al. first described a thermosensitive formulation, consisting of a DPPC/DSPC (3:1) liposome able to selectively release its hydrophilic content when the temperature was raised up of a few degrees above physiological temperature (Yatvin et al., 1978). Since then, many efforts have been made to obtain improved formulations and to accurately monitor temperature variations in the region of interest, where drug release should take place. The fundamental points to be fulfilled to design a good thermosensitive system are: (i) the presence of temperature sensitive phospholipids or polymers in the membrane; (ii) stable encapsulation of drugs at body temperature; (iii) fast and complete drug release upon heat stimulation and (iv) provision of high drug plasma levels during the time span of hyperthermia treatment (Hijnen et al.,

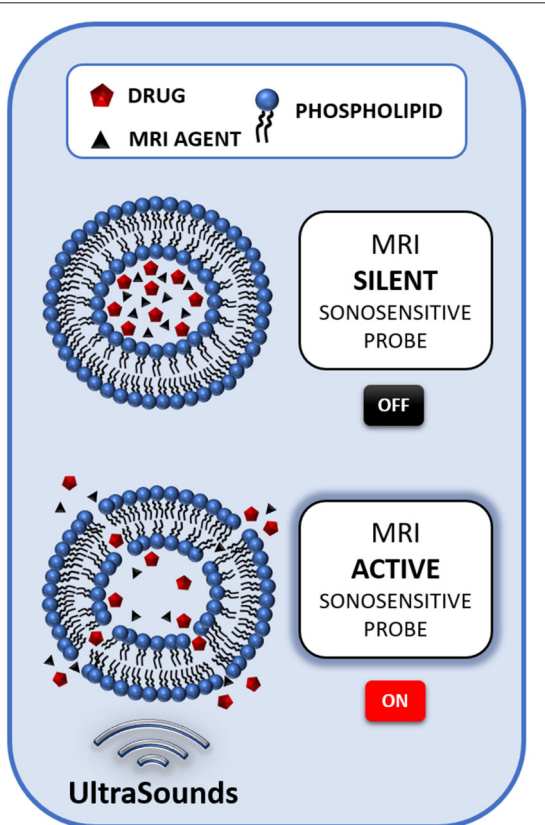


FIGURE 1 | Schematic illustration of the mechanism of a liposome-based sonosensitive MRI agent. The MRI signal of a low water permeable liposome entrapping a relatively high amount of a MRI agent is almost silent, due to the compartmentalization of the probe. However, when the US stimulation triggers the release of the agent, the MRI contrast activates, thus signaling the release of the drug co-loaded in the nanocarrier.

2014). The first thermosensitive liposomes (TSL) developed were mainly composed of phosphatidylcholines, bearing a transition temperature (T_m) in the range of mild hyperthermia (40–43°C). Around T_m , the temperature at which a polymer/phospholipid melts from the gel-ordered phase to the liquid-crystalline phase, a significant drug release was achievable due to grain boundaries between the two phases (Landon et al., 2011). In 1994 Umezaki et al. (1994) added 3% PEGylated phospholipids to a DPPC/DSPC 9:1 formulation, resulting in prolonged circulation time, due to PEG stealth effect, and better therapeutic outcome. PEGylated phospholipids were then considered a basic component.

A breakthrough occurred in 2000, when Needham and co-workers proposed the inclusion of lysolipids ($PP < 1$) into the membrane bilayer (DPPC/MPPC/DSPE-PEG2000 90:10:4), obtaining 80% drug release around T_m in a few seconds, thanks to the formation of lysolipids-stabilized membrane pores (Needham et al., 2000). This innovation led to the birth of ThermoDox®, a TSL formulation containing lysolipids and doxorubicin, that has reached phase III clinical trials for hepatocellular carcinoma treatment (Bulbake et al., 2017). In recent years a myriad of subtle variations have been made to the above-mentioned formulations and different simulated or experimental models have been developed to predict the complex interplay between liposome properties, tumor perfusion, heating regimen, and therapeutic efficacy (Gasselhuber et al., 2010, 2012; Lokerse et al., 2016, 2017). Interestingly, Banno et al. drew the attention on the importance of TSL formulation to retain liposome stability: they reported that 70% of lysolipids was lost within 1 h post injection of TSL, likely due to interactions with the large lipid membrane pool *in vivo*, thus inducing non-triggered drug leakage (Banno et al., 2010). The advantage of using HIFU as heating source is the possibility to obtain a fast and localized temperature increase. Moreover, spatial guidance and temperature monitoring are nowadays available thanks to non-invasive MR-HIFU systems. Among different magnetic resonance thermometry techniques available, Proton Resonance Frequency Shift (PRFS) is by far the most employed, with a precision of approximately 1°C. Using the MR-HIFU platform different focal points can be steered, heating tissues of various volumes, meanwhile sparing vulnerable and crucial structures (Hijnen et al., 2014). It has to be mentioned that MR-thermometry could be perturbed by MRI contrast agents loaded into TSL, due to relaxivity changes induced by the agent accumulation. Conception of correction methods is therefore urgently needed. To overcome this problem, recently Shin et al. proposed the use of perfluorocarbon nanoemulsions as ^{19}F MR contrast agent in sonosensitive systems, in order not to have interferences with ^1H based PRFS (Shin et al., 2017). However, it seems quite challenging to obtain temporal information about drug release using fluorinated compounds.

MRI Reporter Agents

Co-encapsulation of MRI agents into sonosensitive nanovesicles, thus obtaining sonosensitive MRI agents, is of paramount importance in order to monitor and assess in real-time the drug release process. The most diffuse approach consists in encapsulating small hydrophilic paramagnetic compounds,

based on Gd^{3+} or Mn^{2+} ions, in the aqueous core of the nanovesicles. Upon the entrapment the MRI contrast is “silenced,” due to reduced exchange rate of water molecules across the liposomal membrane. When the agent is released, the “quenching effect” is removed, allowing the detection of a contrast enhancement. This contrast enhancement can be estimated and used as reporter of the extent of drug delivery (Ponce et al., 2007; de Smet et al., 2011; Tagami et al., 2011; Rizzitelli et al., 2016). The first TSL encapsulating a MR contrast agent was developed by Viglianti et al. who co-loaded MnSO_4 and doxorubicin in liposomes and detected a change in relaxivity upon heat-triggered drug release (Viglianti et al., 2004). De Smet et al. instead, entrapped into TSL both the clinically approved contrast agent Gd-HPDO3A and doxorubicin, demonstrating that: (i) the paramagnetic compound did not affect doxorubicin loading and release, (ii) the drug and the imaging agent were released simultaneously upon heating and (iii) Gd^{3+} encapsulation within the aqueous core quenched its relaxivity until release occurred (de Smet et al., 2010). However, in both works release was obtained with non-US mediated hyperthermia. Only one year later, the system conceived by de Smet et al. was exploited for MR-HIFU triggered drug release by Negussie et al. co-workers, who demonstrated that upon HIFU stimulation the releases of the drug and the imaging agent were comparable (Negussie et al., 2011), thus paving the way to real-time drug release estimation by MRI using the paramagnetic compound as doxorubicin surrogate. Similar conclusions were drawn by Tagami et al. who co-encapsulated Gd-DTPA and doxorubicin (Tagami et al., 2011), and Rizzitelli et al. who demonstrated the feasibility of stimulating with pulsed Low Intensity Non Focused Ultrasounds (pLINFU) and tracking by MRI drug release from nanovesicles doped with gadoteridol and doxorubicin (Rizzitelli et al., 2014). In 2013, Han et al. developed a sonosensitive system loaded with doxorubicin and endowed of a newly-synthesized Gd-DOTA-DPPE lipid. These vesicles were intended to track drug delivery by MRI, but were unable to report on drug release as Gd^{3+} was incorporated in the vesicle membrane, thus preventing the removal of the so-called “quenching effect” (Han et al., 2013). Original approaches included the use of a dysprosium chelate (Fowler et al., 2013) or Chemical Exchange Saturation Transfer (CEST) contrast agents. Langereis and co-workers loaded into TSL both a chemical shift agent (T_m -HPDO3A, for ^1H lipoCEST detection) and a highly fluorinated compound (hexafluoro-phosphate, for ^{19}F detection). When the two agents were compartmentalized, liposomes could be visualized solely by the CEST effect due to the influence of the paramagnetic shift agent exerted over ^{19}F -NMR resonance, but once the release was triggered the lipoCEST contrast enhancement vanished, while the ^{19}F MRI signal appeared, allowing release quantification (Langereis et al., 2009). Delli Castelli et al. entrapped Eu-HPDO3A in ultrasound-sensitive liposomes, resulting in a “quenched” paraCEST effect at 18 ppm, promptly restored following disruption of the liposomal membrane (Delli Castelli et al., 2014). Finally, iron oxide based contrast agents have been employed. For instance, it has been shown that sonosensitive liposomes coated with

TABLE 1 | Overview of preclinical studies performed with sonosensitive MRI agents.

References	LIPOSOMAL FORMULATION	MRI PROBE	DRUG	DISEASE MODEL	US SETUP
McDannold et al., 2004	DSPC:DSPG (90:10 w/w)	Gd(DTPA-BMA)	No	Liver VX2 tumors (rabbit)	HIFU 1.71 MHz
Negussie et al., 2011	DPPC:MSPC:DSPE-PEG ₂₀₀₀ (85.3:9.7:5.0 mol/mol)	Gd(HPDO3A)	Doxorubicin	VX2 tumor in thigh muscle (rabbit)	HIFU 1.2 MHz
de Smet et al., 2011	DPPC:HSPC:Chol:DPPE-PEG ₂₀₀₀ (50:25:15:3 mol/mol)	Gd(HPDO3A)	Doxorubicin	Subcutaneous 9L gliosarcoma tumors (rat)	HIFU 1.4 MHz
de Smet et al., 2013	DPPC:HSPC:Chol:DPPE-PEG ₂₀₀₀ :DOTA-DSPE (50:25:15:3:1 mol/mol)	Gd(HPDO3A)	Doxorubicin	R1 rhabdomyosarcoma tumors (rat)	HIFU 1.4 MHz
Fowler et al., 2013	DSPE:DSPE-PEG ₂₀₀₀ :Chol (62:8:30 mol/mol)	Gd(DTPA-BMA) Dy(DTPA-BMA)	No	Subcutaneous prostatic adenocarcinoma (rat)	Pulsed HIFU MHz PRF 250 Hz
Rizzitelli et al., 2016	DPPC:DSPC:Chol:DSPE-PEG ₂₀₀₀ (10:5:4:1 mol/mol)	Gd(HPDO3A)	Doxorubicin	Subcutaneous TSA Breast Cancer (mouse)	Pulsed LINFU 1 MHz/3 MHz PRF 1 Hz
Fan et al., 2016	DSPC:DSPG:DSPE-PEG ₂₀₀₀ (21:21:1 mol/mol)	Superparamagnetic iron oxide (SPIO)	Doxorubicin	C6 glioma (rat)	FU 1 MHz
Hijnen et al., 2017	DPPC:HSPC:Chol:DPPE-PEG ₂₀₀₀ (50:25:15:3 mol/mol)	Gd(HPDO3A)	Doxorubicin	R1 rhabdomyosarcoma tumors (rat)	HIFU 1.44 MHz

HIFU, High Intensity Focused Ultrasound; LINFU, Low Intensity Non Focused Ultrasound; FU, Focused Ultrasound.

hydroxyapatite and entrapping nanodots of SPIO in the inorganic shell can release their content upon application of ultrasounds, inducing changes in T_2^*/T_2 MRI contrast (Liu and Huang, 2011). Lorenzato et al. developed temperature-sensitive magnetoliposomes, encapsulating ultrasmall iron oxide particles (USPIO), displaying significant differences in MRI signal enhancement and relaxivities before and after HIFU stimulation (Lorenzato et al., 2013). In the next paragraph the most promising preclinical applications of sonosensitive MRI agents will be reported.

PRECLINICAL STUDIES

A direct comparison of the performance of preclinical studies involving sonosensitive MRI agents is not an easy task as they vary not only in terms of liposomal formulation but also in the type of ultrasounds employed to trigger the release (**Table 1**). Basically, we can gather these works into three groups: (i) HIFU exploited to induce hyperthermia to stimulate both the release of the imaging agent and tissue ablation (no drugs encapsulated); (ii) HIFU employed to trigger the release of both the imaging and the therapeutic agent by hyperthermia; (iii) pLINFU used to trigger the release of the drug and the imaging moiety by mechanical effect. A representative example of the first group is the work reported by McDannold et al. dealing with non-stealth TSL loaded with Gd(DTPA-BMA). The liposomes were injected in rabbits bearing VX2 liver tumors for MR monitoring of thermal therapy carried out with HIFU, obtaining a good

match to traditional MR thermometry methods only in the liver (McDannold et al., 2004). The aim was to provide a less motion-sensitive technique to monitor temperature in real time.

Several works report on the design and testing of TSLs loaded with doxorubicin and Gd³⁺ complexes, to track drug release induced by US thermal effect (de Smet et al., 2011; Negussie et al., 2011). In the study reported by De Smet et al. TSL coencapsulating doxorubicin and Gd-HPDO3A were administered to rats bearing subcutaneous 9L gliosarcoma tumors. Local hyperthermia (42°C) was applied for 30 min through HIFU and drug release was monitored with interleaved T_1 mapping of the tumor tissue, finding out a good correlation between released doxorubicin and Gd³⁺ (de Smet et al., 2011). In 2016 Lokerse et al. seeking for an optimized Dox-TSL formulation, found that the prediction of liposomal efficiency based merely on *in vitro* test is challenging (Lokerse et al., 2016). One year later Hijnen et al. compared different MR-HIFU treatment schemes, assessing that a combination protocol of hyperthermia-induced drug delivery with TSL, followed by ablation, resulted in a homogeneous drug distribution and in the highest therapeutic effect (Hijnen et al., 2017).

The only preclinical study using pLINFU was published by Rizzitelli et al. In this work, Gd-HPDO3A was loaded in a Doxil®-like preparation and administered to mice bearing subcutaneous breast cancer. The most relevant aspect of this study dealt with the achievement of complete tumor regression following the injection of liposomes and the application of pLINFU for drug release and cell membrane sonoporation.

Worth of note is the fact that the used theranostic agent is made of already clinically approved agents (Doxil®, Gd-HPDO3A). The authors outlined that this approach may offer the possibility of predicting the therapeutic outcome in each patient, simply looking at the MRI contrast enhancement 15 min *p.i.* (Rizzitelli et al., 2016). The latter aspect, also known as “dose painting,” is of crucial importance in view of a more and more personalized medicine.

CONCLUSION

This minireview underlines the novelty and the potentiality of the topic, as most of the sonosensitive agents were developed in the last few years. Chemistry plays a fundamental role in the selection of the lipids composing the membrane, in order to boost drug release under US stimuli, while stably trapping the content under physio-pathological conditions in the absence of an external stimulus. It is stressed how special attention has to be devoted to the choice of the encapsulated MRI active compound, that has to act as a quantitative reporter of drug release. Regrettably, making critical comparison is rather difficult at present, due to the lack of standardization of transducers and circuits, often highly customized. However, even if a standardization of the US setting protocol is still lacking, mathematical and practical

models are under development in order to predict the efficiency of the various formulations, and the obtained *in vivo* results appear very promising for a future clinical translation.

AUTHOR CONTRIBUTIONS

FG organized the database and wrote the first draft of the manuscript; ET contributed to the conception and planning of the review, and revised the work critically for important intellectual content. All authors contributed to manuscript revision, read, and approved the submitted version.

FUNDING

Consorzio Interuniversitario di Ricerca in Chimica dei Metalli nei Sistemi Biologici CIRCMSB is gratefully acknowledged for the support. The present work was granted by Compagnia di San Paolo, grant agreement n° CSTO165439, entitled MRI-guided Therapy for combating Ovarian cancer.

ACKNOWLEDGMENTS

Fondazione Umberto Veronesi FUV is gratefully acknowledged for the support.

REFERENCES

- Banno, B., Ickenstein, L. M., Chiu, G. N., Bally, M. B., Thewalt, J., Brief, E., and Wasan, E. K. (2010). The functional roles of poly(ethylene glycol)-lipid and lysolipid in the drug retention and release from lysolipid-containing thermosensitive liposomes *in vitro* and *in vivo*. *J. Pharm. Sci.* 99, 2295–2308. doi: 10.1002/jps.21988
- Barenholz, Y. (2012). Doxil®—the first FDA-approved nano-drug: lessons learned. *J. Control. Release.* 160, 117–134. doi: 10.1016/j.conrel.2012.03.020
- Blanco, E., Shen, H., and Ferrari, M. (2015). Principles of nanoparticle design for overcoming biological barriers to drug delivery. *Nat. Biotechnol.* 33, 941–951. doi: 10.1038/nbt.3330
- Boissenot, T., Bordat, A., Fattal, E., and Tsapis, N. (2016). Ultrasound-triggered drug delivery for cancer treatment using drug delivery systems: from theoretical considerations to practical applications. *J. Control. Release.* 241, 144–163. doi: 10.1016/j.conrel.2016.09.026
- Bulbake, U., Doppalapudi, S., Kommineni, N., and Khan, W. (2017). Liposomal formulations in clinical use: an updated review. *Pharmaceutics* 9:12. doi: 10.3390/pharmaceutics9020012
- Cavalli, R., Argenziano, M., Vigna, E., Giustetto, P., Torres, E., Aime, S., et al. (2015). Preparation and *in vitro* characterization of chitosan nanobubbles as theranostic agents. *Colloids Surf. B Biointerfaces* 129, 39–46. doi: 10.1016/j.colsurfb.2015.03.023
- Castelli D. D., Boffa, C., Giustetto, P., Terreno, E., and Aime, S. (2014). Design and testing of paramagnetic liposome-based CEST agents for MRI visualization of payload release on pH-induced and ultrasound stimulation. *J. Biol. Inorg. Chem.* 19, 207–214. doi: 10.1007/s00775-013-1042-0
- de Smet, M., Heijman, E., Langereis, S., Hijnen, N. M., and Grull, H. (2011). Magnetic resonance imaging of high intensity focused ultrasound mediated drug delivery from temperature-sensitive liposomes: an *in vivo* proof-of-concept study. *J. Control. Release* 150, 102–110. doi: 10.1016/j.conrel.2010.10.036
- de Smet, M., Hijnen, N. M., Langereis, S., Eleveld, A., Heijman, E., Dubois, L., et al. (2013). Magnetic resonance guided high-intensity focused ultrasound mediated hyperthermia improves the intratumoral distribution of temperature-sensitive liposomal doxorubicin. *Invest. Radiol.* 48, 395–405. doi: 10.1097/RLL.0b013e3182806940
- de Smet, M., Langereis, S., van den Bosch, S., and Grull, H. (2010). Temperature-sensitive liposomes for doxorubicin delivery under MRI guidance. *J. Control. Release* 143, 120–127. doi: 10.1016/j.conrel.2009.12.002
- Diederich, C. J., and Hynynen, K. (1999). Ultrasound technology for hyperthermia. *Ultrasound Med. Biol.* 25, 871–887. doi: 10.1016/S0301-5629(99)00048-4
- Evjen, T. J. (2011). *Sonosensitive Liposomes for Ultrasound-Mediated Drug Delivery*. dissertation, [UIT]: University of Tromsø.
- Evjen, T. J., Hupfeld, S., Barnert, S., Fossheim, S., Schubert, R., and Brandl, M. (2013). Physicochemical characterization of liposomes after ultrasound exposure - mechanisms of drug release. *J. Pharm. Biomed. Anal.* 78–79, 118–122. doi: 10.1016/j.jpba.2013.01.043
- Fan, C. H., Cheng, Y. H., Ting, C. Y., Ho, Y. J., Hsu, P. H., Liu, H. L., et al. (2016). Ultrasound/magnetic targeting with SPIO-DOX-microbubble complex for image-guided drug delivery in brain tumors. *Theranostics* 6, 1542–1556. doi: 10.7150/thno.15297
- Fowler, R. A., Fossheim, S. L., Mestas, J. L., Ngo, J., Canet-Soulas, E., and Lafon, C. (2013). Non-invasive magnetic resonance imaging follow-up of sono-sensitive liposome tumor delivery and controlled release after high-intensity focused ultrasound. *Ultrasound Med. Biol.* 39, 2342–2350. doi: 10.1016/j.ultrasmedbio.2013.06.002
- Frenkel, V. (2008). Ultrasound mediated delivery of drugs and genes to solid tumors. *Adv. Drug Deliv. Rev.* 60, 1193–1208. doi: 10.1016/j.addr.2008.03.007
- Gasselhuber, A., Dreher, M. R., Negussie, A., Wood, B. J., Rattay, F., and Haemmerich, D. (2010). Mathematical spatio-temporal model of drug delivery from low temperature sensitive liposomes during radiofrequency tumour ablation. *Int. J. Hyperthermia* 26, 499–513. doi: 10.3109/02656731003623590
- Gasselhuber, A., Dreher, M. R., Rattay, F., Wood, B. J., and Haemmerich, D. (2012). Comparison of conventional chemotherapy, stealth liposomes and temperature-sensitive liposomes in a mathematical model. *PLoS ONE* 7:e47453. doi: 10.1371/journal.pone.0047453
- Giustetto, P., Delli Castelli, D., Boffa, C., Rizzitelli, S., Durando, D., Cutrin, J. C., et al. (2013). Release of a paramagnetic magnetic resonance imaging agent from liposomes triggered by low intensity non-focused ultrasound. *J. Med. Imaging Health Informatics* 3, 356–366. doi: 10.1166/jmihi.2013.1183

- Guo, X., and Szoka, F. C. Jr., (2003). Chemical approaches to triggerable lipid vesicles for drug and gene delivery. *Acc. Chem. Res.* 36, 335–341. doi: 10.1021/ar9703241
- ter Haar, G. (1999). Therapeutic ultrasound. *Eur. J. Ultrasound* 9, 3–9. doi: 10.1016/S0929-8266(99)00013-0
- Han, H. D., Jung, S. H., Seong, H., Cho, S. H., and Shin, B. C. (2013). Dual Functional Gd(III)-DOTA liposomes for cancer therapy and diagnosis as a theragnostic carrier. *Bull. Korean Chem. Soc.* 34:1. doi: 10.5012/bkcs.2013.34.1.154
- Hernot, S., and Klibanov, A. (2008). Microbubbles in ultrasound-triggered drug and gene delivery. *Adv. Drug Deliv. Rev.* 60, 1153–1166. doi: 10.1016/j.addr.2008.03.005
- Hijnen, N., Kneepkens, E., de Smet, M., Langereis, S., Heijman, E., and Grüll, H. (2017). Thermal combination therapies for local drug delivery by magnetic resonance-guided high-intensity focused ultrasound. *Proc. Natl. Acad. Sci. U.S.A.* 114, E4802–E4811. doi: 10.1073/pnas.1700790114
- Hijnen, N., Langereis, S., and Grüll, H. (2014). Magnetic resonance guided high-intensity focused ultrasound for image-guided temperature-induced drug delivery. *Adv. Drug Deliv. Rev.* 72, 65–81. doi: 10.1016/j.addr.2014.01.006
- Kang, M., Huang, G., and Leal, C. (2014). Role of lipid polymorphism in acoustically sensitive liposomes. *Soft Matter.* 10, 8846–8854. doi: 10.1039/C4SM01431F
- Khokhlova, T. D., Haider, Y., and Hwang, J. H. (2015). Therapeutic potential of ultrasound microbubbles in gastrointestinal oncology: recent advances and future prospects. *Therap. Adv. Gastroenterol.* 8, 384–394. doi: 10.1177/1756283X15592584
- Landon, C. D., Park, J. Y., Needham, D., and Dewhirst, M. W. (2011). Nanoscale drug delivery and hyperthermia: the materials design and preclinical and clinical testing of low temperature-sensitive liposomes used in combination with mild hyperthermia in the treatment of local cancer. *Open Nanomed. J.* 3, 38–64. doi: 10.2174/1875933501103010038
- Langereis, S., Keupp, J., van Velthoven, J. L., de Roos, I. H., Burdinski, D., Pikkemaat, J. A., et al. (2009). A temperature-sensitive liposomal 1H CEST and 19F contrast agent for MR image-guided drug delivery. *J. Am. Chem. Soc.* 131, 1380–1381. doi: 10.1021/ja8087532
- Liu, T. Y., and Huang, T. C. (2011). A novel drug vehicle capable of ultrasound-triggered release with MRI functions. *Acta Biomater.* 7:3927. doi: 10.1016/j.actbio.2011.06.038
- Lokerse, W. J., Kneepkens, E. C., ten Hagen, T. L., Eggermont, A. M., Grüll, H., and Koning, G. A. (2016). In depth study on thermosensitive liposomes: Optimizing formulations for tumor specific therapy and *in vitro* to *in vivo* relations. *Biomaterials* 82, 138–150. doi: 10.1016/j.biomaterials.2015.12.023
- Lokerse, W. J. M., Eggermont, A. M. M., Grüll, H., and Koning, G. A. (2017). Development and evaluation of an isolated limb infusion model for investigation of drug delivery kinetics to solid tumors by thermosensitive liposomes and hyperthermia. *J. Control. Release* 18, 282–289. doi: 10.1016/j.jconrel.2017.12.012
- Lorenzato, C., Cernicanu, A., Meyre, M. E., Germain, M., Pottier, A., Levy, L., et al. (2013). MRI contrast variation of thermosensitive magnetoliposomes triggered by focused ultrasound: a tool for image-guided local drug delivery. *Contrast Media Mol. Imaging* 8, 185–192. doi: 10.1002/cmmi.1515
- Maeda, H., Wu, J., Sawa, T., Matsumura, Y., and Hori, K. (2000). Tumor vascular permeability and the EPR effect in macromolecular therapeutics: a review. *J. Control. Release* 65, 271–284. doi: 10.1016/S0168-3659(99)00248-5
- McDannold, N., Fossheim, S. L., Rasmussen, H., Martin, H., Vykhodtseva, N., and Hyynnen, K. (2004). Heat-activated liposomal MR contrast agent: initial *in vivo* results in rabbit liver and kidney. *Radiology* 230, 743–752. doi: 10.1148/radiol.2303021713
- Needham, D., Anyarambhatla, G., Kong, G., and Dewhirst, M. W. (2000). A new temperature-sensitive liposome for use with mild hyperthermia: characterization and testing in a human tumor xenograft model. *Cancer Res.* 60, 1197–1201.
- Negussie, A. H., Yarmolenko, P. S., Partanen, A., Ranjan, A., Jacobs, G., Woods, D., et al. (2011). Formulation and characterisation of magnetic resonance imageable thermally sensitive liposomes for use with magnetic resonance-guided high intensity focused ultrasound. *Int. J. Hyperthermia* 27, 140–155. doi: 10.3109/02656736.2010.528140
- Pitt, W. G., Husseini, G. A., and Staples, B. J. (2004). Ultrasonic drug delivery – a general review. *Expert Opin. Drug Deliv.* 1, 37–56. doi: 10.1517/17425247.1.1.37
- Ponce, A. M., Viglianti, B. L., Yu, D., Yarmolenko, P. S., Michelich, C. R., Woo, J., et al. (2007). Magnetic resonance imaging of temperature-sensitive liposome release: drug dose painting and antitumor effects. *J. Natl. Cancer Inst.* 99, 53–63. doi: 10.1093/jnci/djk005
- Pong, M., Umchid, S., Guarino, A. J., Lewin, P. A., Litniewski, J., Nowicki, A., et al. (2006). *In vitro* ultrasound-mediated leakage from phospholipid vesicles. *Ultrasoundics* 45, 133–145. doi: 10.1016/j.ultras.2006.07.021
- Rizzitelli, S., Giustetto, P., Boffa, C., Delli Castelli, D., Cutrin, J. C., Aime, S., et al. (2014). *In vivo* MRI visualization of release from liposomes triggered by local application of pulsed low-intensity non-focused ultrasound. *Nanomedicine* 10, 901–904. doi: 10.1016/j.nano.2014.03.012
- Rizzitelli, S., Giustetto, P., Cutrin, J. C., Delli Castelli, D., Boffa, C., Ruzza, M., et al. (2015). Sonosensitive theranostic liposomes for preclinical *in vivo* MRI-guided visualization of doxorubicin release stimulated by pulsed low intensity non-focused ultrasound. *J. Control. Release* 202, 21–30. doi: 10.1016/j.jconrel.2015.01.028
- Rizzitelli, S., Giustetto, P., Faletto, D., Delli Castelli, D., Aime, S., and Terreno, E. (2016). The release of Doxorubicin from liposomes monitored by MRI and triggered by a combination of US stimuli led to a complete tumor regression in a breast cancer mouse model. *J. Control. Release* 230, 57–63. doi: 10.1016/j.jconrel.2016.03.040
- Schroeder, A., Avnir, Y., Weisman, S., Najajreh, Y., Gabizon, A., Talmon, Y., et al. (2007). Controlling liposomal drug release with low frequency ultrasound: mechanism and feasibility. *Langmuir* 23, 4019–4025. doi: 10.1021/la0631668
- Sessa, G., and Weissmann, G. (1968). Phospholipid spherules (liposomes) as a model for biological membranes. *J. Lipid Res.* 9, 310–318.
- Shin, S. H., Park, E. J., Min, C., Choi, S. I., Jeon, S., Kim, Y. H., et al. (2017). Tracking perfluorocarbon nanoemulsion delivery by ¹⁹F MRI for precise high intensity focused ultrasound tumor ablation. *Theranostics* 7, 562–572. doi: 10.7150/thno.16895
- Tagami, T., Foltz, W. D., Ernsting, M. J., Lee, C. M., Tannock, I. F., May, J. P., et al. (2011). MRI monitoring of intratumoral drug delivery and prediction of the therapeutic effect with a multifunctional thermosensitive liposome. *Biomaterials* 32, 6570–6578. doi: 10.1016/j.biomaterials.2011.05.029
- Unezaki, S., Maruyama, K., Takahashi, N., Koyama, M., Yuda, T., Suginaka, A., et al. (1994). Enhanced delivery and antitumor activity of doxorubicin using long-circulating thermosensitive liposomes containing amphiphatic polyethylene glycol in combination with local hyperthermia. *Pharm. Res.* 11, 1180–1185. doi: 10.1023/A:1018949218380
- Viglianti, B. L., Abraham, S. A., Michelich, C. R., Yarmolenko, P. S., MacFall, J. R., Bally, M. B., et al. (2004). *In vivo* monitoring of tissue pharmacokinetics of liposome/drug using MRI: illustration of targeted delivery. *Magn. Reson. Med.* 51, 1153–1162. doi: 10.1002/mrm.20074
- Xin, Z., Lin, G., Lei, H., Lue, T. F., and Guo, Y. (2016). Clinical applications of low-intensity pulsed ultrasound and its potential role in urology. *Transl. Androl. Urol.* 5, 255–266. doi: 10.21037/tau.2016.02.04
- Yatin, M. B., Weinstein, J. N., Dennis, W. H., and Blumenthal, R. (1978). Design of liposomes for enhanced local release of drugs by hyperthermia. *Science* 202, 1290–1293. doi: 10.1126/science.364652
- Conflict of Interest Statement:** The authors declare that the research was conducted in the absence of any commercial or financial relationships that could be construed as a potential conflict of interest.
- Copyright © 2018 Garello and Terreno. This is an open-access article distributed under the terms of the Creative Commons Attribution License (CC BY). The use, distribution or reproduction in other forums is permitted, provided the original author(s) and the copyright owner are credited and that the original publication in this journal is cited, in accordance with accepted academic practice. No use, distribution or reproduction is permitted which does not comply with these terms.**



Luminescence Properties of Self-Aggregating Tb^{III}-DOTA-Functionalized Calix[4]arenes

Florian Mayer¹, Sriram Tiruvadi Krishnan¹, Daniel T. Schühle¹, Svetlana V. Eliseeva², Stéphane Petoud², Éva Tóth² and Kristina Djanashvili^{1,2,3*}

¹ Department of Biotechnology, Delft University of Technology, Delft, Netherlands, ² Centre de Biophysique Moléculaire, UPR 4301 Centre National de la Recherche Scientifique, Université d'Orléans, Orléans, France, ³ Le Studium, Loire Valley Institute for Advanced Studies, Orléans, France

OPEN ACCESS

Edited by:

Lorenzo Tei,
Università degli Studi del Piemonte
Orientale, Italy

Reviewed by:

Jean-Claude Georges Bunzli,
École Polytechnique Fédérale de
Lausanne, Switzerland
Maryline Beyler,
University of Western Brittany, France

*Correspondence:

Kristina Djanashvili
k.djanashvili@tudelft.nl

Specialty section:

This article was submitted to
Inorganic Chemistry,
a section of the journal
Frontiers in Chemistry

Received: 28 November 2017

Accepted: 03 January 2018

Published: 30 January 2018

Citation:

Mayer F, Tiruvadi Krishnan S, Schühle DT, Eliseeva SV, Petoud S, Tóth É and Djanashvili K (2018) Luminescence Properties of Self-Aggregating Tb^{III}-DOTA-Functionalized Calix[4]arenes. *Front. Chem.* 6:1. doi: 10.3389/fchem.2018.00001

Self-aggregating calix[4]arenes carrying four DOTA ligands on the *upper rim* for stable complexation of paramagnetic Gd^{III}-ions have already been proposed as MRI probes. In this work, we investigate the luminescence properties of Tb^{III}-DOTA-calix[4]arene-4OPr containing four propyl-groups and compare them with those of the analog substituted with a phthalimide chromophore (Tb^{III}-DOTA-calix[4]arene-3OPr-OPhth). We show that, given its four aromatic rings, the calix[4]arene core acts as an effective sensitizer of Tb-centered luminescence. Substituents on the *lower rim* can modulate the aggregation behavior, which in turn determines the luminescence properties of the compounds. In solid state, the quantum yield of the phthalimide derivative is almost three times as high as that of the propyl-functionalized analog demonstrating a beneficial role of the chromophore on Tb-luminescence. In solution, however, the effect of the phthalimide group vanishes, which we attribute to the large distance between the chromophore and the lanthanide, situated on the opposite rims of the calix[4]arene. Both quantum yields and luminescence lifetimes show clear concentration dependence in solution, related to the strong impact of aggregation on the luminescence behavior. We also evidence the variability in the values of the critical micelle concentration depending on the experimental technique. Such luminescent calix[4]arene platforms accommodating stable lanthanide complexes can be considered valuable building blocks for the design of dual MR/optical imaging probes.

Keywords: calix[4]arenes, DOTA-chelates, lanthanides, terbium, luminescence, optical imaging

INTRODUCTION

Calix[4]arenes were initially proposed as artificial enzyme mimics in the late 70s (Gutsche and Muthukrishnan, 1978) and today represent versatile building blocks with potential for application in industrial, technical and biomedical fields, ranging from wastewater treatment (Konczyk et al., 2016) to medical imaging (Schühle et al., 2011; Sreenivasu Mummidivarapu et al., 2015). The multifunctional constitution of calix[4]arenes consists of four phenol moieties forming a cup-shaped structure with an *upper* and a *lower rim*. Functionalization of the rims can be done in

accordance to the desired properties, including solubility, amphiphilicity, and metal complexation characteristics. The calixarene core is a synthetic backbone that ideally can play an active role in various applications. One example is represented by artificial ion-channels, where the hydrophobic channel-like cavity is of high importance for ion translocation through the membrane (Lawal et al., 2009). Enzyme mimics are also thought to benefit from this basket that resembles hydrophobic pockets in enzymes and serves for positioning of the substrate (Blanchard et al., 1998; Baldini et al., 2012). Despite those exciting examples, most often calix[4]arenes are simply used as platforms to attach the groups of interest in a predetermined spatial arrangement (Modi et al., 2016), which downgrades the core to a mere steric support without further function. Especially, calix[4]arene derivatives intended for medical applications often lack active participation of the core structure itself.

We have been interested in designing imaging agents based on calix[4]arenes for a long time. In the context of contrast agent development for magnetic resonance imaging (MRI), the *upper rim* of the core structure was decorated with four DOTA (1,4,7,10-tetraazacyclododecane-1,4,7,10-tetraacetate) chelating ligands to provide stable complexation of paramagnetic Gd^{III} ions. The Ln^{III} complexes of these calix[4]arenes **1** and **2** (**Figure 1**) are amphiphilic molecules with a very polar *upper rim* and an apolar *lower rim*, tuneable depending on the alkylation of the phenolic OH-groups.

This amphiphilic nature confers them high water solubility due to micelle formation in polar solvents and also opens the possibility for labeling lipid bilayers. Complexes **1** (Schühle et al., 2009) and **2** (Schühle et al., 2010) exhibit high longitudinal proton relaxivities r_1 (expressed in $\text{s}^{-1}\text{mM}^{-1}$ of Gd^{III}), especially when they form micelles, interact with human serum albumin or are incorporated in lipid bilayers.

The four chelating units of calix[4]arenes **1** and **2** can also be complexed with luminescent Ln^{III} ions to design optical probes. Eventually, the combination of Gd^{III} and luminescent Ln^{III} complexes within the same molecular platform could lead to dual MRI/optical imaging probes. To use calix[4]arenes as optical imaging agents, the sensitisation of the Ln^{III} ions has to be ensured. Usually, this is done by surrounding Ln^{III} ion with appropriate aromatic chromophoric units that are able to efficiently absorb excitation energy and transfer it to the lanthanide ion (Bünzli, 2015). An alternative strategy is to exploit the intermolecular energy transfer from an antenna incorporated in e.g., a micellar interior to the Ln^{III} ion (Ln = Tb or Eu) (Escabi-Perez et al., 1977; Darwent et al., 1993).

A few literature examples indicate the potential of calix[4]arene derived compounds for optical imaging in combination with lanthanides (Bünzli et al., 1993, 1998). Fischer et al. designed calix[4]arenes **3** and **4** (**Figure 1**) functionalized with bipyridyl moieties in the *lower rim* which participate in the complexation of Ln^{III} ions (Ln^{III} = Eu^{III}, Tb^{III}) and are at the same time responsible for the excitation of the luminescent center (Fischer et al., 2000). This architecture limits the number of lanthanide-binding sites to one, thus eliminating the great advantage of calix[4]arenes to deliver several active centers per molecule. In addition, the poor water solubility of these apolar

compounds hampers thorough investigation of the luminescence properties and strongly limits biological applicability. In another example, calix[4]arene **5** containing *p*-sulfonate groups was found to exhibit fluorescence upon complexation with Tb^{III} at pH > 10.8 (Sato et al., 1993). The unexpected optical properties of this simple water soluble calix[4]arene were explained by a sandwich structure. The Tb^{III} ion is between two complexing molecules which provide eight coordinating oxygens and push away potential hydration water molecules. However, none of these systems ensure sufficiently stable metal complexation appropriate for biological use.

In the objective of adapting our DOTA-derivative calix[4]arene platform designed for MRI purposes (Schühle et al., 2010) to lanthanide luminescence, we have functionalized one site of the *lower rim* with a phthalimide chromophore while the three other sites bear propyl-groups (DOTA-calix-3OPr-OPht, **Figure 2**, **11a**). Keeping in mind the aggregation tendency of the functionalized calix[4]arenes and the literature examples showing that a direct coordination of the antenna to the luminescent center is not always an absolute requirement (Bonnet et al., 2010), we hypothesized that *lower rim* conjugation with a phthalimide moiety could be sufficient to sensitize Tb-luminescence. The aggregation and the photophysical properties of the Tb^{III} complex have been studied in comparison to the Tb^{III}-DOTA-calix-4OPr analog (**Figure 2**, **11b**) with four propyl residues at the *lower rim*. We show that aggregation has a strong impact on the luminescence behavior. In addition, our data provide a piece of evidence of the variability in the values of the critical micelle concentration depending on the experimental technique.

MATERIALS AND METHODS

General

All reagents and anhydrous solvents used during the synthesis were of commercial quality. 5,11,17,23-Tetra-(*t*-butyl)-25-hydroxy-26,27,28-tripropoxy-calix[4]arene (**6**) was prepared according to the literature (Gutsche and Iqbal, 1990). The *lower rim* of the calix[4]arene backbone was modified in accordance to the described procedures for the propylation (**7a,b**) of the hydroxyl groups (Gutsche and Lin, 1986), as well as condensation of one of the hydroxyls (**8a**) with N-(3-bromo)propylphthalimide (Lalor et al., 2007). The steps, preceding the final conjugation with the DOTA-units (Schühle et al., 2009) included nitration (**9a,b**) of the *upper rim* of the calix[4]arene backbone (Kelderman et al., 1992) followed by the reduction (**10a,b**) of the nitro groups to the amines (Klementová and Vojtíšek, 2007). ¹H NMR spectra were recorded at 25°C on Bruker Avance-400 spectrometer operating at 400.13 MHz and analyzed using BrukerTM TopSpin 2.1 software. The chemical shifts are reported in δ (ppm) using tetramethylsilane (TMS) as an internal reference. Ultra-filtration was performed with a Millipore stirred cell using an Amicon cellulose acetate membrane. All HPLC measurements were carried out on a Shimadzu LC-20 system consisting out of an LC-20AT pump, Sil-20A HT autosampler, CTO-20AC column oven, SPD-M20A PDA detector, CBM-20A controller, and a Waters Fraction

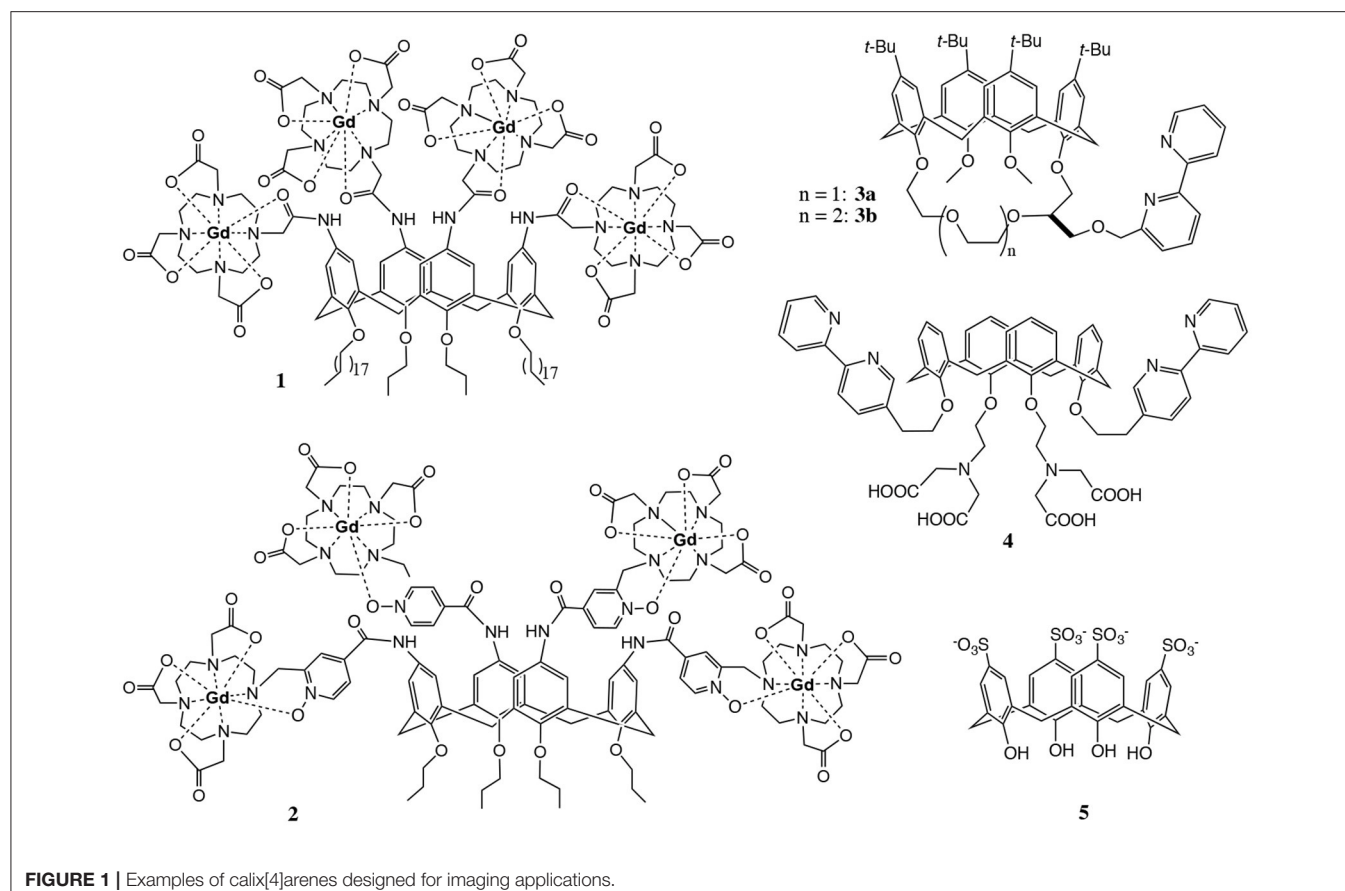


FIGURE 1 | Examples of calix[4]arenes designed for imaging applications.

Collector III; data processing was carried out using Shimadzu Lab Solutions. Both analytical and preparative methods were carried out operating at 40°C using eluents A: H₂O (95%), AcCN (5%), TFA (0.1%) and B: H₂O (5%), AcCN (95%), TFA (0.1%). Mobile phase gradient started with 75% A and 25% B, after 18 min followed by a change linear to 58% A and 42% B, after 2 min a change linear to 100% B, which was hold for 0.5 min and then changed back to starting conditions stabilized for 3.5 min. Analytical measurements used a Waters Xterra 4.6 × 150 mm column and an injection volume of 1 μL, flow was 1 mL/min. Preparative HPLC was performed using Xbridge™ PrepShield RP18-OBD C18-19 × 150 mm column. Mass spectrometry analysis was done with electron spray ionization technique on Waters Qtof Premier MS using a NE-1000 syringe pump for direct infusion; data processing was carried out using Waters Masslynx. Qualitative luminescence measurements were done on a Jasco J815 CD spectrometer using 100 μL of sample in a 3 × 3 mm quartz cuvette. UV absorption spectra were measured on a UV2401 PC Shimadzu spectrometer. For quantitative luminescence measurements, the samples (either powders or solutions in Milli-Q water at concentration 2, 0.2, and 0.04 mM) were placed into 2.4 mm quartz capillaries and measured on a Horiba-Jobin-Yvon Fluorolog 3 spectrofluorimeter equipped with visible (220–800 nm, photon-counting unit R928P) and NIR (950–1,450 nm, photon-counting units H10330-45 from Hamamatsu or DSS-IGA020L Jobin-Yvon solid-state InGaAs

detector, cooled to 77 K) detectors. All spectra were corrected for the instrumental functions. Luminescence lifetimes of Tb^{III}-complexes were determined under excitation at 300 nm provided by a Xenon flash lamp monitoring the signal at 545 nm (⁵D₄ → ⁷F₅ transition). Quantum yields were measured according to an absolute method using an integration sphere (GMP SA). Each sample was measured several times under slightly different experimental conditions. Estimated experimental error for quantum yields determination is 10%. Nile red (NR) fluorescence measurements were performed on a Jasco J-815 CD spectrometer. The temperature was controlled using a Jasco PFD 4252/15 Peltier temperature unit. All samples contained Nile red in 2 μM concentrations and were excited at 550 nm. The maximum Nile red emission wavelength (λ_{max}) was determined as a function of the calix[4]arene concentration.

Synthesis

General Procedure for the Amide Coupling of the Amino-Calix[4]arenes (10a,b) to tris-1,4,7-*tert*-Butoxycarbonyl methyl-10-Carboxymethyl-1,4,7,10-Tetraazacyclododecane (tris-*t*-Bu-DOTA): To a suspension of EDC (2.2 mmol), HOBT (2.2 mmol), and tris-*t*-butyl-DOTA (2.2 mmol) in 20 mL DMF 1.1 mL dry DIPEA was added under N₂ atmosphere and the resulting mixture was stirred for 20 min. A solution of the corresponding calix[4]arene (170 μmol) in 5 mL DMF was added and the reaction mixture was stirred for 2 days before

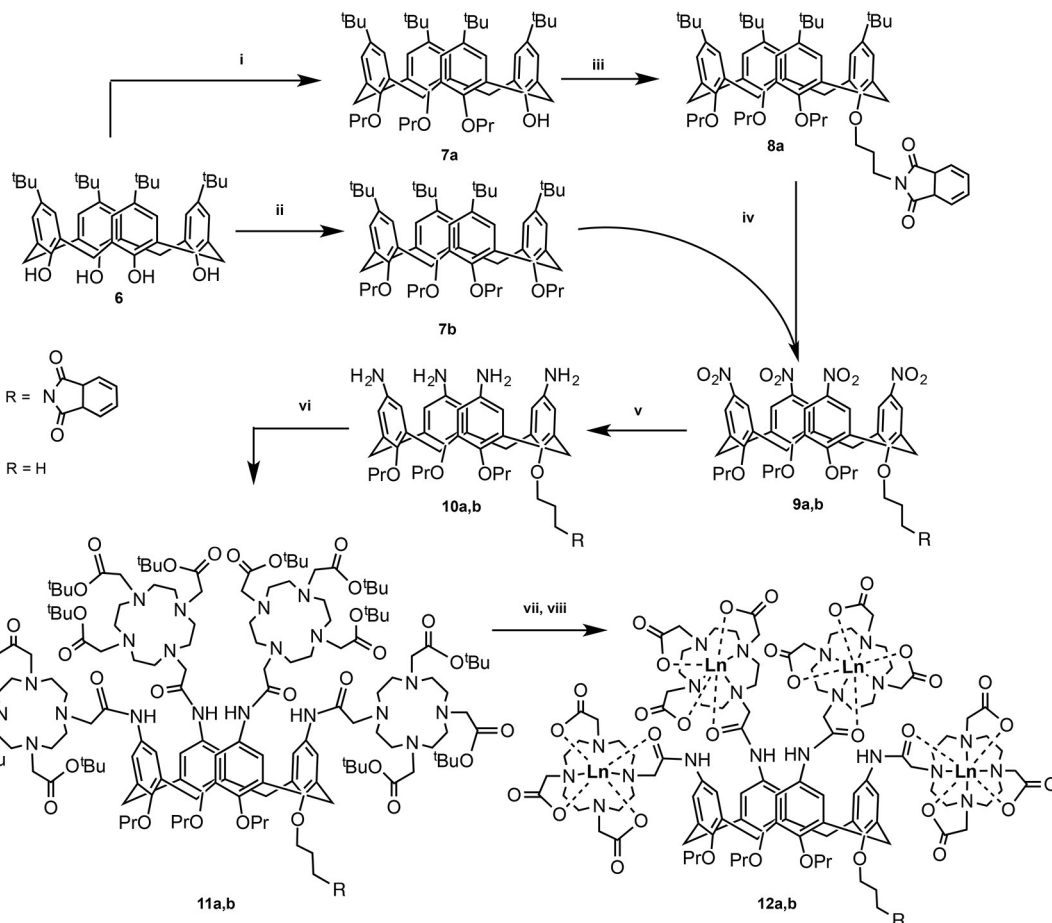


FIGURE 2 | Synthetic pathway for compounds **12a** and **12b**: (i) DMF, $\text{Ba}(\text{OH})_2$, BaO , propylbromide, RT, 1 day; (ii) DMF, NaH, propylbromide, RT, 5 days (Gutsche and Lin, 1986); (iii) DMF, NaH, N-(3-bromo)propylphthalimide, RT, 5 days (Lalor et al., 2007); (iv) (a) CH_2Cl_2 , AcOH, HNO_3 , 0°C , 4 h (Kelderman et al., 1992); (v) MeOH, hydrazine, Raney-Ni, reflux, 6.5 h (Klimešová and Vojtíšek, 2007); (vi) CH_3CN , tris-fert-butoxycarbonylmethyl-1,4,7,10-tetraazacyclododecane (tris-t-Bu-DOTA), Hünig's base, hydroxybenzotriazole, EDC, RT, 36 h; (vii) CH_2Cl_2 , TFA; (viii) TbCl_3 , H_2O , pH 5.5.

removing the solvent *in vacuo*. The remaining solid was dissolved in CH_2Cl_2 (50 mL), washed 2× with brine, 1× with 0.1 N NaOH, and then with water until the pH of the aqueous phase was neutral. The organic phase was dried over Na_2SO_4 and the solvent was evaporated. The crude products **11a** and **11b** were purified from EtOH by ultrafiltration over a 1 kDa membrane with the yield of 80% (410 mg) and 69% (336 mg), respectively.

5,11,17,23-Tetrakis(tris-4,7,10-t-butoxycarbonylmethyl-1,4,7,10-tetraazacyclododec-1-yl-acetamidyl)-25,26,27-tripropoxy-28-phthalimidopropoxycalix[4]arene (11a): $^1\text{H-NMR}$ (300 MHz, DMSO-d₆, 100°C): $\delta = 0.98$ (12 H, *t*, $J = 5.2$ Hz, CH_3), 1.40, 1.46 (108 H, 2 s, t-Bu), 1.88 (8 H, sext, $J = 5.2$ Hz, CH_2CH_3), 2.74–3.30 (100 H, N- CH_2CO , N- $\text{CH}_2\text{-CH}_2\text{-N}$, Ar- $\text{CH}_2\text{-Ar}$), 3.87 (8 H, *t*, $J = 5.2$ Hz, O- CH_2), 4.43 (4 H, *d*, $J = 9.9$ Hz, Ar- $\text{CH}_2\text{-Ar}$), 6.86 (8 H, br s, Ar-H), 9.27 (4 H, brs, NH). ESI-HRMS: calc.: $m/z = 718.7185$ ($\text{M}+4\text{H}^{4+}$, found: 718.7282).

General Procedure for the Deprotection of the t-Bu-DOTA-calix[4]arenes: The t-Bu protected calix[4]arene (150 μmol) was dissolved in CH_2Cl_2 (10 mL) and TFA (10 mL) was added slowly. The reaction mixture was stirred at ambient temperature overnight and subsequently the solvents were removed in vacuum. The obtained solid was re-dissolved in 1 mL of water and freeze-dried to obtain the product as a yellow fluffy powder. The yield was not determined due to the fact that there were still TFA salts in the product, which did not interfere with the next step of the synthesis and could be removed during the purification step of the final product (see below).

5,11,17,23-Tetrakis(tris-4,7,10-t-butoxycarbonylmethyl-1,4,7,10-tetraazacyclododec-1-yl-acetamidyl)-25,26,27,28-tetrapropoxycalix[4]arene (11b): $^1\text{H-NMR}$ (300 MHz, DMSO-d₆,

phthalimidopropoxycalix[4]arene: $^1\text{H-NMR}$ (300 MHz, DMSO-d₆, 100°C): $\delta = 0.89$ (12 H, *t*, *J* = 6.9 Hz, CH₃), 1.80 (8 H, sext, *J* = 6.9 Hz, CH₂CH₃), 3.01–3.61 (100 H, N-CH₂CO, N-CH₂-CH₂-N, Ar-CH₂-Ar), 3.76 (8 H, *t*, *J* = 6.9 Hz, O-CH₂), 4.32 (4 H, *d*, *J* = 12.3 Hz, Ar-CH₂-Ar), 6.91 (8 H, brs, Ar-H), 9.53 (4 H, brs, NH).

5,11,17,23-Tetrakis(tris-4,7,10-carboxymethyl-1,4,7,10-tetraazacyclododec-1-yl-acetamidyl)-25,26,27,28-tripropoxycalix[4]arene: $^1\text{H-NMR}$ (300 MHz, DMSO-d₆, 100°C): $\delta = 0.89$ (12 H, *t*, *J* = 6.9 Hz, CH₃), 1.80 (8 H, sext, *J* = 6.9 Hz, CH₂CH₃), 3.01–3.61 (100 H, N-CH₂CO, N-CH₂-CH₂-N, Ar-CH₂-Ar), 3.76 (8 H, *t*, *J* = 6.9 Hz, O-CH₂), 4.32 (4 H, *d*, *J* = 12.3 Hz, Ar-CH₂-Ar), 6.91 (8 H, brs, Ar-H), 9.53 (4 H, brs, NH).

General Procedure for the Complexation of Tb^{III}-ions in the DOTA-Functionalized Calix[4]arenes (12a,b): The ligands (150 μmol) obtained after the deprotection of *t*-Bu groups were dissolved in water (5 mL) and the pH was adjusted to 5.5 by the addition of 1 M NaOH. Then the TbCl₃ (660 μmol) was added as an aqueous solution and the pH was kept constant using Metrohm Dosimeter 665. After the consumption of NaOH stopped, the solution was stirred overnight and then freeze-dried to result in the crude product that was purified by prep-HPLC. Due to the paramagnetic nature of the Tb^{III} ions, no NMR investigations of the products were possible, therefore MS spectra were taken and compared to the predicted isotopic patterns of the compounds, which were found in a good agreement with the experimental values (Supplementary Figures 1, 2).

Tb^{III}-complex of 5,11,17,23-tetrakis(tris-4,7,10-carboxymethyl-1,4,7,10-tetraazacyclododec-1-yl-acetamidyl)-25,26,27,28-tripropoxy-28-phthalimidopropoxycalix[4]arene (Tb-12a): ESI-HRMS: calc.: *m/z* = 989.9197 (M+2H)³⁺, found: 989.8913.

Tb^{III}-complex of 5,11,17,23-tetrakis(tris-4,7,10-carboxymethyl-1,4,7,10-tetraazacyclododec-1-yl-acetamidyl)-25,26,27,28-tripropoxycalix[4]arene (Tb-12b): ESI-HRMS: calc.: *m/z* = 941.2423 (M+3H)³⁺, found: 941.3101.

RESULTS AND DISCUSSION

The synthetic routes of both compounds **12a** and **12b** are presented in **Figure 2**. In the first step, the hydroxyl groups on the *lower rim* of calix[4]arene **1** are alkylated to yield either three (**7a**) or four (**7b**) O-propyl functionalized calix[4]arenes. In the former case, the remaining OH-group was used for conjugation with propylphthalimide (**8a**). In the next step, the *t*-butyl groups on the *upper rim* were substituted with nitro-groups, which were subsequently reduced to amines to yield compounds **10a** and **10b** (Lalor et al., 2007). The following amide coupling with tris-*tert*-butoxycarbonylmethyl-10-carboxymethyl-1,4,7,10-tetraazacyclodocane resulted in ligands **11a** and **11b**, which after deprotection and purification by prep-HPLC were analyzed and complexed with Tb^{III} ions. The obtained complexes **12a** and **12b** were investigated with respect to their aggregation behavior as well as their luminescent properties in a qualitative and quantitative ways.

In order to assess the role of the calix[4]arene skeleton and of the phthalimide chromophore, the luminescence excitation and emission spectra of Tb^{III}-DOTA-calix-3OPr-OPhth (**12a**) and Tb^{III}-DOTA-calix-4OPr (**12b**) were recorded and compared to

those of Tb^{III}-DOTA. Both **Tb-12a** and **Tb-12b** under excitation at 290 nm exhibit characteristic green emission with four main bands due to $^5\text{D}_4 \rightarrow ^7\text{F}_J$ (*J* = 6–3) transitions, while the reference compound Tb^{III}-DOTA under the same experimental conditions did not show detectable luminescence signal (**Figures 3A,B**). Upon monitoring emission at 545 nm excitation spectra of both **Tb-12a** and **Tb-12b** present broad bands in the UV range up to 315 nm. On the other hand, Tb^{III}-DOTA does not exhibit pronounced transitions in this range. Therefore, in **Tb-12a** and **Tb-12b** characteristic green Tb^{III} emission could be sensitized through “antenna effect” *via* organic ligands, i.e., fully O-propyl or O-propyl and phthalimide functionalized calix[4]arene cores. Interestingly, the maximum luminescence intensity of the two calix[4]arene-complexes shows a dramatically different variation with increasing concentration of the solutions. At concentrations up to \sim 0.1 mM, there is no difference in their luminescence intensities, which remain equally strong for both compounds with a linear correlation to the concentration (**Figures 3C,D**). Upon further increase of the concentration, the luminescence enhancement becomes non-linear. At 1 mM concentration, the emission intensity is two times higher for **Tb-12b** compared to **Tb-12a**. While the luminescence intensity of **Tb-12b** is still increasing above this concentration, that of **Tb-12a** goes through a maximum at 0.5 mM and then slightly decreases. Likewise, a maximum luminescence intensity is found for **Tb-12b** above the concentration of 5 mM (Supplementary Figure 3).

To further quantify the photophysical properties, the excitation and emission spectra of Tb-complexes of calix[4]arenes **12a** and **12b** were acquired in the solid state and at different concentrations in solution (Supplementary Figures 4, 5). It should be noted that in the emission spectra of **12a** and **12b** the crystal-field splitting of Tb^{III} $^5\text{D}_4 \rightarrow ^7\text{F}_J$ (*J* = 6–3) transitions is very similar for the samples in the solid state and solutions of different concentrations reflecting indirectly that the coordination environment around the Tb^{III} ions remains the same upon such variations. The absolute quantum yields upon ligands excitation (Q_{Tb}^L) and observed luminescence lifetimes (τ_{obs}) upon monitoring Tb^{III} emission at 545 nm were also determined (**Table 1**). When comparing the values of τ_{obs} and Q_{Tb}^L for **Tb-12a** and **Tb-12b** in solution, the presence of the phthalimide chromophore in the molecule has essentially no effect on these parameters. This can be likely rationalized by the fact that the distance between the phthalimide and the Tb^{III} center is too long (>15 Å) for an efficient energy transfer (Vázquez López et al., 2010). In contrast, in amorphous solid state the orientation of the molecules is random and the phthalimide units can be located closer to the Tb^{III}-DOTA moieties, making non-covalent energy transfer and Tb^{III} sensitization through this way possible (Howell et al., 2003). Quantum yield values of **Tb-12a** and **Tb-12b** in the solid state are higher by 7.5 and 2.7 times, respectively, compared to these in 0.2 mM solutions, while lifetimes are lower by 25–30%. Such behavior points that in the solid state non-radiative processes are minimized and/or sensitization efficiencies are improved. Higher increase of the Q_{Tb}^L -value in the case of **Tb-12a** compared to the **Tb-12b** might be caused by an appearance of an additional sensitization pathway. Indeed, if we assume that the main

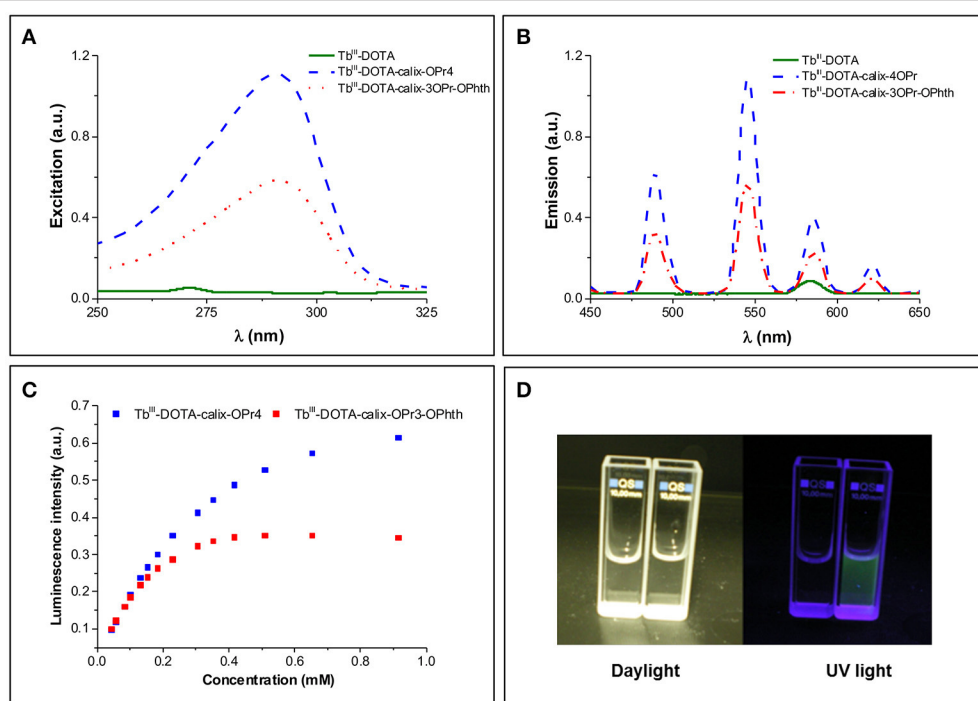


FIGURE 3 | (A) Excitation ($\lambda_{\text{Em}} = 545 \text{ nm}$) and **(B)** emission ($\lambda_{\text{Ex}} = 290 \text{ nm}$) spectra of Tb^{III} -DOTA, **Tb-12a** and **Tb-12b** at a Tb^{III} concentration of 3.68 mM (corresponding to a calix[4]arene concentration of 0.92 mM). The two little signals at 272 nm (excitation) and 580 nm (emission) in the Tb^{III} -DOTA spectra are artifacts from light scattering (double wavelength of excitation); **(C)** The dependence of relative luminescence intensities normalized to the same initial value vs. the concentration of **Tb-12a** and **Tb-12b**; **(D)** Photographic images of Tb^{III} -DOTA (left cuvette) and **Tb-12a** (right cuvette) under daylight and UV irradiation.

energy transfer mechanism is of Förster type (dipole-dipole), the sensitization efficiency depends significantly on distance and is proportional to $(1/r_{\text{Tb-L}})^{-6}$. Thus, small changes in the distance between the chromophore and Tb^{III} ion may have significant effects on the sensitization efficiency. This is also reflected in 3.1-times higher quantum yield value for **Tb-12a** compared to **Tb-12b** while observed luminescence lifetimes are the same for both complexes (Table 1). Moreover, slight broadening and red-shifting of the excitation band is observed for **Tb-12a** vs. **Tb-12b** is observed for **Tb-12a** vs. **Tb-12b** that can indicate that other lower-energy levels are involved in the sensitization of the former complex (Supplementary Figure 4, left). Since this extra shoulder, only present in the solid-state excitation spectrum, overlaps with one of the UV absorption peaks of the phthalimide moiety (Supplementary Figure 6), it may indicate that in the solid state the phthalimide group can indeed participate in the sensitisation of the Tb^{III} luminescence. In addition, the quantum yield values confirm the trend that was observed qualitatively for solutions with different concentrations (Figure 3C vs. Table 1): they increase upon dilution evidencing a non-linear correlation between the luminescence intensity and the concentration of the investigated compounds. Concentration of solutions has also effect on luminescence lifetimes. It should be noted here that for all solutions luminescence decay curves could be best fitted by mono-exponential functions reflecting the presence of only one type of emissive Tb^{III} -containing species. The values of

TABLE 1 | Photo-physical parameters of Tb^{III} complexes in the solid state and aqueous solutions at 298 K.^a

Compound	State/Solvent	c (mM)	τ_{obs} (ms)	Q_{Tb}^L (%)
Tb-12a	Solid	–	1.2(1) ^b	5.87(9)
	H_2O	0.04	1.52(1)	0.78(7)
		0.2	1.51(1)	0.65(1)
		2	0.83(5)	0.51(2)
Tb-12b	Solid	–	1.2(1) ^b	1.89(3)
	H_2O	0.2	1.6(1)	0.71(3)
		2	0.79(5)	0.38(6)

^aUnder excitation at 300 nm. Standard deviations (2σ) are given between parentheses; Estimated relative errors: τ_{obs} , $\pm 5\%$; Q_{Tb}^L , $\pm 10\%$.

^bThe longest values are presented. Luminescence decay curves were best fitted by biexponential functions however the impact of the second short-lived lifetime value (0.17–0.22 ms) was only 5–6%.

τ_{obs} increase by 1.8–2.0 times when going from 2 to 0.2 mM solutions, i.e., following the same trend as absolute quantum yield values.

To get a hint about possible reasons of such changes of luminescent parameters, we have investigated the aggregation of the complexes in details. It has been previously described that the DOTA-functionalized calix[4]arene (**Gd-12b**) is highly amphiphilic and tends to aggregate in aqueous solution. At concentrations above 0.21 mM, they form micelles with a

hydrodynamic radius of 2.2 nm and a narrow size distribution (Schühle et al., 2009). This critical micelle concentration (*cmc*) was determined for the Gd^{III} complex by measuring the water proton relaxation rates as a function of the concentration.

In the current study, the aggregation was demonstrated by using Nile red, a dye exhibiting fluorescence changes in the emission maximum upon changes in the chemical environment. In the samples containing Nile red and increasing concentrations of the Tb^{III} complexes **12a** and **12b**, the fluorescence emissions undergoes strong blue-shifts and intensity increase, which can be associated with a decreasing hydrophilicity and polarity of the environment (Figure 4). Indeed, as the amphiphilic calix[4]arene complexes aggregate to micelles, the Nile red

will enter the internal micellar core and will experience a more hydrophobic environment. From this experiment, the critical micelle concentrations of Tb^{III}-DOTA-calix-3OPr-OPht (Tb-**12a**) and Tb^{III}-DOTA-calix-4OPr (Tb-**12b**) were determined to be 0.12 and 2.3 mM, respectively (Supplementary Figure 7). Obviously, the presence of phthalimide dramatically increases the hydrophobicity of the *lower rim* forces the molecules to aggregate at lower concentrations and thus leads to a lower *cmc*. Interestingly, the determined *cmc*-values correlate nicely with the maxima of the concentration dependent luminescence intensities (Figure 3C and Supplementary Figure 3), which are around 0.35 and 1.6 mM for Tb-**12a** and Tb-**12b**, respectively. This evidences that aggregation of the calix[4]arenes leads to a significant decrease in the intensity of Tb^{III} luminescence. As the aromatic systems come closer to each other, non-radiative energy transfer from the excited π -systems becomes more likely which reduces luminescence quantum yields of the aggregated complexes. As a result, decreased quantum yields and shorter luminescence lifetimes are observed.

Surprisingly, the *cmc*-value previously determined by relaxometric measurements for the Gd-**12b** analog (0.21 mM) is significantly lower than *cmc* found in the Nile red experiment for Tb-**12b** (2.3 mM). It is very unlikely that this is due to the different ions complexed in the DOTA chelates, as lanthanides in general have very similar chemical properties. Furthermore, Gd and Tb are neighbors in the lanthanide series thus have similar ionic radii (difference $\sim 0.1 \text{ \AA}$) and identical charge. The almost one order of magnitude difference in *cmc* can rather be explained by the different experimental methods applied for its determination. The relaxometric method used in the case of the paramagnetic analog Gd^{III}-**12b** is based on the effect of the rotational motion on the r_1 relaxivity (longitudinal

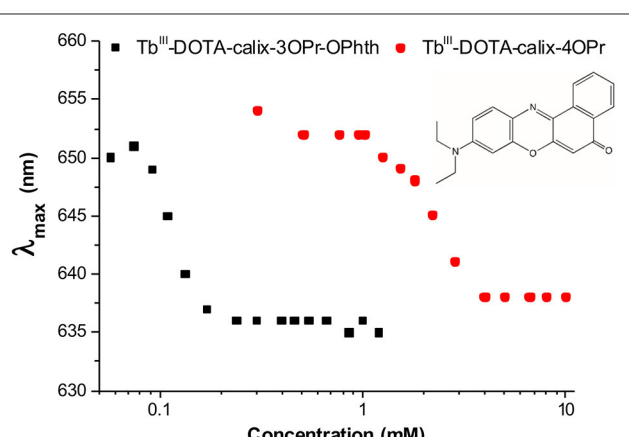


FIGURE 4 | Wavelength of the fluorescence emission maximum (λ_{max}) vs. Tb^{III} concentration in solutions of Tb^{III}-complexes **12a** (black) and **12b** (red) in the presence of Nile red ($\lambda_{\text{Ex}} = 550 \text{ nm}$).

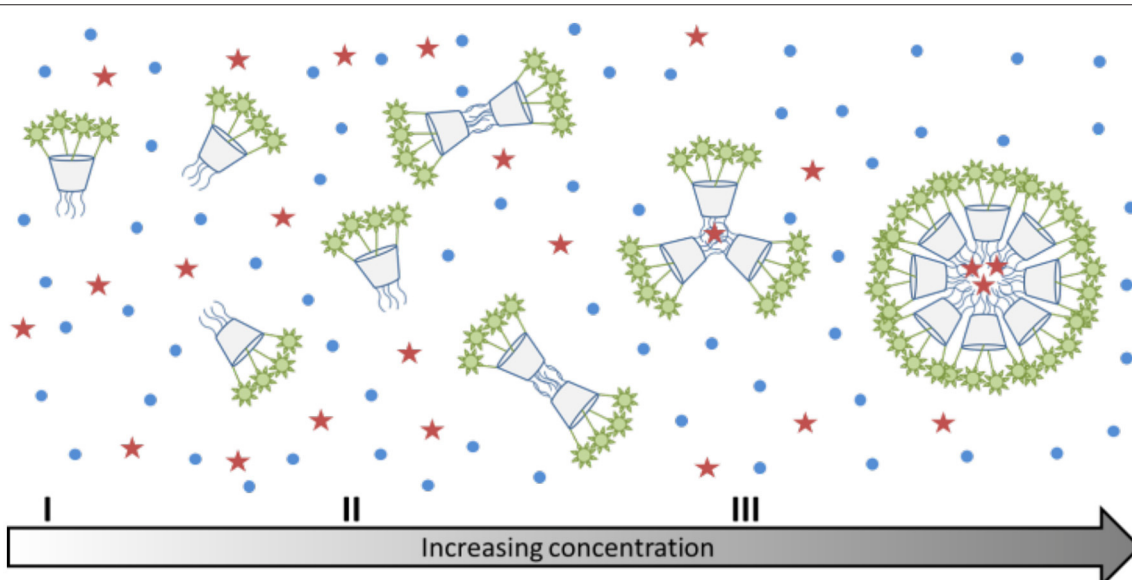


FIGURE 5 | (I-III) Schematic representation of the aggregation behavior of calix[4]arenes **7a** and **7b** with increasing concentration. The red stars indicate the location of Nile red, which can only enter the micelles, when there is a sufficiently large hydrophobic space.

relaxation rate expressed in $\text{mM}^{-1}\text{s}^{-1}$ of Gd^{III}). Indeed, at medium fields, the relaxivity increases with the increasing rotational correlation time, τ_{R} (slower motion) of the complex. While τ_{R} already changes when as few as two molecules start interacting (**Figures 5I,II**), the creation of noticeable hydrophobic compartments in micelles leading to an observable change in the fluorescence of the dye only starts at a higher degree of aggregation, when several amphiphilic molecules aggregate (**Figure 5III**). Therefore, the *cmc* determined by the fluorescence method using Nile red is significantly higher than the one obtained *via* relaxivity measurements. Previous studies have already pointed out that the *cmc*-value obtained can be dependent on the nature of the physical parameter monitored to assess the aggregation and that premicellar aggregation is often responsible for anomalies of various physical parameters (Pérez-Rodríguez et al., 1999; He et al., 2004).

It is interesting to note that the concentration dependent luminescence intensities of **Tb-12b** (**Figure 3C**) start to show a deviation from linearity at $\sim 0.25 \text{ mM}$ concentration, which corresponds to the *cmc* determined from the relaxivity method for the Gd^{III} analog. These results nicely demonstrate that micelle formation is not a sharp transition, but it expands over a concentration range that might cover more than an order of magnitude. As the various techniques used to determine the critical micelle concentration sense different physical parameters, they might lead to method-dependent *cmc*-values.

Upon aggregation of the functionalized calix[4]arenes, the hydrophilic Tb^{III} -DOTA moieties on the *upper rim* will always face the aqueous phase. The lifetimes observed for the aggregated state (0.83 and 0.79 ms) are smaller than those measured for the monomers (1.51 and 1.60 ms) of **12a** and **12b**, respectively. This points to a better protection of the Tb^{III} ion from non-radiative deactivations in the case of the monomers. An increase of Tb-luminescence lifetimes occurs upon exclusion of water molecules from the first coordination sphere of the metal ion (Murru et al., 1993; Chen et al., 2013). In our case, a possible explanation of the shortening of luminescence lifetimes found for the micellar Tb^{III} -DOTA-functionalized calix[4]arenes could be an enhanced cross-relaxation between Tb^{III} ions and the formation of a more defined second coordination sphere around the micelle consisting of water molecules clustered *via* hydrogen bonds.

CONCLUSIONS

In summary, we have synthesized the first luminescent lanthanide complex based on a calix[4]arene platform with

sufficient stability due to the presence of four DOTA chelating units for potential biological use. We have evidenced for this prototype Tb^{III} probe that the calix[4]arene backbone is actively participating to the excitation process of the Tb^{III} -centered luminescence, while the chromophore introduced on the rim opposite to the lanthanide chelate is localized too far to provide efficient sensitization. The substitution pattern of the *lower rim* dictates the aggregation phenomena observed in aqueous solution and can be exploited to tailor the physical-chemical properties of the compound. This micellar aggregation of the calix[4]arene derivatives has a strong impact on their luminescence properties. Upon increasing the complex concentration, the luminescence intensities linearly increase up to the range where micellar aggregation starts to occur, and then they decline. Taking into account these peculiar properties, the future perspectives of the described systems may be based on the complexation of both luminescent Ln^{III} and paramagnetic Gd^{III} ions within the same molecule. This in turn, could yield dual MR/optical imaging probes in a straightforward manner rendering the calix[4]arene backbone a valuable building block for the design of imaging probes.

AUTHOR CONTRIBUTIONS

All authors have contributed equally to the experimental as well as to the writing process of the manuscript. All authors read and approved the final version of the manuscript.

ACKNOWLEDGMENTS

Thanks are due to The Smart Loire Valley Program's Fellowship supported by the European Union's Horizon 2020 research and innovation program under the Marie Skłodowska-Curie grant agreement nr. 665790. The authors thank Mr. Maarten C. J. K. Gorseling (Biotechnology, TU Delft) for the technical support on chromatography. La Ligue Contre le Cancer and La Région Centre (France) are also acknowledged for financial support. SP acknowledges support from the Institut National de la Santé et de la Recherche Médicale (INSERM).

SUPPLEMENTARY MATERIAL

The Supplementary Material for this article can be found online at: <https://www.frontiersin.org/articles/10.3389/fchem.2018.00001/full#supplementary-material>

REFERENCES

- Baldini, L., Cacciapaglia, R., Casnati, A., Mandolini, L., Salvio, R., Sansone, F., et al. (2012). Upper rim guanidinocalix[4]arenes as artificial phosphodiesterases. *J. Org. Chem.* 77, 3381–3389. doi: 10.1021/jo300193y
- Blanchard, S., Le Clainche, L., Rager, M.-N., Chansou, B., Tuchagues, J.-P., Duprat, A. F., et al. (1998). Calixarene-based copper(I) complexes as models for monocopper sites in enzymes. *Angew. Chem. Int. Ed.* 37, 2732–2735.
- doi: 10.1002/(SICI)1521-3773(19981016)37:19<2732::AID-ANIE2732>3.0.CO;2-7
- Bonnet, C. S., Pellegratti, L., Buron, F., Shade, C. M., Villette, S., Kubicek, V., et al. (2010). Hydrophobic chromophore cargo in micellar structures: a different strategy to sensitize lanthanide cations. *Chem. Commun.* 46, 124–126. doi: 10.1039/B918881A
- Bunzli, J. C. G., Froidevaux, P., and Harrowfield, J. M. (1993). Complexes of lanthanoid salts with macrocyclic ligands. 41. Photophysical properties of

- lanthanide dinuclear complexes with p-tert-butylcalix[8]arene. *Inorg. Chem.* 32, 3306–3311. doi: 10.1021/ic00067a019
- Bünzli, J.-C. G. (2015). On the design of highly luminescent lanthanide complexes. *Coord. Chem. Rev.* 293–294, 19–47. doi: 10.1016/j.ccr.2014.10.013
- Bünzli, J.-C. G., Ihringer, F., Dumy, P., Sager, C., and Rogers, R. D. (1998). Structural and dynamic properties of calixarene bimetallic complexes: solution versus solid-state structure of dinuclear complexes of Eu^{III} and Lu^{III} with substituted calix[8]arenes. *J. Chem. Soc. Dalton Trans.* 497–504. doi: 10.1039/a706933b
- Chen, G., Wardle, N. J., Sarris, J., Chatterton, N. P., and Bligh, S. W. A. (2013). Sensitized terbium(III) macrocyclic-phthalimide complexes as luminescent pH switches. *Dalton Trans.* 42, 14115–14124. doi: 10.1039/c3dt51236c
- Darwent, J. R., Dong, W., Flint, C. D., and Sharpe, N. W. (1993). Intermolecular energy transfer between phenanthrene and lanthanide ions in aqueous micellar solution. *J. Chem. Soc. Faraday Trans.* 89, 873–880. doi: 10.1039/ft9938900873
- Escabi-Perez, J. R., Nome, F., and Fendler, J. H. (1977). Energy transfer in micellar systems. steady state and time resolved luminescence of aqueous micelle solubilized naphthalene and terbium chloride. *J. Am. Chem. Soc.* 99, 7749–7754. doi: 10.1021/ja00466a001
- Fischer, C., Sarti, G., Casnati, A., Carrettoni, B., Manet, I., Schuurman, R., et al. (2000). 2,2'-Bipyridine lariat calixcrowns: a new class of encapsulating ligands forming highly luminescent Eu³⁺ and Tb³⁺ complexes. *Chem. Eur. J.* 6, 1026–1034. doi: 10.1002/(SICI)1521-3765(20000317)6:6<1026::AID-CHEM1026>3.0.CO;2-C
- Gutsche, C. D., and Lin, L.-G. (1986). Calixarenes 12. *Tetrahedron* 42, 1633–1640. doi: 10.1016/S0040-4020(01)87580-3
- Gutsche, C. D., and Muthukrishnan, R. (1978). Calixarenes. 1. Analysis of the product mixtures produced by the base-catalyzed condensation of formaldehyde with para-substituted phenols. *J. Org. Chem.* 43, 4905–4906. doi: 10.1021/jo00419a052
- Gutsche, C. D., and Iqbal, M. (1990). p-tert-Butylcalix[4]arene. *Org. Synth.* 68, 234–237. doi: 10.15227/orgsyn.068.0234
- He, X., Liang, H., Huang, L., and Pan, C. (2004). Complex microstructures of amphiphilic diblock copolymer in dilute solution. *J. Phys. Chem. B* 108, 1731–1735. doi: 10.1021/jp0359337
- Howell, C. R., Edwards, H. S., Gajadhar-Plummer, S. A., Kahwa, A. I., Mcpherson, L. G., Mague, T. J., et al. (2003). Phthalimides: supramolecular interactions in crystals, hypersensitive solution ¹H-NMR dynamics and energy transfer to Europium(III) and Terbium(III) States. *Molecules* 8, 565–592. doi: 10.3390/molecules8070565
- Kelderman, E., Verboom, W., Engbersen, J. F. J., Reinhoudt, D. N., Heesink, G. J. T., Van Hulst, N. F., et al. (1992). Nitrocalix [4]arenes as molecules for second-order nonlinear optics. *Angew. Chem. Int. Ed. Engl.* 31, 1075–1077. doi: 10.1002/anie.199210751
- Klimentová, J., and Vojtíšek, P. (2007). New receptors for anions in water: Synthesis, characterization, X-ray structures of new derivatives of 5,11,17,23-tetraamino-25,26,27,28-tetrapropoxycalix[4]arene. *J. Mol. Struct.* 826, 48–63. doi: 10.1016/j.molstruc.2006.04.016
- Konczyk, J., Nowik-Zajac, A., and Kozłowski, C. A. (2016). Calixarene-based extractants for heavy metal ions removal from aqueous solutions. *Sep. Sci. Technol.* 51, 2394–2410. doi: 10.1080/01496395.2016.1209219
- Lalor, R., Digesso, J. L., Mueller, A., and Matthews, S. E. (2007). Efficient gene transfection with functionalised multicalixarenes. *Chem. Commun.* 4907–4909. doi: 10.1039/b712100h
- Lawal, O., Iqbal, K. S. J., Mohamadi, A., Razavi, P., Dodd, H. T., Allen, M. C., et al. (2009). An artificial sodium ion channel from calix[4]arene in the 1,3-alternate conformation. *Supramol. Chem.* 21, 55–60. doi: 10.1080/10610270802528307
- Modi, K., Panchal, U., Mehta, V., Panchal, M., Kongor, A., and Jain, V. K. (2016). Propyl phthalimide-modified thiocalixphenyl[4]arene as a “turn on” chemosensor for Hg(II) ions. *J. Lumin.* 179, 378–383. doi: 10.1016/j.jlumin.2016.07.019
- Murru, M., Parker, D., Williams, G., and Beeby, A. (1993). Luminescence behaviour of stable europium and terbium complexes of tetraaza phosphinates: efficient through-space energy transfer from phenyl to terbium. *J. Chem. Soc. Chem. Commun.* 1116–1118. doi: 10.1039/c39930001116
- Pérez-Rodríguez, M., Varela, L. M., García, M., Mosquera, V., and Sarmiento, F. (1999). Conductivity and relative permittivity of sodium n-dodecyl sulfate and n-dodecyl trimethylammonium bromide. *J. Chem. Eng. Data* 44, 944–947. doi: 10.1021/je980301c
- Sato, N., Yoshida, I., and Shinkai, S. (1993). Energy-transfer luminescence of lanthanide ions complexed with water-soluble calix[n]arenes. *Chem. Lett.* 22, 1261–1264. doi: 10.1246/cl.1993.1261
- Schühle, D. T., Peters, J. A., and Schatz, J. (2011). Metal binding calixarenes with potential biomimetic and biomedical applications. *Coord. Chem. Rev.* 255, 2727–2745. doi: 10.1016/j.ccr.2011.04.005
- Schühle, D. T., Polasek, M., Lukes, I., Chauvin, T., Toth, E., Schatz, J., et al. (2010). Densely packed Gd(III)-chelates with fast water exchange on a calix[4]arene scaffold: a potential MRI contrast agent. *Dalton Trans.* 39, 185–191. doi: 10.1039/B917673J
- Schühle, D. T., Schatz, J., Laurent, S., Vander Elst, L., Muller, R. N., Stuart, M. C. A., et al. (2009). Calix[4]arenes as molecular platforms for magnetic resonance imaging (MRI) contrast agents. *Chem. Eur. J.* 15, 3290–3296. doi: 10.1002/chem.200802099
- Sreenivasu Mummidivaparu, V. V., Hinge, V. K., and Rao, C. P. (2015). Interaction of a dinuclear fluorescent Cd(II) complex of calix[4]arene conjugate with phosphates and its applicability in cell imaging. *Dalton Trans.* 44, 1130–1141. doi: 10.1039/C4DT01726A
- Vázquez López, M., Eliseeva, S. V., Blanco, J. M., Rama, G., Bermejo, M. R., Vázquez, M. E., et al. (2010). Synthesis and photophysical properties of Ln^{III}-DOTA-Bipy complexes and Ln^{III}-DOTA-Bipy-Ru^{II} coordination conjugates. *Eur. J. Inorg. Chem.* 2010, 4532–4545. doi: 10.1002/ejic.20100051

Conflict of Interest Statement: The authors declare that the research was conducted in the absence of any commercial or financial relationships that could be construed as a potential conflict of interest.

Copyright © 2018 Mayer, Tiruvadi Krishnan, Schühle, Eliseeva, Petoud, Tóth and Djanashvili. This is an open-access article distributed under the terms of the Creative Commons Attribution License (CC BY). The use, distribution or reproduction in other forums is permitted, provided the original author(s) and the copyright owner are credited and that the original publication in this journal is cited, in accordance with accepted academic practice. No use, distribution or reproduction is permitted which does not comply with these terms.



A Novel Metal-Based Imaging Probe for Targeted Dual-Modality SPECT/MR Imaging of Angiogenesis

Charalampos Tsoukalas¹, Dimitrios Psimadas¹, George A. Kastis^{1,2}, Vassilis Koutoulidis³, Adrian L. Harris⁴, Maria Paravatou-Petsotas¹, Maria Karageorgou^{1,5}, Lars R. Furenlid^{6,7}, Lia A. Moulopoulos³, Dimosthenis Stamopoulos^{5,8} and Penelope Bouziotis^{1*}

OPEN ACCESS

Edited by:

Lorenzo Tei,
Università degli Studi del Piemonte
Orientale, Italy

Reviewed by:

Graeme J. Stasiuk,
University of Hull, United Kingdom

Johannes Notni,
Technische Universität München,
Germany

Calogero D'Alessandria,
Klinikum rechts der Isar, Technische
Universität München, Germany

*Correspondence:

Penelope Bouziotis
bouzioti@rrp.demokritos.gr

Specialty section:

This article was submitted to
Medicinal and Pharmaceutical
Chemistry,
a section of the journal
Frontiers in Chemistry

Received: 02 March 2018

Accepted: 30 May 2018

Published: 20 June 2018

Citation:

Tsoukalas C, Psimadas D, Kastis GA,
Koutoulidis V, Harris AL,
Paravatou-Petsotas M,
Karageorgou M, Furenlid LR,
Moulopoulos LA, Stamopoulos D and
Bouziotis P (2018) A Novel
Metal-Based Imaging Probe for
Targeted Dual-Modality SPECT/MR
Imaging of Angiogenesis.
Front. Chem. 6:224.
doi: 10.3389/fchem.2018.00224

¹ Radiochemical Studies Laboratory, Institute of Nuclear & Radiological Sciences & Technology, Energy & Safety, National Center for Scientific Research "Demokritos," Athens, Greece, ² Research Center of Mathematics, Academy of Athens, Athens, Greece, ³ First Department of Radiology, School of Medicine, National and Kapodistrian University of Athens, Athens, Greece, ⁴ Weatherall Institute of Molecular Medicine, University of Oxford, Oxford, United Kingdom, ⁵ Department of Solid State Physics, National and Kapodistrian University of Athens, Athens, Greece, ⁶ Department of Medical Imaging, Center for Gamma-Ray Imaging, University of Arizona, Tucson, AZ, United States, ⁷ College of Optical Sciences, University of Arizona, Tucson, AZ, United States, ⁸ Institute of Nanoscience and Nanotechnology, National Center for Scientific Research "Demokritos," Athens, Greece

Superparamagnetic iron oxide nanoparticles with well-integrated multimodality imaging properties have generated increasing research interest in the past decade, especially when it comes to the targeted imaging of tumors. Bevacizumab (BCZM) on the other hand is a well-known and widely applied monoclonal antibody recognizing VEGF-A, which is overexpressed in angiogenesis. The aim of this proof-of-concept study was to develop a dual-modality nanoplateform for *in vivo* targeted single photon computed emission tomography (SPECT) and magnetic resonance imaging (MRI) of tumor vascularization. Iron oxide nanoparticles (IONPs) have been coated with dimercaptosuccinic acid (DMSA), for consequent functionalization with the monoclonal antibody BCZM radiolabeled with ^{99m}Tc, via well-developed surface engineering. The IONPs were characterized based on their size distribution, hydrodynamic diameter and magnetic properties. *In vitro* cytotoxicity studies showed that our nanoconstruct does not cause toxic effects in normal and cancer cells. Fe₃O₄-DMSA-SMCC-BCZM-^{99m}Tc were successfully prepared at high radiochemical purity (>92%) and their stability in human serum and in PBS were demonstrated. *In vitro* cell binding studies showed the ability of the Fe₃O₄-DMSA-SMCC-BCZM-^{99m}Tc to bind to the VEGF-165 isoform overexpressed on M-165 tumor cells. The *ex vivo* biodistribution studies in M165 tumor-bearing SCID mice showed high uptake in liver, spleen, kidney and lungs. The Fe₃O₄-DMSA-SMCC-BCZM-^{99m}Tc demonstrated quick tumor accumulation starting at 8.9 ± 1.88%ID/g at 2 h p.i., slightly increasing at 4 h p.i. (16.21 ± 2.56%ID/g) and then decreasing at 24 h p.i. (6.01 ± 1.69%ID/g). The tumor-to-blood ratio reached a maximum at 24 h p.i. (~7), which is also the case for the tumor-to-muscle ratio (~18). Initial pilot imaging studies on an experimental gamma-camera

and a clinical MR camera prove our hypothesis and demonstrate the potential of Fe_3O_4 -DMSA-SMCC-BCZM- $^{99\text{m}}\text{Tc}$ for targeted dual-modality imaging. Our findings indicate that Fe_3O_4 -DMSA-SMCC-BCZM- $^{99\text{m}}\text{Tc}$ IONPs could serve as an important diagnostic tool for biomedical imaging as well as a promising candidate for future theranostic applications in cancer.

Keywords: SPECT/MRI, bevacizumab, iron oxide nanoparticles, angiogenesis, dual-modality imaging

INTRODUCTION

Through the last two decades researchers have introduced many innovations in the area of imaging and therapy. Nanoparticles (NPs) with or without conjugated target moieties have proven invaluable tools in cancer research for multimodal imaging and targeted drug delivery as well as hyperthermia and/or controlled release treatment (Lee and Chen, 2009; Bouziotis et al., 2013). More specifically, magnetite NPs (IONPs) such as iron oxide NPs have many advantages such as their controlled size, their facile chemical modification and their ability to be manipulated by an external magnetic field, resulting in a specific, topical accumulation of IONPs and a consequent T2-enhanced MRI signal. Development of such novel imaging tools bearing optimized imaging characteristics can lead to early diagnosis and thus improved patient management.

Nanotechnology-based drug delivery platforms have emerged as a “complete system” for cancer diagnosis and therapy. More specifically, NP-based drug delivery systems can improve solubility and circulation time of therapeutic agents, resulting in overcoming limitations e.g., poor pharmacokinetics, relative to conventional drug formulations (van Vlerken and Amiji, 2006; Anselmo and Mitragotri, 2016). The enhanced permeability and retention (EPR) effect is of great importance, because it can “drive” NP systems to accumulate in the disease site by extravasation through leaky blood vessels (Torchilin, 2014). However, this passive diffusion is not enough for selective nanoparticle uptake in cancer cells (Bertrand et al., 2014).

The ability of nanoparticles to effectively travel across the tumor vessel wall to the interstitial space depends on the ratio of particle size to the size of the openings (Chauhan et al., 2012). On one hand, if this ratio is small, the transport of the particle through the pores of the wall is unhindered. On the other hand, if the size of the nanoparticle is comparable to the size of the openings, the particle will interact with the pores and the transport might be severely hindered. Moreover, large nanoparticles (>40 nm in diameter) even if they manage to cross the vessel wall, they might not be able to penetrate the dense extracellular matrix of the tumor interstitial space (Pluen et al., 2001). Indeed in many tumors, a desmoplastic response might occur that can lead to excessive production of extracellular fibers resulting in limited penetration of nanoparticles (Chauhan et al., 2011).

Following another approach, and in order to overcome these problems, NPs have been conjugated/complexed with various targeting moieties (e.g., small molecules, antibodies, peptides, and aptamers) leading to increased retention and accumulation

in the tumor vasculature as well as selective and efficient internalization by target tumor cells (Zhong et al., 2014). These active targeting NP platforms achieve superior specificity, providing enhanced imaging and/or therapeutic performances compared to their passive targeting analogues.

As far as diagnostic imaging is concerned, it is not feasible to obtain all the necessary information for a particular system from a single imaging modality (De Rosales et al., 2011; Lee et al., 2014). The radionuclide-based SPECT (single photon emission computed tomography) or PET (positron emission tomography) imaging techniques offer high sensitivity but poor resolution, while MRI offers high-resolution anatomical information, but suffers from low sensitivity. Using these combinations, imaging scanners nowadays are capable of providing molecular and physiological information with remarkable sensitivity using PET and SPECT radiotracers and, at the same time, anatomical information of the tissues of interest. A hybrid SPECT/MRI probe: a) has the potential to provide better probe concentration quantification from the acquired SPECT signal, and higher spatial resolution from MRI contrast, thus leading to images that offer more relevant biological information than could be acquired from either imaging modality alone (Hoffman et al., 2014) and can highlight the value of validating different imaging methods against one another. Thus, the combination of SPECT/MRI or PET/MRI can offer synergistic advantages and lead to the more accurate *in vivo* interpretation of disease and abnormalities.

Dual modality contrast agents have already started making their mark in medical imaging. The combination of PET/SPECT with MRI can offer synergistic advantages for sensitive, high-resolution, and quantitative imaging, which can lead to the more accurate, noninvasive interpretation of disease and abnormalities and early detection of various diseases e.g., cancer (Ai et al., 2016).

Simultaneous optical and MR imaging of cancers was recently investigated by labeling recombinant humanized monoclonal antibodies or high-affinity small peptides against tumor receptors, which serve as targeting ligands, with near infrared dyes, and conjugating them to MNPs for simultaneous optical and MR imaging of cancers (Lin et al., 2018). Additionally, peptide-modified gadolinium oxide nanoprobes containing fluorescein for targeted MR/optical dual-modality imaging of various cancers have been engineered (Cui et al., 2017). Live-cell imaging studies suggest that amphiphilic dual-modality nanoprobes, containing a fluorophore for optical imaging and a metal ion chelator complexed with Gd for MRI, can self-assemble into supramolecular nanostructures and effectively label cells (Liu et al., 2015). The formation of new blood vessels

de novo (vasculogenesis) normally occurs in fetus and in uterus assuring the supply of nutrients and oxygen to proliferating tissues (Carmeliet, 2005). However, the formation of new blood vessels from pre-existing ones (angiogenesis) is also critical in the development of various disorders including cancer, wound healing and inflammation (Eliceiri and Cheresh, 1999). As far as carcinogenesis is concerned many molecules and receptors are involved in angiogenesis regulation providing important targets for tumor diagnosis and therapy. Vascular endothelial growth factor (VEGF) is a signal protein that stimulates angiogenesis, which can contribute to tumorigenesis when it is overexpressed. The VEGF family of glycoproteins comprises five members, with the VEGF-A being the essential one for the growth and metastasis of tumors. The recombinant humanized monoclonal antibody Bevacizumab (BCZM) is an angiogenesis inhibitor that blocks angiogenesis by binding to VEGF-A (Los et al., 2007). It was developed from a murine antibody (A 4.6.1) and humanized, while retaining the specificity of the original molecule.

BCZM has been approved for the treatment of a variety of metastatic cancers and can be an ideal molecule that can target tumor sites by VEGF-A targeting (Shih and Lindley, 2006). Even though a lot of research has been performed on *in vivo* NP distribution, only a few studies are available on antibody-targeted NPs (Schroeder et al., 2012; Karmani et al., 2013). In the present study we investigated the efficacy of conjugating BCZM onto IONPs and the radiolabeling of the functionalized nanosystems with ^{99m}Tc , for imaging VEGF-expressing tumors. The radiolabeled nanoformulations were evaluated *in vitro* as well as *in vivo* in tumor angiogenesis models. Active targeting afforded by Fe_3O_4 -DMSA-SMCC-BCZM- ^{99m}Tc was evaluated in M165 tumor-bearing mice, in comparison to the non-specific Fe_3O_4 -DMSA- ^{99m}Tc IONPs. In order to prove the efficacy of the targeted approach, preliminary imaging studies on tumor-bearing animals using MRI and gamma-ray scintigraphy were performed, which demonstrate the potential of Fe_3O_4 -DMSA-SMCC-BCZM- ^{99m}Tc for targeted dual-modality imaging.

MATERIALS AND METHODS

Chemicals

All chemicals were reagent grade and were used as such unless otherwise noted. Iron(II) chloride tetrahydrate ($\text{FeCl}_2 \cdot 4\text{H}_2\text{O}$, Reagent Plus, 99%) and iron(III)chloride (FeCl_3 , reagent grade, 97%) were purchased from Sigma-Aldrich. Analytical grade NH_4OH was purchased from AnalytiCals (Carlo Erba). Purified deionized water was prepared by the Milli-Q system (Millipore Co., Billerica, MA, USA). Technetium-99m, in the form of $\text{Na}^{99m}\text{TcO}_4$ in physiological saline, was eluted from a commercial $^{99}\text{Mo}/^{99m}\text{Tc}$ generator acquired from GE Healthcare Ltd (United Kingdom). The monoclonal antibody Bevacizumab (Avastin[®]) was purchased from Roche (United Kingdom). Sulfo-SMCC (sulfosuccinimidyl 4-(N-maleimidomethyl)cyclohexane-1-carboxylate) was purchased from Thermo Fischer Scientific, while *meso*-2,3-Dimercaptosuccinic acid and human serum were acquired from Sigma-Aldrich (St. Louis, MO, USA). The human embryonic kidney cell line HEK293 was acquired from the American Type Culture Corporation, while the MDA MB 231

breast cancer cells transfected with the VEGF-165 isoform (M165) were donated by Cancer Research UK. For cell culturing, Dulbecco's modified Eagle medium (DMEM), fetal bovine serum (FBS), penicillin/streptomycin, L-glutamine, and trypsin/EDTA solution were purchased from PAA Laboratories (GmbH, Austria). The MTT tetrazolium salt, (3-[4,5-dimethylthiazol-2-yl]-2,5-diphenyltetrazolium bromide, was acquired from Thermo Fisher Scientific (Cat. No. M6494).

Equipment

Radioactivity of the TcO_4^- eluent was measured using a dose calibrator (Capintec, Ramsey, NJ). Thin-layer chromatography (TLC) silica gel 60 sheets ($5 \times 10\text{ cm}$) were purchased from Merck (Darmstadt, Germany) and along with a Radio-TLC Scanner (Scan-Ram, LabLogic, Sheffield, UK) were used in the determination of radiolabeling yield/purity and *in vitro* stability studies. Radiolabeling yield of the radiolabeled antibody was assessed by HPLC (Waters). PD-10 columns (GE Healthcare), containing Sephadex G-25 resin, were used for the purification of the mercaptoethanol-reduced monoclonal antibody, while Amicon filters (cut-off value: 100 kD) were used for purification of the radiolabeled antibody. Water was deionized to $18\text{ M}\Omega\text{-cm}$ using an easy-pure water filtration system (Barnstead International, Dubuque, Iowa). A gamma scintillation counter, a Packard Cobra II, was used to measure the radioactivity of each organ and blood samples in *ex vivo* biodistribution studies. An AXIOS-150/EX (Triton Hellas) dynamic light scattering (DLS) apparatus equipped with a 30 mW He-Ne laser emitting at 658 nm and an Avalanche photodiode detector at an angle of 90° was used for the determination of the size distributions of the nanoparticles.

Planar Scintigraphy studies were performed on a compact, high-resolution, gamma-ray camera developed at the Center for Gamma-Ray Imaging of the University of Arizona. Details of the system can be found elsewhere (Furenlid et al., 2004, 2005; Chen et al., 2005). The system comprises a 5-mm thick $\text{NaI}(\text{Ti})$ scintillation crystal, a 12-mm thick quartz light guide, a 3×3 array of 1.5-inch diameter photomultiplier tubes (PMTs), and a 40-mm thick lead parallel-hole collimator with hexagonal holes 1 mm in diameter. The system achieves a spatial resolution of about 2.5 mm at the collimator. The field-of-view of the camera is 4.0×4.0 in, enough to image a whole mouse without any translation.

MRI studies were performed on a 3 Tesla MRI Unit (Philips Ingenia, Philips Medical Systems, Best, The Netherlands).

Experimental

Synthesis of Fe_3O_4 IONPs

Superparamagnetic iron oxide nanoparticles (IONPs) were synthesized in-house, according to a previously reported procedure by mixing 40.5 mg (0.25 mmol) anhydrous FeCl_3 (MW 160.20) and 49.7 mg (0.25 mmol) $\text{FeCl}_2 \cdot 4\text{H}_2\text{O}$ (MW 198.81) in ultrapure water (Stamopoulos et al., 2007). Subsequently, the complete precipitation of the IONPs was achieved by the abrupt addition of 1.5 ml of a solution of NH_4OH ($\text{NH}_4\text{OH}:\text{H}_2\text{O}$ 1:2) to the suspension (pH 9-9.5). The vials were immediately sealed, to avoid exposure to atmospheric

O_2 and were intensely stirred. The solution was subjected to magnetic decantation followed by repeated washing with distilled water (pH 6.5).

Functionalization of IONPs With DMSA

Fe_3O_4 IONPs (1.0 mL, 0.008 mmol) were incubated with 0.027 mmol DMSA dissolved in 1 mL DMSO and left overnight on a stirring apparatus at RT. The supernatant was then removed by magnetic retraction of the NP-DMSA, the nanoconjugate was washed thrice with deionized water and then reconstituted in 1 mL ultrapure water.

Conjugation of BCZM to NP-DMSA

Sulfosuccinimidyl-4-(N-maleimidomethyl)cyclohexane-1-carboxylate (Sulfo-SMCC) was used as the crosslinker between the NP-DMSA and BCZM. For conjugation of the antibody with the crosslinker, 50 μ L of sulfo-SMCC (4.8 mg/mL in H₂O) were added to an aliquot containing \sim 500 μ g (0.003 μ mol in 1 mL PBS) BCZM. The reaction mixture was incubated for 30 min at RT. The excess crosslinker was removed by centrifugation, using an Amicon filter with a 100 kD cut-off value. The purified SMCC-BCZM was then added to 1 mL NP-DMSA and incubated for 30 min at RT, under mechanical stirring. The supernatant was then removed by magnetic retraction of the NP-DMSA-SMCC-BCZM, the nanoconjugate was washed thrice with deionized water and then reconstituted in 1 mL deionized water, for further use in characterization and cytotoxicity experiments.

Size Analysis of Fe_3O_4 , Fe_3O_4 -DMSA and Fe_3O_4 -DMSA-SMCC-BCZM IONPs

Dynamic light scattering (DLS) was used to measure the size distributions of Fe_3O_4 , Fe_3O_4 -DMSA and Fe_3O_4 -DMSA-SMCC-BCZM nanoparticles in aqueous solutions using a DLS apparatus.

In a typical DLS measurement, 100 μ L of Fe_3O_4 IONPs (1.25 mg/ml) diluted with 400 μ L ultrapure water were measured at 22°C. Furthermore, 2 mg of Fe_3O_4 -DMSA IONPs diluted with 800 μ L ultrapure water and 0.1 mg of Fe_3O_4 -DMSA-SMCC-BCZM NPs diluted with 400 μ L ultrapure water were also measured at 22°C. For each dispersion, at least 10 light scattering measurements were collected and the results were averaged.

Magnetic Properties of Fe_3O_4 , Fe_3O_4 -DMSA and Fe_3O_4 -DMSA-SMCC-BCZM IONPs

Magnetic measurements of Fe_3O_4 , Fe_3O_4 -DMSA and Fe_3O_4 -DMSA-SMCC-BCZM powder samples were carried out by means of a SQUID magnetometer (5.5 T MPMS, Quantum Design). Magnetization vs. magnetic field, M(H) was performed both at $T = 300$ K and $T = 10$ K, while magnetization vs. temperature, M(T), was measured at $H = 50$ Oe in both the zero-field cooling (ZFC) and field cooling (FC) modes (ZFC: cooling the sample to the desired temperature under zero magnetic field and then starting measuring its magnetization while progressively increasing the temperature; FC: cooling the sample to the desired temperature under the presence of a specified magnetic field while simultaneously measuring its magnetization).

Antibody Conjugation

UV-Vis spectrophotometry was used to evaluate the conjugation between Fe_3O_4 -DMSA and SMCC-BCZM. All samples were prepared by addition of SMCC-BCZM to Fe_3O_4 -DMSA, intense vortexing for 1 min and consequent shaking for 30 min at RT. To a stable concentration of Fe_3O_4 -DMSA (3 mmol/L), different concentrations of SMCC-BCZM were added, ranging from 0.0625 to 0.75 mg/mL. BCZM concentration was measured in the supernatant, after magnetic retraction of the nanoparticles. A reference BCZM solution ($C = 1$ mg/mL) was used in the control experiment, i.e., in the absence of nanoparticles.

In Vitro Cytotoxicity Study of Fe_3O_4 -DMSA-SMCC-BCZM IONPs

Two epithelial cell lines were used for the evaluation of cytotoxicity of Fe_3O_4 -DMSA-SMCC-BCZM IONPs, namely HEK293T (ATCC CRL-3216) and MDA MB 231 breast cancer cells transfected with the VEGF-165 isoform (M165). HEK293 cells are used as the control group (non-cancerous cell line) in our experiments. Both cell lines were cultured in standard DMEM complete (10% FBS, 1% penicillin/streptomycin, 1% L-glutamine). Cells were incubated at 37°C in a humidified atmosphere of 5% CO₂.

MTT Assay

As a general protocol, 5,000 cells/well were seeded in 96-well plates (Corning-Costar, Corning, NY) and cultured overnight. The positive control of this study had cells with culture medium, which were not exposed to IONPs. The two different cell lines were treated with various concentrations of Fe_3O_4 -DMSA-SMCC-BCZM IONPs (3, 5, 10, 20, 25, 30, 35, 40, 45, 50, 100, 200, 500, and 1,000 μ g/ml) for 24 h. Subsequently, the cells were rinsed once and incubated at 37°C with 100 μ L serum-free medium, containing 0.5 mg/mL MTT. After 2 h, 100 μ L of SDS-HCl was added to each well, mixed with the pipette and incubated for at least 1 h at 37°C. The optical densities were read at 570 nm (reference filter was set at 690 nm), on an ELISA reader.

Radiolabeling of Fe_3O_4 IONPs With Technetium-99m

Radiolabeling of Fe_3O_4 -DMSA With Technetium-99m: Passive Delivery of Nanoparticles

Radiolabeling of Fe_3O_4 -DMSA with ^{99m}Tc was performed via the precursor ^{99m}Tc-gluconate, as follows: A solid mixture containing 1.0 g Na gluconate, 2.0 g NaHCO₃ and 0.015 g SnCl₂ was homogenized and kept dry. A quantity of 0.003 g of the above mixture was dissolved in 1.0 ml of a Na^{99m}TcO₄ solution, containing 370 MBq (10 mCi) of ^{99m}Tc (Varvarigou et al., 2002). An aliquot of the above solution (100 μ L) containing \sim 37 MBq of the reduced ^{99m}Tc was added to 8 μ mol Fe_3O_4 -DMSA. The mixture was left at RT and the exchange reaction was completed in 30 min. The radiolabeling yield was determined by thin layer chromatography analysis (TLC). ITLC-SG was used as the stationary phase. The strips were developed using MEK and a 3/5/1.5 mixture pyridine/acetic acid/H₂O as the mobile phases, to determine free pertechnetate, ^{99m}TcO₂ and Fe_3O_4 -DMSA-^{99m}Tc. With MEK, pertechnetate ions migrate with the solvent front,

while in pyridine/acetic acid/H₂O ^{99m}TcO₂ remains at the spot and Fe₃O₄-DMSA-^{99m}Tc migrates to the front. The radiolabeled sample was purified by magnetic retraction. After washing twice with deionized water, the supernatant was removed and the radiolabeled sample was redispersed in deionized water. The % radiochemical purity of Fe₃O₄-DMSA-^{99m}Tc was determined by TLC, as previously described. A control test was also carried out, in the absence of Fe₃O₄-DMSA-^{99m}Tc.

Radiolabeling of BCZM With ^{99m}Tc and Consequent Conjugation to Fe₃O₄-DMSA: Active Targeting of VEGF-A Expression

BCZM-SMCC was prepared as described above. Thereafter, in order to adequately prepare BCZM for consequent radiolabeling with ^{99m}Tc, its endogenous disulfide bonds were partially reduced with 2-mercaptoethanol. Briefly, BCZM-SMCC (500 μL, C_{Ab} = 2.5 mg/mL) was incubated with 25 μL 2-mercaptoethanol (1,000:1 molar ratio) for 30 min at RT. The reduced antibody conjugate was purified by centrifugation (12,000 rpm, 10 min, AMICON filters MWCO: 100kD) and reconstituted in deionized water. Labeling of BCZM-SMCC was afforded by the addition of the ^{99m}Tc-gluconate precursor (100 μL/37 MBq) (Varvarigou et al., 1996). The radiolabeling yield was determined by HPLC performed on a Waters HPLC system using a TSKgel G3000SWXL size exclusion column (TOSOH Bioscience, Germany). As the eluent, PBS pH 7.4 was used at a flow rate of 0.8 mL/min. Finally, ^{99m}Tc-BCZM-SMCC was added to 8 μmol Fe₃O₄-DMSA, intensely vortexed for 1 min, and shaken at RT for 30 min on a mechanical shaker. The radiolabeled sample was purified by magnetic retraction. After washing thrice with deionized water, the supernatant was removed and the radiolabeled sample was redispersed in 1 mL deionized water. The % radiochemical purity of Fe₃O₄-DMSA-SMCC-BCZM-^{99m}Tc IONPs was determined by TLC, as previously described. A control test was also carried out, in the absence of IONPs.

In Vitro Stability Studies of Fe₃O₄-DMSA and Fe₃O₄-DMSA-SMCC-BCZM-^{99m}Tc IONPs

To evaluate the *in vitro* stability of Fe₃O₄-DMSA-^{99m}Tc and Fe₃O₄-DMSA-SMCC-BCZM-^{99m}Tc, 10 μL samples of each of the radiolabeled nanoconjugates were incubated with 90 μL phosphate buffer saline (PBS) pH 7.4 while shaking at RT. For serum stability studies, 50 μL of each of the radiolabeled nanoconjugates were incubated with 450 μL human serum at 37°C. *In vitro* stability was determined at four time points (1, 2, 4, and 24 h) by TLC, as described above. All experiments were performed in triplicate.

In Vitro Cell Binding Assay

In vitro cell binding experiments were performed on M165 cells, in order to assess the targeting capability of both BCZM-functionalized Fe₃O₄-DMSA-SMCC-BCZM-^{99m}Tc and non-functionalized Fe₃O₄-DMSA-^{99m}Tc (Orocio-Rodríguez et al., 2015; Mendoza-Nava et al., 2016). Cells were cultured as described above for the cytotoxicity experiment. On the day prior to experiments, M165 cells were seeded in 24-well plates and grown to confluence. For the binding experiment, 50 μL

(0.4 μmol) of either nanoconstruct were added to each well and incubated for 1 h at 37°C. Subsequently the supernatant was removed, the cells were washed 3 times with ice-cold PBS and lysed by the addition of 1 M NaOH. Activity was measured, along with an aliquot with the initial activity, representing 100% added activity. The percent cell uptake was then calculated. Non-specific binding was determined in parallel, in the presence of a large excess of unlabeled BCZM, with 1 h of pre-incubation.

Ex Vivo Biodistribution Studies of Bare (Fe₃O₄-DMSA-^{99m}Tc) and Antibody-Functionalized (Fe₃O₄-DMSA-SMCC-BCZM-^{99m}Tc) IONPs

Animal experiments were carried out according to European and national regulations. These studies have been further approved by the Ethics Committee of the NCSR “Demokritos” and animal care and procedures followed are in accordance with institutional guidelines and licenses issued by the Department of Agriculture and Veterinary Policies of the Prefecture of Attiki (Registration Numbers: EL 25 BIO 022 and EL 25 BIO 021). Immunodeficient SCID mice were obtained from the breeding facilities of the Institute of Biosciences and Applications, NCSR “Demokritos.” The animals were housed in air-conditioned rooms under a 12-h light/dark cycle and allowed free access to food and water.

For the development of experimental tumor models, female SCID mice of 8 weeks on the day of inoculation were subcutaneously inoculated with M165 cells (1×10^7 cells). Approximately 2 weeks after inoculation, *ex vivo* biodistribution studies and *in vivo* imaging studies on the tumor-bearing mice were performed. Fe₃O₄-DMSA-^{99m}Tc and Fe₃O₄-DMSA-SMCC-BCZM-^{99m}Tc were evaluated in 2 groups of tumor-bearing SCID mice ($n = 4$ mice, animal weight 18–20 g). The nanoradiotracers were intravenously administered via the tail vein. Each mouse received 100 μL (0.8 μmol/89 μg/2.0 ± 0.3 MBq) of either Fe₃O₄-DMSA-^{99m}Tc (passive delivery) or Fe₃O₄-DMSA-SMCC-BCZM-^{99m}Tc (active targeting). The animals were euthanized at 2, 4, and 24 h post-injection (4 mice per time-point) and the organs of interest, as well as the tumor, were removed, weighed and counted in a NaI well-counter, along with samples of blood, muscles and urine. The remaining radioactivity in the tail, as well as background counts were subtracted, and the radioactivity decay was auto-corrected by the counter. The accumulation of radiolabeled MNPs in each organ was expressed as the percentage injected dose per gram of tissue (%ID/g ± SD) and calculated compared to the activities of a standard dose of the injected solution.

Binding specificity of Fe₃O₄-DMSA-SMCC-BCZM-^{99m}Tc (the targeted nanoconstruct) was assessed in M165 tumor-bearing mice ($n = 4$ mice), after pre-injection of the mice with 2.5 mg (0.016 μmol)/100 μL “cold” bevacizumab 24 h before injection of the radiotracer. These animals were euthanized at 4 h post-injection of Fe₃O₄-DMSA-SMCC-BCZM-^{99m}Tc and were assessed as described above.

In Vivo Imaging Studies (Pilot Studies) Gamma Camera

All animals were bearing a tumor in their left front limb. After tracer injection, the animals were anesthetized with an

intraperitoneal (IP) injection of ketamine (75 mg/kg) and xylazine (5 mg/kg) and placed on the prone position on the camera face. Planar scintigraphy was performed by collecting a 60-min image following tracer injection. Furthermore, all four animals were imaged 24 h after injection by acquiring a 60-min image.

MR Imaging

MRI exams were conducted at the First Department of Radiology of the National and Kapodistrian University of Athens on a 3 Tesla MRI unit, using a surface phased-array coil.

MRI experiments were performed on 3 groups of M165 tumor-bearing SCID mice, as follows: Group 1: Mice injected with Fe_3O_4 -DMSA-SMCC-BCZM (1 mg IONPs/100 μL , $n = 3$ mice); Group 2: Mice injected with Fe_3O_4 -DMSA (1 mg IONPs/100 μL , $n = 3$ mice); and Group 3: Mice injected with saline ($n = 2$ mice). Anesthesia was induced with a mixture of ketamine/xylazine. T2-Weighted images were acquired before the injection of nanoparticles. The next day mice were injected with Fe_3O_4 -DMSA-SMCC and Fe_3O_4 -DMSA-SMCC-BCZM and were imaged 4 h post-injection with the same parameters. MR images were reviewed and signal intensity measurements were performed on a dedicated workstation using diagnostic software (Philips IntelliSpace Portal v9, Philips Healthcare, Best, The Netherlands).

Histopathology Studies

Twenty-four hours post-MRI scanning, the mice were euthanized and the tumors, livers, lungs and kidneys of each mouse were surgically removed. The tissues were then fixed in 10% formalin, embedded in paraffin, sectioned at 6 μm and stained with Perl's reagent (Prussian Blue). The slides and the pictures of each tissue were taken using an Olympus U-TVO.5XC-3 microscope,

equipped with an Infinity1 Lumenera camera (magnification $\times 40$).

Statistical Analysis

The data are presented as means \pm standard deviations. For the biodistribution studies, the data were compared using an unpaired *t*-test with a significance level of $P < 0.05$. All analyses were performed using Microsoft Office Excel.

RESULTS AND DISCUSSION

The aim of the present study was to show that bevacizumab-functionalized IONPs show specific accumulation in VEGF-A expressing tumors, while their non-functionalized counterparts exhibit limited uptake due to the EPR effect. The primary idea behind the design and synthesis of these NPs was to provide a platform for the development of a dual-modality molecular imaging agent.

Synthesis and Characterization of Fe_3O_4 IONPs

The main reason for coating the nanoparticle surface with various molecules is to render them non-toxic, biocompatible and stable (Barrow et al., 2015). 2,3-dimercaptosuccinic acid (DMSA) has been repeatedly used for surface-functionalizing inorganic NPs, as an effective way to increase their biocompatibility (Fauconnier et al., 1997; Auffan et al., 2006; Wang et al., 2011). DMSA is an FDA-approved, orally administered metal-chelating agent often used to coat iron oxide NPs, in order to improve their stability and biocompatibility (Chen et al., 2008). Apart from providing nanoparticle stability under physiological conditions, DMSA offers two functional groups, namely $-\text{COOH}$ and $-\text{SH}$, which can both be exploited

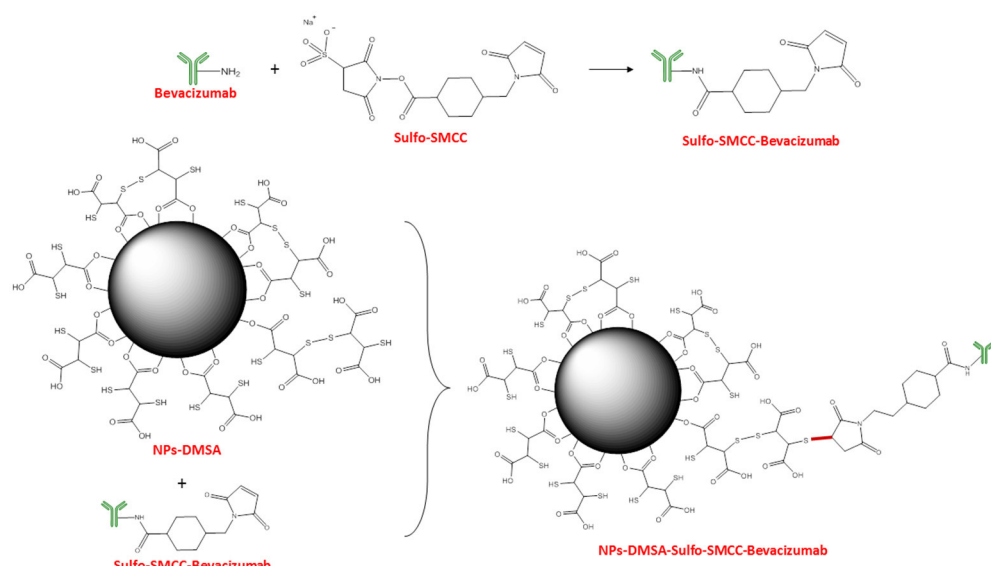


FIGURE 1 | Schematic representation of Fe_3O_4 -DMSA-SMCC-BCZM nanoparticles (FNs).

for the covalent bonding of a variety of organic molecules (Ruiz et al., 2014; Galli et al., 2017). In this study, IONPs were synthesized according to the co-precipitation method, while their surface was modified with DMSA for further functionalization with BCZM-SMCC (**Figure 1**). The ligand DMSA binds to the nanoparticle surface in a bidentate manner through oxygen atoms, and the created Fe-O-C bond is similar to a polar covalent bond (**Figure 1**; Ruiz et al., 2014). Conjugation of BCZM to the thus formed NP-DMSA was accomplished *via* the crosslinker Sulfo-SMCC. Sulfo-SMCC contains an amine-reactive N-hydroxysuccinimide (NHS ester) and a sulfhydryl-reactive maleimide group. The NHS esters of Sulfo-SMCC react with the primary amines of BCZM to form stable amide bonds while the maleimides react with the sulfhydryl groups of NP-DMSA to form stable thioether bonds.

Size Analysis of Fe_3O_4 , Fe_3O_4 -DMSA and Fe_3O_4 -DMSA-SMCC-BCZM IONPs

DLS measurements were carried out on the Fe_3O_4 , Fe_3O_4 -DMSA and Fe_3O_4 -DMSA-SMCC-BCZM IONPs (**Figure 2**). The samples were diluted with ultrapure water and measured at 22°C. Using CONTIN analysis of the DLS measurements, the mean size distribution of intensity weighted hydrodynamic radii of Fe_3O_4 , Fe_3O_4 -DMSA, and Fe_3O_4 -DMSA-SMCC-BCZM IONPs were found to be 335, 206, and 281 nm respectively. This result indicates the general effect of surface coating, which prevents the *in vivo* aggregation of the nanoparticles as it provides sufficient electrostatic (and/or steric) repulsion between them and thus, maintains the nanoparticles apart from one another against attractive forces. The hydrodynamic size of Fe_3O_4 -DMSA and Fe_3O_4 -DMSA-SMCC-BCZM IONPs is close to the upper size limit (400–500 nm) for the extravasation of nanoparticles into tumor tissues, *via* the EPR effect.

Magnetic Properties of Fe_3O_4 , Fe_3O_4 -DMSA, and Fe_3O_4 -DMSA-SMCC-BCZM IONPs

The magnetic properties of Fe_3O_4 , Fe_3O_4 -DMSA, and Fe_3O_4 -DMSA-BZCM nanoparticles, presented in **Figures 3A–C** respectively, were assessed by magnetization measurements vs. magnetic field, $M(H)$, at $T = 300\text{ K}$ and $T = 10\text{ K}$ [panels (A.I–C.I)], as well as by ZFC-FC magnetization at

50 Oe [panels (A.II–C.II)]. The saturation magnetization, M_s , was found to be $M_s = 45 \text{ emu/g}$, $M_s = 41 \text{ emu/g}$ and $M_s = 41 \text{ emu/g}$ at $T = 300\text{ K}$ for Fe_3O_4 , Fe_3O_4 -DMSA, and Fe_3O_4 -DMSA-SMCC-BZCM nanoparticles, respectively. From the comparison of the magnetization measurements, it is concluded that the magnetization of all the samples is preserved and is not affected either by the DMSA coating or by the functionalization of the nanoparticles with the antibody. The values of remanent magnetization and coercivity for all samples at 300 K are zero, which is in accordance to their superparamagnetic behavior (or more appropriately, soft ferromagnetic/ferrimagnetic character). Furthermore, the ZFC-FC magnetization curves of Fe_3O_4 , Fe_3O_4 -DMSA, and Fe_3O_4 -DMSA-SMCC-BZCM nanoparticles exhibit a maximum in the ZFC curve that corresponds to the so-called blocking temperature $T_B = 130$, 100, and 100 K, respectively. These magnetization data show that the Fe_3O_4 IONPs preserve their magnetic properties (high saturation magnetization and zero coercivity) upon functionalization and thus are appropriate for usage in diagnostic imaging application at RT.

Antibody Conjugation

The conjugation between Fe_3O_4 -DMSA and SMCC-BCZM may be reliably proven by means of UV-vis spectrophotometry, as previously reported by our group (Stamopoulos et al., 2007). **Figures 4A,B** present data for the supernatant of Fe_3O_4 -DMSA-SMCC-BCZM samples that were prepared for incubation duration, time = 2 h. (**Figure 4A**) shows data for constant concentration of Fe_3O_4 ($C_{\text{IONPs}} = 3 \text{ mmol/L}$) and for six different concentrations of BCZM, while (**Figure 4B**) shows the respective data for constant concentration of BCZM ($C_{\text{Ab}} = 3 \text{ mmol/L}$) and six different concentrations of Fe_3O_4 IONPs. The data of (**Figure 4A**) clearly show complete conjugation of BCZM to the IONPs for antibody concentrations up to a characteristic value 0.1250 mg/mL. However, the percentage of conjugated BCZM decreases as its initial concentration increases. The data of (**Figure 4B**) prove that the percentage of BCZM conjugated with the IONPs increases as their concentration increases, however it reaches a plateau at a characteristic value 5 mmol/L. These data guided us to choose an optimum concentration ratio between BCZM and IONPs, that

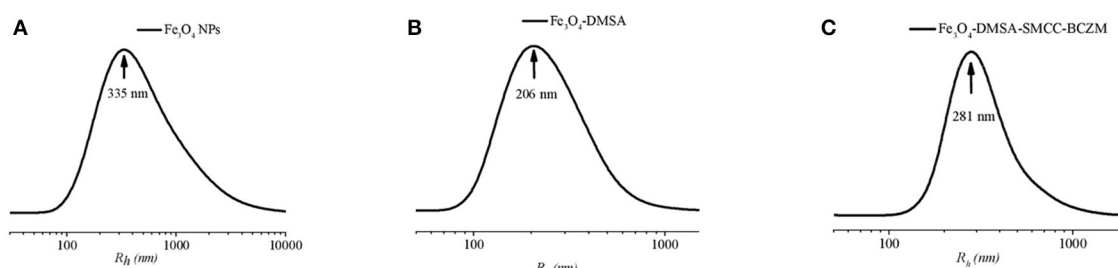


FIGURE 2 | Intensity weighted hydrodynamic radii size distribution of (A) Fe_3O_4 , (B) Fe_3O_4 -DMSA, and (C) Fe_3O_4 -DMSA-SMCC-BCZM.

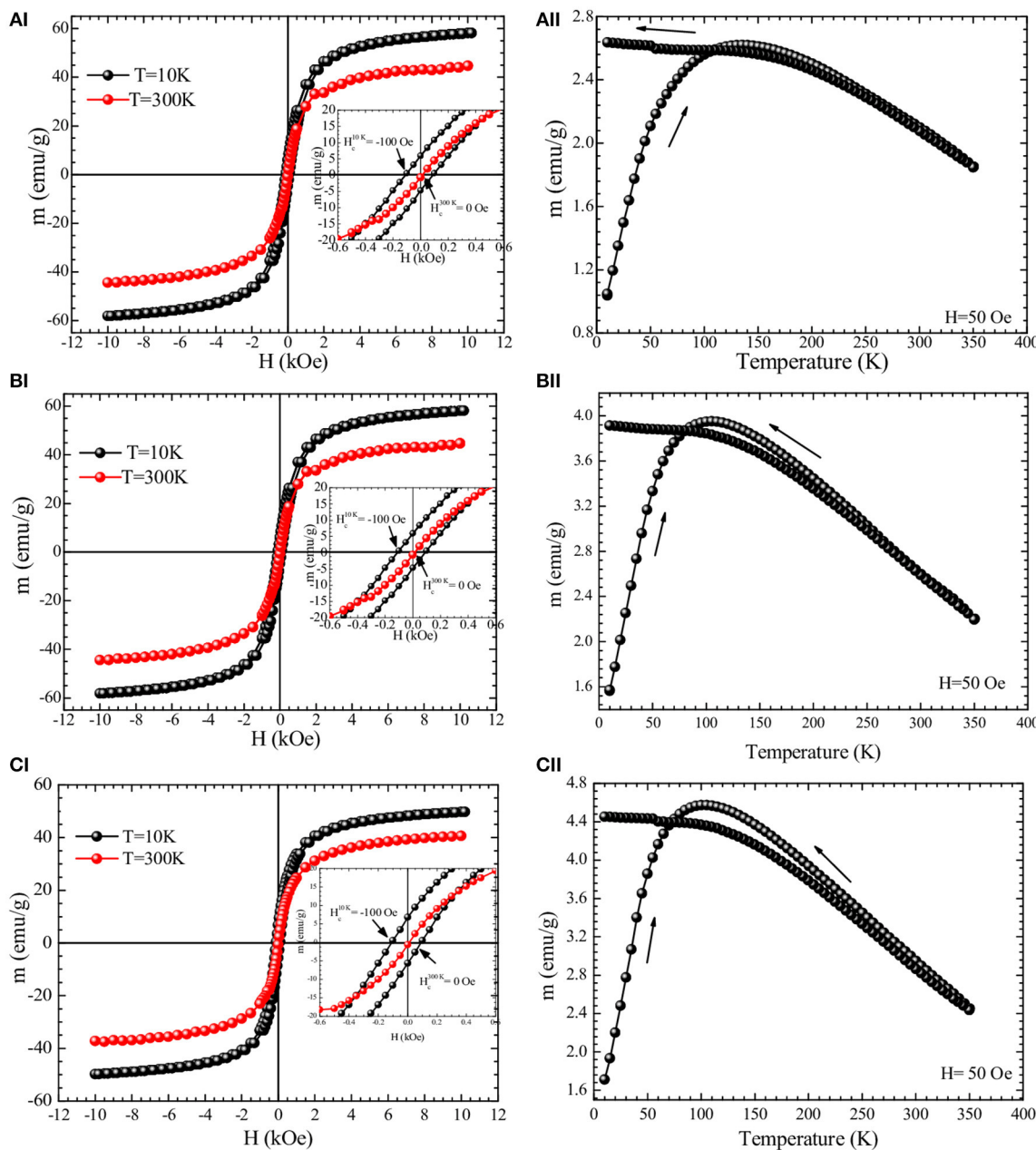


FIGURE 3 | Magnetization measurements **(AI–CI)** vs. magnetic field, at 10 and 300 K, and **(AII–CII)** vs. temperature measured at $H = 50$ Oe for **(AI,AII)** Fe_3O_4 ; **(BI,BII)** Fe_3O_4 -DMSA; and **(CI,CII)** Fe_3O_4 -DMSA-SMCC-BCZM. All samples were in powder form.

is $C_{\text{BCZM}}/C_{\text{IONPs}} = 0.5 \text{ mg/mL}/8 \text{ mmol/L}$, in our subsequent experiments.

In Vitro Cytotoxicity Study of Fe_3O_4 -DMSA-SMCC-BCZM

Cytotoxicity of iron oxide NPs at concentrations $>300 \mu\text{g/mL}$ is mainly due to the production of Reactive Oxidative Species (ROS) (Shukla et al., 2015). Quantitative assays of the metabolic activity of cancer cell lines in the presence of Fe_3O_4 -DMSA-SMCC-BCZM could grant a better knowledge of the mechanisms

implied in the toxicity caused by these IONPs. The MTT viability assay tracks the activity of reductase enzymes, thus measuring the cell viability of M165 and HEK293 cell lines, after a 24 h treatment with various concentrations of Fe_3O_4 -DMSA-SMCC-BCZM IONPs (Jarockyte et al., 2016; Karageorgou et al., 2017). Our experiments demonstrated a similar behavior on both the M165 and HEK293 cell lines, at nanoparticle concentrations ranging from 3 to 1,000 $\mu\text{g/ml}$. Cell viability was over 65% at all concentration points for both cell lines (Figure 5). Keeping in mind that the maximum dose of administered iron oxide

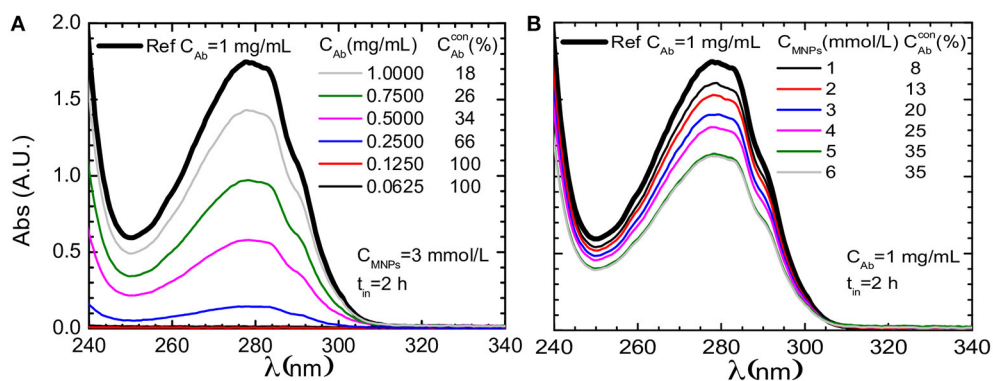


FIGURE 4 | UV-vis data (focused in the range of 240–340 nm) for the supernatant of Fe_3O_4 -DMSA-SMCC-BCZM samples that were prepared for incubation duration, time = 2 h, for six different concentrations of **(A)** BCZM and constant concentration of IONPs ($C_{\text{MNP}_s} = 3 \text{ mmol/L}$) and **(B)** IONPs and constant concentration of BCZM ($C_{Ab} = 3 \text{ mg/mL}$). The respective curve of a reference BCZM solution (1 mg/mL) is also shown, in both cases. The C_{Ab}^{con} presented in both panels refers to the percentage of BCZM conjugated with the Fe_3O_4 IONPs, as this was estimated from the respective set of data. The supernatant of the samples was isolated when the magnetic species were trapped by means of an external magnetic field.

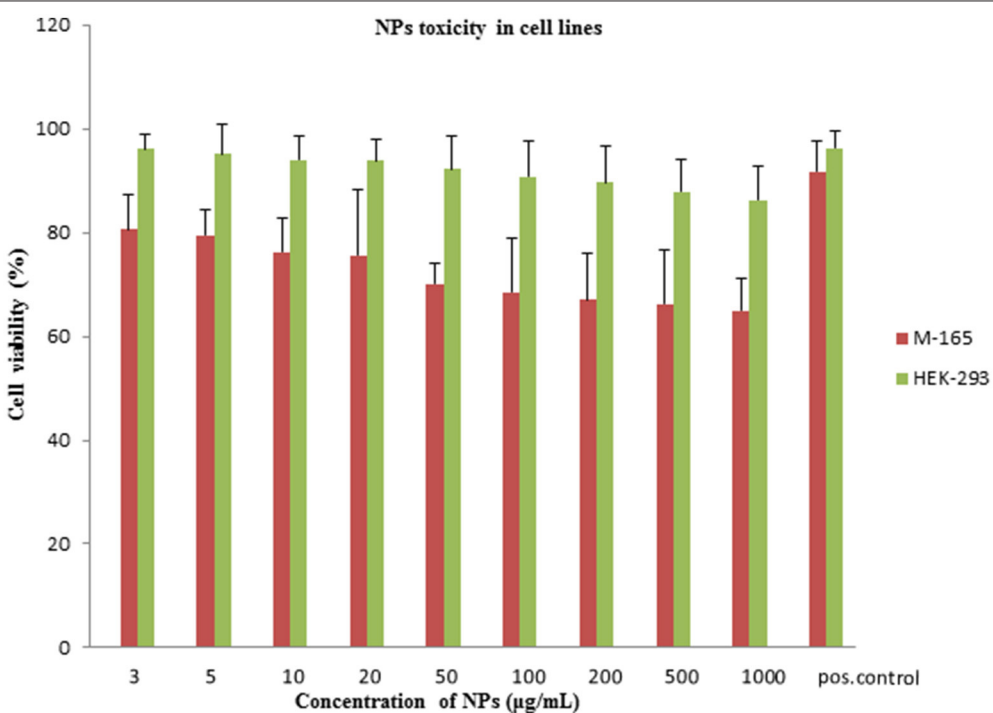


FIGURE 5 | Viability assay on M165 and HEK293 cell lines. Graph of MTT assay after 24 h treatment of M-165 cells and HEK293 cells with various concentrations of NPs. Positive control shows M-165 cells and HEK293 cells without the exposure to NPs. The cell viability is expressed as % cell viability in comparison to a positive control.

NPs in our study is 1,000 $\mu\text{g}/\text{mouse}$ (which is the injected dose for the MR imaging study), our results suggest that our nanoconstruct does not cause toxic effects on either cell line, even at the 1,000 $\mu\text{g}/\text{ml}$ concentration point. These results are in accordance with toxicity results of other DMSA-coated nanoparticles reported in the literature (Mejías et al., 2010, 2013; Ruiz et al., 2013; Paik et al., 2015; Costa et al., 2016; Shelat et al., 2018).

Radiosynthesis and *In Vitro* Stability Studies of Fe_3O_4 -DMSA- $^{99\text{m}}\text{Tc}$ and Fe_3O_4 -DMSA-SMCC-BCZM- $^{99\text{m}}\text{Tc}$

Radiolabeling of Fe_3O_4 -DMSA was achieved by transcomplexation of Sn^{2+} -reduced [$^{99\text{m}}\text{Tc}$]-pertechnetate in the presence of an excess of a low-affinity chelating ligand (gluconate), which ensures that $^{99\text{m}}\text{Tc}$ binds to the exposed thiol groups. Fe_3O_4 -DMSA- $^{99\text{m}}\text{Tc}$ was prepared at a

satisfactory radiolabeling yield (70%) and high radiochemical purity (>95%) post-purification by magnetic retraction, as determined by TLC analysis (Figure S1). Labeling of the SMCC-BCZM conjugate was also performed via the ^{99m}Tc -gluconate precursor at high radiochemical yield (>98%), as determined by HPLC analysis (Figure S2). Incubation of Fe_3O_4 -DMSA with SMCC-BCZM- ^{99m}Tc led to the formation of Fe_3O_4 -DMSA-SMCC-BCZM- ^{99m}Tc at a radiochemical purity of >92% after purification by magnetic retraction (Figure S3).

A significant factor to be considered when developing a new radiolabeled nanoparticle is that the radionuclide must be bound to the nanoparticle to form a stable conjugate under physiological conditions to avoid their separation and non-specific deposition of free ions in tissues. Otherwise, biodistribution and imaging data will not indicate the fate of nanoparticles, as the radionuclide distribution will not reflect that of the nanoparticles. With the aim to assess the *in vitro* stability of Fe_3O_4 -DMSA- ^{99m}Tc and Fe_3O_4 -DMSA-SMCC-BCZM- ^{99m}Tc in biological media, the radiolabeled samples were incubated with PBS and human serum. The results exhibited satisfactory *in vitro* stability in PBS (~80% stable IONPs, Figure S4) and high *in vitro* stability human serum (~90% stable IONPs, Figure S5) for both radiotracers at 24 h post-incubation, as evaluated by TLC analysis. From the *in vitro* serum stability results, it is safe to say that both radiolabeled nanoconstructs are stable enough to be used as *in vivo* imaging agents. Our results are in accordance to previously published works (De Rosales et al., 2011; Karageorgou et al., 2017).

In Vitro Cell Binding Assay

The cell binding assay was performed on the M165 cell line after 24 h incubation with Fe_3O_4 -DMSA-SMCC-BCZM- ^{99m}Tc and Fe_3O_4 -DMSA- ^{99m}Tc (50 μL , 0.04 μmol). Targeted Fe_3O_4 -DMSA-SMCC-BCZM- ^{99m}Tc had specific recognition, as cell uptake was ~4.3 times higher than for Fe_3O_4 -DMSA- ^{99m}Tc , indicating the ability of the immunoconjugate to bind to the VEGF-165 isoform overexpressed on M-165 tumor cells. Specificity of Fe_3O_4 -DMSA-SMCC-BCZM- ^{99m}Tc was further confirmed by blocking the cells with an excess of unlabeled BCZM (Table 1; Morales-Avila et al., 2011; Orocio-Rodríguez et al., 2015; Mendoza-Nava et al., 2016).

In light of the performed cell binding studies, and the demonstrated specificity of Fe_3O_4 -DMSA-SMCC-BCZM- ^{99m}Tc toward M165 cells overexpressing the VEGF-165 isoform, this

should be the nanoconstruct of choice for further *ex vivo* and *in vivo* experimentation.

Ex Vivo Biodistribution Studies

In order to evaluate the potential of the radiolabeled NP-systems as SPECT/MRI imaging agents, *ex vivo* biodistribution experiments were performed. Following i.v. injection, the ^{99m}Tc -labeled ferromagnetic NPs enter the blood stream and after circulating for some time in the body they reach a desired target i.e., tumor, depending on their surface functionalization. The degree of target uptake depends on the affinity between the target molecule and the functionalized NP-system. It is also essential that the administered nanomaterial circulates for long enough time for effective tumor uptake before being eliminated by the organism. The *ex vivo* biodistribution pattern of Fe_3O_4 -DMSA- ^{99m}Tc and Fe_3O_4 -DMSA-SMCC-BCZM- ^{99m}Tc was assessed in xenografted mice. Both species of IONPs were administered via tail-vein injection in M165 tumor-bearing SCID mice. The accumulation of the technetium-labeled IONPs in the organs at all time-points examined is presented in Figure 6, as percentage of injected dose per gram tissue (% ID/gr \pm SD). Blood retention of the nanoparticles was $3.21 \pm 0.65\%$ ID/g and $9.90 \pm 2.07\%$ ID/g at 2 h p.i. for Fe_3O_4 -DMSA- ^{99m}Tc and Fe_3O_4 -DMSA-SMCC-BCZM- ^{99m}Tc , respectively, while the antibody-functionalized conjugate showed a faster blood clearance at 24 h p.i. ($0.81 \pm 0.08\%$ ID/g), compared to the non-functionalized IONPs ($1.54 \pm 0.24\%$ ID/g). After organ distribution through blood, high levels of radioactivity were observed for both NPs in liver, spleen, kidney and lungs even, with different kinetics. In the liver, there was more pronounced uptake for Fe_3O_4 -DMSA- ^{99m}Tc ($23.60 \pm 3.90\%$ ID/g, $26.84 \pm 3.76\%$ ID/g and $17.33 \pm 1.02\%$ ID/g at 2, 4 and 24 h p.i.), while in the spleen the uptake was considerably lower for both radiolabeled nanoconstructs at 24 h p.i. ($8.09 \pm 2.88\%$ ID/g and $5.38 \pm 0.73\%$ ID/g, for Fe_3O_4 -DMSA- ^{99m}Tc and Fe_3O_4 -DMSA-SMCC-BCZM- ^{99m}Tc , respectively). These findings are consistent with the observed faster blood clearance of the non-functionalized IONPs at 2 h p.i., which may be attributed to their rapid accumulation in the liver and lungs. The lower liver uptake for Fe_3O_4 -DMSA-SMCC-BCZM- ^{99m}Tc at all the examined time-points ($17.77 \pm 3.61\%$ ID/g, $15.88 \pm 2.10\%$ ID/g and $7.81 \pm 1.25\%$ ID/g at 2, 4 and 24 h p.i.) can be attributed to the presence of BCZM which is protecting them to a certain degree from being recognized by Kupffer cells (de Souza Albernaz et al., 2018). As concluded from the biodistribution studies, the MNP species investigated here are cleared mostly through the hepatobiliary pathway since their hydrodynamic diameter is significantly larger than the cutoff for renal filtration (~5 nm) (Hong et al., 2012). Nevertheless, there is a significant renal uptake at all time-points which can be attributed to a small extent of renal clearance. Additionally, the high radioactivity concentration in the kidneys particularly for Fe_3O_4 -DMSA-SMCC-BCZM- ^{99m}Tc at 2 and 4 h p.i. ($16.46 \pm 2.8\%$ ID/g and $15.22 \pm 5.37\%$ ID/g respectively) can be partly attributed to the expression of VEGF-A in glomerular podocytes and in tubular epithelial cells, being essential for maintaining the glomerular filtration barrier (Turner et al., 2016). Previous work by the group of Vegt et al has shown that fragments of

TABLE 1 | Cell binding of Fe_3O_4 -DMSA-SMCC-BCZM- ^{99m}Tc and Fe_3O_4 -DMSA- ^{99m}Tc in M165 cells without (w/o) and with blockage by unlabeled BCZM, at 24 h (% of Total Activity \pm SD, $n = 3$).

Nanoradiopharmaceutical	Cell Uptake w/o block (%)	Cell uptake with block (%)
Fe_3O_4 -DMSA-SMCC-BCZM- ^{99m}Tc	25.27 ± 1.84	10.74 ± 0.88
Fe_3O_4 -DMSA- ^{99m}Tc	5.88 ± 1.06	5.07 ± 1.29

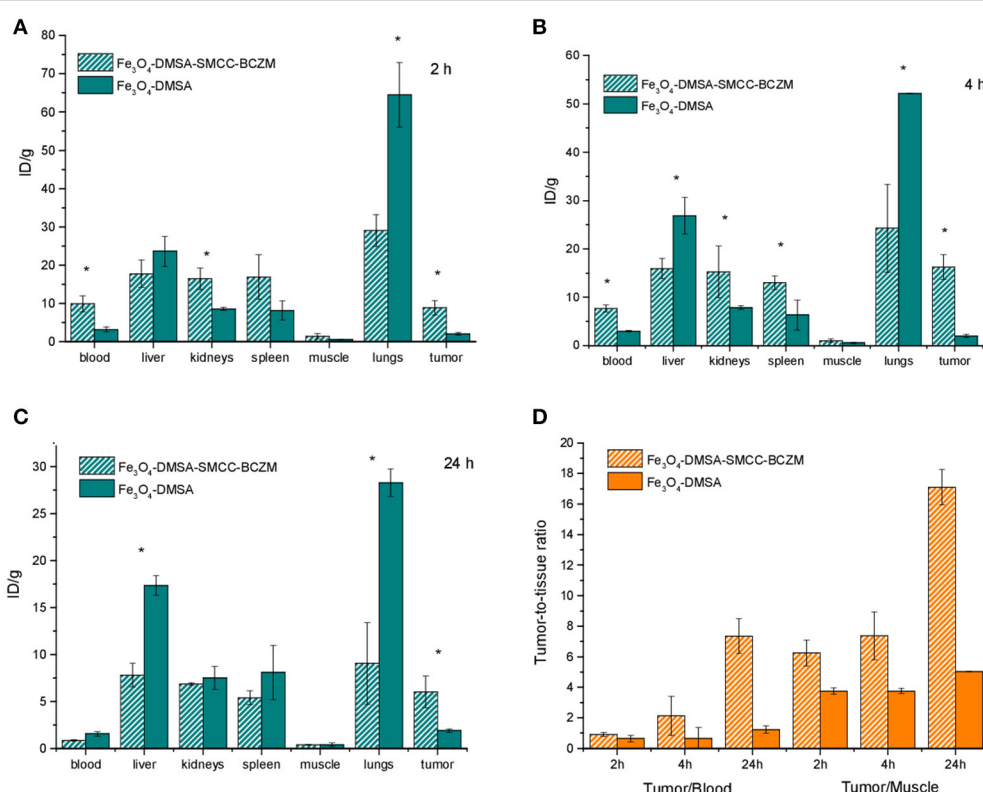


FIGURE 6 | Biodistribution results of M165 tumor-bearing SCID mice injected with Fe_3O_4 -DMSA-SMCC-BCZM- $^{99\text{m}}\text{Tc}$ and Fe_3O_4 -DMSA- $^{99\text{m}}\text{Tc}$ at 2, 4, and 24 h p.i. **(A–C)**. Tumor-to-blood, tumor-to-liver and tumor-to-muscle ratios at 2, 4, and 24 h p.i. **(D)**. Significant differences ($P < 0.05$) are denoted with an asterisk. Numerical data provided in tabulated form in the Supplementary Materials section (Tables S1, S2).

albumin might be suitable for inhibiting tubular reabsorption of peptides, however the effect of pre-administration of these agents on kidney uptake has not been investigated in the present study (Vegt et al., 2008). Lung uptake was high for both species at all time-points examined but it was significantly higher for the non-targeted species ($64.51 \pm 8.44\text{ID/g}$ at 2 h p.i.), remaining quite high even at 24 h p.i. ($28.27 \pm 1.45\text{ID/g}$). This may be attributed to various factors, such as the size of the nanoconstructs, their DMSA coating and, for the Fe_3O_4 -DMSA-SMCC-BCZM- $^{99\text{m}}\text{Tc}$ species, its functionalization with BCZM (Chaves et al., 2002, 2005; Monge-Fuentes et al., 2011).

In the case of Fe_3O_4 -DMSA-SMCC-BCZM- $^{99\text{m}}\text{Tc}$, tumor accumulation was quick, starting at $8.9 \pm 1.88\text{ID/g}$ at 2 h p.i., showed a slight increase at 4 h p.i. ($16.21 \pm 2.56\text{ID/g}$) and then decreased at 24 h p.i. ($6.01 \pm 1.69\text{ID/g}$). At all time-points studied, tumor uptake was significantly different ($P < 0.05$) between the two radiolabeled species, in favor of the BCZM-functionalized MPNs. Even though there is a decrease in tumor uptake in time, the tumor-to-blood ratio reached a maximum at 24 h p.i. (~ 7), which is also the case for the tumor-to-muscle ratio (~ 18) (Figure 6D). A further interesting observation is that the non-targeted Fe_3O_4 -DMSA- $^{99\text{m}}\text{Tc}$ showed practically no decline in tumor uptake value from 4 to 24 h p.i., which leads us to the conclusion that the nanoparticle shell

was stably labeled with $^{99\text{m}}\text{Tc}$, without being the subject of any degradation (Rainone et al., 2004). The decline in tumor uptake witnessed for Fe_3O_4 -DMSA-SMCC-BCZM- $^{99\text{m}}\text{Tc}$ may be attributed to *in vivo* clearance of the nanoconstruct, however even if this is the case, there is significant increase in the tumor/blood ratio from 4 to 24 h p.i. Because of the high tumor contrast exhibited after functionalization of these IONPs with BCZM, showing us favorable tumor-to-background ratios, we expect to witness satisfactory imaging properties for this nanoconstruct. All other organs studied showed low or negligible uptake. The results clearly indicate that biomarker-mediated active targeting provided the best efficiency in breast-cancer-induced angiogenesis detection, compared to simple EPR passive accumulation.

Binding specificity of Fe_3O_4 -DMSA-SMCC-BCZM- $^{99\text{m}}\text{Tc}$ was investigated by performing blocking experiments in M165 tumor-bearing mice at 4 h post-injection of the radiotracer, after pre-injection of the mice with a large excess (2.5 mg) unlabeled BCZM. Tumor uptake was significantly different ($P < 0.05$) between the blocked and unblocked mice ($\sim 75\%$ accumulation decrease in the M165 tumor), thus confirming the binding specificity of Fe_3O_4 -DMSA-SMCC-BCZM- $^{99\text{m}}\text{Tc}$ (Figure S6, Table S3). A significant decrease in kidney uptake was also demonstrated, indicating renal VEGF-A blocking.

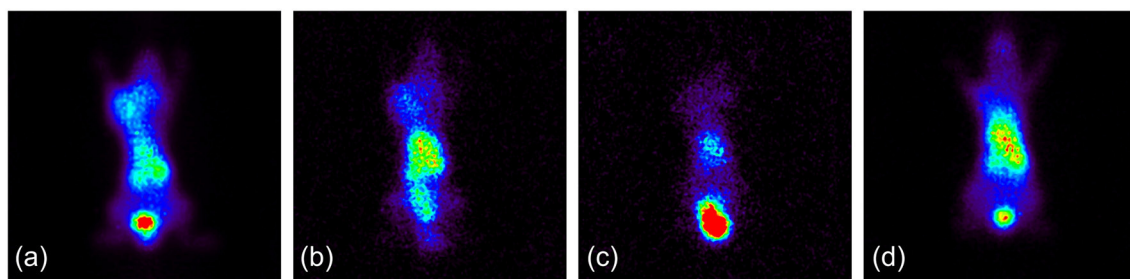


FIGURE 7 | (a) Fe_3O_4 -DMSA-SMCC-BCZM- ^{99m}Tc , imaging at 1 h p.i.; (b) Fe_3O_4 -DMSA-SMCC-BCZM- ^{99m}Tc , imaging at 24 h p.i.; (c) Fe_3O_4 -DMSA-SMCC-BCZM- ^{99m}Tc , blocking with excess BCZM 24 h prior to Fe_3O_4 -DMSA-SMCC-BCZM- ^{99m}Tc administration, imaging at 1 h p.i.; (d) Fe_3O_4 -DMSA- ^{99m}Tc , imaging at 1 h p.i.

In Vivo Imaging Studies (Pilot Studies)

After evidence of tumor accumulation was provided by the *ex vivo* biodistribution study, and in order to evaluate the potential of VEGF-targeting IONPs as a dual-modality imaging agent, initial gamma-ray and MR imaging were performed on M165 tumor-bearing SCID mice to verify our hypothesis. Static planar scintigraphic images of a mouse injected with Fe_3O_4 -DMSA-SMCC-BCZM- ^{99m}Tc at 1 h and 24 h post injection are shown in **Figures 7a,b**. These pilot images show significant accumulation of the radiotracer in the tumor from the first hour p.i., which was retained at the tumor site up to 24 h p.i. However, after administration of an excess of BCZM 24 h prior to injection of Fe_3O_4 -DMSA-SMCC-BCZM- ^{99m}Tc (blocking study), no tumor uptake was present 1 h p.i. (**Figure 7c**). Furthermore, when the animal was injected with Fe_3O_4 -DMSA- ^{99m}Tc (non-targeted nanoconstruct), practically no tumor uptake was seen (**Figure 7d**), as expected.

In the MR imaging experiment which was conducted, T2 weighted images acquired before administration of nanoparticles showed the tumors with high signal intensity. (**Figures 8a–c**). After nanoparticle administration the following day, decreased tumor MR signal intensity was noted, indicating specific uptake of Fe_3O_4 -DMSA-SMCC-BCZM (**Figure 8d**), while the non-targeted nanoconstruct Fe_3O_4 -DMSA showed only a slight drop in signal intensity (**Figure 8e**). M165 tumor-bearing mice which were not injected with nanoparticles served as our control mice, and exhibited no drop in tumor signal intensity (**Figure 8f**).

One of the most significant advantages of SPECT is its sensitivity, which is the reason why SPECT imaging tracers injected at very low concentrations are sufficient to provide high-quality images. However, this approach would prove to be problematic in the case of a dual-modality SPECT/MR imaging agent, since MR imaging requires much higher concentrations of injected contrast agent, in order to provide satisfactory images. Our MRI studies showed that a low-concentration nanomaterial injection (89 $\mu\text{g}/100\mu\text{l}/\text{mouse}$, i.e., the injected dose of radiotracer for the gamma camera imaging) could not provide adequate contrast, while a high-concentration sample (1,000 $\mu\text{g}/100\mu\text{l}/\text{mouse}$, **Figure 8**) was sufficient for contrast.

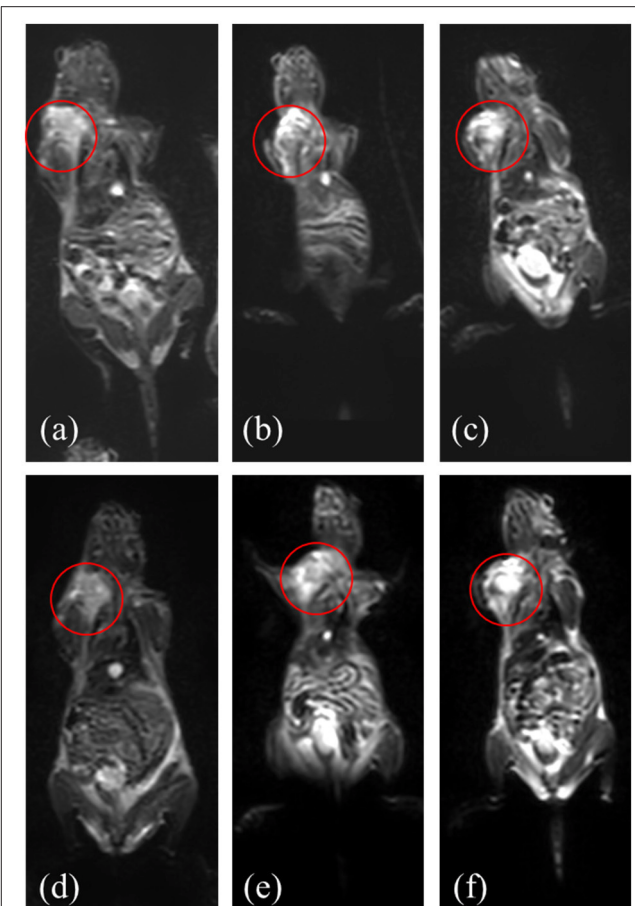
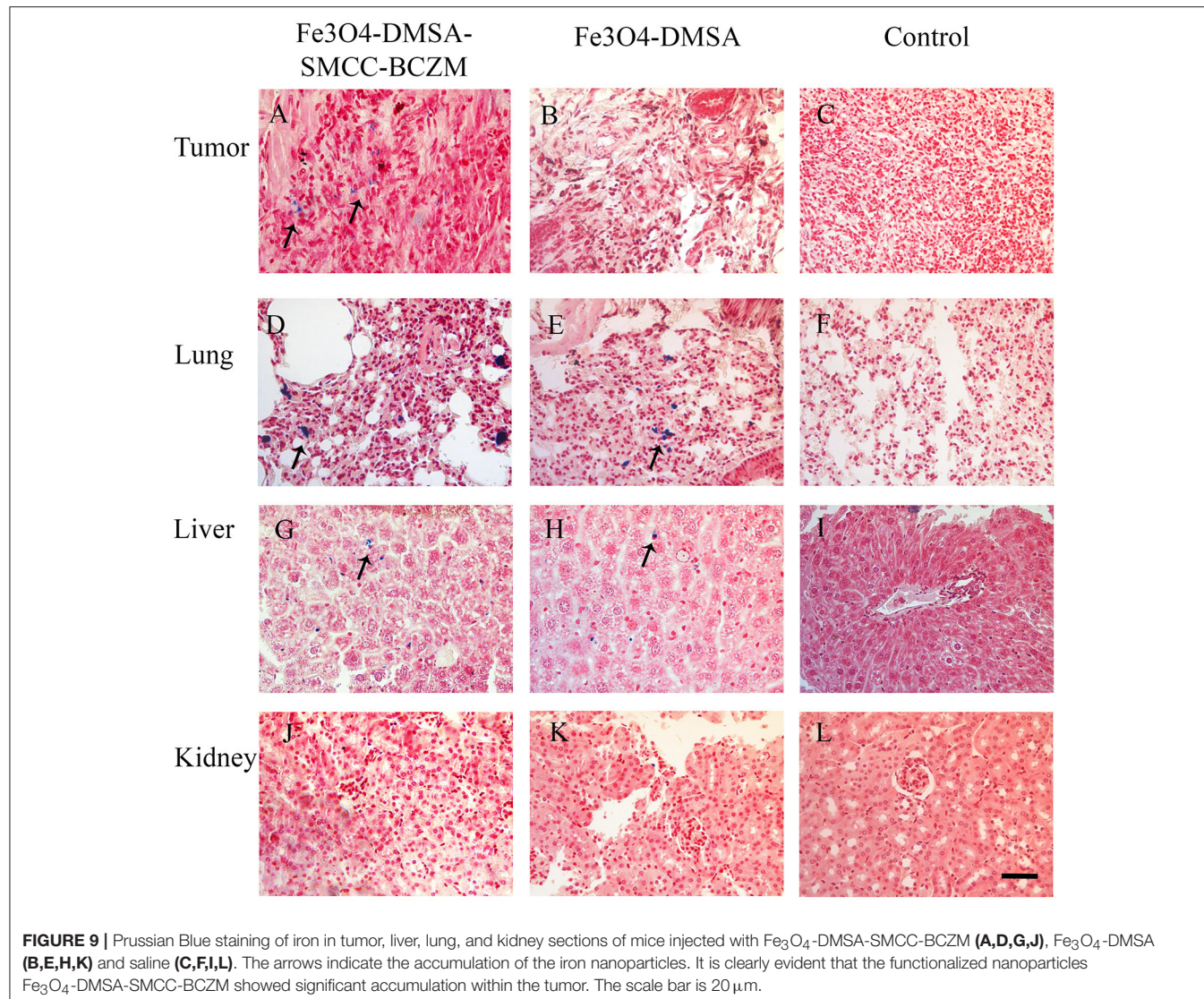


FIGURE 8 | MR imaging of mice injected with Fe_3O_4 -DMSA-SMCC-BCZM (d), Fe_3O_4 -DMSA (e) and without injection of nanoparticles (f, control mice) at 4 h p.i.; images of the mice 1 day before nanoparticle injection (a–c, respectively). Red circles designate the tumor area.

For future applications, we will opt to work with nanoparticle samples having an adequately high concentration for satisfactory MR imaging, and to adjust the amount of radioisotope to provide an imaging tracer for simultaneous SPECT/MR imaging.



Histopathology

Prussian blue staining of resected tumors from mice injected intravenously with non-functionalized Fe₃O₄-DMSA demonstrated little iron accumulation (Figure 9B), while Fe₃O₄-DMSA-SMCC-BCZM showed significant accumulation of iron within the tumor, suggesting improved tumor targeting for the antibody-functionalized nanoparticles (Figure 9A). Iron uptake was strong in the lungs of mice injected with both nanoconstructs (Figures 9D,E), while liver (Figures 9G,H) and kidneys (Figures 9J,K) also showed similar nanoparticle accumulation. Staining of tissues from mice injected with saline (control mice) showed no evidence of nanoparticle accumulation (Figures 9C,F,I,L). These findings are in line with our *ex vivo* and *in vivo* studies, and provide further proof of the targeting capabilities of Fe₃O₄-DMSA-SMCC-BCZM.

By performing this study, our intention was to show that the antibody-functionalized Fe₃O₄-DMSA-SMCC-BCZM exhibited targeted delivery to M165 tumors, while the non-functionalized

nanoconstruct Fe₃O₄-DMSA did not. We believe that both our *ex vivo* and *in vivo* imaging experiments, as well as the performed histopathology study, have proven the concept of our hypothesis.

CONCLUSIONS

In this proof-of-concept study, we have successfully prepared and tested a dual-modality nanoplateform functionalized with the monoclonal antibody BCZM. We have demonstrated that our nanoconstruct does not cause toxic effects in normal and cancer cells and has the ability to bind to the VEGF-165 isoform overexpressed on M165 tumor cells, when labeled with ^{99m}Tc, forming stable constructs. *Ex vivo* biodistribution studies showed that the tumor-to-blood and the tumor-to-muscle ratios reached a maximum at 24 h p.i. (~7 and ~18 respectively), confirming high specificity of the antibody-functionalized tracer toward the overexpressed VEGF-165 isoform. Initial pilot *in vivo* images were in line with the *ex vivo* results, which were further proven

by the histopathology study. The overall encouraging preliminary results we have obtained warrant further investigation into the dual-modality capabilities of the developed probes. However, further modifications may be required to improve the *in vivo* behavior of these nanoconstructs.

The primary idea behind the design and synthesis of these NPs was to provide a platform for the development of a dual-modality molecular imaging agent. We envision that once the targeted nanoconstruct is efficiently delivered to its target, it can be developed into a therapeutic tool, by exploiting its magnetic properties after application of an external magnetic field to heat tissue or activate drug release. The theranostic potential of these NPs could be further enhanced after radiolabeling with Rhenium-188 (¹⁸⁸Re), a therapeutic isotope with chemical properties similar to ^{99m}Tc.

AUTHOR CONTRIBUTIONS

CT, DS, and PB designed the study and analyzed the data. All authors contributed to the experimental execution of

REFERENCES

- Ai, F., Ferreira, C. A., Chen, F., and Cai, W. (2016). Engineering of radiolabeled iron oxide nanoparticles for dual-modality imaging. *Wiley Interdiscip. Rev. Nanomed. Nanobiotechnol.* 8, 619–630. doi: 10.1002/wnnan.1386
- Anselmo, A. C., and Mitragotri, S. (2016). Nanoparticles in the clinic. *Bioeng. Transl. Med.* 1, 10–29. doi: 10.1002/btm2.10003
- Auffan, M., Decome, L., Rose, J., Orsiere, T., De Meo, M., Briois, V., et al. (2006). *In vitro* interactions between DMSA-coated maghemite nanoparticles and human fibroblasts: a physicochemical and cyto-genotoxicity study. *Environ. Sci. Technol.* 40, 4367–4373. doi: 10.1021/es060691k
- Barrow, M., Taylor, A., Murray, P., Rosseinsky, M. J., and Adams, D. J. (2015). Design considerations for the synthesis of polymer coated iron oxide nanoparticles for stem cell labelling and tracking using MRI. *Chem. Soc. Rev.* 44, 6733–6748. doi: 10.1039/C5CS00331H
- Bertrand, N., Wu, J., Xu, X. Y., Kamaly, N., and Farokhzad, O. C. (2014). Cancer nanotechnology: the impact of passive and active targeting in the era of modern cancer biology. *Adv. Drug Deliver. Rev.* 66, 2–25. doi: 10.1016/j.addr.2013.11.009
- Bouziots, P., Psimadas, D., Tsotakos, T., Stamopoulos, D., and Tsoukalas, C. (2013). Radiolabeled iron oxide nanoparticles as dual-modality SPECT/MRI and PET/MRI agents. *Curr. Top. Med. Chem.* 12, 2694–2702. doi: 10.2174/1568026611212230007
- Carmeliet, P. (2005). Angiogenesis in life, disease and medicine. *Nature* 438, 932–936. doi: 10.1038/nature04478
- Chauhan, V. P., Stylianopoulos, T., Boucher, Y., and Jain, R. K. (2011). Delivery of molecular and nanoscale medicine to tumors: transport barriers and strategies. *Annu. Rev. Chem. Biomol. Eng.* 2, 281–298. doi: 10.1146/annurev-chembiomed-061010-14300
- Chauhan, V. P., Stylianopoulos, T., Martin, J. D., Popović, Z., Chen, O., Kamoun, W. S., et al. (2012). Normalization of tumour blood vessels improves the delivery of nanomedicines in a size-dependent manner. *Nat. Nanotechnol.* 7, 383–388. doi: 10.1038/nnano.2012.45
- Chaves, S. B., Lacava, L. M., Lacava, Z. G. M., Silva, O., Pelegrini, F., Buske, N., et al. (2002). Light microscopy and magnetic resonance characterization of a DMSA-coated magnetic fluid in mice. *IEEE Trans. Magn.* 38, 3231–3233. doi: 10.1109/TMAG.2002.802495
- Chaves, S. B., Silva, L. P., Lacava, Z. G. M., Morais, P. C., and Azevedo, R. B. (2005). Interleukin-1 and interleukin-6 production in mice's lungs induced by 2, 3 meso-dimercaptosuccinic-coated magnetic nanoparticles. *J. Appl. Phys.* 97:10Q915. doi: 10.1063/1.1854531
- Chen, Y. C., Furenlid, L. R., Wilson, D. W., and Barrett, H. H. (2005). “Calibration of Scintillation Cameras and Pinhole SPECT Imaging Systems,” in *Small-Animal SPECT Imaging*, eds M. A. Kupinski and H. H. Barrett (New York, NY: Springer), 195–201.
- Chen, Z. P., Zhang, Y., Zhang, S., Xia, J. G., Liu, J. W., Xu, K., et al. (2008). Preparation and characterization of water-soluble monodisperse magnetic iron oxide nanoparticles via surface double-exchange with DMSA. *Colloids Surf. A Physicochem. Eng. Asp.* 316, 210–216. doi: 10.1016/j.colsurfa.2007.09.017
- Costa, C., Brandão, F., Bessa, M. J., Costa, S., Valdiglesias, V., Kiliç, G., et al. (2016). *In vitro* cytotoxicity of superparamagnetic iron oxide nanoparticles on neuronal and glial cells. Evaluation of nanoparticle interference with viability tests. *J. Appl. Toxicol.* 36, 361–372. doi: 10.1002/jat.3213
- Cui, D., Lu, X., Yan, C., Liu, X., Hou, M., Xia, Q., et al. (2017). Gastrin-releasing peptide receptor-targeted gadolinium oxide-based multifunctional nanoparticles for dual magnetic resonance/fluorescent molecular imaging of prostate cancer. *Int. J. Nanomed.* 12, 6787–6797. doi: 10.2147/IJN.S139246
- de Souza Albernaz M, Toma, S. H., Clanton, J., Araki, K., and Santos-oliveira, R. (2018). Decorated superparamagnetic iron oxide nanoparticles with monoclonal antibody and diethylene-triamine-pentaacetic acid labeled with thechneutin-99m and gallium-68 for breast cancer imaging. *Pharm. Res.* 35:24. doi: 10.1007/s11095-017-2320-2
- De Rosales, R. T. M., Tavaré, R., Glaria, A., Varma, G., Protti, A., and Blower, P. J. (2011). ^{99m}Tc-bisphosphonate-iron oxide nanoparticle conjugates for dual-modality biomedical imaging. *Bioconjug. Chem.* 22, 455–465. doi: 10.1021/bc100483k
- Eliceiri, B. P., and Cheresh, D. A. (1999). The role of alphav integrins during angiogenesis: insights into potential mechanisms of action and clinical development. *J. Clin. Invest.* 103, 1227–1230. doi: 10.1172/JCI6869
- Fauconnier, N., Pons, J. N., Roger, J., and Bee, A. (1997). Thiolation of maghemite nanoparticles by dimercaptosuccinic acid. *J. Colloid Interface Sci.* 194, 427–433. doi: 10.1006/jcis.1997.5125
- Furenlid, L. R., Chen, Y. C., and Kim, H. (2005). “SPECT Imager Design and Data-Acquisition System,” in *Small-Animal SPECT Imaging*, eds M. A. Kupinski and H. H. Barrett (New York, NY: Springer), 115–138.
- Furenlid, L. R., Wilson, D. W., Chen, Y. C., Kim, H., Pietraski, P. J., Crawford, M. J., et al. (2004). FastSPECT II: a second-generation high-resolution dynamic SPECT imager. *IEEE Trans. Nucl. Sci.* 51, 631–635. doi: 10.1109/TNS.2004.830975
- Galli, M., Guerrini, A., Cauteruccio, S., Thakare, P., Dova, D., Orsini, F., et al. (2017). Superparamagnetic iron oxide nanoparticles functionalized by peptide nucleic acids. *RSC Adv.* 7, 15500–15512. doi: 10.1039/C7RA00519A

the study, and to the writing process of the manuscript. All authors have read and approved of the final version of the manuscript.

ACKNOWLEDGMENTS

The authors would like to thank Dr. Zili Sideratou (NCSR Demokritos, Institute of Nanoscience and Nanotechnology) for her support and assistance with DLS measurements. The authors would also like to acknowledge Mr. Stavros Xanthopoulos for excellent technical assistance, and Dr. Theodoros Tsotakos for valuable discussions. Finally, the authors kindly thank Dr. N. Kalogeropoulos, Dr. D. Stellas and Ms. E. Salvanou for assistance with the histopathology study.

SUPPLEMENTARY MATERIAL

The Supplementary Material for this article can be found online at: <https://www.frontiersin.org/articles/10.3389/fchem.2018.00224/full#supplementary-material>

- Hoffman, D., Sun, M., Yang, L., McDonagh, P. R., Corwin, F., Sundaresan, G., et al. (2014). Intrinsically radiolabelled [(59)Fe]-SPIONs for dual MRI/radionuclide detection. *Am. J. Nucl. Med. Mol. Imaging* 4, 548–560.
- Hong, H., Yang, K., Zhang, Y., Engle, J. W., Feng, L., Yang, Y., et al. (2012). *In vivo* targeting and imaging of tumor vasculature with radiolabeled, antibody-conjugated nano-graphene. *ACS Nano* 6, 2361–2370. doi: 10.1021/nm204625e
- Jarockyte, G., Daugelaite, E., Stasys, M., Statkute, U., Poderys, V., Tseng, T. C., et al. (2016). Accumulation and toxicity of superparamagnetic iron oxide nanoparticles in cells and experimental animals. *Int. J. Mol. Sci.* 17:1193. doi: 10.3390/ijms17081193
- Karageorgou, M.-A., Vranješ-Djurić, S., Radović, M., Lyberopoulou, A., Antić, B., Rouchota, M., et al. (2017). Gallium-68 labeled iron oxide nanoparticles coated with 2, 3-dicarboxypropane-1,1-diphosphonic acid as a potential PET/MR imaging agent: a proof-of-concept study. *Contrast Media Mol. Imaging* 2017:6951240. doi: 10.1155/2017/6951240
- Karmani, L., Labar, D., Valembois, V., Bouchat, V., Nagaswaran, P. G., Bol, A., et al. (2013). Antibody-functionalized nanoparticles for imaging cancer: influence of conjugation to gold nanoparticles on the biodistribution of 89Zr-labeled cetuximab in mice. *Contrast Media Mol. Imaging* 8, 402–408. doi: 10.1002/cmmi.1539
- Lee, S., and Chen, X. (2009). Dual-modality probes for *in vivo* molecular imaging. *Mol. Imaging* 8, 87–100. doi: 10.2310/7290.2009.00013
- Lee, S. Y., Jeon, S. I., Jung, S., Chung, I. J., and Ahn, C.-H. (2014). Targeted multimodal imaging modalities. *Adv. Drug Deliv. Rev.* 76, 60–78. doi: 10.1016/j.addr.2014.07.009
- Lin, R., Huang, J., Wang, L., Li, Y., Lipowska, M., Wu, H., et al. (2018). Bevacizumab and near infrared probe conjugated iron oxide nanoparticles for vascular endothelial growth factor targeted MR and optical imaging. *Biomater. Sci.* doi: 10.1039/C8BM00225H
- Liu, S., Zhang, P., Ray Banerjee, S., Xu, J., Pomper, M. G., and Cui, H. (2015). Design and assembly of supramolecular dual-modality nanoprobes. *Nanoscale* 7, 9462–9466. doi: 10.1039/C5NR01518A
- Los, M., Roodhart, J. M., and Voest, E. E. (2007). Target practice: lessons from phase iii trials with bevacizumab and vatalanib in the treatment of advanced colorectal cancer. *Oncologist* 12, 443–450. doi: 10.1634/theoncologist.12-2-443
- Mejías, R., Gutiérrez, L., Salas, G., Pérez-Yagüe, S., Zotes, T. M., Lázaro, F. J., et al. (2013). Long term biotransformation and toxicity of dimercaptosuccinic acid-coated magnetic nanoparticles support their use in biomedical applications. *J. Control. Release* 171, 225–233. doi: 10.1016/j.jconrel.2013.07.019
- Mejías, R., Pérez-Yagüe, S., Roca, A. G., Pérez, N., Villanueva, A., Cañete, M., et al. (2010). Liver and brain imaging through dimercaptosuccinic acid-coated iron oxide nanoparticles. *Nanomedicine* 5, 397–408. doi: 10.2217/nnm.10.15
- Mendoza-Nava, H., Ferro-Flores, G., Ramírez, F. D. M., Ocampo-García, B., Santos-Cuevas, C., Aranda-Lara, L., et al. (2016). 177Lu-dendrimer conjugated to folate and bombesin with gold nanoparticles in the dendritic cavity: a potential theranostic radiopharmaceutical. *J. Nanomater.* 2016, 1–11. doi: 10.1155/2016/1039258
- Monge-Fuentes, V., García, M. P., Henriques, M. C., Teixeira, D. S., Tomaz, C., and Azevedo, R. B. (2011). Biodistribution and biocompatibility of DMSA-stabilized maghemite magnetic nanoparticles in nonhuman primates. *Nanomedicine* 6, 1529–1544. doi: 10.2217/nnm.11.47
- Morales-Avila, E., Ferro-Flores, G., Ocampo-García, B. E., De Leon-Rodriguez, L. M., Santos-Cuevas, C. L., García-Becerra, R., et al. (2011). Multimeric system of Tc-99m-labeled gold nanoparticles conjugated to c[RGDFK(C)] for molecular imaging of tumor alpha(v)beta(3) expression. *Bioconjug. Chem.* 22, 913–922. doi: 10.1021/bc100551s
- Orocio-Rodríguez, E., Ferro-Flores, G., Santos-Cuevas, C. L., Ramírez, F. de, M., and Ocampo-García, B. E., Azorín-Vega, E., et al. (2015). Two novel nanosized radiolabeled analogues of somatostatin for neuroendocrine tumor imaging. *J. Nanosci. Nanotechnol.* 15, 4159–4169. doi: 10.1166/jnn.2015.9620
- Paik, S.-Y.-R., Kim, J.-S., Shin, S., and Ko, S. (2015). Characterization, quantification, and determination of the toxicity of iron oxide nanoparticles to the bone marrow cells. *Int. J. Mol. Sci.* 16, 22243–22257. doi: 10.3390/ijms160922243
- Pluen, A., Boucher, Y., Ramanujan, S., McKee, T. D., Gohongi, T., di Tomaso, E., et al. (2001). Role of tumor-host interactions in interstitial diffusion of macromolecules: cranial vs. subcutaneous tumors. *Proc. Natl. Acad. Sci. U.S.A.* 98, 4628–4633. doi: 10.1073/pnas.081626898
- Rainone, P., Riva, B., Belloli, S., Sudati, F., Ripamonti, M., Verderio, P., et al. (2004). Development of ^{99m}Tc-radiolabeled nanosilica for targeted detection of HER 2-positive breast cancer. *Int. J. Nanomed.* 12, 3447–3461. doi: 10.2147/IJN.S129720
- Ruiz, A., Morais, P. C., Bentes de Azevedo, R., Lacava, Z. G. M., Villanueva, A., and del Puerto Morales, M. (2014). Magnetic nanoparticles coated with dimercaptosuccinic acid: development, characterization, and application in biomedicine. *J. Nanoparticle Res.* 16:2589. doi: 10.1007/s11051-014-2589-6
- Ruiz, A., Salas, G., Calero, M., Hernández, Y., Villanueva, A., Herranz, F., et al. (2013). Short-chain PEG molecules strongly bound to magnetic nanoparticle for MRI long circulating agents. *Acta Biomater.* 9, 6421–6430. doi: 10.1016/j.actbio.2012.12.032
- Schroeder, A., Heller, D. A., Winslow, M. M., Dahlman, J. E., Pratt, G. W., Langer, R., et al. (2012). Treating metastatic cancer with nanotechnology. *Nat. Rev. Cancer* 12, 39–50. doi: 10.1038/nrc3180
- Shelat, R., Chandra, S., and Khanna, A. (2018). Detailed toxicity evaluation of β-cyclodextrin coated iron oxide nanoparticles for biomedical applications. *Int. J. Biol. Macromol.* 110, 357–365. doi: 10.1016/j.ijbiomac.2017.09.067
- Shih, T., and Lindley, C. (2006). Bevacizumab: an angiogenesis inhibitor for the treatment of solid malignancies. *Clin. Ther.* 28, 1779–1802. doi: 10.1016/j.clinthera.2006.11.015
- Shukla, S., Jadaun, A., Arora, V., Sinha, R. K., Biyani, N., and Jain, V. K. (2015). *In vitro* toxicity assessment of chitosan oligosaccharide coated iron oxide nanoparticles. *Toxicol. Rep.* 2, 27–39. doi: 10.1016/j.toxrep.2014.11.002
- Stamopoulos, D., Benaki, D., Bouziotis, P., and Zirogiannis, P. N. (2007). *In vitro* utilization of ferromagnetic nanoparticles in hemodialysis therapy. *Nanotechnology* 18: 495102. doi: 10.1088/0957-4484/18/49/495102
- Torchilin, V. P. (2014). Multifunctional, stimuli-sensitive nanoparticulate systems for drug delivery. *Nat. Rev. Drug Discov.* 13, 813–827. doi: 10.1038/nrd4333
- Turner, R. J., Eikmans, M., Bajema, I. M., Bruijn, J. A., and Baelde, H. J. (2016). Stability and species specificity of renal VEGF-A Splicing patterns in kidney disease. *PLoS ONE* 11:e0162166. doi: 10.1371/journal.pone.0162166
- Varvarigou, A. D., Scopinaro, F., Leondiadis, L., Corleto, V., and Schillaci, O., De Vincentis, G., et al. (2002). Synthesis, chemical, radiochemical and radiobiological evaluation of a new ^{99m}Tc-labelled bombesin-like peptide. *Cancer Biother. Radiopharm.* 17, 317–326. doi: 10.1089/10849780260179288
- van Vlerken, L. E., and Amiji, M. M. (2006). Multi-functional polymeric nanoparticles for tumour-targeted drug delivery. *Expert Opin. Drug Deliv.* 3, 205–216. doi: 10.1517/17425247.3.2.205
- Varvarigou, A. D., Archimandritis, S. C., Sekeri-Pataryas, K. E., Sourlingas, T. G., Sivolapenko, G., and Paschali, E. (1996). Radiochemical and radioimmunological data of ^{99m}Tc-anti-CEA labelled by two diverse methods. *Nucl. Med. Commun.* 17, 80–88. doi: 10.1097/00006231-199601000-00014
- Vegt, E., van Eerd, J. E., Eek, A., Oyen, W. J., Wetzel, J. F., de Jong, M., et al. (2008). Reducing renal uptake of radiolabeled peptides using albumin fragments. *J. Nucl. Med.* 49, 1506–1511. doi: 10.2967/jnumed.108.053249
- Wang, Y., Wang, Y., Wang, L., Che, Y., Li, Z., and Kong, D. (2011). Preparation and evaluation of magnetic nanoparticles for cell labeling. *J. Nanosci. Nanotechnol.* 11, 3749–3756. doi: 10.1166/jnn.2011.3822
- Zhong, Y., Meng, F., Deng, C., and Zhong, Z. (2014). Ligand-directed active tumor-targeting polymeric nanoparticles for cancer chemotherapy. *Biomacromolecules* 15, 1955–1969. doi: 10.1021/bm5003009
- Conflict of Interest Statement:** The authors declare that the research was conducted in the absence of any commercial or financial relationships that could be construed as a potential conflict of interest.
- Copyright © 2018 Tsoukalas, Psimadas, Kastis, Koutoulidis, Harris, Paravatou-Petsotas, Karageorgou, Furenlid, Moulopoulos, Stamopoulos and Bouziotis. This is an open-access article distributed under the terms of the Creative Commons Attribution License (CC BY). The use, distribution or reproduction in other forums is permitted, provided the original author(s) and the copyright owner are credited and that the original publication in this journal is cited, in accordance with accepted academic practice. No use, distribution or reproduction is permitted which does not comply with these terms.**



Synthesis of Symmetrical Tetrameric Conjugates of the Radiolanthanide Chelator DOTPI for Application in Endoradiotherapy by Means of Click Chemistry

OPEN ACCESS

Edited by:

Lorenzo Tei,
Università degli Studi del Piemonte
Orientale, Italy

Reviewed by:

Steve J. Archibald,
University of Hull, United Kingdom
Kristina Djanashvili,
Delft University of Technology,
Netherlands

*Correspondence:

Johannes Notni
johannes.notni@tum.de

[†]These authors have contributed
equally to this work.

#Present Address:

Adrienn Vágner,
Scandomed Ltd., Debrecen, Hungary

Specialty section:

This article was submitted to
Inorganic Chemistry,
a section of the journal
Frontiers in Chemistry

Received: 24 January 2018

Accepted: 22 March 2018

Published: 10 April 2018

Citation:

Wurzer A, Vágner A, Horváth D, Fellegi F, Wester H-J, Kálman FK and Notni J (2018) Synthesis of Symmetrical Tetrameric Conjugates of the Radiolanthanide Chelator DOTPI for Application in Endoradiotherapy by Means of Click Chemistry. *Front. Chem.* 6:107.
doi: 10.3389/fchem.2018.00107

Alexander Wurzer^{1†}, Adrienn Vágner^{2‡}, Dávid Horváth², Flóra Fellegi², Hans-Jürgen Wester¹, Ferenc K. Kálman² and Johannes Notni^{1*}

¹ Pharmaceutical Radiochemistry, Technische Universität München, Munich, Germany, ² Department of Inorganic and Analytical Chemistry, University of Debrecen, Debrecen, Hungary

Due to its 4 carbonic acid groups being available for bioconjugation, the cyclen tetraphosphinate chelator DOTPI, 1,4,7,10-tetraazacyclododecane-1,4,7,10-tetrakis[methylene(2-carboxyethyl)phosphinic acid]), represents an ideal scaffold for synthesis of tetrameric bioconjugates for labeling with radiolanthanides, to be applied as endoradiotherapeutics. We optimized a protocol for bio-orthogonal DOTPI conjugation via Cu(I)-catalyzed Huisgen-cycloaddition of terminal azides and alkynes (CuAAC), based on the building block DOTPI(azide)₄. A detailed investigation of kinetic properties of Cu(II)-DOTPI complexes aimed at optimization of removal of DOTPI-bound copper by transchelation. Protonation and equilibrium properties of Ca(II)-, Zn(II), and Cu(II)-complexes of DOTPI and its tetra-cyclohexylamide DOTPI(Chx)₄ (a model for DOTPI conjugates) as well as kinetic inertness (transchelation challenge in the presence of 20 to 40-fold excess of EDTA) were investigated by pH-potentiometry and spectrophotometry. Similar stability constants of Ca^{II}--, Zn^{II}- and Cu^{II}-complexes of DOTPI ($\log K_{(\text{CaL})} = 8.65$, $\log K_{(\text{ZnL})} = 15.40$, $\log K_{(\text{CuL})} = 20.30$) and DOTPI(Chx)₄ ($\log K_{(\text{CaL})} = 8.99$, $\log K_{(\text{ZnL})} = 15.13$, $\log K_{(\text{CuL})} = 20.42$) were found. Transchelation of Cu(II)-complexes occurs via proton-assisted dissociation, whereafter released Cu(II) is scavenged by EDTA. The corresponding dissociation rates [$k_d = 25 \times 10^{-7}$ and $5 \times 10^{-7} \text{ s}^{-1}$ for Cu(DOTPI) and Cu(DOTPI(Chx)₄), respectively, at pH 4 and 298 K] indicate that conjugation increases the kinetic inertness by a factor of 5. However, demetallation is completed within 4.5 and 7.2 h at pH 2 and 25°C, respectively, indicating that Cu(II) removal after formation of CuAAC can be achieved in an uncomplicated manner by addition of excess H₄EDTA. For proof-of-principle, tetrameric DOTPI conjugates of the prostate-specific membrane antigen (PSMA) targeting motif Lys-urea-Glu (KuE) were synthesized via CuAAC as well as dibenzo-azacyclooctine (DBCO) based, strain-promoted click chemistry (SPAAC), which were labeled with Lu-177 and subsequently evaluated

in vitro and in SCID mice bearing subcutaneous LNCaP tumor (PSMA+ human prostate carcinoma) xenografts. High affinities (3.4 and 1.4 nM, respectively) and persistent tumor uptakes (approx. 3.5% 24 h after injection) confirm suitability of DOTPI-based tetramers for application in targeted radionuclide therapy.

Keywords: Huisgen-reaction, potentiometry, spectrophotometry, phosphinate, radiopharmaceuticals, endoradiotherapy, prostate-specific membrane antigen, theranostics

INTRODUCTION

Endoradiotherapy (also termed molecular radiotherapy, radioligand therapy or, if addressing peptide receptors, peptide receptor radionuclide therapy (PRRT) or, if involving alpha-emitting nuclides, targeted alpha therapy) (Oyen et al., 2007) refers to the internal application of radionuclides for therapeutic purposes, above all, for curing cancer. In the respective disease management schemes, radiotherapeutics represent the natural complements to imaging tracers. In a tandem application of both types of agents, referred to as “theranostics,” one targeting mechanism is exploited for delivery of different sorts of radionuclides to tissues, either for diagnostic purposes, that is, with the intention to localize lesions by means of external detection of emitted gamma photons, or to achieve a therapeutic effect via local absorption of particle (i.e., alpha- or beta) radiation. The corresponding radiopharmaceuticals are frequently based on peptides, peptidomimetics, enzyme inhibitors, or similar molecules capable of recognizing a specific cell surface receptor, membrane-bound enzyme, ion channel, or comparable target. The bioactive structures are often decorated with a chelate ligand for kinetically inert complexation of a metal ion radionuclide (Wadas et al., 2010). At present, radiotherapeutics most frequently rely on lanthanide(III)- or chemically related ions, such as ¹⁷⁷Lu, ⁹⁰Y, ²²⁵Ac, or ²¹³Bi (Notni and Wester, 2018). Recognizing malignant cells by overexpression of above-mentioned surface markers, the radiolabeled bioconjugates deliver these beta- or alpha-emitting isotopes in the lesion, resulting in a local irradiation which kills malignant cells.

In this context, the chelator DOTA (**Figure 1**) plays an important role (Stasiuk and Long, 2013) since it forms stable and sufficiently inert complexes with virtually all relevant metal ions. DOTA is usually attached to e.g., peptides via amide formation on one side arm, resulting in derivatives of DOTA-monoamide which is the actual chelator structure in such conjugates (commonly dubbed “DOTA peptides”). However, a likewise functionalization of more than one acetic acid side arm of DOTA yields conjugates whose metal complexes either lack kinetic inertness (e.g., in case of the positron emitter ⁶⁸Ga^{III}) or show very slow formation kinetics (namely, with lanthanide(III) ions) (Baranyai et al., 2007; Pasha et al., 2007), limiting practical applicability in radiopharmacy. Conjugates comprising more than one biomolecule (multimers) are nevertheless desirable because a multitude of similar bioactive structure elements in a single framework usually results in enhanced target affinities, and sometimes increases uptake of the respective

radiolabeled compounds in target tissues (Maschauer et al., 2017).

For this purpose, we recently designed the DOTA-analog tetraphosphinate chelator DOTPI (**Figure 1**) featuring four terminal carboxylic acid moieties, which are not required for metal ion complexation and, therefore, are available for bioconjugation (Šimeček et al., 2013). However, similar to the observations made for its smaller congener TRAP (1,4,7-triazacyclonane-1,4,7-tris[methylene(2-carboxyethylphosphinic acid)]) (Notni et al., 2014), amide functionalization of these carboxylates using standard peptide coupling reagents is sometimes complicated by instability of the active ester intermediates (Baranyai et al., 2015). Similar to TRAP, functionalization of DOTPI via “click chemistry,” (Cu^I-catalyzed alkyne-azide cycloaddition, CuAAC) (Meldal and Tornøe, 2008) employing respective DOTPI-derivatives decorated with “clickable” functional groups, such as DOTPI(azide)₄ (**Figure 1**) (Wurzer et al., 2018), appeared to be a valuable alternative. Since the presence of ionic Cu inevitably results in copper complexes of the desired conjugates wherein the Cu ion blocks the coordination site intended for accommodation of the radiometal, removal of chelator-bound Cu, ultimately being transformed to oxidation state +2 during workup, is mandatory to restore the radiolabeling properties. As discussed previously, demetalation with sulfide or cyanide frequently causes problems, while proton-assisted dissociation, promoted by excess of a competing chelator, should be widely applicable and compatible with many synthetic tasks (Notni and Wester, 2016). Against this background, we investigated the metal coordination properties of DOTPI and a model conjugate thereof, DOTPI(Chx)₄ (**Figure 1**), with a particular emphasis on Cu^{II} complexes, in order to facilitate optimization of respective demetallation protocols and to support application of CuAAC for elaboration of DOTPI-based multimers.

RESULTS

In order to enhance legibility, charge, and protonation state of ligands and complexes is indicated only where necessary for comprehension and where possible without ambiguity, e.g., in case it is referred to a single, well defined species and not to a mixture, as is mostly the case due to protonation equilibria. The animal experiments were conducted in accordance with the German Animal Welfare Act (Tierschutzgesetz), and an ethics approval was obtained from the responsible authority (Regierung von Oberbayern).

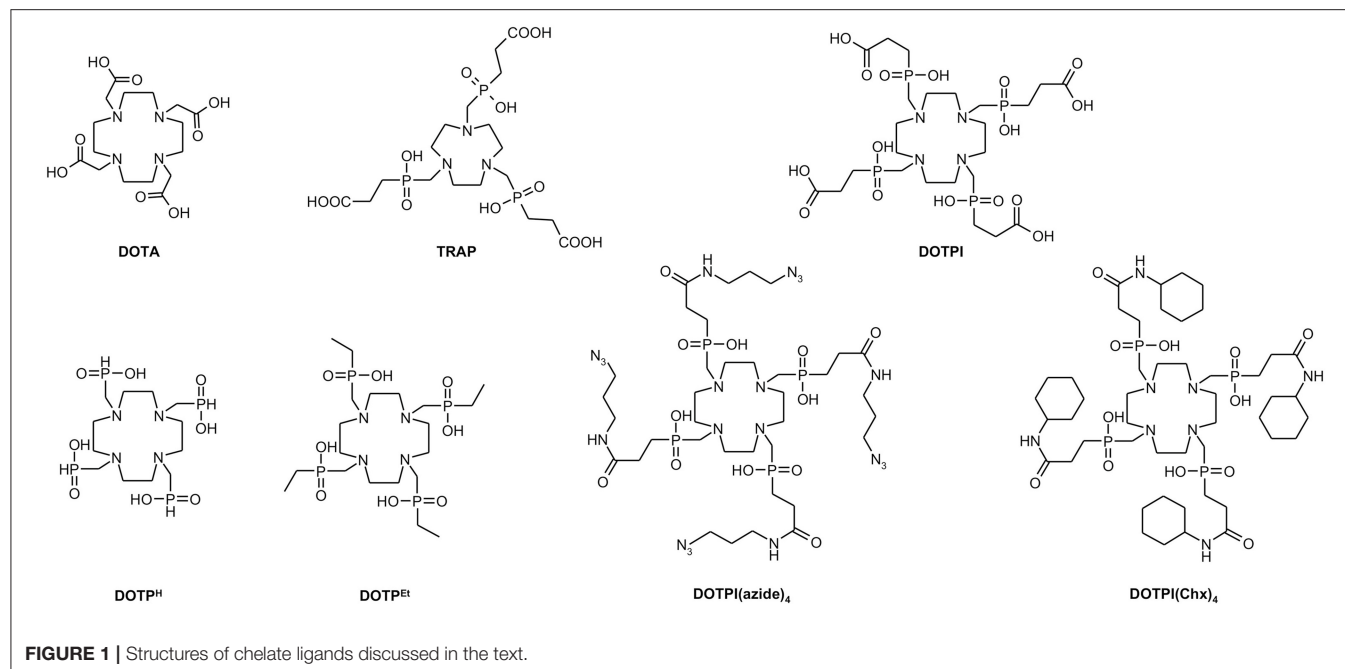


FIGURE 1 | Structures of chelate ligands discussed in the text.

Solution Thermodynamics

Protonation schemes of cyclens bearing four *N*-substituents with additional donors (often referred to as DOTA-like ligands) have been thoroughly investigated in the past (Desreux et al., 1981; Bianchi et al., 2000; Takács et al., 2014). **Table 1** displays the respective data for DOTPI in comparison to DOTA (Baranyai et al., 2010) and the most closely related tetraphosphinate analogs, DOTPH (Bazakas and Lukeš, 1995; Kotková et al., 2009) and DOTPEt (Lázár et al., 1991) (**Figure 1**). According to previous literature, it is assumed that the first and second protonation of all chelators under investigation occur at two opposite ring nitrogen atoms. The subsequent protonation steps most likely take place at protonation sites located at the side arms (if available, at the carboxylate groups), due to greater charge separation and lower electrostatic repulsion between the distant protonated donor atoms. Protonations of the phosphinate moieties, characterized by the $\log K_7^H$ and $\log K_8^H$ for DOTPI and $\log K_3^H$ for DOTPI(Chx)₄, occur only in the acidic pH region (Rohovec et al., 2000), which is why these phosphinate ligands are generally capable of metal complexation and rapid radiolabeling at much lower pH values than chelators with acetic acid side arms, such as DOTA.

The equilibrium properties of chelates based on the 1,4,7,10-tetraazacyclododecane-1,4,7,10-tetrakis(methylenephosphinic acid) scaffold depend on the electronic properties of the substituents on the phosphorus atoms (Kotková et al., 2009). $\log K_1^H$ and $\log K_2^H$ values for DOTPI(Chx)₄ are somewhat lower than those of DOTPI, while this lower basicity of the ring nitrogens might be explained by the presence of the more electronegative amide substituents on the pendant arms. However, the lower $\log K_1^H$ value measured for DOTA in 0.15 M

NaCl has another reason; it is explained by the formation of relatively stable $[\text{Na}(\text{DOTA})]^{3-}$ complex ($\log K_{\text{NaL}} = 4.38$) (Chaves et al., 1992). Our data indicate that DOTPI forms a similar NaL complex, entailing a lower $\log K_1^H$ value in presence of 0.15 M NaCl than in 0.1 M Me₄NCI (Šimeček et al., 2013).

Total basicity of ligands ($\Sigma \log K_i^H$, **Table 1**) generally correlates with thermodynamic stability constants (K_{ML}) of their metal complexes, while in order to obtain chemically meaningful values, the $\log K_i^H$ values of the distant carboxylate groups were not considered for calculation of $\Sigma \log K_i^H$ value of DOTPI because they are not involved in metal ion coordination. That being said, it is not surprising that the $\log K_{\text{ML}}$ value of $[\text{Ca}(\text{DOTA})]$, $[\text{Zn}(\text{DOTA})]$, and $[\text{Cu}(\text{DOTA})]$ complexes is about 2–5 logK unit higher than phosphinic acid analogs, because DOTA shows a significantly higher total basicity (**Table 2**).

Among the tetraphosphinates, total basicities $\Sigma \log K_i^H$ of DOTPI(Chx)₄, DOTPI, and DOTPEt ligands are similar but about 1–3 orders of magnitude higher than that of DOTPH which, as expected, is reflected by similar $\log K_{\text{CuL}}$ and $\log K_{\text{ZnL}}$ values for Cu^{II} and Zn^{II} complexes of the *P*-substituted ligands but somewhat lower stabilities for those of DOTPH. Thermodynamic stabilities of the Ca^{II} complexes are, however, similar for all phosphinate ligands. This might be explained by differences in the preferred coordination number of these divalent metal ions (Cu^{II} and Zn^{II}: 6, Ca^{II}: 6–8) owing to their different size (Cu^{II}: 73 p.m., Zn^{II}: 74 p.m., Ca^{II}: 100 p.m.), entailing different structures for Cu^{II} and Zn^{II} complexes as observed for Ca^{II} complexes. Based on available structural data (Riesen et al., 1986), it is assumed that the smaller cations are bound in an N₄O₂ coordination environment involving only two side arm oxygens, whereas Ca^{II} is surrounded by a N₄O₄

TABLE 1 | Protonation constants of DOTPI(Chx)₄, DOTPI, DOTP^H, DOTP^{Et}, and DOTA at 25°C (for structures see **Figure 1**).

DOTPI(Chx) ₄		DOTPI		DOTP ^H		DOTP ^{Et}		DOTA	
I	0.15 M NaCl	0.15 M NaCl	0.1 M Me ₄ NCl (Šimeček et al., 2013)		0.1 M KNO ₃		0.1 M KNO ₃		0.15 M NaCl
$\log K_1^H$	9.89 (1)	10.27 (1)		11.58		10.41, 10.58		10.94	9.14
$\log K_2^H$	7.73 (1)	8.42 (1)		8.90		6.83, 6.93		8.24	9.21
$\log K_3^H$	3.34 (1)	5.45 (2)		5.65		1.97, 1.90		3.71	4.48
$\log K_4^H$	–	4.78 (2)		4.98		–		–	4.03
$\log K_5^H$	–	4.42 (2)		4.61		–		–	1.99
$\log K_6^H$	–	3.88 (2)		4.07		–		–	1.58
$\log K_7^H$	–	2.83 (2)		3.12		–		–	–
$\log K_8^H$	–	1.17 (2)		1.31		–		–	–
$\Sigma \log K_i^H$	20.96	22.69		24.91		19.21, 19.41		22.89	30.43

Equivalent protonations, occurring for DOTPI and DOTPI(Chx)₄ at the first and second phosphinate oxygen, are denoted by $\log K_7^H/\log K_8^H$ and $\log K_3^H/\log K_4^H$, respectively.

TABLE 2 | Stability constants ($\log K_{ML}$) for non-protonated DOTPI(Chx)₄, DOTPI, DOTP^H, DOTP^{Et}, and DOTA complexes formed with divalent metals at 25°C, determined by UV/Vis spectroscopy (a) or potentiometry (b).

DOTPI(Chx) ₄		DOTPI		DOTP ^H (Baranyai et al., 2007)		DOTP ^{Et} (Desreux et al., 1981)		DOTA (Takács et al., 2014)	
I	0.15 M NaCl	0.15 M NaCl	0.1 M Me ₄ NCl (Lázár et al., 1991)		0.1 M KNO ₃		0.1 M KNO ₃		0.15 M NaCl
CuL	20.42 (1)^a	20.30 (5)^a	23.11		18.03		19.59		21.97 (1)
ZnL	15.13 (1) ^b	15.40 (2) ^b	18.57		14.60		15.80		17.35 (1)
CaL	8.99 (2) ^b	8.65 (3) ^b	12.48		9.46		9.39		13.84 (1)

Stepwise protonation constants of the complexes as well as details on experimental procedures and UV/VIS signals used for calculation are given in the Supplementary Information.

donor set involving all side arms. Hence, side arm basicity and protonation presumably affects the complexation equilibria in a different manner.

Formation of several protonated Cu(H_xL) species at pH < 7 has been confirmed by pH-potentiometric and spectrophotometric studies of solutions containing Cu^{II} and DOTPI(Chx)₄ or DOTPI, respectively, while both ligands form Cu^{II} complexes already in acidic solution (pH 1.5 and lower). Since molar absorptivities of the protonated Cu(H_xDOTPI) and non-protonated Cu(DOTPI) species were found to be essentially equal, it can be assumed that stepwise protonation of Cu(DOTPI) starts with the non-coordinating carboxylates, resulting in Cu(HL), Cu(H₂L), Cu(H₃L), and Cu(H₄L). Two further protonations at comparable pH are observed for Cu^{II} complexes of both DOTPI(Chx)₄ and DOTPI, while it appears most plausible that they occur on phosphinate oxygens because two of these moieties do not coordinate to Cu^{II} and can thus be protonated.

Kinetic Inertness and Transchelation

In order to provide the necessary information for optimization of demetallation protocols, we investigated the pH-dependent kinetics of the transchelation of Cu^{II} from CuDOTPI and CuDOTPI(Chx)₄ complexes to ethylenediamine-tetraacetic acid (EDTA). Reactions were monitored by UV spectrophotometry at the absorption bands of Cu(DOTPI) and Cu(DOTPI(Chx)₄) over a pH range of 1.5–4.5, using a 20- and 40-fold excess of EDTA (see Supplementary information).

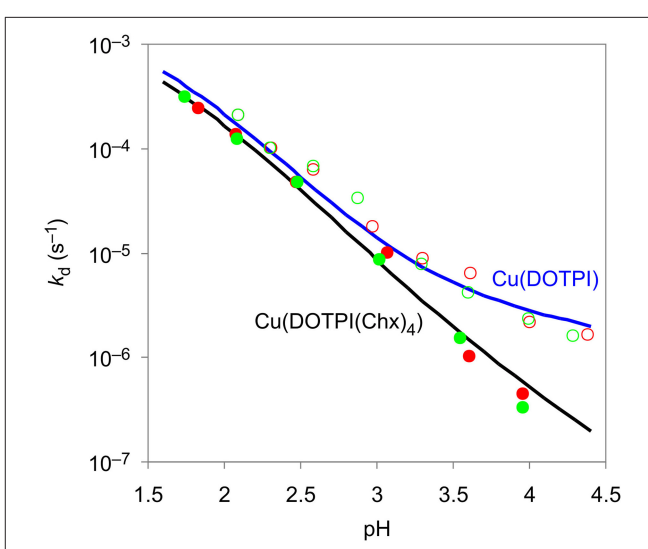
**FIGURE 2 |** Pseudo-first-order rate constants at 25°C in 0.15 M NaCl for the reaction of Cu^{II} complexes of DOTPI (empty symbols) and DOTPI(Chx)₄ (filled symbols) with a 20- (red) and 40-fold (green) excess of EDTA at different pH values. Respective k_d functions were calculated from kinetic and equilibrium data.

Figure 2 shows that the obtained pseudo-first-order rate constants do not depend on the excess of EDTA, and increase with decreasing pH. Hence, it can be assumed that the

TABLE 3 | Rate constants ($k_{\text{Cu}(\text{H}_i\text{L})}$) and half-lives ($t_{1/2} = \ln 2/k_d$) characterizing the dissociation reactions of Cu(DOTPI) and Cu(DOTPI(Chx)₄) complexes (0.15 M NaCl, 25°C).

	Cu(DOTPI)	Cu(DOTPI(Chx) ₄)	Cu(TRAP) (Baranyai et al., 2015)	Cu(TRAP(Chx) ₃) (Baranyai et al., 2015)
$k_{\text{CuL}} (\text{s}^{-1})$	–	–	–	6×10^{-7}
$K_{\text{Cu}(\text{HL})} (\text{s}^{-1})$	–	$(1.7 \pm 0.3) \times 10^{-5}$	–	2.3×10^{-3}
$K_{\text{Cu}(\text{H}_2\text{L})} (\text{s}^{-1})$	–	$(2.9 \pm 0.4) \times 10^{-3}$	5×10^{-6}	–
$K_{\text{Cu}(\text{H}_3\text{L})} (\text{s}^{-1})$	$(1.0 \pm 0.5) \times 10^{-6}$	–	6.7×10^{-5}	–
$K_{\text{Cu}(\text{H}_4\text{L})} (\text{s}^{-1})$	$(3.1 \pm 0.6) \times 10^{-6}$	–	2.1×10^{-3}	–
$K_{\text{Cu}(\text{H}_5\text{L})} (\text{s}^{-1})$	$(4.6 \pm 0.5) \times 10^{-5}$	–	–	–
$K_{\text{Cu}(\text{H}_6\text{L})} (\text{s}^{-1})$	$(2.0 \pm 0.2) \times 10^{-3}$ ($K_{\text{Cu}(\text{H}_6\text{L})} = 17 \pm 8$)	–	–	–
$K_d (\text{h}^{-1})$ at pH = 3.0	5.0×10^{-2}	3.1×10^{-2}	4.4×10^{-1}	2.4×10^{-1}
$t_{1/2}$ (h) at pH = 3.0	13.8	22.4	1.57	2.94

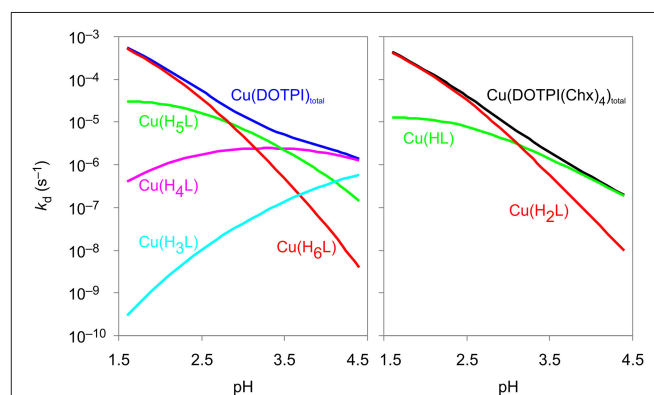
Literature data for corresponding TRAP complexes (Baranyai et al., 2015) are included for comparison.

transchelation of Cu(DOTPI) and Cu(DOTPI(Chx)₄) occurs by initial protonation, followed by spontaneous dissociation of the protonated Cu^{II} complexes as rate-determining step, while irreversibility is granted by scavenging the released Cu^{II} with EDTA. Similar data and mechanistic implications have been found for Cu^{II} complexes of the smaller triphosphinate macrocycle TRAP (Baranyai et al., 2015), underscoring wide applicability of the transchelation approach for demetallation of chelator conjugates after CuAAC coupling (Notni and Wester, 2016).

Table 3 summarizes rate (k) and equilibrium constants (K) of all possible pathways for dissociation of the protonated species Cu(H_xDOTPI) and Cu(H_yDOTPI(Chx)₄) ($x = 3,4,5,6$; $y = 1,2$; for details see Supplementary Information). According to the proposed mechanism, that is, a fast protonation equilibrium followed by a first-order dissociation reaction rendered irreversible by competitor excess, cleavage of the protonated Cu(H_xL) complex is promoted by transfer of the proton, which is initially located on the pendant arm, to a ring nitrogen, resulting in the most labile intermediate, an off-cage complex (Baranyai et al., 2015). Overall, the proton displaces the Cu^{II} ion from the coordination cage, causing dissociation of the Cu(H_xL) complex.

A comparison of the rate constants ($k_{\text{Cu}(\text{H}_i\text{L})}$) obtained for protonated species Cu(H_xDOTPI) and Cu(H_yDOTPI(Chx)₄) confirms that dissociation of the uncharged species, [Cu(H₂DOTPI(Chx)₄)] and [Cu(H₆DOTPI)], which likely contains two non-coordinated and protonated phosphinic oxygen atoms, occurs with a very similar rate. Moreover, the dissociation rates of [Cu(H₆DOTPI)] and [Cu(H₂DOTPI(Chx)₄)] are very similar to those of [Cu(H₄TRAP)] and [Cu(HTRAP(Chx)₃)] (Baranyai et al., 2015), which might be explained by similar activation parameters characterizing the proton transfer process from the phosphinate oxygen to the ring nitrogen, resulting in comparable dissociation rate constants at pH < 2.

Figure 3 shows the calculated contributions of individual dissociation rates for all protonated Cu(H_xDOTPI) and Cu(H_yDOTPI(Chx)₄) species to the overall demetallation

**FIGURE 3 |** Contributions of Cu(DOTPI) and Cu(DOTPI(Chx)₄) complexes in different protonation states to the overall rates of the dissociation reaction.

rates (see also Figures S3, S6), which decrease with increasing pH. In the pH range 1.5–4.5, dissociation of Cu(DOTPI) and Cu(DOTPI(Chx)₄) occurs by the decomplexation of the various protonated species, respectively. In this respect, [Cu(H₆DOTPI)] and [Cu(H₂DOTPI(Chx)₄)] are equivalent as they both carry two phosphinate-bound protons and hence, show similar dissociation rates. Since these species are prevailing at pH < 2, they govern overall dissociation rates which are, therefore, nearly identical (see also **Figure 2**). On the other hand, at pH > 4, a substantial amount of protonated (and thus, labile) species is observed only for the Cu(DOTPI) system, explaining the higher inertness of Cu(DOTPI(Chx)₄) complexes.

Figure 4 displays the quintessence of the kinetic studies for practical consideration, namely, the dissociation half-lives ($t_{1/2}$) of Cu(DOTPI) and Cu(DOTPI(Chx)₄) as functions of pH (see Supplemental information, Equation 18). It shows that loss of protonable carboxylates by amide functionalization results in higher $t_{1/2}$ of the respective Cu(DOTPI(Chx)₄) complexes at higher pH; at pH > 4, the increase exceeds one order of magnitude. On the other hand, Cu^{II} removal from both neat and decorated DOTPI occurs with similar efficiency at lower

pH. In view of the calculated $t_{1/2}$, it appears recommendable to carry out such reactions at pH values below 3, preferably at pH = 2, while slightly elevated temperature (e.g., 50°C) will also substantially accelerate the reaction (Baranyai et al., 2015). Apart from that, a $t_{1/2}$ of > 4,000 h for dissociation of Cu(DOTPI(Chx)₄) at pH > 5 suggests compatibility with the positron emitter ⁶⁴Cu ($T_{1/2} = 12.7$ h) for application in ⁶⁴Cu-PET imaging.

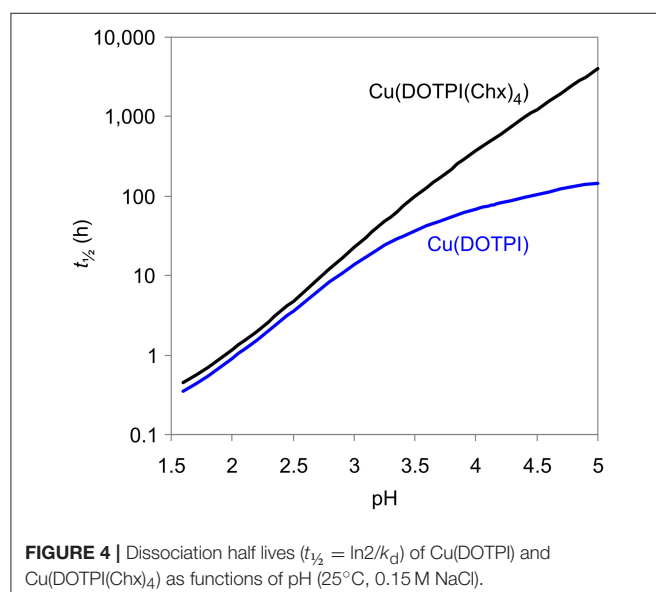


FIGURE 4 | Dissociation half lives ($t_{1/2} = \ln 2/k_d$) of Cu(DOTPI) and Cu(DOTPI(Chx)₄) as functions of pH (25°C, 0.15 M NaCl).

Application

In order to demonstrate utility of the CuAAC/demetallation tandem reaction for assembly of large multimeric bioconjugates and application in the design of therapeutic radiopharmaceuticals, the 4-fold azide-decorated building block DOTPI(azide)₄ (Wurzer et al., 2018) was reacted with alkyne-functionalized KuE (lysine-urea-glutamic acid, an inhibitor motif for prostate-specific membrane antigen, PSMA, EC 3.4.17.21; synonyms: glutamate carboxypeptidase II, NAALADase (Mesters et al., 2006); a membrane-bound zinc hydrolase which is overexpressed by malignant human prostate cancers). As an alternative, the inhibitor was equipped with dibenzo-azacyclooctyne (DBCO) (Agard et al., 2004) for conjugation via “copper-free click chemistry” (strain-promoted alkyne-azide cycloaddition, SPAAC) according to path **B** in **Figure 5**. Although this approach circumvents the entire demetallation problem, potentially obviating the above study, the disadvantages of SPAAC are limiting its practical value in the present context. Firstly, reaction rates for SPAAC are several orders of magnitude lower than those of CuAAC, requiring adjustment of reaction conditions, for example, a higher excess of reactants, in order to achieve reasonable yields. Secondly, the isomerism of the formed linker moiety gives rise to a total of 6 stereoisomers of DOTPI(DBCO-KuE)₄ which are hard to separate, if at all. While the isomers are not likely to exhibit noticeable differences regarding their pharmacodynamics, justifying use of the mixture for *in-vivo* application, such action might nonetheless lead to regulatory issues upon clinical translation. Third, introduction of several large, non-polar linker groups usually affects pharmacokinetics, above all, due to

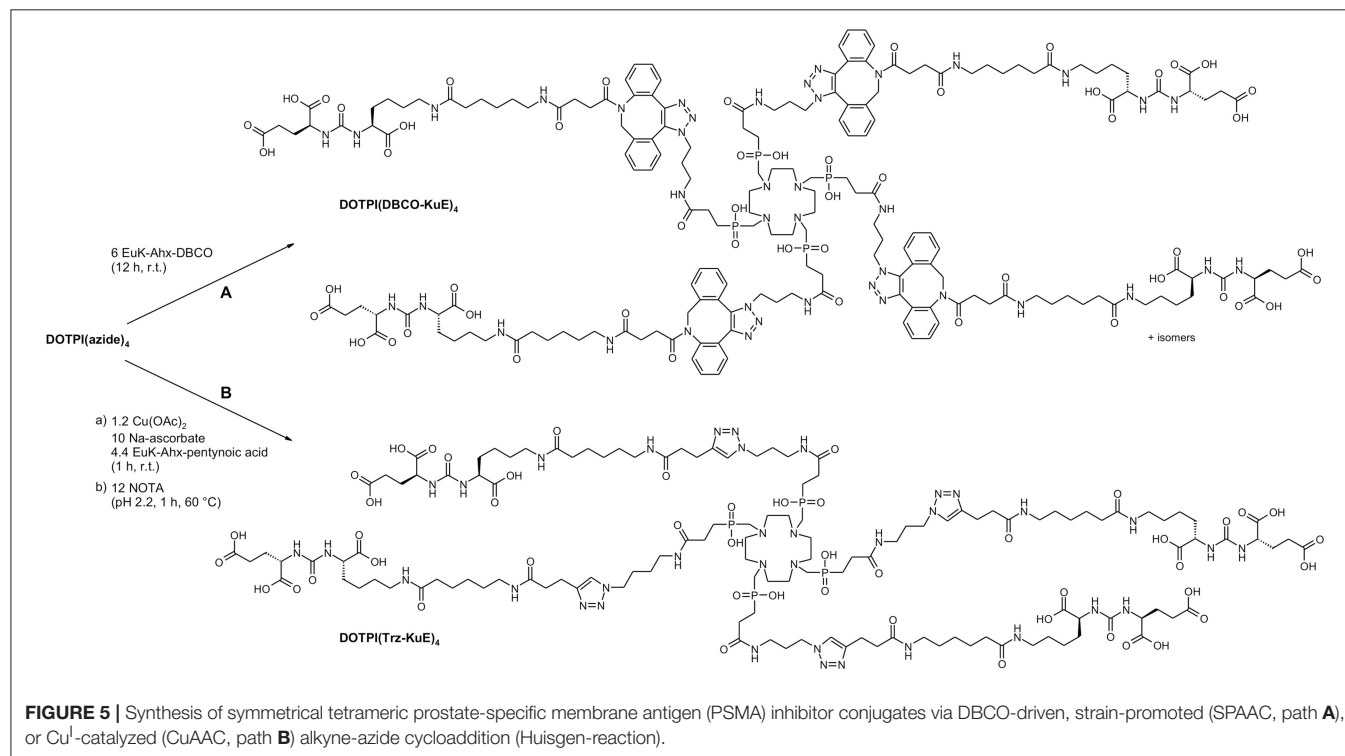


FIGURE 5 | Synthesis of symmetrical tetrameric prostate-specific membrane antigen (PSMA) inhibitor conjugates via DBCO-driven, strain-promoted (SPAAC, path **A**), or Cu¹-catalyzed (CuAAC, path **B**) alkyne-azide cycloaddition (Huisgen-reaction).

increased plasma protein binding. The overall simplicity of the CuAAC/demetallation approach (**Figure 5**, path A) thus appears preferable for this type of synthetic task, not least because of the known robustness and pharmacokinetic inertness of the 1,3-triazole linkage (Horne et al., 2004, 2009; Bock et al., 2007; Liu et al., 2008; Pedersen and Abell, 2011; Davis et al., 2012; Tischler et al., 2012).

Because the ^{177}Lu -labeled tetramers feature nearly identical linker lengths and differ only in the type of linkage, the effect of the dibenzo-azacyclooctane system annulated to the triazole moiety becomes clearly apparent. While PSMA affinities of both tetramers are, as expected (Maschauer et al., 2017), higher than that of clinically applied monomers (Weineisen et al., 2014; Benešová et al., 2016), it is conspicuous that the $^{\text{nat}}\text{Lu}$ -DOTPI(DBCO-KuE)₄ exhibits a higher affinity than $^{\text{nat}}\text{Lu}$ -DOTPI(Trz-KuE)₄ which is featuring simple 1,2,3-triazole linkages ($\text{IC}_{50} = 1.4 \pm 0.5$ vs. 3.4 ± 0.1 , respectively). This is because apart from the primary KuE binding site, namely, the catalytic center which contains two hydroxo-bridged Zn^{II} ions, the enzyme PSMA features another hydrophobic site in close proximity (Zhang et al., 2010) which can be addressed by lipophilic groups in the linker (Kularatne et al., 2009; Banerjee et al., 2010). With regard to the DBCO moieties, a virtue is hence made of necessity, because these hydrophobic structure elements contribute to a divalent binding mode. Since the observed increase of affinity is linked to the particular combination of binding sites of the target PSMA, this favorable effect of DBCO cannot be generalized.

Apart from that, **Figure 6** shows that the higher degree of hydrophilicity of ^{177}Lu -DOTPI(Trz-KuE)₄ ($\log D = -5.0 \pm 0.1$) results in a remarkably low kidney uptake and a much faster washout from non-target tissues as compared to ^{177}Lu -DOTPI(DBCO-KuE)₄ ($\log D = -4.0 \pm 0.1$). A virtually similar tumor uptake of both compounds after 24 h gives rise to substantially better tumor-to-organ ratios for ^{177}Lu -DOTPI(Trz-KuE)₄. However, although the acquired data are sufficient for proof-of-principle in the context of this study, a more detailed investigation of the compounds is necessary in order to draw a reliable conclusion regarding their clinical potential.

DISCUSSION

Replacement of the acetate with amide groups in the pendant arms of DOTPI does not affect the thermodynamic stability ($\log K_{\text{ML}}$ values) of the Ca^{II} -, Zn^{II} -, and Cu^{II} -complexes, while dissociation half-lives of the Cu^{II} chelates at pH > 3 show a clear trend toward higher kinetic inertness. This is another example for the notion that thermodynamic stability constants of complexes do not necessarily correlate with their kinetic inertness, requiring more than just equilibrium data for prediction or confirmation of the suitability of (radio-)metal chelates for *in-vivo* applications. This applies even more because any data acquired under ideal conditions, e.g., in neat solvents or well-defined buffers, should be treated with care in view of a limited transferability to more complex systems, such as living organisms. For example, the aforementioned demetallation half-life of more than 4,000 h

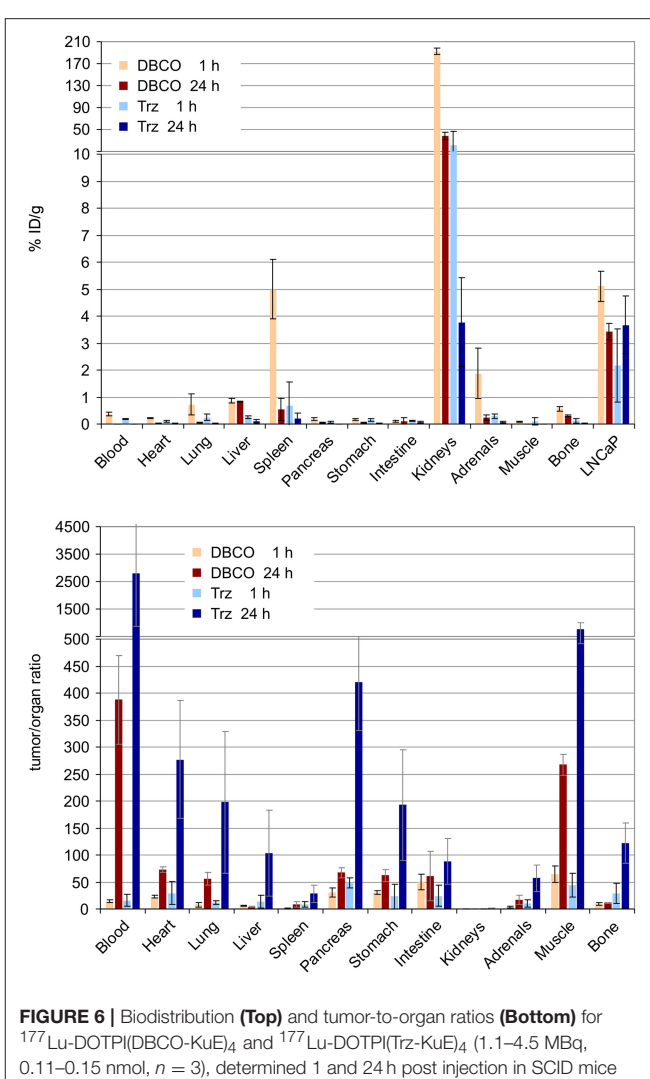


FIGURE 6 | Biodistribution (**Top**) and tumor-to-organ ratios (**Bottom**) for ^{177}Lu -DOTPI(DBCO-KuE)₄ and ^{177}Lu -DOTPI(Trz-KuE)₄ (1.1–4.5 MBq, 0.11–0.15 nmol, $n = 3$), determined 1 and 24 h post injection in SCID mice bearing subcutaneous LNCaP (PSMA-expressing human prostate carcinoma) xenografts.

for Cu(DOTPI(Chx)₄) at pH > 5 is no ultimate proof that such conjugates are indeed applicable for ^{64}Cu -PET imaging, because other mechanisms than proton-assisted dissociation may contribute to *in-vivo* loss of ^{64}Cu , even from highly stable and inert chelates (Bass et al., 2000; Zarschler et al., 2014). A final conclusion on this matter cannot be drawn without further evidence and an *in-vivo* proof of concept, which however is beyond the focus of this study.

CONCLUSION

A sufficiently low kinetic inertness of Cu^{II} complexes of amide-functionalized DOTPI derivatives at low pH warrants the practical applicability of the CuAAC/demetallation tandem protocol, which can be conveniently conducted as a one-pot reaction, for the synthesis of symmetrical tetrameric DOTPI conjugates. In view of the inherent limitations of

strain-promoted AAC, such as slower reaction kinetics and isomerism/lipophilicity of linkages, CuAAC appears to be the preferable method for this purpose. A pilot *in-vivo* study showed that the DOTPI-based PSMA-targeted radiotherapeutics combine high affinity with excellent clearance from non-target tissues, thus demonstrating the potential of DOTPI as a scaffold for the elaboration of therapeutic radiopharmaceuticals.

MATERIALS AND METHODS

Chemical Synthesis

General

The protected amino acid analogs were purchased from Bachem (Bubendorf, Switzerland) or Iris Biotech (Marktredwitz, Germany). All necessary solvents and other organic reagents were purchased from either, Alfa Aesar (Karlsruhe, Germany), Sigma-Aldrich (Munich, Germany), or VWR (Darmstadt, Germany). The DOTPI chelator (1,4,7,10-tetraazacyclododecane-1,4,7,10-tetrakis[methylene(2-carboxyethylphosphinic acid)]) (Šimeček et al., 2013) and its azide-functionalized derivative DOTPI(azide)₄ (Wurzer et al., 2018) were synthesized, as described previously. CheMatech (Dijon, France) delivered the NOTA chelator (1,4,7-triazacyclononane-1,4,7-triacetic acid). The PSMA-addressing binding motifs (DBCO-KuE and Trz-KuE) were prepared according to previously published procedures (Wurzer et al., 2018). Analytical and preparative HPLC were performed on Shimadzu gradient systems with a SPD-20A dual wavelength UV/Vis detector (220, 254 nm) with mobile phase gradients combined of purified water (component A; from Millipore system) and acetonitrile (component B; J.T.Baker® Ultra Gradient HPLC grade, supplemented with 5% H₂O), both containing 0.1% trifluoroacetic acid. A Nucleosil 100-5 C18 column (125 × 4.6 mm) was used for analytical measurements at a flow rate of 1 mL/min. Preparative HPLC purification was done using a Multospher 100 RP 18-5 μ column (250 × 10 mm) at a flow rate of 5 mL/min. Electrospray ionization (ESI) mass spectra were acquired on a Varian 500-MS Ion Trap spectrometer (Varian, by Agilent Technologies).

DOTPI(Chx)₄

DOTPI·2 H₂O (85.0 mg, 105 μmol, 1.0 eq) was dissolved in a mixture of anhydrous DMSO (420 μL) and DIPEA (320 μL, 1.89 mmol, 20 eq). Then cyclohexylamine (72.9 mg, 736 μmol, 7.0 eq) and HATU (439 mg, 1.16 mmol, 11 eq) were added in one portion with stirring. After 1 h at room temperature, the red reaction mixture was quenched with water (900 μL). The crude product was purified by size exclusion chromatography (Sephadex G-10 medium, column size: 40 × 3 cm, mobile phase: water, adjusted to pH 3 with HCl), yielding DOTPI(Chx)₄, as a yellow-green solid (57.7 mg, 53 μmol, 51%). MW (calcd. for C₄₈H₉₂N₈O₁₂P₄): 1097.20. HPLC (30–90% B in 15 min): t_R = 13.2 min. ¹H-NMR (300 MHz, D₂O, 300 K) δ = 1.13–1.36 (m, 20H), 1.57–1.60 (m, 4H), 1.69–1.74 (m, 8H, C(O)-CH₂), 1.78–1.87 (m, 16H), 2.37–2.45 (m, 8H, P-CH₂-C), 3.13–3.29 (m, 8H, P-CH₂-N), 3.42 (bs,

16H, ring-CH₂), 3.52–3.59 (m, 4H, C(O)-NH-CH) ppm. MS (ESI, positive): m/z = 1098.2 [M+H⁺], 1119.9 [M+Na⁺], 549.7 [M+2 H⁺].

DOTPI(DBCO-KuE)₄

DOTPI(azide)₄·TFA (2.00 mg, 1.65 μmol, 1.0 eq) and DBCO-KuE (7.13 mg, 9.90 μmol, 6.0 eq) were dissolved in a 1:1 mixture (v/v, 2.2 mL) of H₂O and *tert*-butanol and stirred for 12 h at room temperature. Subsequent purification by preparative HPLC yielded DOTPI(DBCO-KuE)₄·TFA as a colorless solid (6.02 mg, 1.47 μmol, 89%). MW (calcd. for C₁₈₄H₂₅₂N₄₀O₅₂P₄): 3980.10. HPLC (10–90% B in 15 min): t_R = 9.2 min. MS (ESI, positive): m/z = 1327.9 [M+3H⁺], 1335.6 [M+2H⁺+Na⁺], 1991.4 [M+2H⁺].

DOTPI(Trz-KuE)₄

DOTPI(azide)₄ (6.0 mg, 4.94 μmol, 1.0 eq), sodium ascorbate (97.9 mg, 494 μmol, 100 eq), and Trz-KuE (11.1 mg, 21.7 μmol, 4.4 eq) were dissolved in a 1:1 mixture (v/v, 2 mL) of H₂O and *tert*-butanol. After adding copper(II) acetate monohydrate (1.18 mg, 5.93 μmol, 1.2 eq) dissolved in H₂O (250 μL) a deep blue reaction mixture was formed, which was stirred for 1 h at room temperature. For demetallation, the mixture was diluted to 6 mL with H₂O, and NOTA (37.6 mg, 124 μmol, 25 eq) was added. After adjusting the pH to 2.2 by adding 1 M HCl, the solution was heated to 60°C for 2 h. Subsequent preparative HPLC-purification afforded DOTPI(Trz-KuE)₄·TFA as a colorless solid (1.6 mg, 0.49 μmol, 10%). MW (calcd. for C₁₂₈H₂₁₆N₃₆O₄₈P₄): 3151.24. HPLC (10–60% B in 15 min): t_R = 6.9 min. MS (ESI, positive): m/z = 1576.6 [M+2H⁺], 1051.2 [M+3H⁺], 788.7 [M+4H⁺].

Equilibrium Studies (Protonation and Stability Constants)

The chemicals used for the experiments were of the highest analytical grade. CaCl₂, ZnCl₂, and CuCl₂ solutions were prepared from solid MCl₂ (Aldrich; 99.9%). Concentration of CaCl₂, ZnCl₂, and CuCl₂ solutions were determined by complexometric titration with standardized Na₂H₂EDTA and xylenol orange (ZnCl₂), murexid (CuCl₂), and *Patton & Reeder* (Ca²⁺) as indicators. The concentration of the DOTPI(Chx)₄, DOTPI, and EDTA was determined by pH-potentiometric titration in the presence and absence of a large (40-fold) excess of CaCl₂. All the equilibrium measurements were made at constant ionic strength maintained by 0.15 M NaCl at 25°C.

For determining the protonation constants of DOTPI(Chx)₄ and DOTPI three parallel pH-potentiometric titration were made with 0.2 M NaOH in 0.002 M ligand solutions. The stability and protonation constants of the Ca^{II} and Zn^{II} complexes formed with DOTPI(Chx)₄ and DOTPI ligands have been determined by direct pH-potentiometric titration made at 1:1 and 2:1 metal to ligand concentration ratios. (the concentration of ligands was 0.002 M). For the calculation of the logK_{ML} and logK_{MLHi} values, the mL base–pH data used were obtained in the pH range 1.7–12.0.

Stability constant of Cu(DOTPI) complex was determined by spectrophotometry, studying the Cu^{II}-DOTPI systems at the

absorption band of Cu^{II}-complex at [H⁺] = 0.01–0.2 M over the wavelength range of 400–800 nm. Concentrations of Cu^{II} and DOTPI were 1 mM. The H⁺ concentration in the samples was adjusted by addition of calculated amounts of 2.0 M HCl, while ionic strength was not constant in these samples. Samples were kept at 25°C for a week. Absorbance values were determined at 9 wavelengths (550, 575, 600, 625, 650, 675, 700, 725, and 750 nm). For calculation of stability and protonation constants of Cu(DOTPI), molar absorptivities of CuCl₂, and Cu(H_xL) species (wherein x = 0, 1, 2 ... 5) were determined by recording the spectra of 1.0 × 10⁻³, 2.0 × 10⁻³ and 3.0 × 10⁻³ M solutions of CuCl₂ and Cu(DOTPI) in the pH range of 1.7–11.7. The protonation constants of the complexes Cu(DOTPI) and the stability and protonation constants of the dinuclear Cu₂(DOTPI) complexes were determined by pH-potentiometric titrations, made at 1:1 and 2:1 metal to ligand concentration ratios.

The stability constant of the Cu(DOTPI(Chx)₄) complex has been determined by spectrophotometry with the use of competition reactions between DOTPI(Chx)₄ and EDTA for the Cu²⁺ at pH = 5.0. The concentration of Cu(EDTA) was 0.2 mM, while that of the DOTPI(Chx)₄ was varied between 0.1 and 1.0 mM (5 samples). The samples were kept at 25°C for 2 weeks. The absorbance values and the molar absorptivities of CuCl₂, Cu(DOTPI(Chx)₄), and Cu(EDTA) have been determined at 11 wavelength (300, 304, 308, 312, 316, 320, 324, 328, 332, 336, and 340 nm) values between 300 and 340 nm. The molar absorptivities of CuCl₂, Cu(DOTPI(Chx)₄), and Cu(EDTA) were determined in 0.05, 0.1, 0.2, 0.3, and 0.4 mM solutions. The absorbance and pH values were determined in the samples after the equilibrium was reached (the time needed to reach the equilibria was determined by spectrophotometry). The spectrophotometric measurements were made with the use of 1.0 cm cells with a Cary 1E spectrophotometer at 25°C. The protonation constants of Cu(DOTPI(Chx)₄) complex were determined by pH-potentiometric titrations at 1:1 metal to ligand molar ratio.

For pH measurements and titrations, a *Metrohm 785 DMP Titrino* titration workstation and a *Metrohm-6.0233.100* combined electrode were used. Equilibrium measurements were carried out at a constant ionic strength (0.15 M NaCl) in 6 mL samples at 25°C. The solutions were stirred, and constantly purged with N₂. The titrations were performed in a pH range of 1.7–11.7. KH-phthalate (pH = 4.005) and borax (pH = 9.177) buffers were used to calibrate the pH meter. For calculation of [H⁺] from measured pH values, the method proposed by Irving et al. was used (Irving et al., 1967). A 0.01 M HCl solution was titrated with the standardized NaOH solution in the presence of 0.1 M NaCl. Differences between the measured (pH_{read}) and calculated pH (-log[H⁺]) values were used to obtain the equilibrium H⁺ concentration from the pH values, measured in the titration experiments. For the equilibrium calculations, the stoichiometric water ionic product (*pK_w*) is also needed to calculate [H⁺] values in basic conditions. The V_{NaOH} – pH_{read} data pairs of the HCl – NaOH titration obtained in the pH range 10.5–12 have been used to calculate the *pK_w* value (*pK_w* = 13.85). For the calculation of the equilibrium constants the program PSEQUAD (Zekany and Nagypal, 1985) was used.

Kinetic Studies

The rates of the ligand exchange reactions of Cu(DOTPI) and Cu(DOTPI(Chx)₄) with EDTA ligand were studied by following the dissociation of Cu(DOTPI) and Cu(DOTPI(Chx)₄) complexes with spectrophotometry at 340 nm, in the pH range 1.7–4.5, in the presence of the 20- and 40-fold excess of EDTA in order to maintain pseudo-first order kinetic conditions. Concentrations of Cu(DOTPI) and Cu(DOTPI(Chx)₄) were 0.1 mM. Kinetic studies were performed with *Cary 1E* and *Cary 100 Bio* spectrophotometers, using cell holders thermostated to 25°C. The pre-thermostated solutions were mixed in tandem cells (l = 0.874 cm). The ionic strength of the solutions was kept constant at 0.15 M with NaCl. In order to keep the pH values constant, dichloro-acetic acid (DCA) (pH range 1.5–2.5), chloro-acetic acid (MCA) (pH range 2.5–3.5) and 1,4-dimethylpiperazine (DMP) (pH = 3.1–4.5) buffers (0.01 M) were used. Pseudo-first-order rate constants (*k_d*) were calculated by fitting the absorbance values to the equation

$$A_t = (A_0 - A_e)e^{(-k_d t)} + A_e \quad (1)$$

wherein A₀, A_e, and A_t are the absorbance values at the start, at equilibrium and at the time t of the reaction, respectively. The calculation of the kinetic parameters were performed by the fitting of the absorbance-time data pairs with the *Micromath Scientist* computer program (version 2.0, Salt Lake City, UT, USA).

Radiochemistry

For ¹⁷⁷Lu-labeling, 10 μL aqueous NH₄OAc buffer (1 M, pH = 5.9) were added to 1.0 nmol of the labeling precursor (1 mM in DMSO), 10–40 MBq ¹⁷⁷LuCl₃ (Specific Activity > 3,000 GBq/mg, 740 MBq/mL, 0.04 M HCl, ITG, Garching, Germany) and finally filled up to 100 μL with H₂O. The reaction mixture was heated for 30 min at 95°C and the radiochemical purity was determined using radio-TLC (Silica gel 60, mobile phase: 1:1 mixture of 1 M aqueous ammonium acetate and DMF).

In Vitro and in Vivo Evaluation

Determination of PSMA Affinities

PSMA-expressing LNCaP (human prostate carcinoma) cells were grown in Dublecco modified Eagle medium/Nutrition Mixture F-12 with Glutamax-I (1:1) (Invitrogen), supplemented with 10% fetal calf serum and maintained at 37°C in a humidified 5% CO₂ atmosphere. For determination of the PSMA affinity (IC₅₀), cells were harvested 24 ± 2 h before the experiment and seeded in 24-well plates (1.5 × 10⁵ cells per 1 mL well). The competitive binding assay was carried out as described previously, using the radioiodinated PSMA ligand (¹²⁵I-BA)KuE (Weineisen et al., 2014).

Octanol-Water Distribution Coefficients

Approximately 1 MBq of the ¹⁷⁷Lu-labeled tracer was added to a mixture of 0.5 mL phosphate buffered saline (PBS, pH 7.4) and 0.5 mL n-octanol in an Eppendorf tube (n = 6). After vigorous mixing of the suspension for 3 min, the vial was centrifuged

at 11.500 g for 3 min for phase separation. 200 μ L aliquots of each phase were withdrawn and measured in a gamma counter.

Biodistribution

The experiments were carried out in accordance with the German Animal Welfare Act (Tierschutzgesetz), and were previously approved by the responsible authority (Regierung von Oberbayern). The animal model, male CB-17 SCID mice bearing subcutaneous LNCaP tumor xenografts, were generated as described before (Weineisen et al., 2014). Approximately 1–4 MBq (varying molar activities; absolute molar amounts of active compound ranging from 0.11 to 0.15 nmol) of the ^{177}Lu -labeled PSMA inhibitors were injected into the tail vein of the animals, which were sacrificed 1 and 24 h post injection ($n = 3$ per tracer per time point). Selected organs were removed, weighted and the activities contained were measured in a γ -counter.

AUTHOR CONTRIBUTIONS

AW: Performed chemical synthesis, radiochemistry, and *in-vivo* studies; AV and DH: Performed the equilibrium and kinetic

measurements; FF, FK, and H-JW: Performed interpretation of data and critically reviewed the manuscript; JN: Conceived the study, interpreted the data, and wrote the manuscript. All authors approved the final version of the manuscript.

ACKNOWLEDGMENTS

Support by the Deutsche Forschungsgemeinschaft (grant #NO822/4-1 and SFB 824, project A10), the EU and the European Regional Development Fund (projects GINOP-2.3.2-15-2016-00008 and GINOP-2.3.3-15-2016-00004), and a János Bolyai Research Scholarship of the Hungarian Academy of Science awarded to FK is gratefully acknowledged. We furthermore thank Prof. Imre Tóth and particularly Dr. Zsolt Baranyai (University of Debrecen & Bracco Imaging) for helpful discussions and proofreading.

SUPPLEMENTARY MATERIAL

The Supplementary Material for this article can be found online at: <https://www.frontiersin.org/articles/10.3389/fchem.2018.00107/full#supplementary-material>

REFERENCES

- Agard, N. J., Prescher, J. A., and Bertozzi, C. A. (2004). A strain-promoted [3 + 2] azide–alkyne cycloaddition for covalent modification of biomolecules in living systems. *J. Am. Chem. Soc.* 126, 15046–15047. doi: 10.1021/ja04996f
- Banerjee, S. R., Pullambhatla, M., Byun, Y., Nimmagadda, S., Green, G., Fox, J. J., et al. (2010). ^{68}Ga -labeled inhibitors of prostate-specific membrane antigen (PSMA) for Imaging prostate cancer. *J. Med. Chem.* 53, 5333–5341. doi: 10.1021/jm100623e
- Baranyai, Z., Bányai, I., Brücher, E., Király, R., and Terreno, E. (2007). Kinetics of the formation of $[\text{Ln}(\text{DOTAM})]^{3+}$ complexes. *Eur. J. Inorg. Chem.* 49, 3639–3645. doi: 10.1002/ejic.200700178
- Baranyai, Z., Palinkas, Z., Uggeri, F., and Brücher, E. (2010). Equilibrium studies on the Gd^{3+} , Cu^{2+} and Zn^{2+} complexes of BOPTA, DTPA and DTPA-BMA ligands: kinetics of metal-exchange reactions of $[\text{Gd}(\text{BOPTA})]^{2-}$. *Eur. J. Inorg. Chem.* 1948–1956. doi: 10.1002/ejic.200901261
- Baranyai, Z., Reich, D., Vágner, A., Weineisen, M., Tóth, I., Wester, H. J., et al. (2015). A shortcut to high-affinity Ga-68 and Cu-64 radiopharmaceuticals: one-pot click chemistry trimerisation on the TRAP platform. *Dalton Trans.* 44, 11137–11146. doi: 10.1039/C5DT00576K
- Bass, L. A., Wang, M., Welch, M. J., and Anderson, C. J. (2000). *In vivo* transchelation of copper-64 from TETA-octreotide to superoxide dismutase in rat liver. *Bioconjug. Chem.* 11, 527–532. doi: 10.1021/bc9901671
- Bazakas, K., and Lukeš, I. (1995). Synthesis and complexing properties of polyazamacrocycles with pendant N-methylenephosphinic acid. *J. Chem. Soc. Dalton Trans.* 1133–1137. doi: 10.1039/dt950001133
- Benešová, M., Bauder-Wüst, U., Schäfer, M., Klika, K. D., Mier, W., Haberkorn, U., et al. (2016). Linker modification strategies to control the prostate-specific membrane antigen (PSMA)-targeting and pharmacokinetic properties of DOTA-conjugated PSMA inhibitors. *J. Med. Chem.* 59, 1761–1775. doi: 10.1021/acs.jmedchem.5b01210
- Bianchi, A., Calabi, L., Giorgi, C., Losi, P., Mariani, P., Paoli, P., et al. (2000). Thermodynamic and structural properties of Gd^{3+} complexes with functionalized macrocyclic ligands based upon 1,4,7,10-tetraazacyclododecane. *J. Chem. Soc. Dalton Trans.* 697–705. doi: 10.1039/a909098c
- Bock, V. D., Speijer, D., Hiemstra, H., and van Maarseveen, J. H. (2007). 1,2,3-Triazoles as peptide bond isosteres: synthesis and biological evaluation of cyclotetrapeptide mimics. *Org. Biomol. Chem.* 5, 971–975. doi: 10.1039/b616751a
- Chaves, S., Delgado, R., and Da Silva, J. J. (1992). The stability of the metal complexes of cyclic tetra-aza tetra-acetic acids. *Talanta* 39, 249–254. doi: 10.1016/0039-9140(92)80028-C
- Davis, M. R., Singh, E. K., Wahyudi, H., Alexander, L. D., Kunicki, J. B., Nazarova, L. A., et al. (2012). Synthesis of sansalvamide A peptidomimetics: triazole, oxazole, thiazole, and pseudoproline containing compounds. *Tetrahedron* 68, 1029–1051. doi: 10.1016/j.tet.2011.11.089
- Desreux, J. F., Merciny, E., and Loncin, M. F. (1981). Nuclear magnetic resonance and potentiometric studies of the protonation scheme of two tetraaza tetraacetic macrocycles. *Inorg. Chem.* 20, 987–991. doi: 10.1021/ic50218a008
- Horne, S. W., Olsen, C. A., Beierle, J. M., Montero, A., and Ghadiri, R. M. (2009). Probing the bioactive conformation of an archetypal natural product HDAC inhibitor using conformationally homogeneous triazole-modified cyclic tetrapeptides. *Angew. Chem. Int. Ed. Engl.* 48, 4718–4724. doi: 10.1002/anie.200805900
- Horne, W. S., Yadav, M. K., Stout, C. D., and Ghadiri, M. R. (2004). Heterocyclic peptide backbone modifications in an alpha-helical coiled coil. *J. Am. Chem. Soc.* 126, 15366–15367. doi: 10.1021/ja0450408
- Irving, H. M., Miles, M. G., and Pettit, L. D. (1967). A study of some problems in determining the stoichiometric proton dissociation constants of complexes by potentiometric titrations using a glass electrode. *Anal. Chim. Acta* 38, 475–488. doi: 10.1016/S0003-2670(01)80616-4
- Šimeček, J., Hermann, P., Havlíčková, J., Herdtweck, E., Kapp, T. G., Engelbogen, N., et al. (2013). A cyclen-based tetraphosphinate chelator for preparation of radiolabeled tetrameric bioconjugates. *Chem. Eur. J.* 19, 7748–7757. doi: 10.1002/chem.201300338
- Kotková, Z., Pereira, G. A., Djanashvili, K., Kotek, J., Rudovsky, J., Hermann, P., et al. (2009). Lanthanide(III) complexes of phosphorus acid analogues of H4DOTA as model compounds for the evaluation of the second-sphere hydration. *Eur. J. Inorg. Chem.* 119–136. doi: 10.1002/ejic.200800859
- Kularatne, S. A., Zhou, Z., Yang, J., Post, C. B., and Low, P. S. (2009). Design, synthesis, and preclinical evaluation of prostate-specific membrane antigen targeted $^{99\text{m}}\text{Tc}$ -radioimaging agents. *Mol. Pharm.* 6, 790–800. doi: 10.1021/mp9000712
- Lázár, I., Sherry, A. D., Ramasamy, R., and Brücher, E. (1991). Synthesis and complexation properties of a new macrocyclic

- polyaza polyphosphinate ligand, DOTEP (1,4,7,10-tetraazacyclododecane-1,4,7,10-tetrakis(methyleneethylphosphinate)). *Inorg. Chem.* 30, 5016–5019. doi: 10.1021/ic00026a030
- Liu, Y. Q., Zhang, L. H., Wan, J. P., Li, Y. S., Xu, Y. H., and Pan, Y. J. (2008). Design and synthesis of cyclo-[Arg-Gly-Asp-Ψ(triazole)-Gly-Xaa] peptide analogues by click chemistry. *Tetrahedron* 64, 10728–10734. doi: 10.1016/j.tet.2008.08.090
- Maschauer, S., Einsiedel, J., Reich, D., Hübner, H., Gmeiner, P., Wester, H.-J., et al. (2017). Theranostic value of multimers: lessons learned from trimerization of neuropeptide receptor ligands and other targeting vectors. *Pharmaceuticals* 10:29. doi: 10.3390/ph10010029
- Meldal, M., and Tornøe, C. W. (2008). Cu-catalyzed azide–alkyne cycloaddition. *Chem. Rev.* 108, 2952–3015. doi: 10.1021/cr0783479
- Mesters, J. R., Barinka, C., Li, W., Tsukamoto, T., Majer, P., Slusher, B. S., et al. (2006). Structure of glutamate carboxypeptidase II, a drug target in neuronal damage and prostate cancer. *EMBO J.* 25, 1375–1384. doi: 10.1038/sj.emboj.7600969
- Notni, J., Šimeček, J., and Wester, H. J. (2014). Phosphinic acid functionalized polyazacycloalkane chelators for radiodiagnostics and radiotherapeutics: unique characteristics and applications. *Chem. Med. Chem.* 9, 1107–1115. doi: 10.1002/cmdc.201400055
- Notni, J., and Wester, H. J. (2016). A practical guide on the synthesis of metal chelates for molecular imaging and therapy by means of click chemistry. *Chem. Eur. J.* 22, 11500–11508. doi: 10.1002/chem.201600928
- Notni, J., and Wester, H. J. (2018). Re-thinking the role of radiometal isotopes: towards a future concept for theranostic radiopharmaceuticals. *J. Label. Compd. Radiopharm.* 61, 141–153. doi: 10.1002/jlcr.3582
- Oyen, W. J., Bodei, L., Giannarile, F., Maecke, H. R., Tennvall, J., Luster, M., et al. (2007). Targeted therapy in nuclear medicine—current status and future prospects. *Ann. Onc.* 18, 1782–1792. doi: 10.1093/annonc/mdm111
- Pasha, A., Tircsó, G., Benyó, E. T., Brücher, E., and Sherry, A. D. (2007). Synthesis and Characterization of DOTA-(amide)4 derivatives: equilibrium and kinetic behavior of their lanthanide(III) complexes. *Eur. J. Inorg. Chem.* 49, 4340–4349. doi: 10.1002/ejic.200700354
- Pedersen, D. S., and Abell, A. (2011). 1,2,3-Triazoles in peptidomimetic chemistry. *Eur. J. Org. Chem.* 2399–2411. doi: 10.1002/ejoc.201100157
- Riesen, A., Zehnder, M., and Kaden, T. A. (1986). Metal complexes of macrocyclic ligands. Part XXIII. Synthesis properties, and structures of mononuclear complexes with 12- and 14-membered tetraazamacrocycles-N,N',N'',N'''-tetraacetic Acids. *Helv. Chim. Acta* 69, 2067–2073. doi: 10.1002/hlca.19860690830
- Rohovec, J., Kyvala, M., Vojtíšek, P., Hermann, P., and Lukeš, I. (2000). Synthesis and coordination behavior of symmetrical tetraamine phosphinic acids. *Eur. J. Inorg. Chem.* 195–203. doi: 10.1002/(SICI)1099-0682(200001)2000:1<195::AID-EJIC195>;3.0.CO;2-6
- Stasiuk, G. J., and Long, N. J. (2013). The ubiquitous DOTA and its derivatives: the impact of 1,4,7,10-tetraazacyclododecane-1,4,7,10-tetraacetic acid on biomedical imaging. *Chem. Commun.* 49, 2732–2746. doi: 10.1039/c3cc38507h
- Takács, A., Napolitano, R., Purgel, M., Benyei, A. C., Zekany, L., Brücher, E., et al. (2014). Solution structures, stabilities, kinetics, and dynamics of DO3A and DO3A-sulphonamide complexes. *Inorg. Chem.* 53, 2858–2872. doi: 10.1021/ic4025958
- Tischler, M., Nasu, D., Empting, M., Schmelz, S., Heinz, D. W., Rottmann, P., et al. (2012). Braces for the peptide backbone: insights into structure-activity relationships of protease inhibitor mimics with locked amide conformations. *Angew. Chem. Int. Ed. Engl.* 51, 3708–3712. doi: 10.1002/anie.201108983
- Wadas, T. J., Wong, E. H., Weisman, G. R., and Anderson, C. J. (2010). Coordinating radiometals of copper, gallium, indium, yttrium, and zirconium for PET and SPECT imaging of disease. *Chem. Rev.* 110, 2858–2902. doi: 10.1021/cr900325h
- Weineisen, M., Šimeček, J., Schottelius, M., Schwaiger, M., and Wester, H. J. (2014). Synthesis and preclinical evaluation of DOTAGA-conjugated PSMA ligands for functional imaging and endoradiotherapy of prostate cancer. *EJNMMI Res.* 4:63. doi: 10.1186/s13550-014-0063-1
- Wurzer, A., Seidl, C., Morgenstern, A., Bruchertseifer, F., Schwaiger, M., Wester, H.-J., et al. (2018). Dual-nuclide radiopharmaceuticals for positron emission tomography based dosimetry in radiotherapy. *Chem. Eur. J.* 24, 547–550. doi: 10.1002/chem.201702335
- Zarschler, K., Kubeil, M., and Stephan, H. (2014). Establishment of two complementary *in vitro* assays for radiocopper complexes achieving reliable and comparable evaluation of *in vivo* stability. *RSC Adv.* 4, 10157–10164. doi: 10.1039/c3ra47302c
- Zekany, L., and Nagypál, I. (1985). “PSEQUAD,” in *Computational Methods for Determination of Formation Constants*, ed D. J. Leget (New York, NY: Plenum Press), 291–353.
- Zhang, A. X., Murelli, R. P., Barinka, C., Michel, J., Cocalcea, A., Jorgensen, W. L., et al. (2010). A remote arene-binding site on prostate specific membrane antigen revealed by antibody-recruiting small molecules. *J. Am. Chem. Soc.* 132, 12711–12716. doi: 10.1021/ja104591m

Conflict of Interest Statement: The handling editor declared a past co-authorship with several of the authors, AV, H-JW, JN.

The other authors declare that the research was conducted in the absence of any commercial or financial relationships that could be construed as a potential conflict of interest.

Copyright © 2018 Wurzer, Vágner, Horváth, Fellegi, Wester, Kálmán and Notni. This is an open-access article distributed under the terms of the Creative Commons Attribution License (CC BY). The use, distribution or reproduction in other forums is permitted, provided the original author(s) and the copyright owner are credited and that the original publication in this journal is cited, in accordance with accepted academic practice. No use, distribution or reproduction is permitted which does not comply with these terms.



Equilibrium Thermodynamics, Formation, and Dissociation Kinetics of Trivalent Iron and Gallium Complexes of Triazacyclononane-Triphosphinate (TRAP) Chelators: Unraveling the Foundations of Highly Selective Ga-68 Labeling

OPEN ACCESS

Edited by:

Federico Cesano,
Università degli Studi di Torino, Italy

Reviewed by:

Francesca Garello,
Università degli Studi di Torino, Italy

Jan Kotek,

Charles University, Czechia

Janet R. Morrow,

University at Buffalo, United States

***Correspondence:**

Zsolt Baranyai
zsolt.baranyai@bracco.com

[†]These authors have contributed equally to this work.

Specialty section:

This article was submitted to
Inorganic Chemistry,
a section of the journal
Frontiers in Chemistry

Received: 09 February 2018

Accepted: 27 April 2018

Published: 23 May 2018

Citation:

Vágner A, Forgács A, Brücher E, Tóth I, Maiocchi A, Wurzer A, Wester H-J, Notni J and Baranyai Z (2018) Equilibrium Thermodynamics, Formation, and Dissociation Kinetics of Trivalent Iron and Gallium Complexes of Triazacyclononane-Triphosphinate (TRAP) Chelators: Unraveling the Foundations of Highly Selective Ga-68 Labeling. *Front. Chem.* 6:170. doi: 10.3389/fchem.2018.00170

Adrienn Vágner^{1†}, Attila Forgács^{1†}, Ernő Brücher¹, Imre Tóth¹, Alessandro Maiocchi², Alexander Wurzer³, Hans-Jürgen Wester³, Johannes Notni³ and Zsolt Baranyai^{1,2*}

¹ Department of Inorganic and Analytical Chemistry, University of Debrecen, Debrecen, Hungary, ² Bracco Imaging S.p.a., Bracco Research Centre, Colleretto Giacosa, Italy, ³ Radiopharmaceutical Chemistry, Technische Universität München, Garching bei München, Germany

In order to rationalize the influence of Fe^{III} contamination on labeling with the ⁶⁸Ga eluted from ⁶⁸Ge/⁶⁸Ga-generator, a detailed investigation was carried out on the equilibrium properties, formation and dissociation kinetics of Ga^{III}- and Fe^{III}-complexes of 1,4,7-triazacyclononane-1,4,7-tris(methylene[2-carboxyethyl]phosphinic acid]) (H₆TRAP). The stability and protonation constants of the [Fe(TRAP)]³⁻ complex were determined by pH-potentiometry and spectrophotometry by following the competition reaction between the TRAP ligand and benzhydroxamic acid (0.15 M NaNO₃, 25°C). The formation rates of [Fe(TRAP)] and [Ga(TRAP)] complexes were determined by spectrophotometry and ³¹P-NMR spectroscopy in the pH range 4.5–6.5 in the presence of 5–40 fold H_xTRAP^(x-6) excess (x = 1 and 2, 0.15 M NaNO₃, 25°C). The kinetic inertness of [Fe(TRAP)]³⁻ and [Ga(TRAP)]³⁻ was examined by the trans-chelation reactions with 10 to 20-fold excess of H_xHBED^(x-4) ligand by spectrophotometry at 25°C in 0.15 M NaCl (x = 0, 1 and 2). The stability constant of [Fe(TRAP)]³⁻ ($\log K_{\text{FeL}} = 26.7$) is very similar to that of [Ga(TRAP)]³⁻ ($\log K_{\text{GaL}} = 26.2$). The rates of ligand exchange reaction of [Fe(TRAP)]³⁻ and [Ga(TRAP)]³⁻ with H_xHBED^(x-4) are similar. The reactions take place quite slowly via spontaneous dissociation of [M(TRAP)]³⁻, [M(TRAP)OH]⁴⁻ and [M(TRAP)(OH)₂]⁵⁻ species. Dissociation half-lives ($t_{1/2}$) of [Fe(TRAP)]³⁻ and [Ga(TRAP)]³⁻ complexes are 1.1×10^5 and 1.4×10^5 h at pH = 7.4 and 25°C. The formation reactions of [Fe(TRAP)]³⁻ and [Ga(TRAP)]³⁻ are also slow due to the formation of the unusually stable monoprotonated [^{*}M(HTRAP)]²⁻ intermediates [^{*}log $K_{\text{Ga(HL)}} = 10.4$ and ^{*}log $K_{\text{Fe(HL)}} = 9.9$], which are much more stable than the [^{*}Ga(HNOTA)]⁺ intermediate [^{*}log $K_{\text{Ga(HL)}} = 4.2$]. Deprotonation

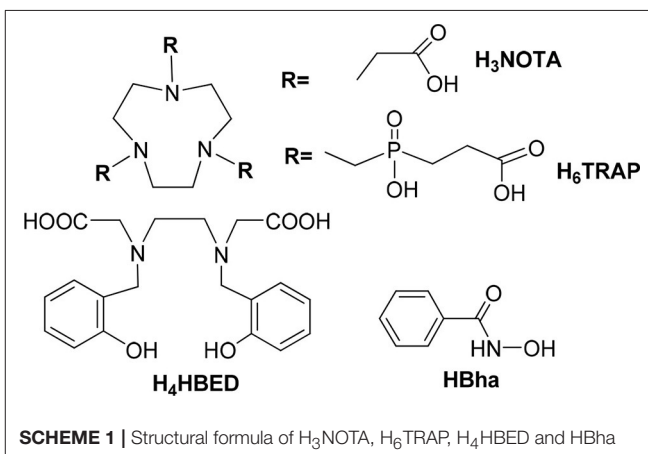
and transformation of the monoprotonated $[{}^*\text{M}(\text{HTRAP})]^{2-}$ intermediates into the final complex occur via OH^- -assisted reactions. Rate constants (k_{OH}) characterizing the OH^- -driven deprotonation and transformation of $[{}^*\text{Ga}(\text{HTRAP})]^{2-}$ and $[{}^*\text{Fe}(\text{HTRAP})]^{2-}$ intermediates are $1.4 \times 10^5 \text{ M}^{-1}\text{s}^{-1}$ and $3.4 \times 10^4 \text{ M}^{-1}\text{s}^{-1}$, respectively. In conclusion, the equilibrium and kinetic properties of $[\text{Fe}(\text{TRAP})]$ and $[\text{Ga}(\text{TRAP})]$ complexes are remarkably similar due to the close physico-chemical properties of Fe^{III} and Ga^{III} -ions. However, a slightly faster formation of $[\text{Ga}(\text{TRAP})]$ over $[\text{Fe}(\text{TRAP})]$ provides a rationale for a previously observed, selective complexation of ${}^{68}\text{Ga}^{\text{III}}$ in presence of excess Fe^{III} .

Keywords: chelates, gallium, iron, thermodynamics, kinetics, reaction mechanism, positron emission tomography

INTRODUCTION

Due to the wealth of obtainable information resulting in a high diagnostic value, medical imaging plays an ever-increasing role in modern personalized healthcare. In this context, radionuclide based imaging modalities which exploit George Hevesy's tracer principle (Levi, 1976) allow for unique functional diagnostics, because they enable monitoring of biological processes without significant interference with the investigated subject owing to minuscule amounts of administered active compound. Although the majority of nuclear imaging procedures (estimated >85%) still are scintigraphic or single photon emission computed tomography (SPECT) scans relying on the gamma-emitter ${}^{99\text{m}}\text{Tc}$, recent times have seen a strong surge in positron emission tomography (PET), following introduction of scanners capable of simultaneous functional and morphological imaging utilizing PET and computed tomography (CT) in 2001 (Beyer et al., 2000). While most PET investigations rely on the positron emitter ${}^{18}\text{F}$ (more precisely, on the radiofluorinated glucose derivative $[{}^{18}\text{F}]2\text{-fluoro-2-deoxy-D-glucose}$), some positron-emitting metal ion radionuclides have also received considerable attention in recent times (Wadas et al., 2010). Among these, ${}^{68}\text{Ga}$ has arguably the highest value for preclinical and translational studies (Notni and Wester, 2018), mainly because it is obtained for a low price per dose from radionuclide generators. These small benchtop devices, which act as cyclotron-independent continuous on-site nuclide sources, contain ${}^{68}\text{Ge}$ adsorbed on an inorganic matrix, such as SnO_2 or TiO_2 , while decay of ${}^{68}\text{Ge}$ produces ${}^{68}\text{Ga}^{\text{III}}$ which can be eluted with dilute HCl (Notni, 2012; Rösch, 2013). Notably, such eluate frequently contains small amounts of impurities originating from the sorbent (Simecek et al., 2013), such as Ti^{IV} but also Fe^{III} , Cu^{II} , Zn^{II} , or Al^{III} in form of their aqua or chlorido complexes.

${}^{68}\text{Ga}$ -labeling of biomolecules usually requires prior decoration with a suitable multidentate ligand capable of binding the ${}^{68}\text{Ga}^{\text{III}}$ ion into a kinetically inert complex (Wadas et al., 2010) and a plethora of ligands have been proposed for this purpose (Frank and Patrick, 2010; Velikyan, 2011). Against the background of aforementioned metal ion impurities in the generator eluate, an investigation of the radionuclide complexation efficiency of certain macrocycle-based chelators, among them TRAP (Notni et al., 2014) and NOTA (Mariko and Susumu, 1977; **Scheme 1**) pointed at a markedly different



SCHEME 1 | Structural formula of H_3NOTA , H_6TRAP , H_4HBED and HBha chelates (H_3NOTA : 1,4,7-triazacyclononane-1,4,7-triacetic acid; H_6TRAP : 1,4,7-triazacyclononane-1,4,7-tris(methylene)[2-carboxyethylphosphinic acid]); H_4HBED : N, N' -Bis(2-hydroxybenzyl)ethylenediamine- N, N' -diacetic acid; HBha : benzhydroxamic acid).

influence of non- Ga^{III} metal ions present in the ${}^{68}\text{Ga}^{\text{III}}$ solutions used for radiolabeling (Simecek et al., 2013). In particular, TRAP was shown to tolerate much higher concentrations of Zn^{II} , Cu^{II} , and Fe^{III} . Although highly similar structural features of $[\text{Fe}(\text{H}_3\text{TRAP})]$ and $[\text{Ga}(\text{H}_3\text{TRAP})]$ point at a close relation of both systems (Notni et al., 2010), it was found that even a threefold stoichiometric excess of Fe^{III} over TRAP or its mono-conjugable congener NOPO (Simecek et al., 2014) did not result in a significant decrease of ${}^{68}\text{Ga}$ incorporation, whereas labeling of NOTA was almost completely inhibited. Particularly in view of the known similarity of Fe^{III} and Ga^{III} , this discrepancy sheds a light on the mechanisms governing the superior ${}^{68}\text{Ga}$ labeling properties of 1,4,7-triazacyclononanes bearing (methylene)phosphinic acid N -substituents (Notni et al., 2011). In order to gain a more detailed understanding, thermodynamics as well as formation and dissociation kinetic studies were performed for Ga^{III} - and Fe^{III} -complexes formed with TRAP and NOTA.

MATERIALS AND METHODS

Materials

The chemicals used for the experiments were of the highest analytical grade. $\text{Ga}(\text{NO}_3)_3$ and $\text{Fe}(\text{NO}_3)_3$ were prepared by

dissolving Ga_2O_3 (99.9%, Fluka) and Fe_2O_3 (99.9% Fluka) in 6M HNO_3 and evaporating of the excess acid. The solid $\text{Ga}(\text{NO}_3)_3$ and $\text{Fe}(\text{NO}_3)_3$ were dissolved in 0.1 M HNO_3 solution. The concentration of the $\text{Ga}(\text{NO}_3)_3$ and $\text{Fe}(\text{NO}_3)_3$ solutions were determined by complexometry with the use of standardized $\text{Na}_2\text{H}_2\text{EDTA}$ in excess. The excess of the $\text{Na}_2\text{H}_2\text{EDTA}$ was measured with standardized ZnCl_2 solution and xylenol orange as indicator. The H^+ concentration of the $\text{Ga}(\text{NO}_3)_3$ and $\text{Fe}(\text{NO}_3)_3$ solutions was determined by pH potentiometric titration in the presence of $\text{Na}_2\text{H}_2\text{EDTA}$ excess. The concentration of the H_6TRAP , H_4HBED , benzohydroxamic acid (HBha) and H_3NOTA (provided by Prof. Petr Hermann, Department of Inorganic Chemistry, Faculty of Science, Charles University, Prague, Czech Republic) was determined by pH-potentiometric titration in the presence and absence of a large (40-fold) excess of CaCl_2 . All the measurements were made at constant ionic strength maintained by 0.15 M NaNO_3 or NaCl at 25°C.

Equilibrium Studies

For determining the protonation constants of H_6TRAP and H_3NOTA ligands three parallel pH-potentiometric titration were made with 0.2 M NaOH in 0.002 M ligand solutions.

Stability constant of $[\text{Fe}(\text{Bha})]^{2+}$ complex was determined by spectrophotometry, studying the $\text{Fe}^{\text{III}}\text{-HBha}$ systems at the absorption band of Fe^{III} -complex over the wavelength range of 400–800 nm in two sets of experiments. Individual samples were prepared in the first series in which the concentrations of Fe^{III} and HBha was constant 0.2 and 2.0 mM, while that of the H^+ was varied between 0.04 and 1.0 mM (eight samples, Figure S1). The H^+ concentration in the samples was adjusted by addition of calculated amounts of 2.0 M HNO_3 . The ionic strength was constant in the samples with $[\text{H}^+] < 0.15 \text{ M}$ ($[\text{H}^+] + [\text{Na}^+] = 0.15 \text{ M}$). Samples were kept at 25°C for a week. Absorbance values were determined at 11 wavelengths (400, 415, 430, 445, 460, 475, 490, 505, 520, 535, and 550 nm). In the second set, spectrophotometric titrations were done with samples containing HBha ligand in 2.0 mM concentration, whereas the concentration of Fe^{III} was varied between 0.1–0.3 mM (Figures S2–S4). The pH of the samples was adjusted using concentrated NaOH and HNO_3 solutions in the pH range 1.7–11.0 (0.15 M NaNO_3 and 25°C). For calculation of the equilibrium constants, the best fit of the absorbance–pH data was obtained by assuming formation of $[\text{Fe}(\text{Bha})]^{2+}$, $[\text{Fe}(\text{Bha})]^{+}$, $[\text{Fe}(\text{Bha})]_3$, and $[\text{Fe}(\text{Bha})_2(\text{OH})_2]^-$ species (Figure S5). The molar absorptivity of $[\text{Fe}(\text{Bha})]^{2+}$, $[\text{Fe}(\text{Bha})]^{+}$, $[\text{Fe}(\text{Bha})]_3$ and $[\text{Fe}(\text{Bha})_2(\text{OH})_2]^-$ species were also determined at the same 11 wavelengths in these experiments (Figure S6).

The stability constant of the $[\text{Fe}(\text{TRAP})]^{3-}$ complex has been determined by spectrophotometry, using competition reactions between HTRAP⁵⁻ and Bha⁻ for Fe^{III} at pH = 10.0. Concentration of $[\text{Fe}(\text{TRAP})]^{3-}$ was 0.2 mM, while that of HBha was varied between 0.0 and 1.5 mM (6 samples). The samples were kept at 25°C for 2 weeks. Absorbance values of the $\text{Fe}^{\text{III}}\text{-HTRAP}^{5-}\text{-Bha}^-$ systems were determined at 11 wavelengths (400, 415, 430, 445, 460, 475, 490, 505, 520, 535, and 550 nm). The molar absorptivities of $[\text{Fe}(\text{TRAP})]^{3-}$ and

$[\text{Fe}(\text{TRAP})\text{OH}]^{4-}$ in equilibrium solutions were determined by recording the absorption spectra of 0.1, 0.2, and 0.3 mM solution of $[\text{Fe}(\text{TRAP})]^{3-}$ in the pH range 6.0–12.0. The molar absorptivity of $[\text{Fe}(\text{Bha})_2(\text{OH})_2]^-$ species was determined in the separate experiments. Absorbance and pH values were determined in the samples after equilibration (the time needed to reach the equilibria was determined by spectrophotometry). Spectrophotometric measurements were done using 1.0 cm cells with a Cary 1E spectrophotometer at 25°C. Protonation constants of the Fe^{III} complex formed with TRAP⁶⁻ were determined by direct pH-potentiometric titration at 1:1 metal to ligand ratios (both concentrations were 0.002 M). For calculation of the $\log K_{\text{MHIL}}$ values, the mL base–pH data used were measured in the pH range 1.7–12.0.

For pH measurements and titrations, a *Metrohm 785 DMP Titrino* titration workstation and a *Metrohm-6.0233.100* combined electrode were used. Equilibrium measurements were carried out at a constant ionic strength (0.15 M NaNO_3 or NaCl) in 6 mL samples at 25°C. Solutions were stirred and continuously purged with N_2 . Titrations were performed in a pH range of 1.7–12.0. KH-phthalate (pH = 4.005) and borax (pH = 9.177) buffers were used to calibrate the pH meter. For calculation of $[\text{H}^+]$ from measured pH values, the method proposed by Irving et al. was used (Irving et al., 1967). A 0.01 M HNO_3 or HCl solution was titrated with the standardized NaOH solution in the presence of 0.15 M NaNO_3 or NaCl . Differences between the measured (pH_{read}) and calculated pH ($-\log[\text{H}^+]$) values were used to obtain the equilibrium H^+ concentration from the pH values, measured in the titration experiments. For equilibrium calculations, the stoichiometric water ionic product (pK_w) is also needed to calculate $[\text{H}^+]$ values in basic conditions. The $\text{V}_{\text{NaOH}}\text{-pH}_{\text{read}}$ data pairs of the $\text{HNO}_3\text{-NaOH}$ or $\text{HCl}\text{-NaOH}$ titration obtained in the pH range 10.5–12.0 have been used to calculate the pK_w value ($\text{pK}_w = 13.84$). For calculation of the equilibrium constants, the program PSEQUAD (Zekany and Nagypal, 1985) was used. The standard deviation (SD) of the equilibrium parameters calculated by the program PSEQUAD is defined by Equation (1)

$$\text{SD} = \sqrt{\frac{\sum_{j=1}^{j=N} \text{res}_j^2}{N - m}} \times \sqrt{[(J^T \cdot J)^{-1}]_{ii}} \quad (1)$$

where res , N , m , J and J^T are the residual, number of fitted data, number of refined parameters, Jacobian matrix and the transpose of Jacobian matrix, respectively.

Kinetic Studies

Formation Kinetics of $[\text{Fe}(\text{TRAP})]$ and $[\text{Ga}(\text{TRAP})]$

Formation rates of $[\text{Fe}(\text{TRAP})]$ were studied by spectrophotometry at 260 nm in the pH range of about 4.5–6.5. Kinetic studies were carried out with *Cary 1E* and *Cary 100 Bio* spectrophotometers, using cell holders thermostated to 25°C. The pre-thermostated solutions were mixed in tandem cells ($l = 0.874 \text{ cm}$). Formation of Fe^{III} complexes were studied in the presence of a 5- to 40-fold ligand excess in order to maintain pseudo-first-order conditions ($[\text{Fe}^{\text{III}}] = 0.1 \text{ mM}$).

Pseudo-first-order rate constants ($k = k_{\text{obs}}$) were calculated by fitting the absorbance values to the equation:

$$A_t = (A_0 - A_e)e^{(-kt)} + A_e \quad (2)$$

wherein A_0 , A_e , and A_t are the absorbance values at the start ($t = 0$ s), at equilibrium and at the time t of the reaction, respectively. Formation of $[\text{Ga}(\text{TRAP})]^{3-}$ was monitored by ^{31}P -NMR spectroscopy on the signal of the forming $\text{Ga}(\text{TRAP})$ complex. ^{31}P -NMR spectra were recorded by a Bruker DRX 400 spectrometer (^{31}P , 161.97 MHz, 9.4 T) equipped with Bruker VT-1000 thermocontroller, using a 5 mm broad band probe. Kinetic experiments were performed at a constant temperature of 25.0°C. The formation rates were studied in the pH range of about 4.5–6.3. For these experiments, $\text{Ga}(\text{NO}_3)_3$ and H_6TRAP solutions were prepared in H_2O (a capillary with D_2O was used for lock). In all experiments, the concentration of Ga^{III} was 1 mM, while that of the H_6TRAP was varied between 5 and 30 fold excess in order to maintain pseudo-first-order conditions. Pseudo-first-order rate constants ($k = k_{\text{obs}}$) were calculated by fitting the integral signal values to the Equation (2). The ionic strength of the solutions was kept constant at 0.15 M with NaNO_3 . To keep the pH values constant, N -methylpiperazine (pH range of 4.1–5.2) and piperazine (pH range of 4.7–6.6) buffers (0.01 M) were used.

Dissociation Kinetics of Fe(TRAP) and Ga(TRAP)

The rates of the ligand exchange reactions of Fe(TRAP) and Ga(TRAP) with $\text{H}_x\text{HBED}^{x-4}$ ($x = 0, 1$ and 2) ligand were studied by following the formation of $[\text{Fe}(\text{HBED})]^-$ and $[\text{Ga}(\text{HBED})]^-$ complexes by spectrophotometry at 470 nm and 290 nm, respectively. All experiments were performed in the presence of 10- and 20-fold excess of $\text{H}_x\text{HBED}^{x-4}$ ($x = 1$ and 2) in order to maintain pseudo-first order kinetic conditions ($[\text{Fe}(\text{TRAP})] = [\text{Ga}(\text{TRAP})] = 0.2$ mM). The pseudo-first-order rate constants ($k = k_d$) were calculated by fitting the absorbance values to the Equation (2). Kinetic studies were performed with Cary 1E and Cary 100 Bio spectrophotometers, using cell holders thermostated to 25°C. The pre-thermostated solutions were mixed in tandem cells ($l = 0.874$ cm). The ionic strength of the solutions was kept constant at 0.15 M with NaCl. The ligand exchange reactions were followed at 25°C in the pH range 9.0–14.0. The OH^- concentration at pH > 12 was adjusted by addition of calculated amounts of 4.0 M NaOH solution. Buffers were not used to keep the pH constant due to the high buffer capacity of the $\text{H}_x\text{HBED}^{x-4}$ ($x = 1$ and 2) excess at pH < 12. Calculation of the kinetic parameters was performed with the Micromath Scientist computer program (version 2.0, Salt Lake City, UT, USA).

RESULTS AND DISCUSSION

Solution Thermodynamics

Protonation equilibria of the TRAP⁶⁻, NOTA³⁻ and Bha⁻ ligands were studied by pH-potentiometry. The protonation constants ($\log K_i^H$) of ligands defined by Equation (3) are listed in Table 1 (standard deviations are shown in parentheses). The

charges of ligands and complexes will be indicated when it is necessary.

$$K_i^H = \frac{[\text{H}_i\text{L}]}{[\text{H}_{i-1}\text{L}][\text{H}^+]} \quad i = 0, 1, 2 \dots 6 \quad (3)$$

The protonation schemes of TRAP⁶⁻ and NOTA³⁻ ligands were well characterized by both spectroscopic and potentiometric methods (Bevilacqua et al., 1987; Geraldes et al., 1991; Notni et al., 2010). These studies reveal that the first and second protonations occur at two ring nitrogen atoms, whereas the third, fourth and fifth protonations occur at the carboxylate groups of NOTA³⁻ and TRAP⁶⁻. The sixth proton of the TRAP⁶⁻ ligand binds on the phosphinate oxygen atom. Interestingly, not all phosphinate groups are protonated, even under very acidic conditions (pH < 1), which is why they are still able to coordinate to metal ions. A comparison of protonation constants of TRAP⁶⁻ and NOTA³⁻ indicates that $\log K_i^H$ value of TRAP⁶⁻ is significantly lower than that of NOTA³⁻ (Table 1). The lower first protonation constant of TRAP⁶⁻ can be attributed to formation of a weaker H-bond between the protonated ring nitrogen and the phosphinate oxygens than that formed between the protonated ring nitrogen and the carboxylate oxygens in HNOTA²⁻. Comparison of the protonation constants obtained in 0.15 M NaNO_3 or NaCl, 0.1 M KCl and 0.1 M Me_4NCl solutions indicates that the $\log K_i^H$ values of TRAP⁶⁻ are independent of the ionic strength, whereas the $\log K_i^H$ value of NOTA³⁻ is significantly lower in the presence of K^+ and Na^+ ions, which can be attributed to formation of $[\text{K}(\text{NOTA})]^{2-}$ and $[\text{Na}(\text{NOTA})]^{2-}$ complexes. Total basicity of ligands ($\Sigma \log K_i^H$, Table 1) generally correlates with the stability constants (K_{ML}) of their metal complexes. (For the calculation of $\Sigma \log K_i^H$ value of TRAP⁶⁻, the $\log K_i^H$ values of the carboxylate groups were not considered because they do not participate in the coordination of metal ions). The $\Sigma \log K_i^H$ values (Table 1) show that the total basicity of TRAP⁶⁻ is significantly lower than that of NOTA³⁻ because of the lower protonation constant of the ring nitrogen ($\log K_1^H$) and phosphinate oxygen atoms of the TRAP⁶⁻ ligand. Therefore, lower stability constants should be expected for the TRAP⁶⁻ complexes than those of NOTA³⁻ complexes.

Stability and protonation constants of TRAP⁶⁻ and NOTA³⁻ complexes formed with Fe^{III} were determined by pH-potentiometry and UV/Vis spectrophotometry. The stability and protonation constants of the metal complexes formed with the TRAP⁶⁻ and NOTA³⁻ ligands listed in Table 2 are defined by Equations (4–6):



$$K_{\text{ML}} = \frac{[\text{ML}]}{[\text{M}][\text{L}]} \quad (5)$$



$$K_{\text{MH}_i\text{L}} = \frac{[\text{MH}_i\text{L}]}{[\text{MH}_{i-1}\text{L}][\text{H}^+]} \quad (5)$$



$$K_{\text{M(L)OH}} = \frac{[\text{ML}]}{[\text{M(L)OH}][\text{H}^+]} \quad (6)$$

TABLE 1 | Protonation constants of TRAP⁶⁻, NOTA³⁻, and Bha⁻ ligands (25°C).

	I	$\log K_1^H$	$\log K_2^H$	$\log K_3^H$	$\log K_4^H$	$\log K_5^H$	$\log K_6^H$	$\Sigma \log K_i^H$
TRAP ⁶⁻	0.15 M NaNO ₃	11.60(2)	5.39(2)	4.42(2)	4.19(3)	3.46(3)	1.60(2)	18.59 9
	0.15 M NaCl ^a	11.74	5.46	4.80	4.16	3.49	1.50	18.70 9
	0.1 M Me ₄ NCl ^b	11.48	5.44	4.84	4.23	3.45	1.66	18.58 9
NOTA ³⁻	0.15 M NaNO ₃	11.94(2)	5.71(3)	3.14(3)	1.60(2)	—	—	22.39
	0.15 M NaCl ^a	12.16	5.75	3.18	1.90	—	—	22.99
	0.1 M KCl ^c	11.98	5.65	3.18	—	—	—	—
Bha ⁻	0.15 M NaNO ₃	13.17	5.74	3.22	1.96	—	—	24.09
	0.2 M KCl ^e	8.53(3)	—	—	—	—	—	—
	0.2 M NaNO ₃	8.69	—	—	—	—	—	—

^aRef. (Baranyai et al., 2015); ^bRef. (Notni et al., 2010); ^cRef. (Clarke and Martell, 1991); ^dRef. (Drahos et al., 2011); ^eRef. (Farkas et al., 1998); ^fTotal ligand basicity ($\Sigma \log K_i^H$) characterizes the sum of basicity of donor atoms; ^gThe protonation constants of the acetate pendants ($\log K_3^H$, $\log K_4^H$ and $\log K_5^H$) of TRAP⁶⁻ were not considered in the calculation of $\Sigma \log K_i^H$ values.

TABLE 2 | Stability and protonation constants ($\log K$) of Fe^{III} and Ga^{III}-complexes formed with TRAP⁶⁻, NOTA³⁻, and Bha⁻ ligand (25°C).

	TRAP ⁶⁻		NOTA ³⁻		Bha ⁻	
	Fe ^{III}	Ga ^{III}	Fe ^{III}	Ga ^{III}	Fe ^{III}	
I	0.15 M NaNO ₃	0.1 M Me ₄ NCl ^a	0.1 M KCl ^b	0.1 M Me ₄ NCl ^c	0.15 M NaNO ₃	0.2 M KCl ^d
ML	26.73(8)	26.24	28.3	29.60	10.80(2)	11.08
MHL	5.07(2)	5.18	—	0.9	—	—
MH ₂ L	4.34(2)	4.55	—	—	—	—
MH ₃ L	3.20(2)	3.77	—	—	—	—
MH ₄ L	—	0.7	—	—	—	—
M(L)OH	9.76(2)	9.84	9.12(4) ^e	9.83	—	—
ML ₂	—	—	—	—	9.03(2)	10.12
ML ₃	—	—	—	—	7.41(3)	7.60
log $\beta_{\text{FeL}2(\text{OH})2}$	—	—	—	—	6.68(5)	—

^aRef. (Notni et al., 2010); ^bRef. (Clarke and Martell, 1991); ^cRef. (Simecek et al., 2012); ^dRef. (Farkas et al., 1998); ^eIn this work (0.15 M NaNO₃, 25°C).

wherein $i = 1, 2$, or 3 . Since the $[\text{Fe}(\text{TRAP})]^{3-}$ and $[\text{Fe}(\text{NOTA})]$ complexes are highly stable, formation of Fe^{III} complexes was practically completed at about pH < 2.0. Therefore, from the data obtained by pH-potentiometric titrations performed at 1:1 metal to ligand concentration ratio, only the protonation constants of the $[\text{Fe}(\text{TRAP})]^{3-}$ and $[\text{Fe}(\text{NOTA})]$ complexes could be calculated. In order to determine the $\log K_{\text{FeL}}$ value, we studied the competition reactions between HTRAP⁵⁻ and Bha⁻ for Fe^{III} [Equation (7)] by spectrophotometry in the wavelength range 400–800 nm. To calculate the stability constant of $[\text{Fe}(\text{TRAP})]^{3-}$, the equilibrium constants characterizing the species formed in the Fe^{III}-HBha system have been determined from the data obtained by pH-potentiometric and spectrophotometric measurements (experimental detail and calculation procedures used for the characterization of Fe^{III}-HBha system are summarized in the Supplementary information).

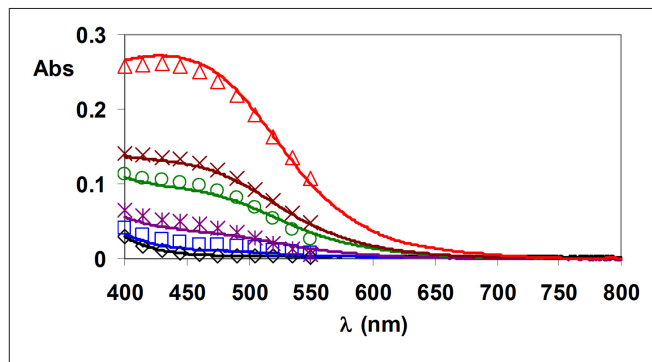
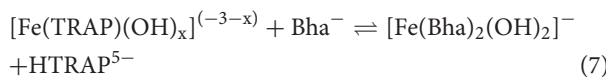
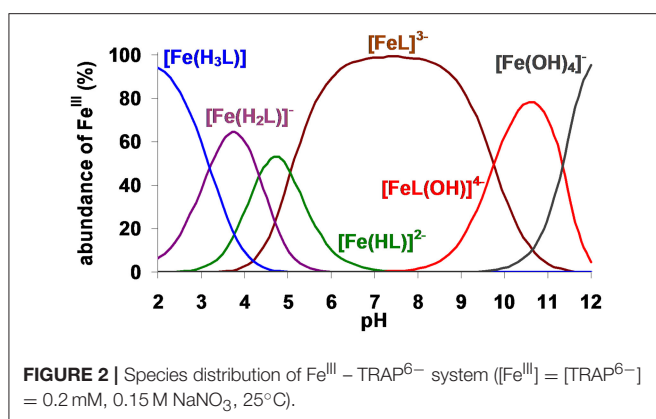


FIGURE 1 | Absorption spectra of Fe^{III}-HTRAP⁵⁻-Bha⁻ equilibrium systems. Open symbols and solid lines represent experimental and calculated absorbance values, respectively. $([\text{Fe}(\text{TRAP})(\text{OH})_x]^{(-3-x)}) = 0.2 \text{ mM}$, $[\text{HBha}] = 0.0 \text{ mM}$ (black), 0.25 mM (blue), 0.5 mM (purple), 0.75 mM (green), 1.0 mM (brown), and 1.5 mM (red), $x = 0$ and 1 , pH = 10.0, 0.15 M NaNO₃, 25°C.



wherein $x = 0$ and 1 . The pH of the samples was 10.0, when $[\text{Fe}(\text{TRAP})]^{3-}$, $[\text{Fe}(\text{TRAP})\text{OH}]^{4-}$ and $[\text{Fe}(\text{Bha})_2(\text{OH})_2]^-$ were formed. Some characteristic absorption spectra of Fe^{III}-HTRAP⁵⁻-Bha⁻ systems are shown in Figure 1.

The stability and protonation constants of $[\text{Fe}(\text{TRAP})]^{3-}$ complex have been calculated by the combination of the pH-potentiometric data obtained by the titration of $[\text{Fe}(\text{TRAP})]^{3-}$ complex with NaOH solution in the pH range 1.7–12.0 (Figure S7) with the spectrophotometric data acquired at pH = 10.0 in Fe^{III}-HTRAP⁵⁻-Bha⁻ system (Figure 1). For calculation of the $\log K_{\text{FeL}}$ value, protonation constants of Bha⁻ (Table 1), the stability constant (Table 2) and the molar absorptivity of the $[\text{Fe}(\text{Bha})_2(\text{OH})_2]^-$ complex were used. Stability and protonation constants obtained for $[\text{Fe}(\text{TRAP})]^{3-}$ are shown in Table 2.



Comparison of stability constants in **Table 2** reveals that the $\log K_{\text{ML}}$ values of $[\text{Fe}(\text{TRAP})]^{3-}$ and $[\text{Ga}(\text{TRAP})]^{3-}$ complexes are essentially equal and 2–3 $\log K$ unit smaller than those of the corresponding NOTA $^{3-}$ complexes. The higher stability constant of $[\text{Fe}(\text{NOTA})]$ and $[\text{Ga}(\text{NOTA})]$ complexes can be attributed to higher total basicity of NOTA $^{3-}$. The stability constant of $[\text{Fe}(\text{NOTA})]$ is about one $\log K$ unit lower than that of $[\text{Ga}(\text{NOTA})]$, which corresponds to a lower $\log K_1^{\text{H}}$ value of NOTA $^{3-}$ obtained in 0.1 M KCl solution. The triazacyclononane macrocyclic ligands with carboxylate or phosphinate pendant arms show similar affinity to Fe^{III} and Ga^{III} , which is readily explained by the facts that Ga^{3+} and Fe^{3+} have similar ionic radii (0.62 Å and 0.65 Å, respectively), and share the same charge and preferred coordination number ($\text{CN} = 6$).

The species distribution diagram of the Fe^{III} -TRAP $^{6-}$ system (**Figure 2**) shows that the Fe^{III} complex is fully formed even at $\text{pH} < 2$ in the form of a tri-protonated $[\text{Fe}(\text{H}_3\text{L})]$ species. Upon rising the pH from 2.0 to 7.0, stepwise deprotonation results in consecutive formation of $[\text{Fe}(\text{H}_2\text{L})]^-$ and $[\text{Fe}(\text{HL})]^{2-}$. Since the protonation constants characterizing the formation of the $[\text{Fe}(\text{HL})]^{2-}$, $[\text{Fe}(\text{H}_2\text{L})]^-$ and $[\text{Fe}(\text{H}_3\text{L})]$ species are very similar to the $\log K_3^{\text{H}}$, $\log K_4^{\text{H}}$ and $\log K_5^{\text{H}}$ values of the free TRAP $^{6-}$ ligand, $[\text{Fe}(\text{TRAP})]^{3-}$ is protonated on the non-coordinating carboxylate pendant arms. According to the known solid state structures of $[\text{Fe}(\text{H}_3\text{TRAP})]$, the coordination environment of Fe^{III} is characterized by the trigonal antiprismatic structure formed by the parallel ring-N₃ and phosphinate-O₃ planes, whereas the carboxylate groups are protonated and non-coordinated (the solid state structure of $[\text{Ga}(\text{H}_3\text{TRAP})]$ complex is very similar to that of $[\text{Fe}(\text{H}_3\text{TRAP})]$) (Notni et al., 2010). The $[\text{Fe}(\text{TRAP})]^{3-}$ complex predominates in the pH range 6.0–9.0. The pH-potentiometric titration data, obtained at $\text{pH} > 8$ for $[\text{Fe}(\text{TRAP})]^{3-}$, indicate a base-consuming process, which can be attributed to substitution of one of the phosphinate oxygens with a OH^- ion in the coordination sphere of Fe^{III} upon formation of the $[\text{Fe}(\text{TRAP})\text{OH}]^{4-}$ species [Equation (6)]. Similar processes were also identified for $[\text{Ga}(\text{TRAP})]^{3-}$, $[\text{Fe}(\text{NOTA})]$ (Figure S8 and **Table 2**) and $[\text{Ga}(\text{NOTA})]$ complexes (Notni et al., 2010; Simecek et al., 2012).

Formation Kinetics of Fe(TRAP) and Ga(TRAP) Complexes

The formation reactions between NOTA and various metals, such as lanthanide(III) ions (Ln^{III}) but also Ga^{III} , are typically slow at pH around 2.0–5.0 (Brucher and Sherry, 1990; Morfin and Toth, 2011). Since formation of Ln^{III} and Ga^{III} complexes of open-chain ligands is generally fast, the slow formation kinetics of the NOTA complexes can be attributed to the rigidity of the triaza-cyclononane macrocycle. Incorporation of Ln^{III} - and Ga^{III} -ions into the preformed coordination cage of NOTA is slow because of formation of stable mono-protonated $[\text{*Ln}(\text{HNOTA})]^+$ and $[\text{*Ga}(\text{HNOTA})]^+$ intermediates, which has been confirmed earlier by spectrophotometry measurements (Brucher and Sherry, 1990) and ^1H NMR spectroscopy (Morfin and Toth, 2011). Stability constants of such intermediates have furthermore been determined from kinetic data obtained by spectrophotometry (Brucher and Sherry, 1990) and ^1H NMR spectroscopy (Morfin and Toth, 2011). In the intermediate, the proton is most likely attached to a macrocyclic nitrogen, and the electrostatic repulsion between the proton and a Ln^{III} - or Ga^{III} -ion can inhibit fast entrance of the metal ion into the coordination cage. Formation rates of the $[\text{Ln}(\text{NOTA})]$ and $[\text{Ga}(\text{NOTA})]$ complexes are directly proportional to the OH^- concentration, meaning that a rate-determining OH^- assisted deprotonation and rearrangement of the monoprotonated intermediate is followed by entrance of the Ln^{III} - or Ga^{III} -ion into the N_3O_3 coordination cage of NOTA $^{3-}$ (Brucher and Sherry, 1990; Morfin and Toth, 2011).

In the present work, formation kinetics of M(TRAP) complexes ($\text{M}^{\text{III}} = \text{Fe}^{\text{III}}$ and Ga^{III}) have been studied by spectrophotometry on the absorption band of the forming $\text{Fe}(\text{TRAP})$ ($\lambda = 260 \text{ nm}$) and by ^{31}P -NMR spectroscopy following the integral value of the forming Ga(TRAP) complex in the pH range 4–6. UV-absorption as well as ^{31}P -NMR spectra, recorded after mixing of solutions containing $\text{Fe}(\text{NO}_3)_3$ or $\text{Ga}(\text{NO}_3)_3$ with HTRAP $^{5-}$ as functions of time, are shown in Figures S9, S10. For the reaction mixture of Fe^{III} -HTRAP $^{5-}$ at $\text{pH} = 6.0$, the absorption band observed between $\lambda = 245$ –320 nm (Figure S9) can be explained by the formation of the intermediate. The absorbance values in the $\lambda = 250$ –280 nm range increase with time, allowing for the conclusion that the intermediate is transformed into the final $[\text{Fe}(\text{TRAP})]^{3-}$ in-cage complex. Formation of the intermediate in Ga^{III} -TRAP reactions mixtures was previously proven by ^{31}P - and ^{71}Ga -NMR spectroscopy (Notni et al., 2010). Based on the similarity of TRAP and NOTA, it can be assumed that protonation of the ring nitrogen below $\text{pH} = 10.0$ initially hampers the formation of in-cage TRAP complexes while the three carboxylate and three phosphinate oxygen atoms of HTRAP $^{5-}$ can be coordinated to the metal ions to form a mono-protonated $[\text{*M}(\text{HTRAP})]^{2-}$ intermediate, in which the Fe^{III} and Ga^{III} -ion is situated outside of the coordination cage. To complete the complex formation, the proton has to be removed from the ring nitrogen via a OH^- -assisted reaction, followed by the rearrangement of the intermediate to the final $[\text{Fe}(\text{TRAP})]^{3-}$ and $[\text{Ga}(\text{TRAP})]^{3-}$ complexes (**Scheme 2**).

The formation rates of $[\text{Fe}(\text{TRAP})]^{3-}$ and $[\text{Ga}(\text{TRAP})]^{3-}$ have been studied under pseudo-first-order conditions in the presence of high excess of $\text{H}_x\text{TRAP}^{(x-6)}$ ($[\text{Fe}^{\text{III}}] = 1.0 \times 10^{-4}$ M; $[\text{TRAP}]_t = 0.5-4.0 \times 10^{-3}$ M; $[\text{Ga}^{\text{III}}] = 1.0 \times 10^{-3}$ M; $[\text{H}_x\text{TRAP}]_t = 5.0-30 \times 10^{-3}$ M, $x = 1$ and 2). Under such conditions the rate of formation reactions can be expressed by Equation (8).

$$\frac{d[\text{ML}]_t}{dt} = k_{\text{obs}} [\text{M}^{\text{III}}]_t \quad (8)$$

wherein $[\text{ML}]_t$ is the concentration of the $[\text{Fe}(\text{TRAP})]^{3-}$ and $[\text{Ga}(\text{TRAP})]^{3-}$ complexes, $[\text{M}^{\text{III}}]_t$ is the total concentration of species containing the Fe^{III} and Ga^{III} ions not bound to the $\text{H}_x\text{TRAP}^{(x-6)}$ ligand, and k_{obs} is a pseudo-first-order rate constant. As expected, the k_{obs} vs. $[\text{H}_x\text{TRAP}]_t$ curves (Figures 3, 4) are saturation curves indicating the formation of the $[\text{*M(HTRAP)}]^{2-}$ intermediates characterized by the stability constant defined by Equation (9).

$${}^*\text{K}_{\text{M(HL)}} = \frac{[\text{*M(HTRAP)}]}{[\text{M}^{\text{III}}][\text{HTRAP}]} \quad (9)$$

The rate-determining step of the reactions is the deprotonation and rearrangement of the $[\text{*M(HTRAP)}]^{2-}$ intermediates followed by the entrance of the metal ion into the coordination cage of the TRAP⁶⁻ ligand:

$$\begin{aligned} \frac{d[\text{ML}]_t}{dt} &= k_{\text{obs}} [\text{M}^{\text{III}}]_t = k_f [\text{*M(HTRAP)}] \\ &= k_f {}^*\text{K}_{\text{M(HTRAP)}} [\text{M}^{\text{III}}][\text{HTRAP}] \end{aligned} \quad (10)$$

wherein $[\text{*M(HTRAP)}]$ is the concentration of $[\text{*M(HTRAP)}]^{2-}$ intermediate and k_f is the rate constant characterizing the deprotonation and rearrangement of the intermediate to the $[\text{M(TRAP)}]^{3-}$ complex. In the pH range studied, the concentration of the non-complexed ligand ($[\text{TRAP}]_{\text{free}}$) can be expressed by Equation (11) using the protonation constants of TRAP⁶⁻ ligand (Table 1).

$$\begin{aligned} [\text{TRAP}]_{\text{free}} &= [\text{HTRAP}] (1 + K_2^{\text{H}}[\text{H}^+] + K_2^{\text{H}}K_3^{\text{H}}[\text{H}^+]^2 + \dots \\ &\quad + K_2^{\text{H}}K_3^{\text{H}}K_4^{\text{H}}K_5^{\text{H}}K_6^{\text{H}}[\text{H}^+]^5) = (1 + \alpha_{\text{H}})[\text{HTRAP}] \end{aligned} \quad (11)$$

where $\alpha_{\text{H}} = K_2^{\text{H}}[\text{H}^+] + K_2^{\text{H}}K_3^{\text{H}}[\text{H}^+]^2 + \dots + K_2^{\text{H}}K_3^{\text{H}}K_4^{\text{H}}K_5^{\text{H}}K_6^{\text{H}}[\text{H}^+]^5$. Under the conditions used in our experiments ($\text{pH} = 4.0-6.0$), hydrolysis of Fe^{III} and Ga^{III} may occur by formation of $[\text{M(OH)}]^{2+}$, $[\text{M(OH}_2]^+$ and M(OH)_3 species, i.e., OH^- ions may compete with $\text{H}_x\text{TRAP}^{(x-6)}$ for formation of $[\text{*M(HTRAP)}]^{2-}$ intermediate. Considering the hydrolysis of Fe^{III} and Ga^{III} , the total metal ion concentration can be expressed

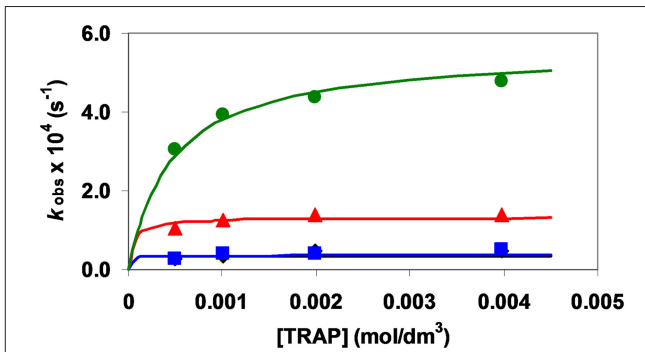


FIGURE 3 | k_{obs} pseudo-first order rate constants for the formation reaction of $[\text{Fe}(\text{TRAP})]^{3-}$ as a function of $[\text{H}_x\text{TRAP}]_t$ ($[\text{Fe}^{\text{III}}] = 0.1$ mM, $\text{pH} = 4.5$ (black diamond), 5.0 (blue square), 5.5 (red triangle), and 6.0 (green circle), $x = 1$ and 2, 0.15 M NaNO_3 and 25°C).

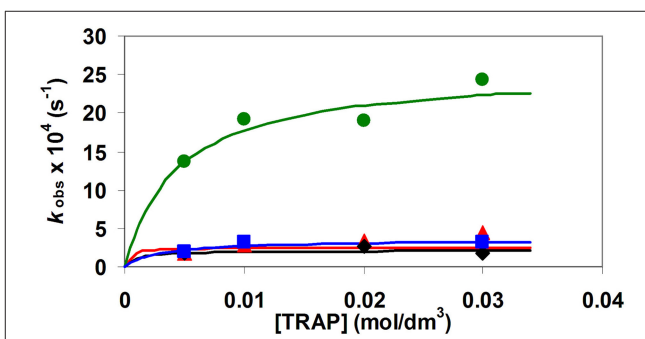
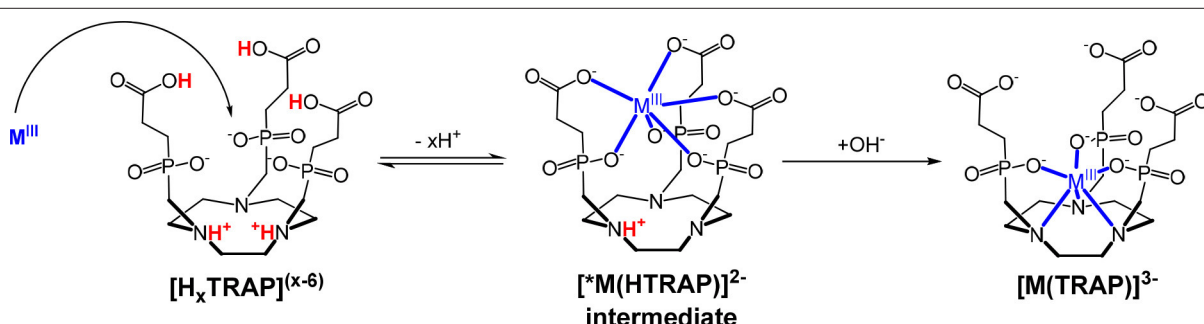


FIGURE 4 | k_{obs} pseudo-first order rate constants for the formation reaction of $[\text{Ga}(\text{TRAP})]^{3-}$ as a function of $[\text{H}_x\text{TRAP}]_t$ ($[\text{Ga}^{\text{III}}] = 1$ mM, $\text{pH} = 4.6$ (black diamond), 5.0 (blue square), 5.6 (red triangle), and 6.0 (green circle), $x = 1$ and 2, 0.15 M NaNO_3 and 25°C).



by Equation (12).

$$[\text{M}^{\text{III}}]_t = [{}^*\text{M}(\text{HTRAP})] + [\text{M(OH)}] + [\text{M(OH)}_2] + [\text{M(OH)}_3] + [\text{M}^{\text{III}}] \quad (12)$$

By taking into account the stability constant of the $[{}^*\text{M}(\text{HTRAP})]^{2-}$ intermediate [Equation (9)] and the equilibrium constants characterizing the hydrolysis of Fe^{III} and Ga^{III} ($\beta_x = [\text{M(OH)}_x][\text{H}^+]^x/[\text{M}^{\text{III}}]$, $x = 1, 2$, and 3), the total metal ion concentration can be expressed as follows:

$$[\text{M}^{\text{III}}]_t = [\text{M}^{\text{III}}] \left(1 + \frac{{}^*\text{K}_{\text{M}(\text{HTRAP})}[\text{TRAP}]_{\text{free}}}{1 + \alpha_{\text{OH}}} + \frac{\beta_1^{\text{OH}}}{[\text{H}^+]} + \frac{\beta_2^{\text{OH}}}{[\text{H}^+]^2} + \frac{\beta_3^{\text{OH}}}{[\text{H}^+]^3} \right) = [\text{M}^{\text{III}}] \left(1 + \frac{{}^*\text{K}_{\text{M}(\text{HTRAP})}[\text{TRAP}]_{\text{free}}}{1 + \alpha_{\text{OH}}} + \alpha_{\text{OH}} \right) \quad (13)$$

wherein $\alpha_{\text{OH}} = \beta_1^{\text{OH}}/[\text{H}^+] + \beta_2^{\text{OH}}/[\text{H}^+]^2 + \beta_3^{\text{OH}}/[\text{H}^+]^3$ ($\log \beta_1^{\text{OH}} = -2.19$; $\log \beta_2^{\text{OH}} = -5.67$ and $\log \beta_3^{\text{OH}} = -12.0$ for Fe^{III} and $\log \beta_1^{\text{OH}} = -2.97$; $\log \beta_2^{\text{OH}} = -5.92$ and $\log \beta_3^{\text{OH}} = -8.2$ for Ga^{III} ion; Baes and Mesmer, 1976). Considering the protonation constants of TRAP^{6-} (Table 1), the stability constant of the $[{}^*\text{M}(\text{HTRAP})]^{2-}$ intermediate [Equation (9)], the total concentration of the M^{III} ion [Equation (13)], the concentration of the non-complexed $\text{TRAP}_{\text{free}}$ ligand [Equation (11) and Equation (10)], the pseudo-first order rate constant can be expressed by Equation (14).

$$k_{\text{obs}} = \frac{k_f {}^*\text{K}_{\text{M}(\text{HTRAP})}[\text{TRAP}]_{\text{free}}}{1 + \frac{{}^*\text{K}_{\text{M}(\text{HTRAP})}[\text{TRAP}]_{\text{free}}}{1 + \alpha_{\text{H}}} + \alpha_{\text{OH}}} \quad (14)$$

The pseudo-first-order rate constants determined at various pH and $[\text{TRAP}]_t$ values (Figures 3, 4) were fitted to Equation (14) and the stability constant of the $[{}^*\text{M}(\text{HTRAP})]^{2-}$ intermediates $[{}^*\text{K}_{\text{M}(\text{HL})}]$ and the k_f rate constants were calculated.

The stability constants of the $[{}^*\text{Fe}(\text{HTRAP})]^{2-}$ and $[{}^*\text{Ga}(\text{HTRAP})]^{2-}$ intermediates [$\log {}^*\text{K}_{\text{M}(\text{HL})}$] are 9.9 ± 0.1 and 10.4 ± 0.1 , respectively. The $\log {}^*\text{K}_{\text{M}(\text{HL})}$ values of the $[{}^*\text{Fe}(\text{HTRAP})]^{2-}$ and $[{}^*\text{Ga}(\text{HTRAP})]^{2-}$ intermediates are significantly higher than those of the mono-protonated $[{}^*\text{Ga}(\text{HNOTA})]^+$ ($\log {}^*\text{K}_{\text{Ga}(\text{HL})} = 4.2$), (Morfin and Toth, 2011) $[{}^*\text{Ce}(\text{HNOTA})]^+$ ($\log {}^*\text{K}_{\text{Ce}(\text{HL})} = 3.2$), (Brucher and Sherry, 1990) $[{}^*\text{Gd}(\text{HNOTA})]^+$ ($\log {}^*\text{K}_{\text{Gd}(\text{HL})} = 3.6$) (Brucher and Sherry, 1990) and $[{}^*\text{Er}(\text{HNOTA})]^+$ ($\log {}^*\text{K}_{\text{Er}(\text{HL})} = 3.8$) (Brucher and Sherry, 1990) intermediates. In the $[{}^*\text{Fe}(\text{HTRAP})]^{2-}$ and $[{}^*\text{Ga}(\text{HTRAP})]^{2-}$ intermediates, Fe^{III} and Ga^{III} are presumably coordinated by three carboxylate and three phosphinate oxygen donor atoms, whereas the metal ions in $[{}^*\text{M}(\text{HNOTA})]^+$ intermediates are coordinated by three carboxylate oxygen donor atoms, resulting in lower $\log {}^*\text{K}_{\text{M}(\text{HL})}$ values.

The calculated k_f rate constants obtained for formation of $[\text{Fe}(\text{TRAP})]^{3-}$ and $[\text{Ga}(\text{TRAP})]^{3-}$ complexes are shown in Figure 5 as functions of $[\text{OH}^-]$. Kinetic data in Figure 5 show that the k_f values increase monotonously with increasing OH^- concentration, while interception of linear extrapolations at the origin indicates that under our experimental conditions, deprotonation and transformation of the $[{}^*\text{M}(\text{HTRAP})]^{2-}$ intermediate to the final $[\text{M}(\text{TRAP})]^{3-}$ complex predominantly occurs by an OH^- -catalyzed pathway. The k_{OH} rate constants

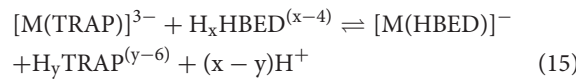
calculated from the slopes of the straight lines in Figure 5 are shown in Table 3.

Comparison of the k_{OH} rate constants presented in Table 3 shows that the formation rates of $[\text{Ga}(\text{TRAP})]^{3-}$ and $[\text{Ga}(\text{NOTA})]$ complexes in this pathway are similar and about two orders of magnitude lower than those of $[\text{Ln}(\text{NOTA})]$ complexes. The results of the labeling experiments with the TRAP and NOTA chelates of ${}^{68}\text{Ga}^{\text{III}}$ at identical conditions (10 nM ligand, pH = 3.3 and 20 °C) shows that the formation

rate of ${}^{68}\text{Ga}(\text{TRAP})]^{3-}$ surpasses that of ${}^{68}\text{Ga}(\text{NOTA})]$ (Notni et al., 2010). The faster formation of ${}^{68}\text{Ga}(\text{TRAP})]^{3-}$ can be explained by the higher stability $[{}^*\text{K}_{\text{Ga}(\text{HL})}]$ and consequently the higher concentration of the kinetically active $[{}^*\text{Ga}(\text{HTRAP})]^{2-}$ intermediate that results in the more rapid formation of ${}^{68}\text{Ga}(\text{TRAP})]^{3-}$ in the same labeling condition. On the other hand, the formation rate of $[\text{Fe}(\text{TRAP})]^{3-}$ is about 3 times lower than that of $\text{Ga}(\text{TRAP})$, which allows to perform selective labeling of TRAP with ${}^{68}\text{Ga}^{\text{III}}$ even in presence of Fe^{III} contaminations in the eluate.

Kinetic Inertness and Transchelation Reaction of Complexes

In order to compare the kinetic inertness, the rates of transchelation reactions of $\text{Fe}(\text{TRAP})$ and $\text{Ga}(\text{TRAP})$ complexes with $\text{H}_x\text{HBED}^{x-4}$ ($x = 0, 1$ and 2) ligand were studied because of the high stability of the $[\text{Fe}(\text{HBED})]^-$ and $[\text{Ga}(\text{HBED})]^-$ complexes [$\log K_{\text{Fe}(\text{HBED})} = 39.01$, $\log K_{\text{Ga}(\text{HBED})} = 38.51$, 0.1 M KCl, 25 °C, (Ma et al., 1994)]. The transchelation reactions were followed by spectrophotometry on the absorption band of the forming $[\text{Fe}(\text{HBED})]^-$ and $[\text{Ga}(\text{HBED})]^-$ complexes in the pH ranges 11.0–14.0 and 9.0–12.0, respectively. The absorption spectra of the protonated HHBED^{3-} and $\text{H}_2\text{HBED}^{2-}$ ligands and $[\text{Ga}(\text{HBED})]^-$ complex are different, whereas that of the deprotonated HBED^{4-} ligand and $[\text{Ga}(\text{HBED})]^-$ complex are very similar. Therefore, the transchelation reactions of $[\text{Ga}(\text{TRAP})]^{3-}$ with HHBED^{3-} and $\text{H}_2\text{HBED}^{2-}$ could be monitored by spectrophotometry only up to pH = 12.0 (HBED^{4-} : $\log K_1^{\text{H}} = 12.57(4)$, $\log K_2^{\text{H}} = 11.41(3)$, $\log K_3^{\text{H}} = 8.22(5)$, $\log K_4^{\text{H}} = 4.73(6)$ and $\log K_5^{\text{H}} = 1.45(6)$, 0.15 M NaCl, 25 °C). Some characteristic absorption spectra of $[\text{Fe}(\text{TRAP})]^{3-}-\text{H}_x\text{HBED}^{x-4}$ and $[\text{Ga}(\text{TRAP})]^{3-}-\text{H}_x\text{HBED}^{x-4}$ ($x = 0, 1$ and 2) reacting systems are shown in Figures S11, S12, respectively. The transchelation reactions can be described by Equation (15)



wherein M^{III} is Fe^{III} or Ga^{III} , $x = 0, 1$ and 2 and $y = 0$ and 1 . The rates of the transchelation reactions have been studied in the presence of 10- and 20-fold excess of $\text{H}_x\text{HBED}^{(x-4)}$, so a pseudo-first order kinetic model can be applied and the rates of reaction

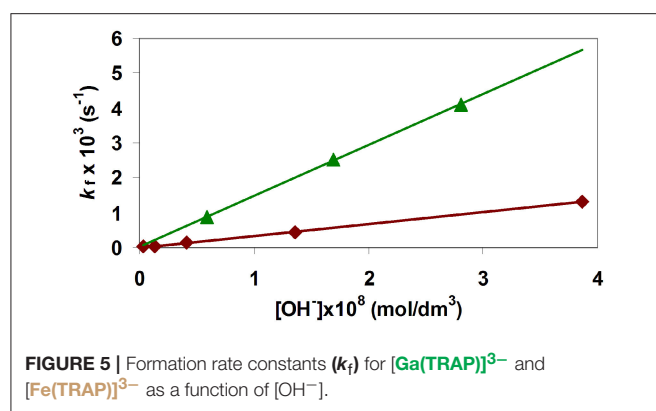
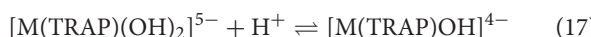


FIGURE 5 | Formation rate constants (k_f) for $[\text{Ga}(\text{TRAP})]^{3-}$ and $[\text{Fe}(\text{TRAP})]^{3-}$ as a function of $[\text{OH}^-]$.

Equation (15) can be expressed by Equation (16):

$$-\frac{d[\text{M}(\text{TRAP})]_t}{dt} = k_d [\text{M}(\text{TRAP})]_t \quad (16)$$

wherein k_d is a pseudo-first-order rate constant, $[\text{M}(\text{TRAP})]_t$ is the total concentration of $[\text{Fe}(\text{TRAP})]^{3-}$ and $[\text{Ga}(\text{TRAP})]^{3-}$ complexes. The pseudo-first-order rate constants (k_d) characterizing the transchelation reactions of $[\text{Fe}(\text{TRAP})]^{3-}$ and $[\text{Ga}(\text{TRAP})]^{3-}$ with $\text{H}_x\text{HBED}^{(x-4)}$ at different $-\log[\text{H}^+]$ and $[\text{OH}^-]$ values are shown in Figure 6. The kinetic data presented in Figure 6 show that the k_d values are independent of the concentration of $\text{H}_x\text{HBED}^{(x-4)}$ and increase with $-\log[\text{H}^+]$ and $[\text{OH}^-]$, indicating that the rate-determining step of the transchelation reactions is the dissociation of the $[\text{Fe}(\text{TRAP})]^{3-}$ and $[\text{Ga}(\text{TRAP})]^{3-}$ complexes, followed by fast reaction of free Fe^{III} and Ga^{III} with $\text{H}_x\text{HBED}^{(x-4)}$. The k_d values presented in Figure 6 show the similar behavior of $[\text{Fe}(\text{TRAP})]^{3-}$ and $[\text{Ga}(\text{TRAP})]^{3-}$ complexes in their transchelation reactions. The k_d vs. $-\log[\text{H}^+]$ and k_d vs. $[\text{OH}^-]$ curves (Figure 6) obtained for $[\text{Ga}(\text{TRAP})]^{3-}$ and $[\text{Fe}(\text{TRAP})]^{3-}$ reach saturation of the k_d values at $[\text{OH}^-] > 0.015 \text{ M}$ and $[\text{OH}^-] > 1.0 \text{ M}$, respectively. Based on the species distribution of the $\text{Ga}^{\text{III}}\text{-TRAP}^{6-}$ (Notni et al., 2010) and $\text{Fe}^{\text{III}}\text{-TRAP}^{6-}$ (Figure 2) systems, the transchelation reaction of $[\text{Ga}(\text{TRAP})]^{3-}$ and $[\text{Fe}(\text{TRAP})]^{3-}$ with $\text{H}_x\text{HBED}^{(x-4)}$ may occur by the spontaneous dissociation of $[\text{M}(\text{TRAP})]^{3-}$ (k_0) and $[\text{M}(\text{TRAP})\text{OH}]^{4-}$ species (${}^{\text{M(L)}}\text{OH}k_{\text{OH}}$), whereas the pH-independent dissociation rate (k_d) of $[\text{M}(\text{TRAP})]^{3-}$ under more basic conditions corresponds to formation [$K_{\text{M(L)}}(\text{OH})_2$, Equation (17)] and slow dissociation of the bis(hydroxo) $[\text{M}(\text{TRAP})(\text{OH})_2]^{5-}$ intermediate.



$$K_{\text{M(L)}}(\text{OH})_2 = \frac{[\text{M}(\text{TRAP})\text{OH}]}{[\text{M}(\text{TRAP})(\text{OH})_2][\text{H}^+]}$$

It can be assumed that in the $[\text{M}(\text{TRAP})(\text{OH})_2]^{5-}$ intermediate, TRAP⁶⁻ is coordinating via four donor atoms, whereas the remaining two coordination sites of Ga^{III} and Fe^{III} are occupied by two OH^- ions. Hence, a spontaneous dissociation of the $[\text{M}(\text{TRAP})(\text{OH})_2]^{5-}$ intermediate is more probable, which is reflected by the ${}^{\text{M(L)}}\text{OH}k_{\text{OH}}$ rate constants. The mechanisms of

the transchelation reactions of $[\text{Fe}(\text{TRAP})]^{3-}$ and $[\text{Ga}(\text{TRAP})]^{3-}$ are summarized in Scheme 3.

By taking into account all possible pathways (Scheme 3), the dissociation rate of $[\text{Fe}(\text{TRAP})]^{3-}$ and $[\text{Ga}(\text{TRAP})]^{3-}$ can be expressed by Equation (18).

$$-\frac{d[\text{ML}]_t}{dt} = k_d [\text{ML}]_t = k_0[\text{ML}] + {}^{\text{M(L)}}\text{OH}k_{\text{OH}}[\text{M(L)}\text{OH}] + {}^{\text{M(L)}}(\text{OH})_2k_{\text{OH}}[\text{M(L)}(\text{OH})_2] \quad (18)$$

Considering the total concentrations of $[\text{Fe}(\text{TRAP})]^{3-}$ and $[\text{Ga}(\text{TRAP})]^{3-}$ ($[\text{ML}]_t = [\text{ML}] + [\text{M(L)}\text{OH}] + [\text{M(L)}(\text{OH})_2]$) and the protonation constants of $[\text{M(L)}\text{OH}]^{4-}$ ($K_{\text{M(L)}}\text{OH}$, Equation (6), Table 2) and $[\text{M(L)}(\text{OH})_2]^{5-}$ intermediates ($K_{\text{M(L)}}(\text{OH})_2$, Equation (17)), the k_d pseudo-first-order rate constants presented in Figure 6 can be expressed by Equation (19).

$$k_d = \frac{k_0 K_{\text{M(L)}}\text{OH}[\text{H}^+] + {}^{\text{M(L)}}\text{OH}k_{\text{OH}} + {}^{\text{M(L)}}(\text{OH})_2k_{\text{OH}}(K_{\text{M(L)}}\text{OH}[\text{H}^+])^{-1}}{1 + K_{\text{M(L)}}\text{OH}[\text{H}^+] + (K_{\text{M(L)}}(\text{OH})_2[\text{H}^+])^{-1}} \quad (19)$$

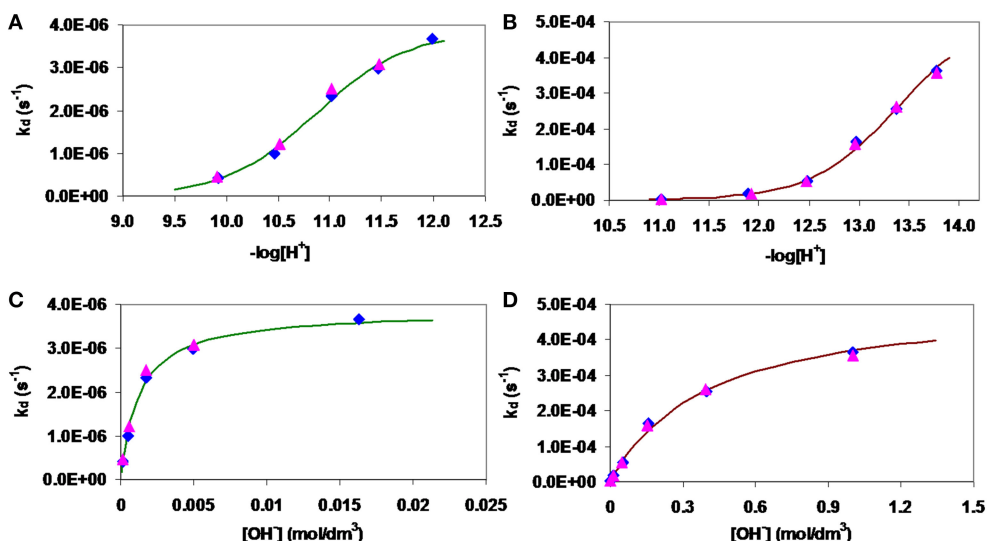
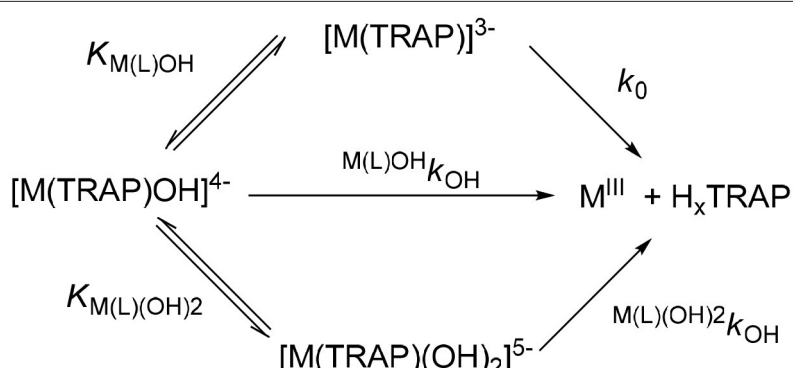
wherein k_0 , ${}^{\text{M(L)}}\text{OH}k_{\text{OH}}$ and ${}^{\text{M(L)}}(\text{OH})_2k_{\text{OH}}$ are the rate constants characterizing the spontaneous dissociation of $[\text{M}(\text{TRAP})]^{3-}$, and $[\text{M}(\text{TRAP})\text{OH}]^{4-}$ complexes and $[\text{M}(\text{TRAP})(\text{OH})_2]^{5-}$ intermediates, whereas $K_{\text{M(L)}}(\text{OH})_2$ is the equilibrium constant characterizing the formation of the bis(hydroxo) $[\text{M}(\text{TRAP})(\text{OH})_2]^{5-}$ intermediates.

The rate and protonation constants characterizing the transchelation reactions of $[\text{Fe}(\text{TRAP})]^{3-}$ and $[\text{Ga}(\text{TRAP})]^{3-}$ with $\text{H}_x\text{HBED}^{(x-4)}$ have been calculated by fitting the k_d values presented in Figure 6 to the Equation (19), and the resulting values are shown in Table 3. We obtained a very low value with a large error for k_0 ; therefore, the spontaneous dissociation of $[\text{Fe}(\text{TRAP})]^{3-}$ and $[\text{Ga}(\text{TRAP})]^{3-}$ is negligible under our experimental conditions. The ${}^{\text{M(L)}}\text{OH}k_{\text{OH}}$ rate constants characterizing the spontaneous dissociation of $[\text{Fe}(\text{TRAP})\text{OH}]^{4-}$ and $[\text{Ga}(\text{TRAP})\text{OH}]^{4-}$ complexes are very similar, which indicates that the kinetic inertness of $[\text{Fe}(\text{TRAP})\text{OH}]^{4-}$ and $[\text{Ga}(\text{TRAP})\text{OH}]^{4-}$ are comparable. Interestingly, the $K_{\text{M(L)}}(\text{OH})_2$ protonation constants indicate that the formation of $[\text{Fe}(\text{TRAP})(\text{OH})_2]^{5-}$ intermediate takes place at significantly higher $-\log[\text{H}^+]$ values than that of $[\text{Ga}(\text{TRAP})(\text{OH})_2]^{5-}$. However, the ${}^{\text{M(L)}}(\text{OH})_2k_{\text{OH}}$ rate constant of $[\text{Fe}(\text{TRAP})(\text{OH})_2]^{5-}$ intermediate is about two orders of magnitude higher than that of $[\text{Ga}(\text{TRAP})(\text{OH})_2]^{5-}$, which indicates the considerably lower kinetic inertness of the $[\text{Fe}(\text{TRAP})(\text{OH})_2]^{5-}$ intermediate.

In order to compare the kinetic inertness directly, the half-lives ($t_{1/2} = \ln 2/k_d$) of the dissociation reactions of $[\text{Fe}(\text{TRAP})]^{3-}$ and $[\text{Ga}(\text{TRAP})]^{3-}$ at pH = 7.4 have been calculated, utilizing the rate and equilibrium constants presented in Table 3. The $t_{1/2}$ values of Fe(TRAP) and Ga(TRAP) are 1.1×10^5 and 1.4×10^5 h, respectively, which indicates a similar kinetic inertness of $[\text{Fe}(\text{TRAP})]^{3-}$ and $[\text{Ga}(\text{TRAP})]^{3-}$ due to comparable ${}^{\text{M(L)}}\text{OH}k_{\text{OH}}$ rate constants of the $[\text{Fe}(\text{TRAP})\text{OH}]^{4-}$

TABLE 3 | Rate constants characterizing the formation (k_{OH}) and dissociation ($\text{M(L)}\text{OH}k_{\text{OH}}$, $\text{M(L)}(\text{OH})_2k_{\text{OH}}$) of $[\text{Fe}(\text{TRAP})]^{3-}$, $[\text{Ga}(\text{TRAP})]^{3-}$, $[\text{Ga}(\text{NOTA})]$, and $[\text{Ln}(\text{NOTA})]$ complexes (25°C).

	Formation kinetics			Dissociation kinetics		
	$k_{\text{OH}} / \text{M}^{-1}\text{s}^{-1}$	$\text{M(L)}\text{OH}k_{\text{OH}}/\text{s}^{-1}$	$\text{M(L)}(\text{OH})_2k_{\text{OH}}/\text{s}^{-1}$	$\log K_{\text{M(L)}(\text{OH})_2}$	k_d/s^{-1} at pH = 7.4	$t_{1/2}/\text{h}$ at pH = 7.4
$[\text{Fe}(\text{TRAP})]^{3-}$	$(3.37 \pm 0.02) \times 10^4$	$(4 \pm 1) \times 10^{-7}$	$(5.2 \pm 0.4) \times 10^{-4}$	13.4 (1)	1.8×10^{-9}	1.1×10^5
$[\text{Ga}(\text{TRAP})]^{3-}$	$(1.47 \pm 0.02) \times 10^5$	$(4.3 \pm 0.5) \times 10^{-7}$	$(3.8 \pm 0.2) \times 10^{-6}$	10.9 (1)	1.4×10^{-9}	1.4×10^5
$[\text{Ga}(\text{NOTA})]^a$	1.14×10^5	—	—	—	—	—
$[\text{Ce}(\text{NOTA})]^b$	6.3×10^7	—	—	—	—	—
$[\text{Gd}(\text{NOTA})]^b$	7.1×10^7	—	—	—	—	—
$[\text{Er}(\text{NOTA})]^b$	5.5×10^7	—	—	—	—	—

^aRef. (Morfin and Toth, 2011); ^bRef. (Brucher and Sherry, 1990).**FIGURE 6 |** Pseudo-first-order rate constants (k_d) of the ligand exchange reactions of $[\text{Ga}(\text{TRAP})]^{3-}$ (A,C) and $[\text{Fe}(\text{TRAP})]^{3-}$ (B,D) with $\text{H}_x\text{HBED}^{(x-4)}$ as a function of $-\log[\text{H}^+]$ and $[\text{OH}^-]$ ($x = 0, 1$, and 2). Solid lines and symbols represent calculated and experimental k_d pseudo-first-order rate constants, respectively. ($[\text{Ga}(\text{TRAP})] = [\text{Fe}(\text{TRAP})] = 0.2 \text{ mM}$, $[\text{H}_x\text{HBED}] = 2.0 \text{ mM}$ (blue diamonds), and 4.0 mM NaCl, 25°C).**SCHEME 3 |** Proposed mechanism of the dissociation of $[\text{Fe}(\text{TRAP})]^{3-}$ and $[\text{Ga}(\text{TRAP})]^{3-}$ complexes ($x = 0$ and 1).

and $[Ga(TRAP)OH]^{4-}$ complexes. On the other hand, reliability of our kinetic data is supported by a good agreement of the dissociation half-life for $[Ga(TRAP)]^{3-}$ at pH = 11 determined in this study ($t_{1/2} = 86$ h) with the literature value of $t_{1/2} \approx 60$ h (Notni et al., 2010).

CONCLUSION

Due to the availability of $^{68}\text{Ge}/^{68}\text{Ga}$ generators, recent years have seen an ever-growing interest in the radionuclide $^{68}\text{Ga}^{\text{III}}$ for PET examinations. The corresponding radiopharmaceuticals generally contain $^{68}\text{Ga}^{\text{III}}$ in form of chelates, for which purpose dedicated bifunctional chelators are usually conjugated to biological targeting vectors. The carrier-free $^{68}\text{Ga}^{\text{III}}$ obtained by acidic elution from the generator may contain some metal ions as impurities in trace amounts. These metal ions, like Ti^{IV} , Fe^{III} , Cu^{II} , and Zn^{II} , may compete with the $^{68}\text{Ga}^{\text{III}}$ for the chelator's binding sites. Hence, knowledge of the possible interactions of these ions and Ga^{III} with chelates are highly important.

In this work, the interaction of Ga^{III} and Fe^{III} ions with H_6TRAP , a phosphinic acid analog of H_3NOTA , were studied and compared. The stability constants of the $[Ga(\text{TRAP})]^{3-}$ and $[\text{Fe}(\text{TRAP})]^{3-}$ complexes were found to be very similar, as are their very low dissociation rates at physiological pH. The dissociation predominantly occurs via spontaneous dissociation of mono-hydroxo $[\text{M}(\text{TRAP})\text{OH}]^{4-}$ complexes and bis(hydroxo) $[\text{M}(\text{TRAP})(\text{OH})_2]^{5-}$ intermediates. Similarly to the respective NOTA complexes, formation of $\text{Ga}(\text{TRAP})$ and $\text{Fe}(\text{TRAP})$ is slow and occurs by formation of the monoprotonated $[\text{M}(\text{HTRAP})]^{2-}$ intermediates. The stability of these intermediates is very high, presumably because both the phosphinate and carboxylate groups of the ligand are coordinated. However, although we observed an extraordinary similarity of the thermodynamic and kinetic properties of the $\text{Ga}(\text{TRAP})$ and $\text{Fe}(\text{TRAP})$ complexes, there is a small but important difference between the two systems: the formation rate of $\text{Ga}(\text{TRAP})$ is approximately three times higher than that of the $\text{Fe}(\text{TRAP})$, which has implications for the influence of Fe^{III} contaminations on ^{68}Ga labeling of TRAP.

Apparently, the previously observed selectivity of TRAP for $^{68}\text{Ga}^{\text{III}}$ over Fe^{III} is rooted in a totally different mechanism than the preference of TRAP for Ga^{III} over Cu^{II} and Zn^{II} (Simecek et al., 2013). Because $\text{Fe}(\text{TRAP})$ is formed more slowly than $\text{Ga}(\text{TRAP})$, formation of $^{68}\text{Ga}(\text{TRAP})$ is preferred and even a

3-fold excess of Fe^{III} over TRAP does not substantially reduce the labeling yield. However, $\text{Fe}(\text{TRAP})$ is kinetically inert, and a higher excess of Fe^{III} ultimately inhibits the $^{68}\text{Ga}^{\text{III}}$ incorporation due to an irreversible consumption of all available TRAP. On the other hand, the TRAP complexes of Zn^{II} and Cu^{II} are formed much faster but they are not inert (Baranyai et al., 2015). Unlike Fe^{III} , TRAP-bound Cu^{II} and particularly Zn^{II} may therefore be readily displaced by Ga^{III} (Simecek et al., 2013), driven by a much higher thermodynamic stability of $[Ga(\text{TRAP})]^{3-}$ as compared to $[\text{Zn}(\text{TRAP})]^{4-}$ and $[\text{Cu}(\text{TRAP})]^{4-}$ ($\log K_{\text{ML}}$ of 26.24, 16.07, and 19.09, respectively) (Notni et al., 2010; Baranyai et al., 2015). Hence, in contrast to Fe^{III} , even high concentrations of Cu^{II} and particularly that of Zn^{II} do not completely inhibit ^{68}Ga labeling of TRAP, likewise resulting in a pronounced tolerance of these potential contaminants. We conclude that even a phenomenon of elementary character, namely, the selectivity of TRAP for Ga^{III} which manifests itself in a tolerance of remarkably high concentrations of different metal ion impurities during $^{68}\text{Ga}^{\text{III}}$ labeling, may rely on a variety of driving forces and molecular properties, thus requiring a detailed investigation of mechanistic details for thorough understanding.

AUTHOR CONTRIBUTIONS

AV and AF contributed to the equilibrium and kinetic characterizations; AW performed the ligand synthesis; EB, IT, AM, H-JW, JN, and ZB contributed to the evaluation of the physico-chemical parameters and to the manuscript preparation.

ACKNOWLEDGMENTS

Support by the Deutsche Forschungsgemeinschaft (grant #NO822/4-1 and SFB 824, project A10), the EU and the European Regional Development Fund (projects GINOP-2.3.2-15-2016-00008 and GINOP-2.3.3-15-2016-00004) are gratefully acknowledged. The project has been carried out in the frame of the EU COST Action CA15209: European Network on NMR Relaxometry.

SUPPLEMENTARY MATERIAL

The Supplementary Material for this article can be found online at: <https://www.frontiersin.org/articles/10.3389/fchem.2018.00170/full#supplementary-material>

REFERENCES

- Baes, C. F., and Mesmer, R. E. (1976). *The Hydrolysis of Cations*. New York, NY; London; Sydney; Toronto, ON: John Wiley & Son.
- Baranyai, Z., Reich, D., Vagner, A., Weinreisen, M., Toth, I., Wester, H. J., et al. (2015). A shortcut to high-affinity Ga-68 and Cu-64 radiopharmaceuticals: one-pot click chemistry trimerisation on the TRAP platform. *Dalton Trans.* 44, 11137–11146. doi: 10.1039/C5DT00576K
- Bevilacqua, A., Gelb, R. I., Hebard, W. B., and Zompa, L. J. (1987). Equilibrium and thermodynamic study of the aqueous complexation of 1,4,7-triazacyclononane-N,N',N"-triacetic acid with protons, alkaline-earth-metal cations, and copper(II). *Inorg. Chem.* 26, 2699–2706. doi: 10.1021/ic00263a029
- Beyer, T., Townsend, D. W., Brun, T., Kinahan, P. E., Charron, M., Roddy, R., et al. (2000). A combined PET/CT scanner for clinical oncology. *J. Nucl. Med.* 41, 1369–1379.
- Brucher, E., and Sherry, A. D. (1990). Kinetics of formation and dissociation of the 1,4,7-triazacyclononane-N,N',N"-triacetate complexes of cerium(III), gadolinium(III), and erbium(III) ions. *Inorg. Chem.* 29, 1555–1559. doi: 10.1021/ic00333a022

- Clarke, E. T., and Martell, A. E. (1991). Stabilities of the Fe(III), Ga(III) and In(III) chelates of N,N',N''-triazacyclononanetriacetic acid. *Inorg. Chim. Acta* 181, 273–280. doi: 10.1016/S0020-1693(00)86821-8
- Drahos, B., Kubicek, V., Bonnet, C. S., Hermann, P., Lukes, I., and Toth, E. (2011). Dissociation kinetics of Mn²⁺ complexes of NOTA and DOTA. *Dalton Trans.* 40, 1945–1951 doi: 10.1039/c0dt01328e
- Farkas, E., Kozma, E., Petho, M., Herlihy, K. M., and Micera, G. (1998). Equilibrium studies on copper(II)- and iron(III)-monohydroxamates. *Polyhedron* 17, 3331–3342. doi: 10.1016/S0277-5387(98)00113-2
- Frank, R., and Patrick, J. R. (2010). The renaissance of the ⁶⁸Ge/⁶⁸Ga radionuclide generator initiates new developments in ⁶⁸Ga radiopharmaceutical chemistry. *Curr. Top. Med. Chem.* 10, 1633–1668. doi: 10.2174/156802610793176738
- Geraldes, C. F. G. C., Sherry, A. D., Marques, M. P. M., Alpoim, M. C., and Cortes, S. (1991). Protonation scheme for some triaza macrocycles studied by potentiometry and NMR spectroscopy. *J. Chem. Soc. Perkin Trans. 2*, 137–146. doi: 10.1039/p29910000137
- Irving, H. M., Miles, M. G., and Pettit, L. D. (1967). A study of some problems in determining the stoichiometric proton dissociation constants of complexes by potentiometric titrations using a glass electrode. *Anal. Chim. Acta* 38, 475–488. doi: 10.1016/S0003-2670(01)80616-4
- Levi, H. (1976). George von Hevesy memorial lecture. George Hevesy and his concept of radioactive indicators in retrospect. *Eur. J. Nucl. Med.* 1, 3–10. doi: 10.1007/BF00253259
- Ma, R., Motekaitis, R. J., and Martell, A. E. (1994). Stability of metal ion complexes of N,N'-bis(2-hydroxybenzyl)ethylenediamine-N,N'-diacetic acid. *Inorg. Chim. Acta* 224, 151–155. doi: 10.1016/0020-1693(94)04012-5
- Mariko, T., and Susumu, T. (1977). The preparation of trivalent metal chelates with some N3O3-type ligands. *Bull. Chem. Soc. Jpn.* 50, 3413–3414. doi: 10.1246/bcsj.50.3413
- Morfin, J. F., and Toth, E. (2011). Kinetics of Ga(NOTA) formation from weak Ga-citrate complexes. *Inorg. Chem.* 50, 10371–10378. doi: 10.1021/ic201445e
- Notni, J. (2012). With Gallium-68 into a New Era? *Nachr. Chem.* 60, 645–649. doi: 10.1515/nachrchem.2012.60.6.645
- Notni, J., Hermann, P., Havlickova, J., Kotek, J., Kubicek, V., Plutnar, J., et al. (2010). A triazacyclonane-based bifunctional phosphinate ligand for the preparation of multimeric ⁶⁸Ga tracers for positron emission tomography. *Chem. Eur. J.* 16, 7174–7185. doi: 10.1002/chem.200903281
- Notni, J., Simecek, J., Hermann, P., and Wester, H. J. (2011). TRAP, a powerful and versatile framework for gallium-68 radiopharmaceuticals. *Chem. Eur. J.* 17, 14718–14722. doi: 10.1002/chem.201103503
- Notni, J., Simecek, J., and Wester, H. J. (2014). Phosphinic acid functionalized polyazacycloalkane chelators for radiodiagnostics and radiotherapeutics: unique characteristics and applications. *ChemMedChem.* 9, 1107–1115. doi: 10.1002/cmde.201400055
- Notni, J., and Wester, H.-J. (2018). Re-thinking the role of radiometal isotopes: towards a future concept for theranostic radiopharmaceuticals. *J. Label. Compd. Radiopharm.* 61, 141–153. doi: 10.1002/jlcr.3582
- Rösch, F. (2013). Past, present and future of ⁶⁸Ge/⁶⁸Ga generators. *Appl. Rad. Isot.* 76, 24–30 doi: 10.1007/978-3-642-27994-2_1
- Simecek, J., Hermann, P., Wester, H. J., and Notni, J. (2013). How is ⁶⁸Ga labeling of macrocyclic chelators influenced by metal ion contaminants in ⁶⁸Ge/⁶⁸Ga generator eluates? *ChemMedChem.* 8, 95–103. doi: 10.1002/cmde.201200471
- Simecek, J., Schulz, M., Notni, J., Plutnar, J., Kubicek, V., Havlickova, J., et al. (2012). Complexation of metal ions with TRAP (1,4,7-triazacyclononane phosphinic acid) ligands and 1,4,7-triazacyclonone-1,4,7-triacetic acid: phosphinate-containing ligands as unique chelators for trivalent gallium. *Inorg. Chem.* 51, 577–590. doi: 10.1021/ic202103v
- Simecek, J., Zemeck, O., Hermann, P., Notni, J., and Wester, H. J. (2014). Tailored Gallium(III) chelator NOPO: synthesis, characterization, bioconjugation, and application in preclinical Ga-68-PET imaging. *Mol. Pharm.* 11, 3893–3903. doi: 10.1021/mp400642s
- Velikyan, I. (2011). Positron emitting [68G]Ga-based imaging agents: chemistry and diversity. *Med. Chem.* 7, 345–379. doi: 10.2174/157340611796799195
- Wadas, T. J., Wong, E. H., Weisman, G. R., and Anderson, C. J. (2010). Coordinating radiometals of copper, gallium, indium, yttrium, and zirconium for PET and SPECT imaging of disease. *Chem. Rev.* 110, 2858–2902. doi: 10.1021/cr900325h
- Zekany, L., and Nagypal, I. (1985). “PSEQUAD,” in *Computational Methods for the Determination of Formation Constants*, ed D. Leggett (Springer), 291–353.

Conflict of Interest Statement: The authors declare that the research was conducted in the absence of any commercial or financial relationships that could be construed as a potential conflict of interest.

The reviewer, FG, and handling Editor declared their shared affiliation.

Copyright © 2018 Vágner, Forgács, Brücher, Tóth, Maiocchi, Wurzer, Wester, Notni and Baranyai. This is an open-access article distributed under the terms of the Creative Commons Attribution License (CC BY). The use, distribution or reproduction in other forums is permitted, provided the original author(s) and the copyright owner are credited and that the original publication in this journal is cited, in accordance with accepted academic practice. No use, distribution or reproduction is permitted which does not comply with these terms.

Advantages of publishing in Frontiers



OPEN ACCESS

Articles are free to read for greatest visibility and readership



FAST PUBLICATION

Around 90 days from submission to decision



HIGH QUALITY PEER-REVIEW

Rigorous, collaborative, and constructive peer-review



TRANSPARENT PEER-REVIEW

Editors and reviewers acknowledged by name on published articles



REPRODUCIBILITY OF RESEARCH

Support open data and methods to enhance research reproducibility



DIGITAL PUBLISHING

Articles designed for optimal readership across devices



FOLLOW US
@frontiersin



IMPACT METRICS
Advanced article metrics track visibility across digital media



EXTENSIVE PROMOTION
Marketing and promotion of impactful research



LOOP RESEARCH NETWORK
Our network increases your article's readership

Frontiers

Avenue du Tribunal-Fédéral 34
1005 Lausanne | Switzerland

Visit us: www.frontiersin.org

Contact us: info@frontiersin.org | +41 21 510 17 00